JET Art. 14 - Contract JE 3 /9009

"LIDAR-Thomson Scattering"

Final Report / June 15, 1984

G. Brederlow[+], J.E. Gruber[++], K. Hirsch[+++],
H. Röhr[++], H. Salzmann[+++], K.J. Witte[+]

IPP 1/299 June 1984

IPF-84-3

MAX-PLANCK-INSTITUT FÜR PLASMAPHYSIK

8046 GARCHING BEI MÜNCHEN

MAX-PLANCK-INSTITUT FÜR PLASMAPHYSIK

GARCHING BEI MÜNCHEN

JET Art. 14 - Contract JE 3 /9009
"LIDAR-Thomson Scattering"
Final Report / June 15, 1984

G. Brederlow[+], J.E. Gruber[++], K. Hirsch[+++],
H. Röhr[++], H. Salzmann[+++], K.J. Witte[+]

IPP 1/299 June 1984
IPF-84-3

[+]) MPI für Quantenoptik, 8046 Garching
[++]) MPI für Plasmaphysik, 8046 Garching
[+++]) Institut für Plasmaforschung, Univ. Stuttgart

Die nachstehende Arbeit wurde im Rahmen des Vertrages zwischen dem Max-Planck-Institut für Plasmaphysik und der Europäischen Atomgemeinschaft über die Zusammenarbeit auf dem Gebiete der Plasmaphysik durchgeführt.

IPP 1/299
IPF-84-3

G. Brederlow, J.E. Gruber,
K. Hirsch, H. Röhr,
H. Salzmann, K.J. Witte

JET Art. 14 - Contract
JE 3/9009
"LIDAR-Thomson Scattering"
Final Report / June 15,1984

Abstract

This report describes the design of a LIDAR (Light Detection and Ranging) Thomson scattering system.

The time-resolved measurement of the backscattered light from a sub-nanosecond laser enables spatial resolution via time-of-flight measurements. A spatial resolution of 12 cm is achieved using an iodine laser (15 J at 657 nm, 300 ps pulse duration) in combination with microchannelplate photomultipliers (response time 400 ps FWHM) and a 1 GHz oscilloscope.

The statistical errors of the electron temperature and density measurements are calculated. For a five channel spectrometer a dynamic range (defined by $\Delta T_e/T_e \leq 10\%$ at $n_e = 1 \times 10^{13}$ cm^{-3}) of 0.7 keV to 15 keV can be achieved. The minimum statistical errors $\Delta T_e/T_e = 4\%$ and $\Delta n_e/n_e = 2.6\%$ are reached at 5 keV.

Several laser input and collection optics for measuring vertical spatial profiles over a 2.5 m chord length are examined and compared. A spatial scanning option enabling measurements at the inner part of the plasma cross section is considered. Suppression of stray light is accomplished by means of suitable stops. Alignment and calibration methods are discussed.

With a small, frequency-doubled test laser system the feasibility of 1 Hz operation over a sequence of 10 shots has been demonstrated successfully. The design of a 15 J frequency-doubled laser system is considered in detail.

The performance of a high-speed MCP photomultiplier was investigated experimentally. Risetime, saturation recovery and gating properties were determined. The results show that the detector is well suited for the intended use.

The stray light level to be expected was determined in a full-scale

optical set-up using a low-energy, frequency-doubled iodine laser. It is shown that the stray light will constitute no problem for the Thomson scattering experiments due to the good gating properties of the detector. Even Rayleigh scattering measurements for absolute calibration at 1 Torr hydrogen filling pressure should be possible.

In summary, the design study shows that the proposed LIDAR Thomson scattering technique is applicable to JET and to future large fusion devices.

CONTENTS

1 INTRODUCTION

LIDAR Thomson scattering is a laser backscatter technique proposed recently /1/. It uses a time-of-flight method to measure spatial profiles along the laser beam. For this purpose a high energy, subnanosecond laser and a sensitive highspeed detection technology are needed.

The LIDAR scattering method seems promising with respect to the following points of view:

1. Simple optics. Only a small number of optical components is located in the torus hall.
2. Only a small window is needed on the torus vessel.
3. Plasma background radiation is negligible for the short observation times and does not deteriorate the measurements.
4. Stable alignment. No feedback alignment is required.

This study investigates whether a LIDAR Thomson scattering technique can be applied to measure electron temperature and density profiles on JET.

First, we establish what results can be obtained using a 15 J / 300 ps frequency doubled iodine laser pulse (λ = 657 mm). The statistical errors to be expected for the electron temperature and density are calculated. The spatial resolution along the laser beam is obtained from simple arguments as well as from a numerical simulation.

Second, we describe in detail an optical laser input and scattered light collection system whose parameters are consistent with the above considerations. This optics is designed to measure a vertical spatial chord of JET. The alignment and stability problems of the optical system are discussed and calibration techniques are investigated.

Third, an iodine laser system is described which produces laser pulses with the required parameters. The operation of such an exi-

sting laser system at 1 Hz repetition rate is investigated. Maintenance and lifetime problems are discussed.

Fourth, the properties of a high-speed photomultiplier (risetime less than 200 ps) are examined. Especially, it is investigated how to gate this detector. Gating of the photomultiplier is necessary since an intense stray light pulse in advance of the measuring signal is expected for a backscatter set-up.

Fifth, the level of stray light is measured in a full scale set-up of the proposed input and collection optics.

2 SUMMARY OF RESULTS

The results of the investigations conducted under contract JE 3/9009 show that the proposed LIDAR Thomson scattering diagnostic is technically feasible on JET. In the following, the results are summarized briefly under the headings of the sections where the investigations are described in detail.

Statistical Errors of Electron Temperature and Density

An analytical treatment yields that at $n_e = 1 \times 10^{13}$ cm^{-3} and T_e = 5 keV a statistical error of ± 4 % is to be expected for the electron temperature. The dynamic range of the described 5-channel filter polychromator (defined by errors ≤ ± 10 %) is about 0.7 keV to 15 keV. It can be shifted by changing the spectral filters. The corresponding statistical errors of the electron density measurement are 2.6 % at 5 keV, 10 % at 0.5 keV and 5 % at 20 keV.

The errors of both the electron temperature and the density will improve approximately with the square root of the density.

Spatial Resolution

A simple consideration shows that the spatial resolution Δl is given by $\Delta l = \frac{C}{2}(\tau_L + \tau_{DET.})$, where τ_L is the laser pulse duration and τ_{DET} is the response time of the detection system. For our case a resolution of 13 cm is obtained. Thus a single laser shot yields a radial profile consisting of about 16 measurements. A numerical simulation taking a $\sin^2$ - shaped laser pulse (FWHM = 300 ps) and an available 1 GHz-detection system confirms this result. It shows in addition that the spatial resolution can be improved by using numerical unfolding techniques.

Laser Input and Collection Optics

Different laser input and collection optics for measuring vertical spatial profiles over a 2.5 m chord length are examined and compa-

red. The optical systems are identical with respect to solid angle of collection and transmission, parameters being used to evaluate the expected error bars. Each optical system requires two 10 cm dia. ducts through the ceiling. These ducts are inclined to ease radiological shielding. Laser and detection system are located in the roof laboratory.

The optical solution which is favourable from the point of view of its remote handling capability features a telescopic collection optics mounted to the limbs of the magnetic circuit. A total number of 3 optical components to be aligned individually will be located in the torus hall.

Scanning Option

LIDAR scattering in principle offers the possibility to scan the plasma with the laser beam without the need of realigning the collection optics. This could give access to the inner part of the plasma. However, an experimental test is still needed to check the impurity production by the laser pulse hitting a beam dump on the inner wall of the torus vessel.

Alignment

A simple procedure for first alignment is described. Due to the rather large tolerances of the alignment precision, no feedback realignment is necessary.

Calibration

At the stray light level expected on the basis of measurements on a full-scale optical set-up and taking advantage of the measured gating properties of the detector, Rayleigh scattering will be one feasible calibration technique. Changes of the spectral transmission of the window are included in the calibration of the relative sensitivity of the spectral channels by viewing a blackbody light source through the vessel. Comparison with the electron line den-

sity obtained from DCN interferometry will constitute a further calibration method.

Laser System

With a small test laser consisting of a water-cooled mode-locked oscillator, a pulse selecting system, one air-cooled amplifier and a frequency doubling KD*P crystal the feasibility of a 1 Hz-operation extending over a sequence of 10 shots could be successfully demonstrated. At 2ω (657 nm) the pulse had an energy of 40 mJ and a duration of 950 ps whereby a conversion efficiency of 45 % was achieved. According to our present experience a system meeting the required specifications of 10 pulses with 1 Hz repetition rate and 15 J/0.3 ns per pulse at 657 nm can be confidentially built based upon the technology and design considerations employed in the small test laser.

A 2- to 3- Hz operation seems feasible if the flow velocity of the laser medium is correspondingly increased and all amplifier quartz tubes are water-cooled. Eventually the flashlamps have also to be gas-cooled.

The projected laser system can be operated by a single technician. The envisaged service times and their frequency are such that they will not interfere with the routine operation of the diagnostic system.

Detector Tests

A high-speed microchannelplate photomultiplier with a gain of 10^5 was tested experimentally. A risetime of 180 ps was measured. The FWHM response time is less than 400 ps (thus rendering the 1 GHz oscilloscope the bandwidth limiting component of the detection system).

Saturating the detector by overloading does not affect the measurements at the next laser pulse (at 1 Hz repetition rate).

The gating tests show that light pulses containing up to 10^9 photons within the response time of the detector can be tolerated 18 ns in front of the measuring signal. This time interval corresponds to the time lapse between the stray light pulse from the entrance window and the scattering signal from the plasma boundary.

Stray Light Measurements

Since the level of stray light cannot be predicted reliably, measurements were performed on a full-scale optical set-up using a frequency doubled 1 ns iodine laser. The measurements yield that the entrance window will cause ~ 2×10^{10} stray light photons incident on the detector in case of the investigated optical system.

3 DESIGN CONSIDERATIONS

3.1 Statistical Errors of Electron Temperature and Density

3.1.1 Method of evaluation

In order to facilitate a check of the calculated statistical errors we have chosen an analytical method for their evaluation. With this analytical procedure the error of the measurement of T_e is considered first. For this purpose the n signals from the n spectral channels are used to perform n-1 independent temperature measurements by using the two channel ratio method /2,3/. The error propagation in this method can be treated very easily. From the calculated statistical errors of the n-1 independent measurements the error of the mean is then obtained in the usual way.

Second, the error of the electron density measurement is treated. For this purpose the ratio R of the number N of scattered photons within the spectral range of detection to the number N_{tot} of scatterede photons within the whole spectrum is calculated as a function of the electron temperature. The uncertainty of the factor R is calculated from the statistical error of the electron temperature. Then the number of scattered photons within the spectral range of detection is obtained by summing up the no. of photoelectrons within the spectral channels, weighted with the corresponding quantum efficiency of the detector. The error of this quantity is obtained from the errors of the photoelectron numbers. Finally the total number of scattered photons (the measure of the electron density) and its error is calculated taking into account the correction factor R and its error.
In detail the procedure is as follows:

1) The spectral channels are chosen.
2) The expected number n_i^p of background photoelectrons in each spectral channel i is calculated for parabolic plasma profiles and given central density and temperature.

3) The number n_i^s of photoelectrons due to scattered light is calculated for each spectral channel i as a function of the electron temperature.

4) The results for the 5 spectral channels are used to calculate the 10 possible ratios n_k^s/n_i^s as a function of T_e.

5) The errors of the numbers n_i^s at the photocathode of the detector (photomultiplier or streak camera + image intensifier) are given by the inverse of the corresponding SNR

$$\frac{\Delta n_i^s}{n_i^s} = (SNR_i)^{-1} = \frac{\sqrt{n_i^s + n_i^p}}{n_i^s}$$

6) At the output of the detector the SNR will be deteriorated by the excess noise of the amplification process. This effect is described by the excess noise factor which is defined here as

$$F = \frac{SNR_{OUTPUT}}{SNR_{CATHODE}}$$

Thus

$$\frac{\Delta n_i^s}{n_i^s} = F \frac{\sqrt{n_i^s + n_i^p}}{n_i^s}$$

7) These errors propagate to the rations n_k^s/n_i^s as

$$\frac{\Delta\left(\frac{n_k^s}{n_i^s}\right)}{\frac{n_k^s}{n_i^s}} = \sqrt{\left(\frac{\Delta n_k^s}{n_k^s}\right)^2 + \left(\frac{\Delta n_i^s}{n_i^s}\right)^2}$$

8) The error of n_k^s/n_i^s propagates to the electron temperature when using the two channel ratio method and results in an electron temperature error of

$$\Delta T_e = \frac{\partial T_e}{\partial\left(\frac{n_k^s}{n_i^s}\right)} \Delta\left(\frac{n_k^s}{n_i^s}\right)$$

Thus

$$\Delta T_e^{k,i} = F \frac{n_k^s}{n_i^s} \sqrt{\frac{n_k^s + n_k^p}{n_k^{s2}} + \frac{n_i^s + n_i^p}{n_i^{s2}}} \cdot \frac{1}{\partial\left(\frac{n_k^s}{n_i^s}\right)/\partial T_e}$$

9) From the obtained 10 values $T_e \pm \Delta T_e$ those 4 with the lowest errors ΔT_e are chosen which are evaluated from independent ratios n_k^s/n_i^s.

10) The errors of these 4 independent sample measurements yield an error of the mean given by /4/

$$\Delta T_e^2 = \frac{1}{\sum_{\ell=1}^{4} \left(\frac{1}{\Delta T_e^\ell}\right)^2}$$

11) The ration of detectable photons to the number of photons contained within the whole spectrum is calculated (see Sec. 3.1.4)

$$R(T_e) = \frac{\int_{\varepsilon_1}^{\varepsilon_2} (\varepsilon+1)\, S(\varepsilon)\, d\varepsilon}{\int_{-1}^{\infty} (\varepsilon+1)\, S(\varepsilon)\, d\varepsilon}$$

12) The error of the electron temperature determined by steps 1) to 10) results in an error

$$\Delta R(T_e) = \frac{\partial R}{\partial T_e} \Delta T_e$$

13) The numbers N_i^s of scattered photons contained in the spectral channels are summed up assuming an average quantum efficiency of each spectral channel

$$N = \sum_i \frac{n_i^s}{\eta_i}$$

The error of the sum is

$$\Delta N = \left\{ \sum_i \left(\frac{\Delta n_i^s}{\eta_i} \right)^2 \right\}^{1/2}$$

14) The number N_{tot} of photons contained in the whole spectrum (the measure of the electron density) is given by

$$N_{tot} = \frac{N}{R(Te)}$$

and its error by

$$\frac{\Delta N_{tot}}{N_{tot}} = \sqrt{\left(\frac{\Delta N}{N}\right)^2 + \left(\frac{\Delta R}{R}\right)^2}$$

15) Thus finally

$$\frac{\Delta n_e}{n_e}(T_e, n_e) = \sqrt{\frac{\sum_i (\Delta n_i^s/\eta_i)^2}{\left(\sum_i (n_i^s/\eta_i)\right)^2} + \left[\frac{\frac{\partial R}{\partial Te}(T_e) \cdot \Delta T_e(T_e)}{R(T_e)}\right]^2}$$

3.1.2 Set of parameters

The statistical errors of the measurement calculated in the following are obtained for the parameters:

Laser energy at 6576 Å (2ω)	15 J
Laser beam diameter	7.5 cm
Laser beam divergence	5 x diffraction limit
Laser pulse duration	300 ps
Focal length of focusing lens	840 cm
Focal spot location	85 cm above equatorial plane
Focal length of collection optics (surrounding the focusing lens)	420 cm

Diameter of collection optics	25 cm outer dia. 7.5 cm inner dia.
Spatial chord length	2.5 m (40 cm below equatorial plane to upper plasma edge)
Resulting observed plasma volume (stop diameter chosen to allow collection of scattered light from the whole spatial chord length without vignetting)	$V = \frac{\pi}{4} \cdot 5^2$ cm^2 x 420 cm
Resulting solid angle for observation of plasma centre	$d\Omega_o = 5.22 \times 10^{-4}$ sr
Transmission of collection optics	T = 0.1
No polarizer used in the detection optics	
Spectral channels	I 6247 Å - 6027 Å II 6027 - 5587 III 5587 - 5037 IV 5037 - 4487 V 4487 - 3937
Detector quantum efficiency	S 20
Excess noise factor of detection system	F = 1.8
Bandwidth of detection system	1 Ghz → τ = 600 ps
Resulting length of spatial channel	L = 13 cm
Electron density profile	parabolic $N_e = n_e^o(1-(\frac{r}{r_o})^2)$, r_o = 2.1 m
Electron temperature profile	parabolic $T_e = T_e^o(1-(\frac{r}{r_o})^2)$
Plasma central density	1 x 10^{13} cm^{-3}
Plasma central temperature	5 keV
Plasma radiation	100 x pure hydrogen bremsstrahlung

3.1.3 Plasma Radiation

Assuming parabolic profiles of electron density and temperature the spatial profile of the emission coefficient reads

$$\varepsilon_{ff}(\lambda, r) = \varepsilon_{ff}(\lambda, 0)\left(1-\left(\frac{r}{r_0}\right)^2\right)^{3/2}$$

For calculating the number of background photoelectrons the small variation of solid angle of collection along the spatial chord has been neglected. The quantum efficiency η is assumed to be constant within the wavelength interval $\Delta\lambda$ of the spectral channel centred at λ. Thus

$$n_\lambda^p \approx 100\,\eta(\lambda)\,V\,d\Omega_0\,\tau\,\Delta\lambda\,\frac{\varepsilon_{ff}(\lambda,0)}{\frac{hc}{\lambda}}\int_{-r_0}^{r_0}\left(1-\left(\frac{r}{r_0}\right)^2\right)^{3/2}dr$$

which yields the numbers given in Table 3.I. In the mean time the plasma radiation from JET was measured to be 5 x 10^{11} photons /cm^2/s/sr/nm at 524 nm. This is ~ 7 times less than in this estimate.

Spectral channel	T_e^o = 1 keV	T_e^o = 5 keV	T_e^o = 20 keV
I	4	2	1
II	12	5	3
III	22	10	5
IV	32	14	8
V	42	19	10

Table 3.I
Number of photoelectrons n_i^p due to background radiation. Parameters as given in 3.1.2.

3.1.4 Scattering Signal

The spectral density function S(ε) of the relativistic Thomson backscattering spectrum is calculated from the formulas given by Mattioli et al. /5/ which yield exactly the same results as those given by Zhuravlev /6/. In /5/ the scattering cross section σ is given by

$$\sigma(\lambda, \theta = 180^\circ) = \frac{r_0^2}{\sqrt{\pi T_e}} \cdot \frac{\left(\frac{\lambda_L}{\lambda_s}\right)^4}{\sqrt{1 + 2\frac{\lambda_L}{\lambda_s} + \left(\frac{\lambda_L}{\lambda_s}\right)^2}} \cdot \frac{1}{1 + \frac{15}{16} T_e + \frac{105}{512} T_e^2} \cdot \exp\left\{-\frac{1}{T_e}\left(\sqrt{\frac{\lambda_s}{\lambda_L} + 2 + \frac{\lambda_L}{\lambda_s}} - 2\right)\right\}$$

where T_e is normalised to the electron rest mass energy $T_e \to 2kT_e/mc^2$ and λ_L and λ_s are the laser wavelength and the wavelength of the scattered light.

r_o is the classical electron radius. Introducing $\varepsilon = \frac{\lambda_s}{\lambda_L} - 1$

$$\sigma(\varepsilon, 180^\circ) = \frac{r_0^2}{\sqrt{\pi T_e}} \cdot \frac{1}{(\varepsilon+1)^3(\varepsilon+2)} \cdot \frac{1}{1 + \frac{15}{16} T_e + \frac{105}{512} T_e^2} \cdot \exp\left\{-\frac{1}{T_e}\left(\frac{\varepsilon+2}{\sqrt{\varepsilon+1}} - 2\right)\right\}$$

Defining the spectral density function S(ε) as

$$S(\varepsilon) = \frac{\sigma(\varepsilon)}{r_0^2}$$

shown in Fig. 3.1 the number of electrons released from a photocathode per unit interval of ε for a laser pulse of energy E_L is given by

$$\frac{dn^s(\varepsilon)}{d\varepsilon} = n_e L \frac{E_L}{h\nu_L} r_0^2 \Delta\Omega T \eta(\varepsilon)(\varepsilon+1) S(\varepsilon)$$

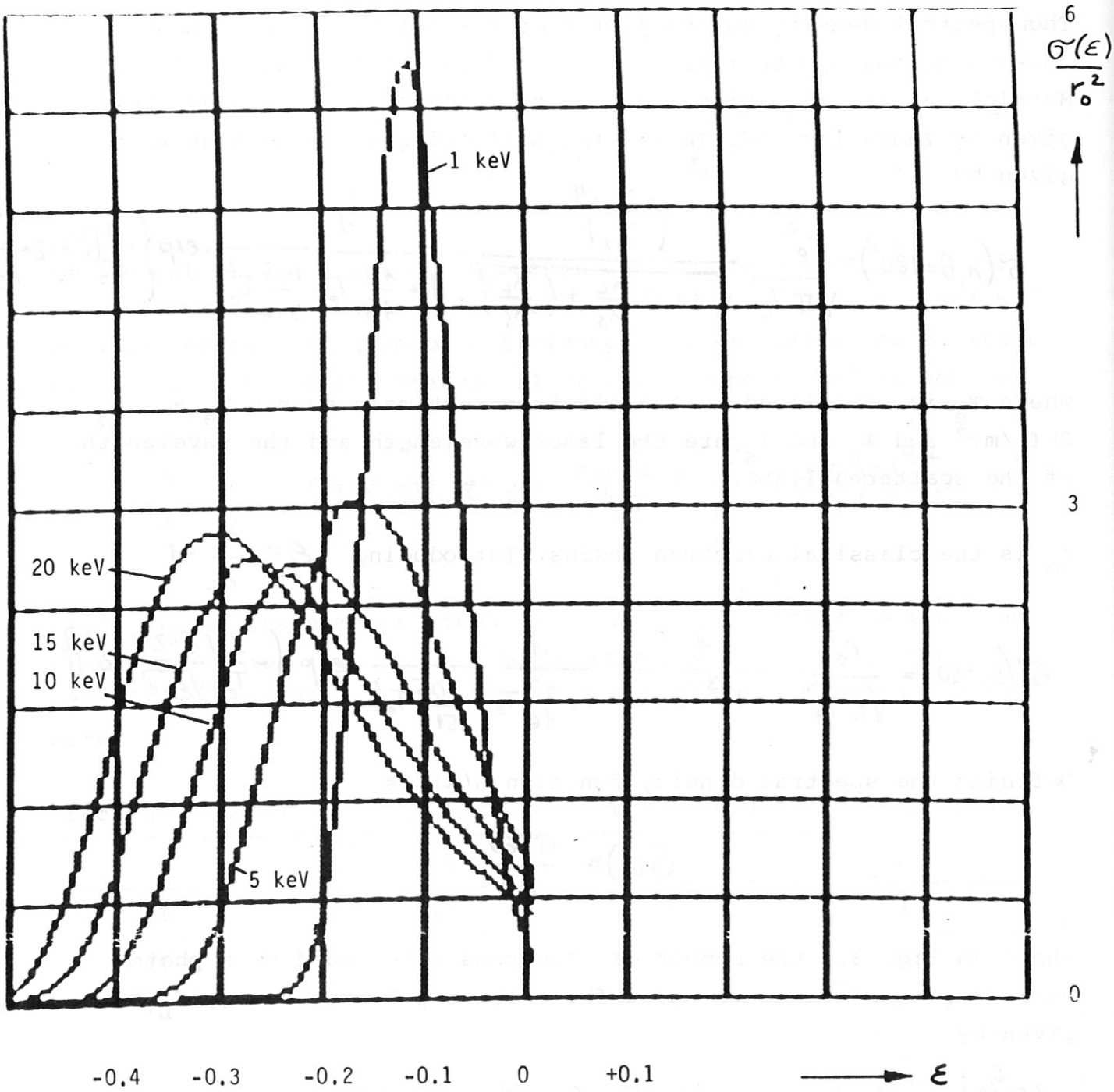

Fig. 3.1

Spectral density function $\sigma(\varepsilon)/r_o^2$ versus $\varepsilon = \frac{\lambda_s}{\lambda_L} - 1$

This function is plotted in Fig. 3.2. The quantum efficiency of the S 20 cathode was thereby approximated by

$$\eta(\varepsilon) = 0.225 - 0.45(\varepsilon + 0.4)$$

Integration over the width of the spectral channels yields the numbers of signal photoelectrons n_i^s in channel i = 1 - 5 as function of the electron temperature. These functions are shown in Fig. 3.3. Please note that the results shown in Fig. 3.2 and 3.3 apply to $n_e = 5 \times 10^{13}$ cm^{-3}, $\Delta\Omega = 1 \times 10^{-3}$ sr and a length of the scattering volume of 18 cm. The numbers of signal photoelectrons obtained from the spatial channel located at the plasma centre at the given reference conditions ($n_e^o = 1 \times 10^{13}$ cm^{-3}) are listed in Table 3.II. Since we are interested in the errors of single shots, photoelectron numbers of the order of 1 and below in the spectral channels cannot be used for an evaluation as indicated in Table 3.II.

3.1.5 Statistical error of the electron temperature

Figs. 3.4 - 3.7 show the ratios of the signals from the different spectral channels versus electron temperature. Using the ratio method small temperature errors will be obtained in temperature ranges where the ratio depends strongly upon temperature and where the number of signal photoelectrons in both channels is large.

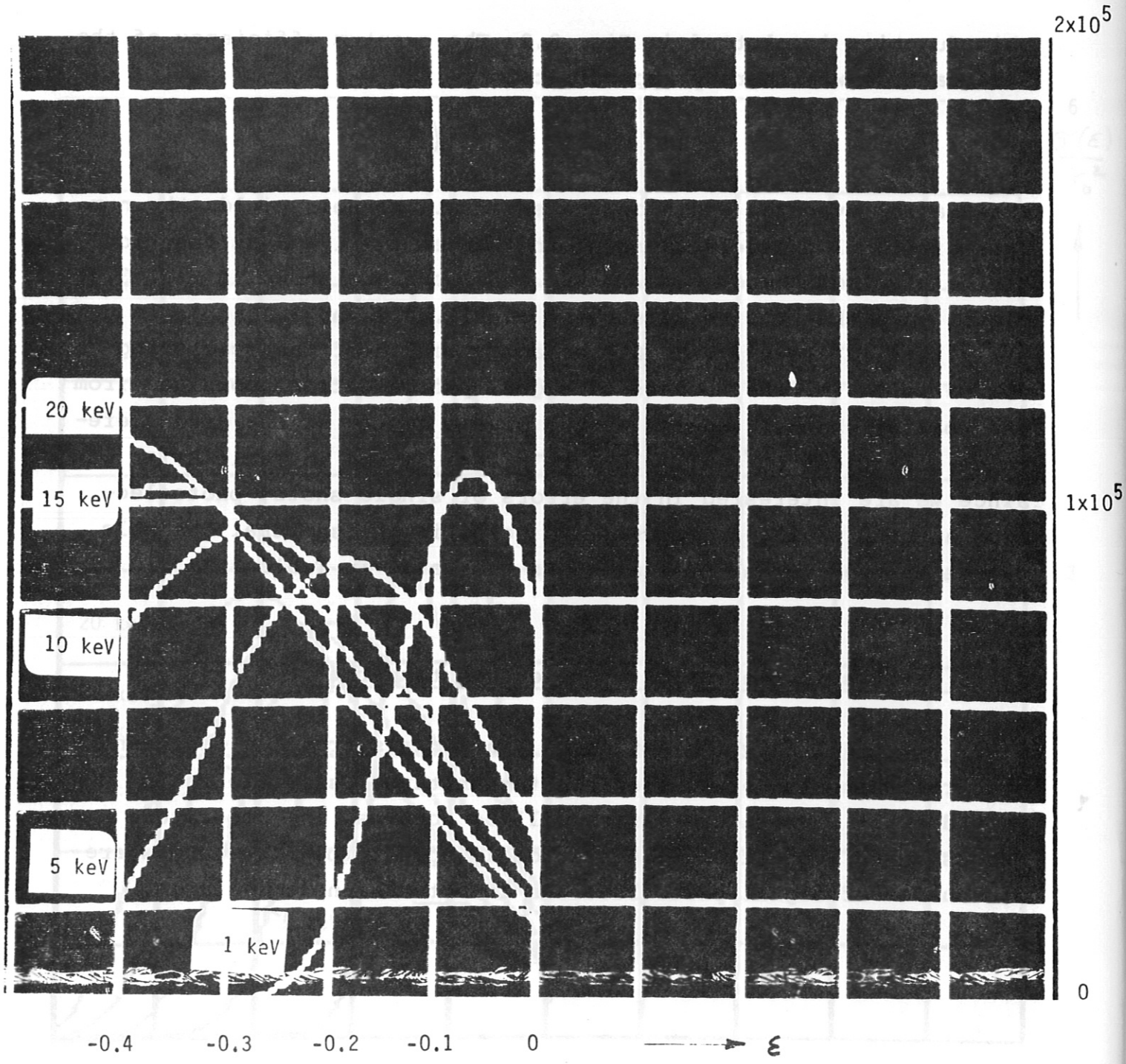

Fig. 3.2

Number of photoelectrons per unit of ε

Parameters: Laser energy 15 J at 6576 Å, $n_e = 5 \times 10^{13}$ cm^{-3}

$d\Omega = 1 \times 10^{-3}$ sr,

L = 18 cm, T = 0.1, S 20 - photocathode.

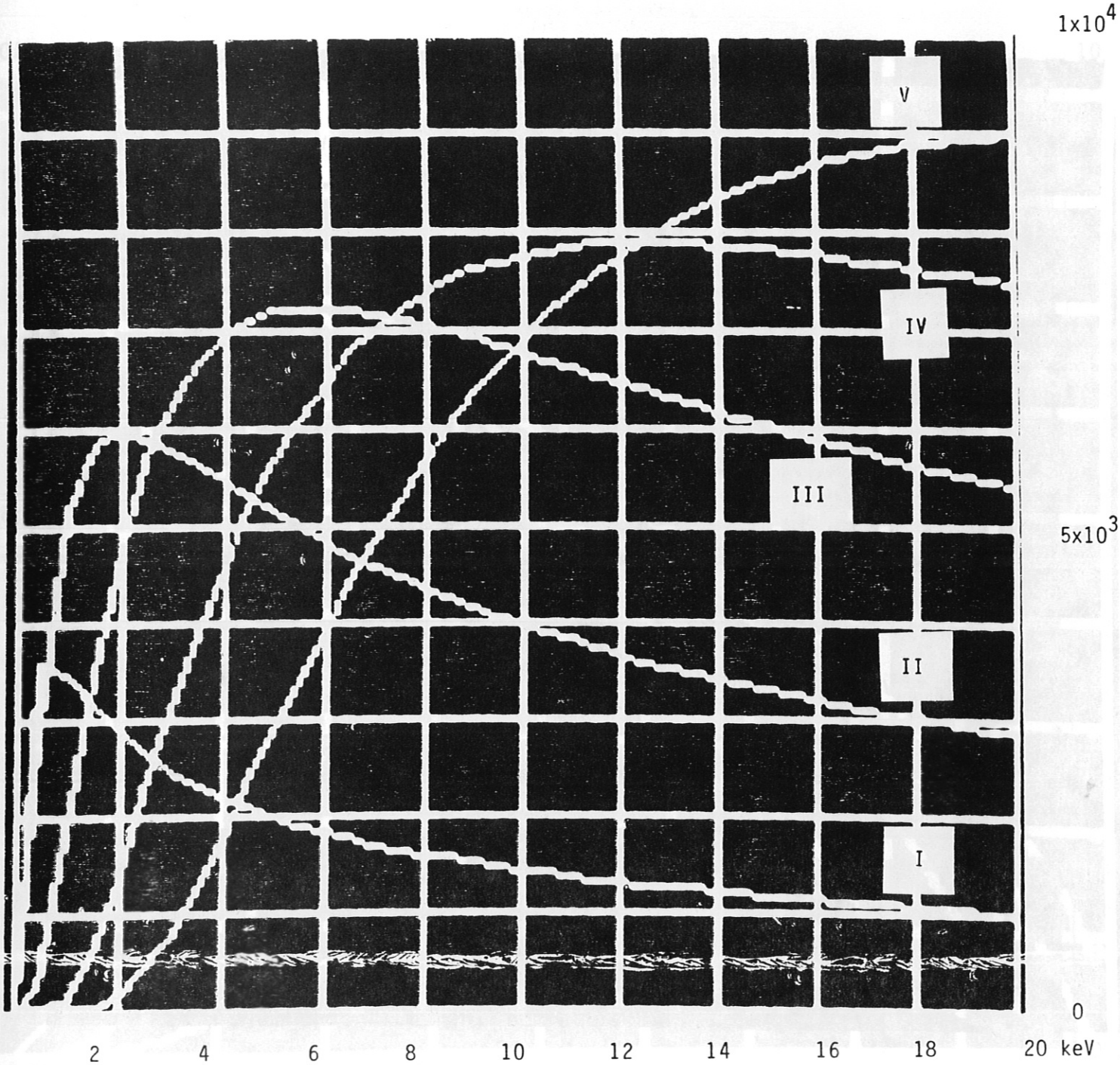

Fig. 3.3

Number of photoelectrons per spectral channel.

Parameters: Laser energy 15 J at 6576 Å, $n_e = 5 \times 10^{13}$ cm^{-3}

$d\Omega = 1 \times 10^{-3}$ sr,

L = 18 cm, T = 0.1, S 20 - photocathode.

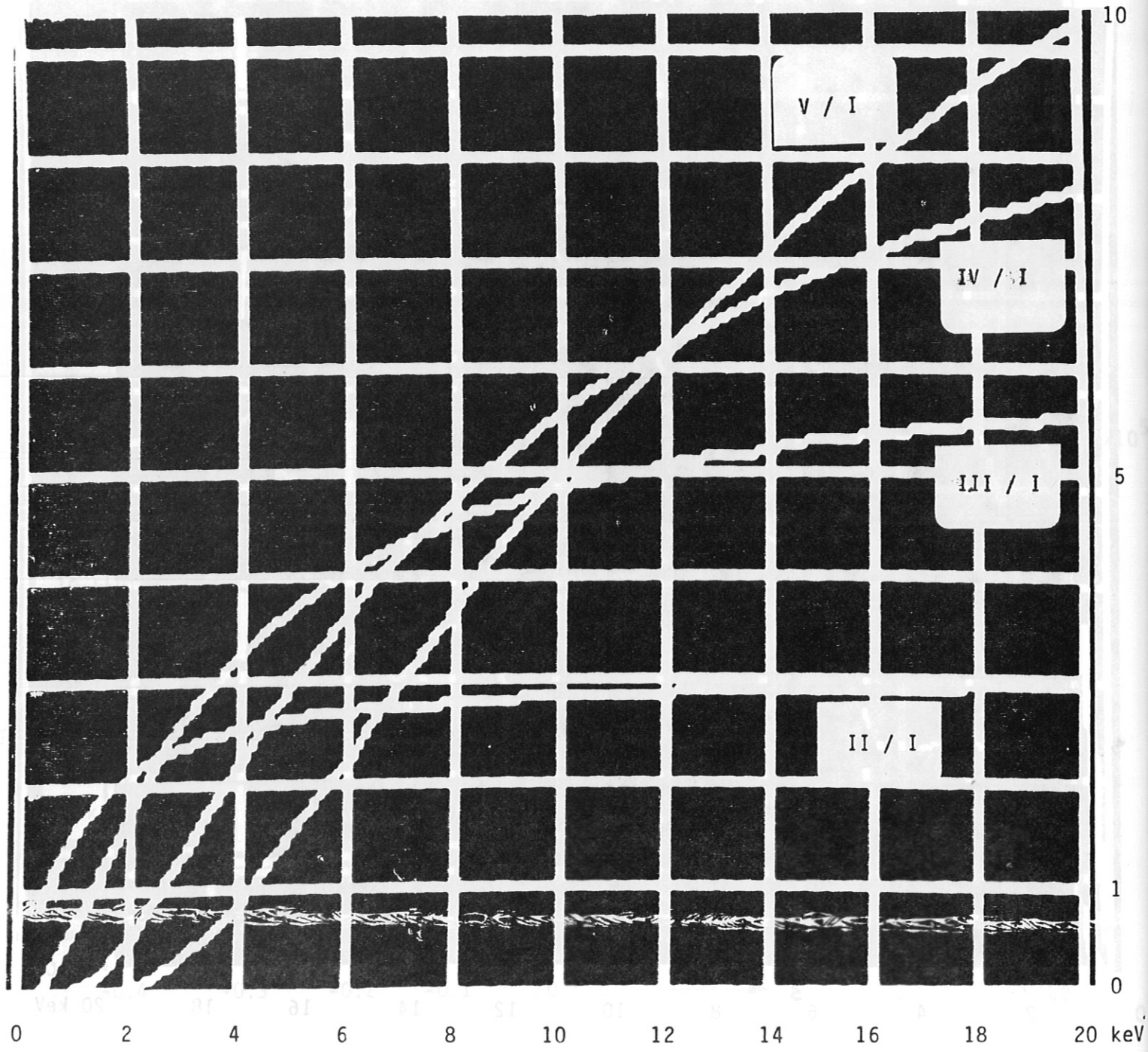

Fig. 3.4

Ratio of photoelectrons per channel

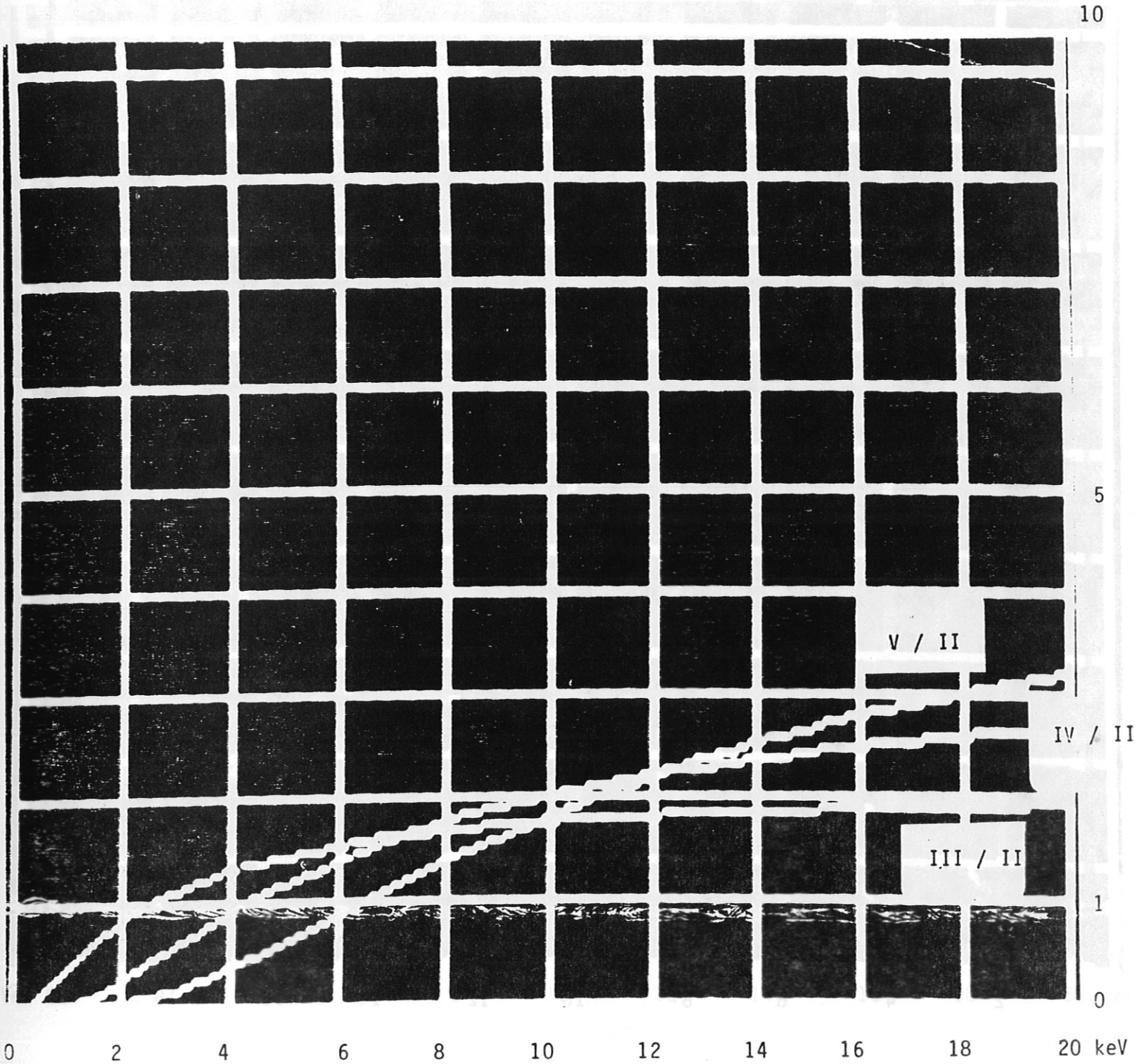

Fig. 3.5

Ratio of photoelectrons per spectral channel

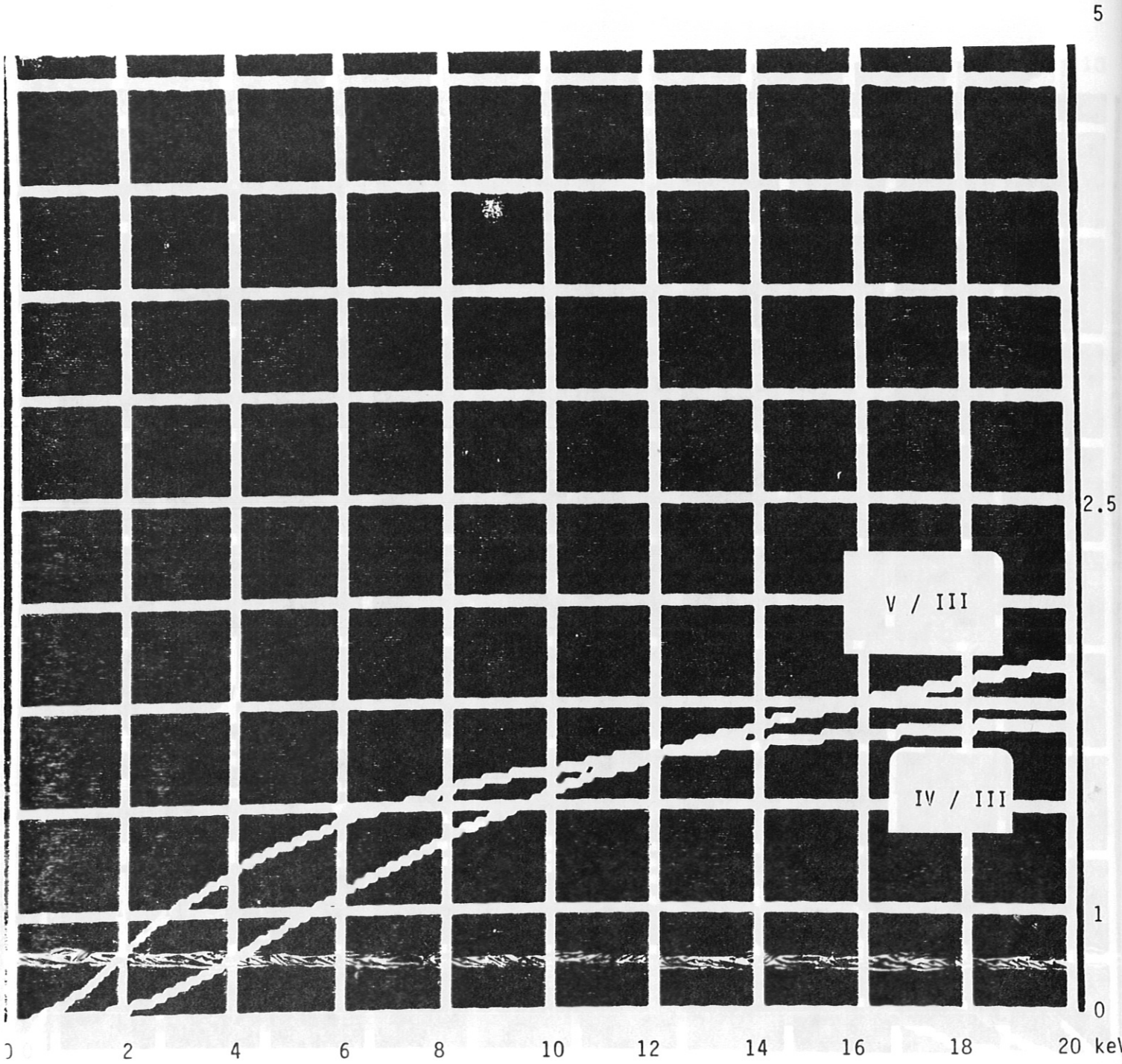

Fig. 3.6

Ratio of photoelectrons per spectral channel

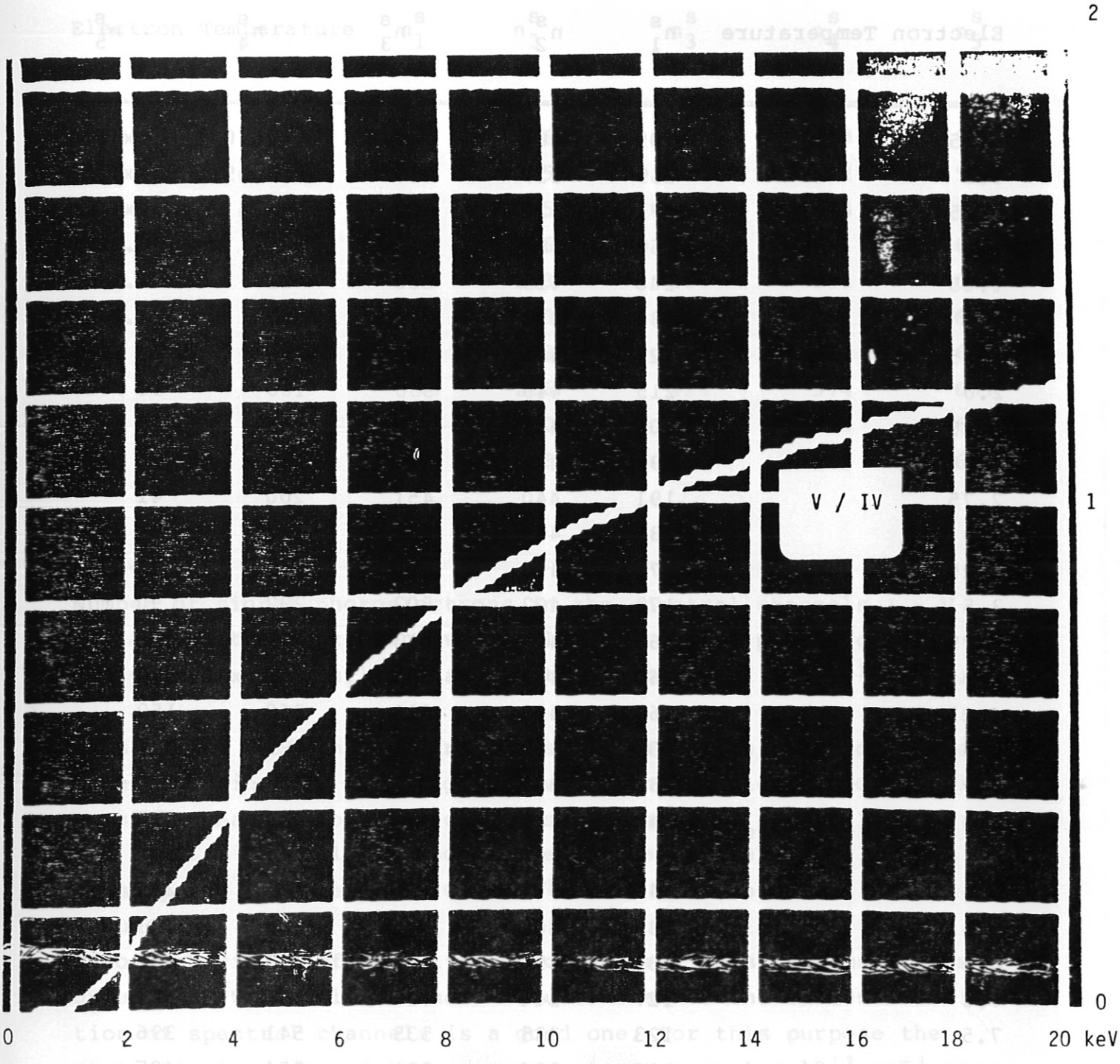

Fig. 3.7

Ratio of photoelectrons per spectral channel

Electron Temperature	n_1^s	n_2^s	n_3^s	n_4^s	n_5^s
0.25 keV	209	61	0.4	4×10^{-6}	1×10^{-14}
0.5	269	217	18	0.05	3×10^{-6}
0.75	271	323	67	1.4	2×10^{-3}
1.0	260	385	133	8	0.06
1.25	248	419	200	21	0.5
1.5	236	437	261	43	1.8
1.75	225	446	314	69	5
2.0	215	449	358	100	10
2.25	206	448	396	133	18
2.5	199	444	426	167	28
2.75	191	440	451	200	41
3.0	185	434	472	233	55
3.25	179	428	488	263	72
3.5	173	422	502	292	90
3.75	168	416	513	319	109
4.0	164	410	521	345	130
4.25	160	403	528	368	150
4.5	156	397	533	389	171
4.75	152	391	537	409	192
5.0	148	385	540	427	213
5.5	142	374	543	459	254
6.0	136	363	543	486	293
6.5	131	353	542	508	330
7.0	127	344	539	526	364
7.5	123	335	535	541	396
8.0	119	326	531	554	425
8.5	115	319	526	564	452
9.0	112	311	521	572	477
9.5	109	304	515	578	499
10.0	106	298	509	583	519

continued on next page

Electron Temperature	n_1^s	n_2^s	n_3^s	n_4^s	n_5^s
11.0 keV	101	286	498	590	554
12.0	97	275	486	592	583
13.0	93	265	475	593	606
14.0	90	256	464	591	625
15.0	86	248	453	588	640
16.0	83	240	443	584	651
17.0	81	233	433	579	660
18.0	78	226	424	574	667
19.0	76	220	415	568	672
20.0	74	215	406	562	676

Table 3.II
Number of signal photoelectrons in the spectral channels I - V in case of the scattering volume located at the plasma centre ($d\Omega = 5.22 \times 10^{-4}$ sr) and an electron density of 1×10^{13} cm^{-3}.

Figs. 3.8 - 3.11 show the relative errors of the electron temperature determined by applying the two channel ratio method to all possible channel combinations. The curves $\Delta T_e/T_e = f(T_e)$ apply to the spatial channel located at the plasma centre. The electron density was taken as 1×10^{13} cm^{-3} and F = 1 (no excess noise) was assumed).
Before showing profiles with expected error bars, let us discuss briefly on the basis of these results whether the chosen distribution of spectral channels is a good one. For this purpose the statistical errors of the measurements at $n_e = 1 \times 10^{13}$ cm^{-3} are listed in Table 3.III. The numbers are obtained using an excess noise factor of 1.8 as specified by the producers of microchannel-plates.
Table 3.III describes the dynamic range of the chosen distribution of spectral channels. For low temperatures the numbers of photoelectrons in the spectral channels III - V are so small that only the ratio II / I can be used for measurements. For high temperatures the numbers of photoelectrons in the different channels are of

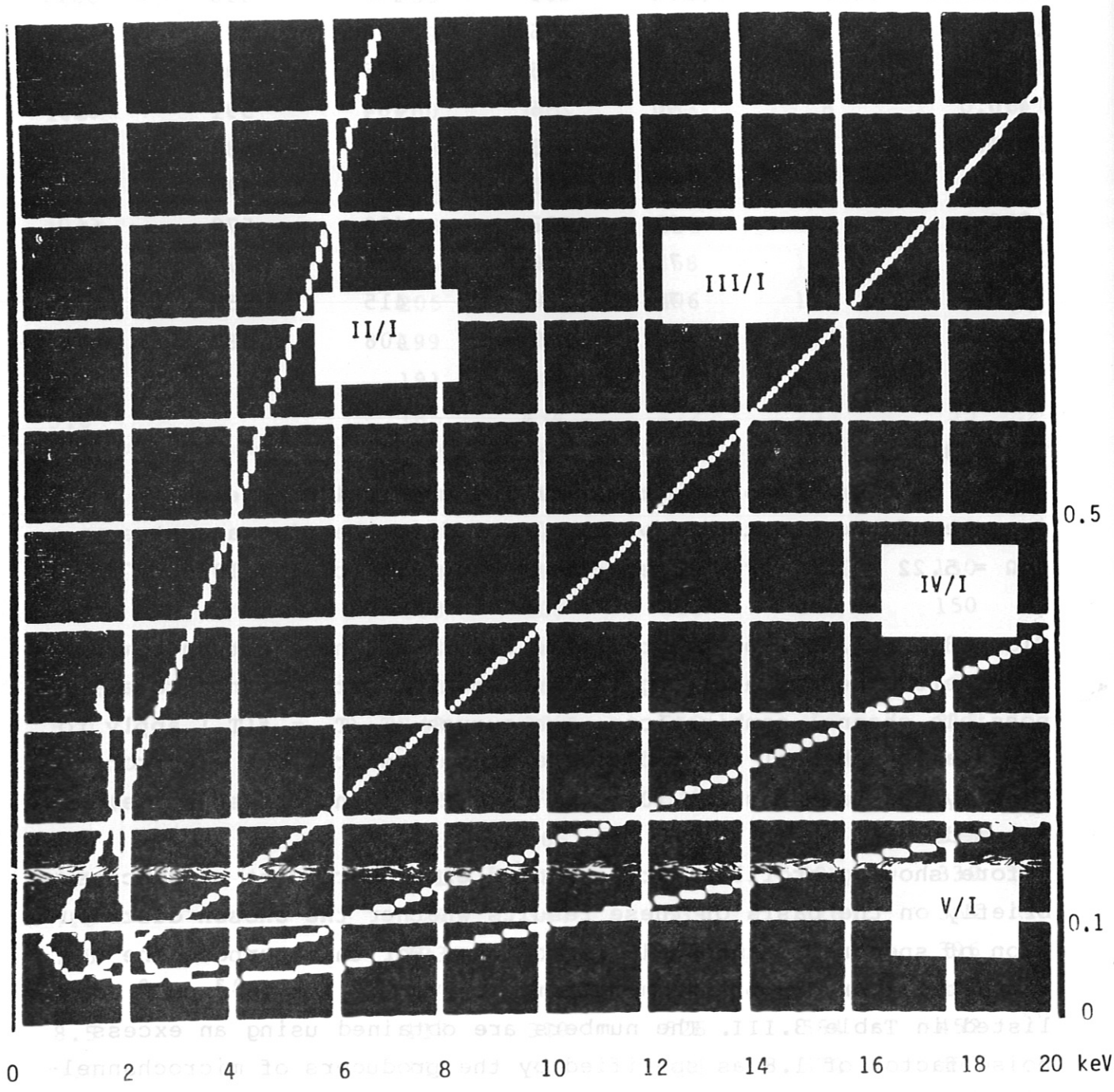

Fig. 3.8

Error of electron temperature measurement versus electron temperature; n_e = 1 x 10^{13} cm^{-3}, excess noise factor 1, central spatial channel

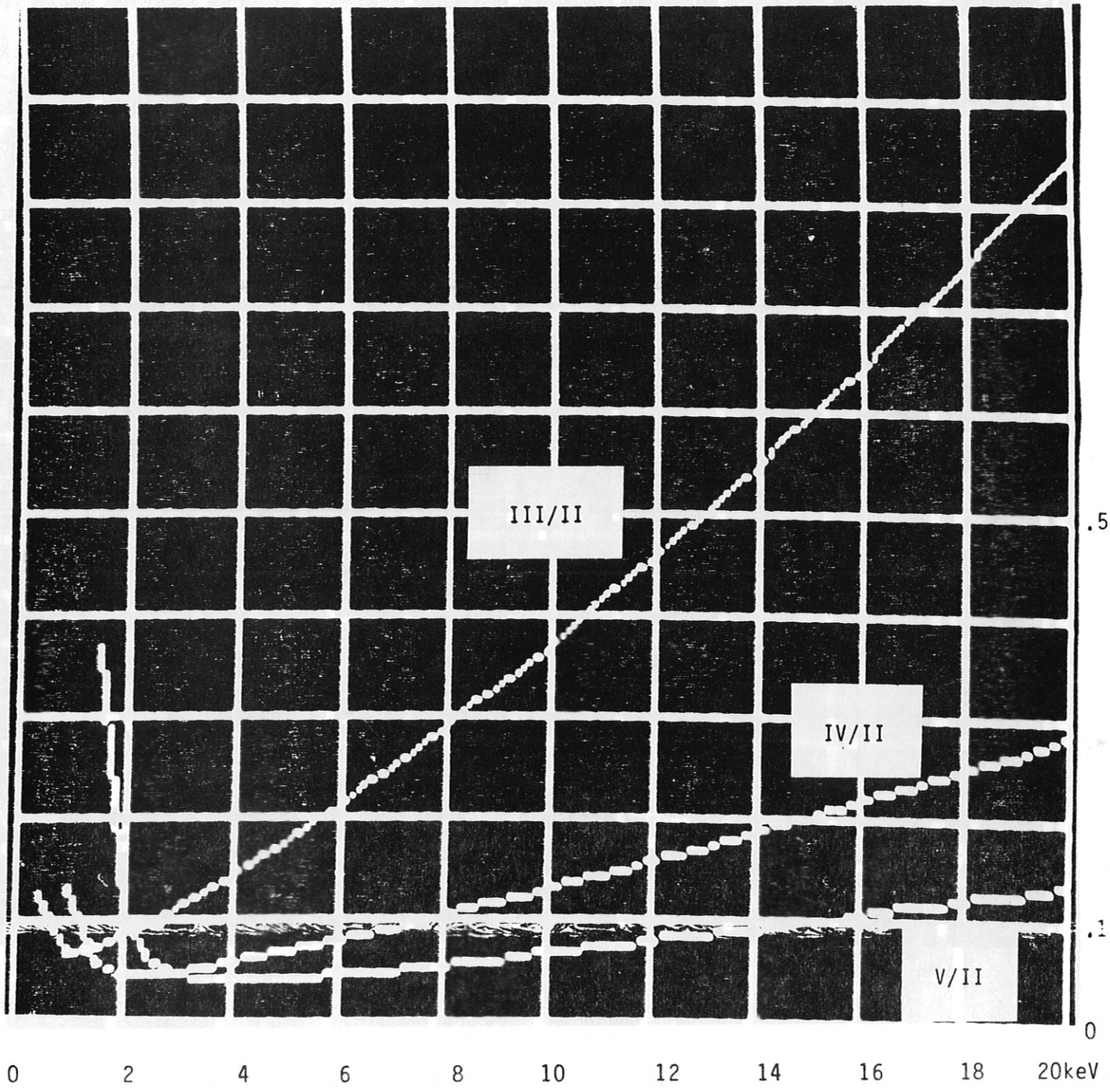

Fig. 3.9

Error of electron temperature measurement versus electron temperature; $n_e = 1 \times 10^{13}$ cm^{-3}, excess noise factor 1, central spatial channel

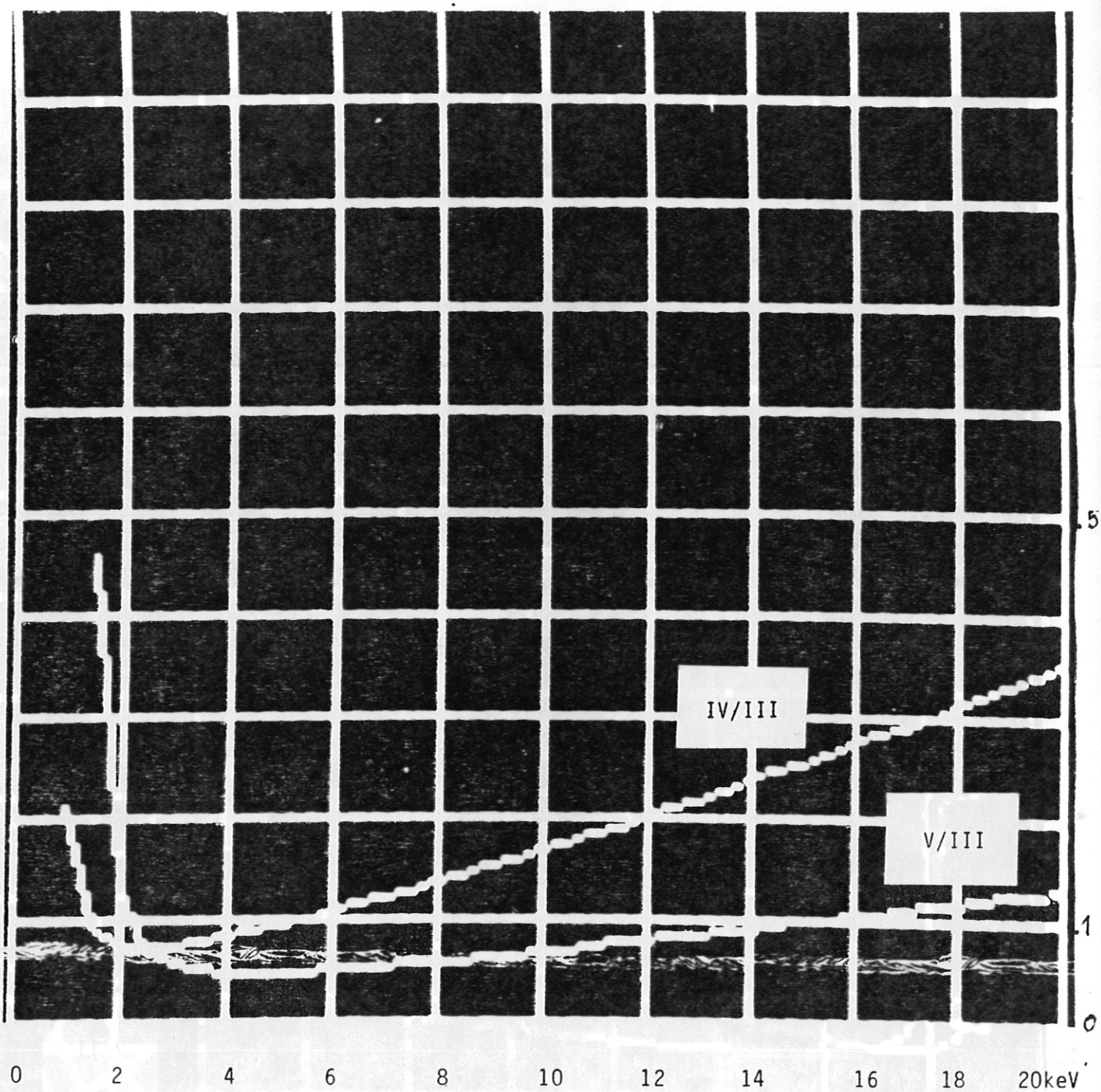

Fig. 3.10

Error of electron temperature measurement versus electron temperature; $n_e = 1 \times 10^{13}$ cm^{-3}, excess noise factor 1, central spatial channel

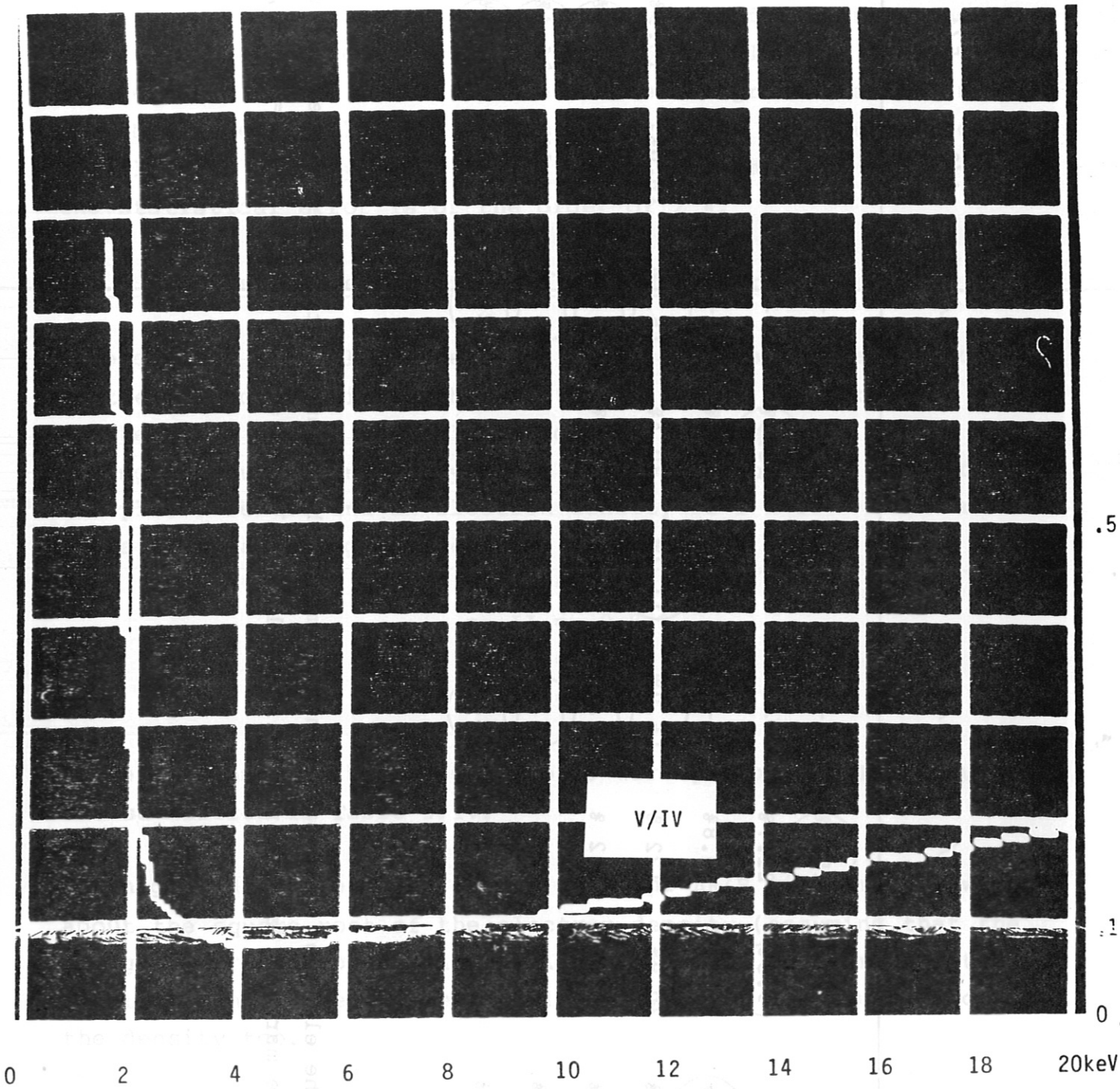

Fig. 3.11
Error of electron temperature measurement versus electron temperature; $n_e = 1 \times 10^{13}$ cm^{-3}, excess noise factor 1, central spatial channel

T_e	5/1	4/1	3/1	2/1	5/2	4/2	3/2	5/3	4/3	5/4	$\frac{\Delta T_e}{T_e}$
0.5 keV	-	-	-	15.4%	-	-	-	-	-	-	15,4 %
1.0 keV	-	-	9.3%	21.7%	-	-	12.3%	-	-	-	7.4 %
2.0 keV	-	8.0%	12.4%	40.8%	-	8.5%	14.5%	-	13.5%	-	5.3 %
5.0 keV	8.1%	13.6%	30.9%	122 %	6.9%	11.3%	30.4%	8.0%	16.0%	13.5%	4.0 %
10.0 keV	15.5%	29.7%	70.8%	342 %	11.1%	22.1%	62.0%	11.6%	29.5%	18.1%	6.6 %
15.0 keV	25.4%	50.8%	138 %	....	17.4%	36.8%	....	16.8%	44.1%	25.4%	10.0 %
20.0 keV	36.9%	71.6%	....	....	22.9%	43.9%	....	22.3%	53.3%	35.3%	13.5 %

Table 3.III
Statistical errors of the electron temperature measurement. The channel ratios used for evaluating the electron temperature are marked. Parameters: $n_e = 1 \times 10^{13}$ cm^{-3}, $d\Omega = 5.22 \times 10^{-4}$ sr, L = 13 cm, F = 1.8, T = 0.1

the same order of magnitude, but only the number n_5^s changes appreciably with temperature. Thus for high temperatures (>10 keV) a sixth spectral channel in the uv would be helpful whereas the channel distribution seems to be adequate for the low and medium temperature range. Since the influence of the background radiation on the SNR is negligible, the errors improve with the square root of the electron density, e.g. at $n_e = 5 \times 10^{13}$ cm^{-3} and $T_e = 5$ keV the statistical error is of the order of 2 %.

3.1.6 Statistical error of the electron density

According to step 11 of the described procedure the ratio R of scattered photons within the spectral range of the detection system to the total number was calculated. Fig. 3.12 shows R versus T_e. Taking the numbers n_i^s applying to the spatial channel located at the plasma centre and an electron density of 1×10^{13} cm^{-3} from Table 3.II, assuming mean quantum efficiencies of

$$\eta \quad I = 7.5\ \%$$
$$\eta \quad II = 9.8\ \%$$
$$\eta \quad III = 13.1\ \%$$
$$\eta \quad IV = 16.9\ \%$$
$$\eta \quad V = 20.6\ \%$$

for each channel, the steps 13 to 15 were performed. The results are summarized in Table 3.IV.

For higher densities both errors $\Delta N/N$ and $\Delta R/R$ will improve with about the square root of the electron density (assuming that the background radiation remains negligible). Thus the error of the electron density measurement will improve with the square root of the density too.

The errors have been calculated assuming a solid angle of the collection optics of 5.22×10^{-4} sr in case of the scattering volume at the plasma centre. This value is achieved with a 140 mm useful diameter window located at a distance of 4.8 m from the torus horizontal plane. If an array of smaller windows must be used the solid angle will be reduced by a factor of 2 - 3 (e.g. using windows of 74 mm useful diameter and an outer diameter of 100 mm). This will result in an increase of the given errors by a factor of about 1.7.

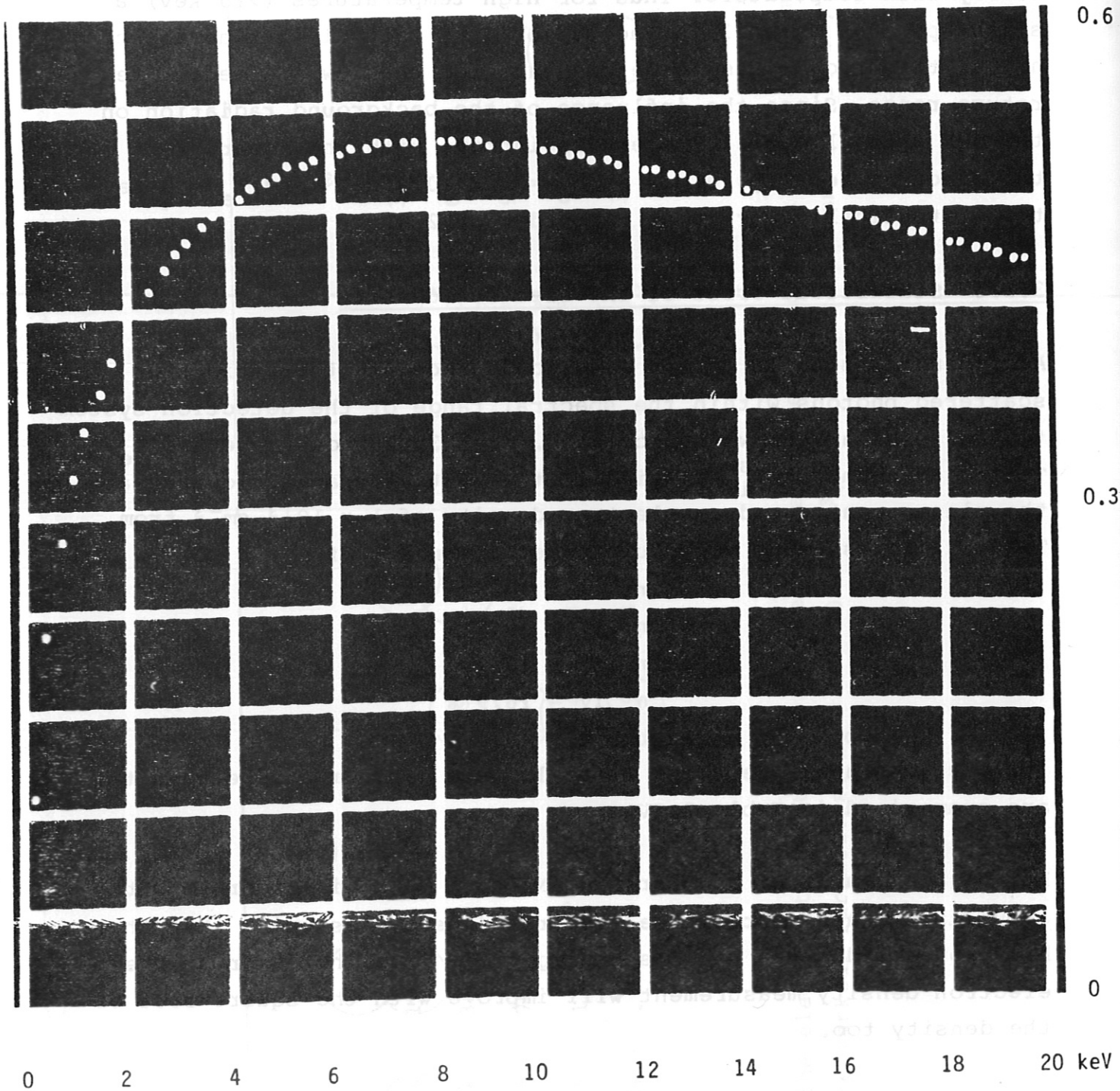

Fig. 3.12

R versus electron temperature

T_e	$R(T_e)$	$\frac{\partial R}{\partial T_e}$ /keV^{-1}	$\frac{\Delta N}{N}$	$\frac{\Delta R}{R}$	$\frac{\Delta N_{tot}}{N_{tot}} = \frac{\Delta n_e}{n_e}$
0.5 keV	0.2355	0.30	4.7 %	8.9 %	10.1 %
1.0 keV	0.3286	0.13	3.7 %	2.7 %	4.6 %
2.0 keV	0.4125	0.06	2.8 %	1.4 %	3.1 %
5.0 keV	0.5039	0.01	2.5 %	0.5 %	2.6 %
10.0 keV	0.5161	0.005	2.2 %	0.6 %	2.3 %
15.0 keV	0.4841	0.008	2.3 %	2.4 %	3.3 %
20.0 keV	0.4458	0.008	2.4 %	4.5 %	5.1 %

Table 3.IV
Statistical error of the electron density measurement (Central spatial channel, errors of T_e as given in Table 3.III)

The expected error bars of the electron temperature and density measurements are shown in Figs. 3.13 and 3.14 for parabolic profiles with T_{eo} = 5 keV and n_{eo} = 1 x 10^{13} cm^{-3}. When calculating the error bars for these profiles the variation of temperature, density and solid angle of collection along the spatial chord is taken into account. However, the inhomogeneity of the electron density and temperature within the scattering volumes has been neglected.

The calculations have been performed for a given set of spectral channels. This channel distribution can be changed to shift the dynamic range versus lower or higher temperatures. The dynamic range can be increased too, by adding spectral channels, one near the laser line and the other located in the uv.

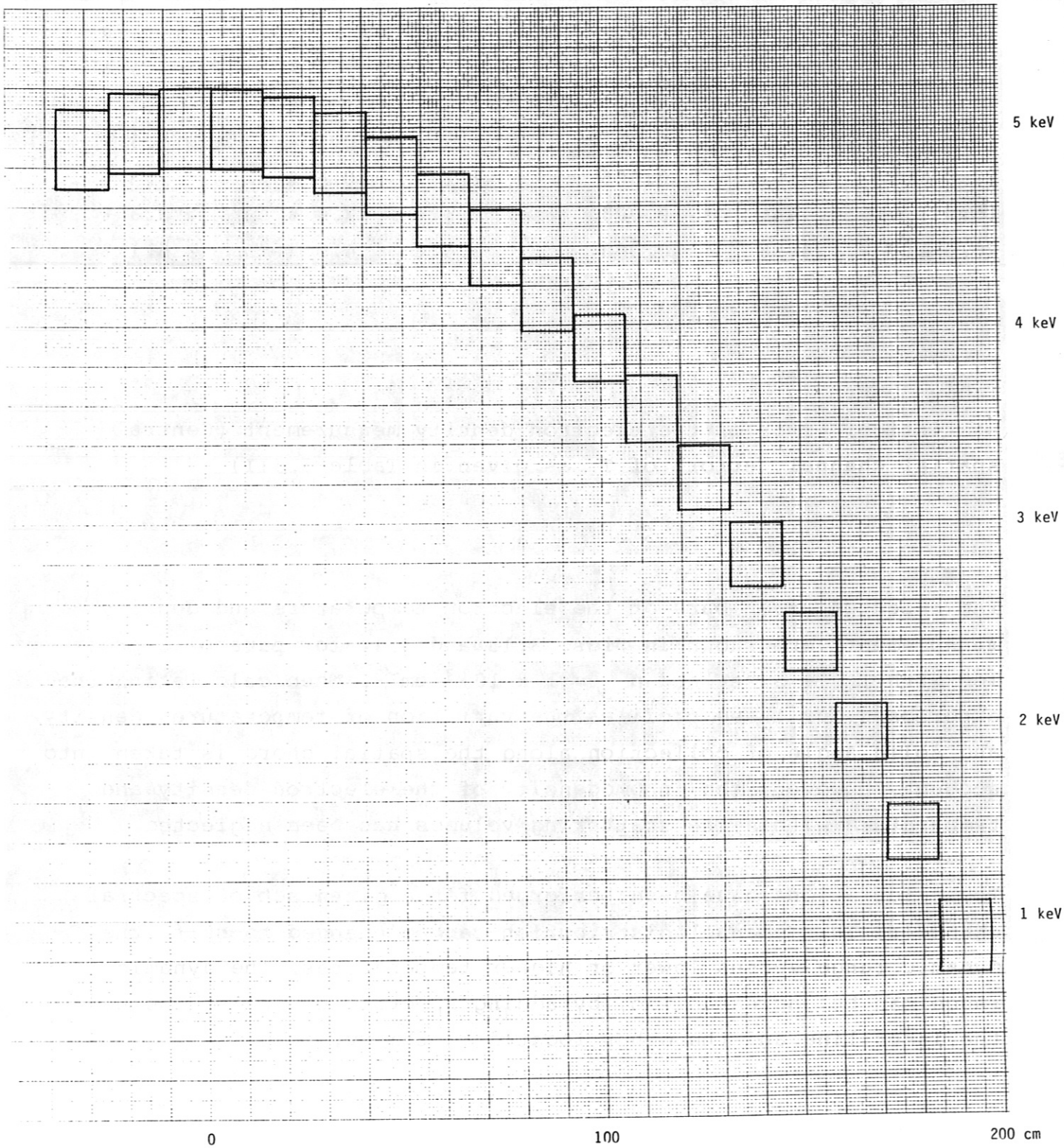

Fig. 3.13 : Error Bars of a parabolic Temperature Profile at a Centre Electron Density of 1 x 10^{13} cm^{-3}

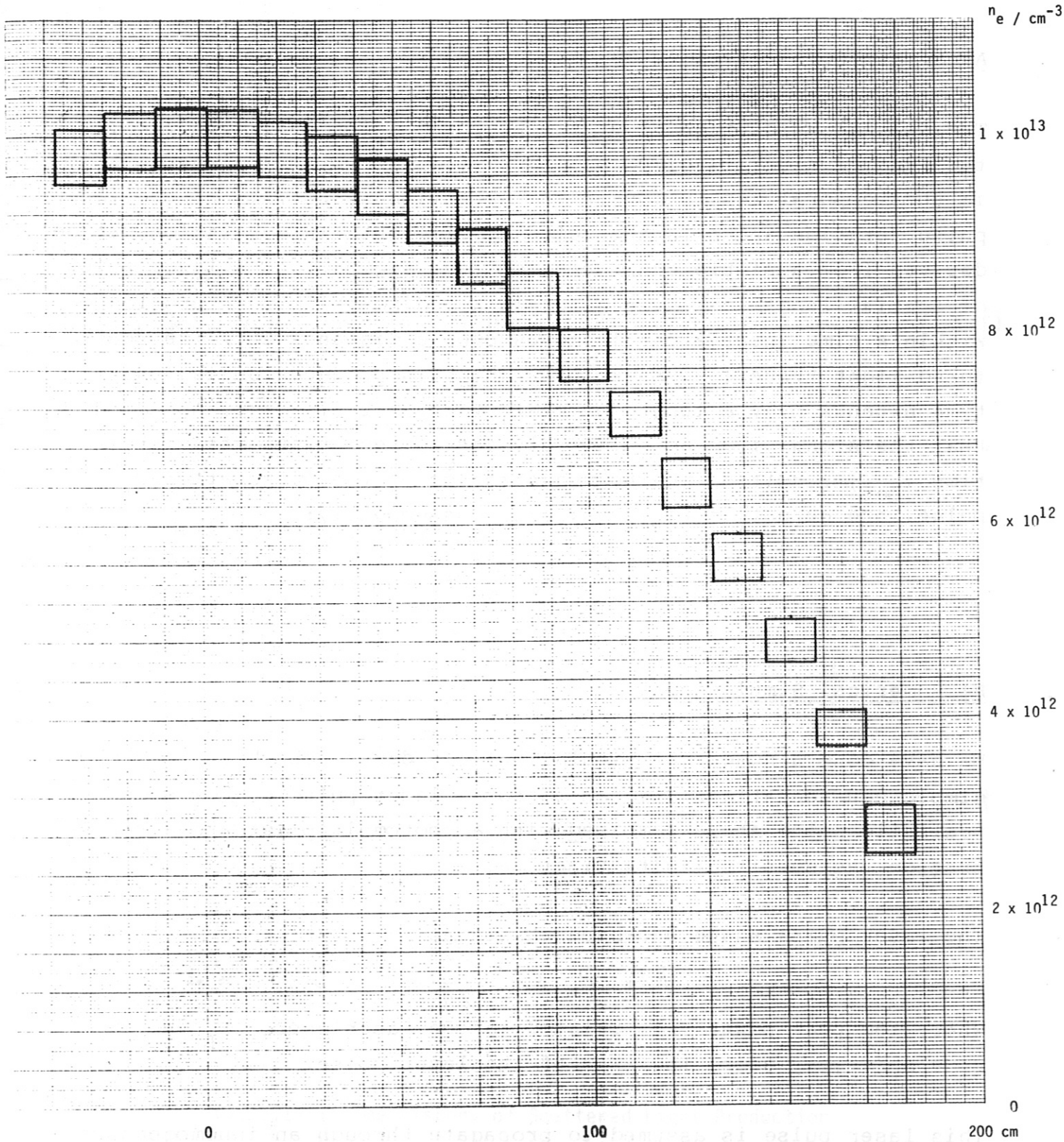

Fig. 3.14 : Error Bars of a parabolic Density Profile at a Centre Electron Temperature of 5 keV

3.2 Spatial Resolution

A) Simple Considerations

The spatial resolution Δl of the proposed diagnostic method along the line of sight is given by $\Delta l = \frac{c}{2} (\tau_{Det} + \tau_L)$ /7/, where τ_{Det} is the temporal resolution of the detection system, τ_L is the laser pulse duration and c is the velocity of light. This relation can be derived from a simple consideration (see Fig. 3.15). A laser pulse of spatial length $c\tau_L$ propagates in a medium which scatters light. Within a time interval t_1 it moves over a distance ct_1. The scattered light travelling backwards, which is produced during that time extends over a length of $c(2t_1 + \tau_L) = 2\,\Delta l - c\tau_L$. Assuming that the signal from an infinitely fast detector is gated for a time τ_{Det}, resulting in the registration of the backscattered pulse, one gets $t_1 = (\tau_{Det} - \tau_L)/2$. Consequently:

$$\Delta l = c\,(\tau_{Det} + \tau_L)/2$$

B) Numerical Simulation

We have done a numerical simulation in order to check whether the simple considerations still hold for a laser pulse with a more realistic pulse shape combined with a photomultiplier and a registration system with finite risetime.

The laser pulse shape has been chosen as

$$P_L = P_o \sin^2 \frac{\pi t}{2\tau_L} \qquad 0 \le t \le 2\tau_L$$

where the peak power P_o is related to the laser energy E_L by $P_o = E_L/\tau_L$, τ_L being the FWHM of the laser pulse.

This laser pulse is assumed to propagate through an inhomogeneous plasma characterized by $n_e(x)$ and $T_e(x)$. Refractive index effects being negligible, $P_L(x,t)$ is given by

$$P_L(x,t) = \frac{E_L}{\tau_L} \sin^2 \frac{(x-ct)}{2\tau_L c} \qquad ct \le x \le ct + 2c\tau_L$$

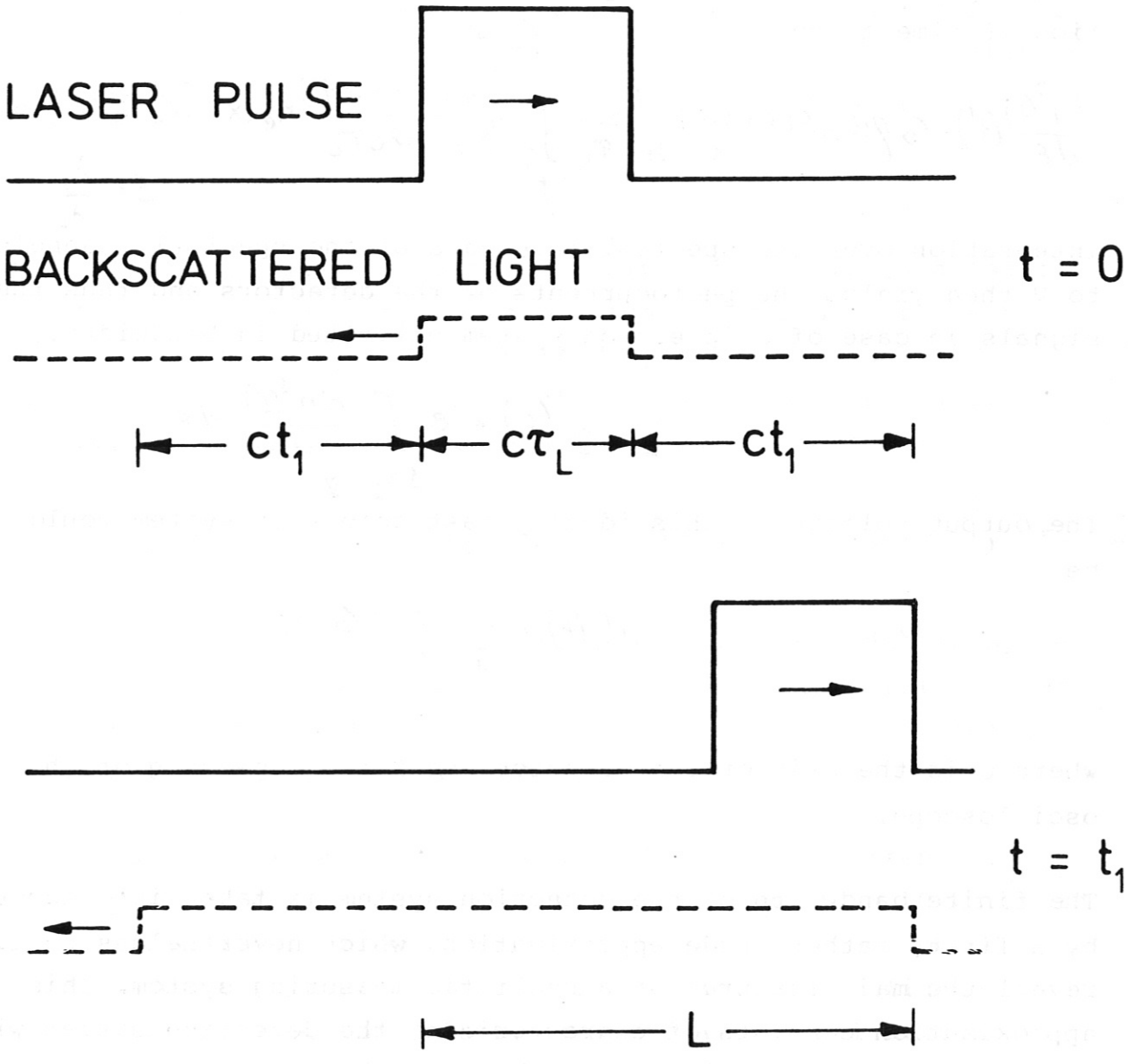

Fig. 3.15 : Time History of Scattered Light Production

A detector located at x = 0 will then receive scattered light produced by a laser pulse at a retarded time t' = t - x/c. Thus, with the same denominations as used in the section on the statistical errors of the measurement, the number of photoelectrons per normalized spectral interval and per time interval is given as a function of time t' by

$$\frac{dn^s(\varepsilon)}{d\varepsilon}(t') = r_0^2 \eta(\varepsilon)(\varepsilon+1)\Delta\Omega T \frac{E_L}{h\nu_L \tau_L} \int_{\frac{ct'}{2}}^{c\tau_L+\frac{ct'}{2}} \sin^2 \frac{\pi(2x-ct')}{2c\tau_L} n_e(x) S(\varepsilon, T_e(x))\, dx$$

$$\varepsilon = \frac{\lambda_s}{\lambda_L} - 1$$

Integration over the spectral intervals of the spectral channels I to V then yields the photocurrents of the detectors and thus the signals in case of a detection system unlimited in bandwidth:

$$i_{I\,..\,V}(t') = e \int_{\Delta\varepsilon_{I...V}} \frac{dn^s(\varepsilon)}{d\varepsilon}\, d\varepsilon$$

The output voltage of this ideally fast detection system would then be

$$U_0(t) = i_{I..V}(t') \cdot G \cdot R$$

where G is the gain of the detector and R the impedance of the oscilloscope.

The finite bandwidth of the detection system is taken into account by a first, rather crude approximation, which nevertheless should reveal the main features of a realistic measuring system. This approximation consists of characterizing the detection system with respect to its temporal response by a simple RC-circuit.

The risetimes of the F 4128 photomultiplier (τ_1 = 125 ps) and of the TEK 7104 oscilloscope (τ_2 = 350 ps) - defined as the time interval between the 10 % and the 90 % points of the signal response to a step function - yield a risetime of the complete system $\Delta t_{10-90} = \sqrt{\tau_1^2 + \tau_2^2}$ = 370 ps. The falltime of the detector is larger than its risetime (ITT Electro-Optical Products Div., Techn.

Note No. 127, 1980). Combining its value of 280 ps with the fall-time of the oscilloscope (350 ps) gives Δt_{90-10} = 450 ps. In our numerical simulation we have used a rise- and falltime of 440 ps which corresponds to a RC time constant of 2×10^{-10} s.

Describing the detection system by a simple RC-circuit model, the measured signal U(t) is then obtained by integrating the differential equation

$$U(t) + RC \frac{dU(t)}{dt} = U_0(t)$$

Figs. 3.16 to 3.18 give results for a situation in which a laser pulse of E_L = 15 J and τ_L = 320 ps propagates over a distance of 60 cm in a plasma of constant density, $n_e = 1 \times 10^{13}$ cm^{-3}. The electron temperature is a step function, the step occuring at x = 30 cm. The other parameters are as given in the section on statistical errors:

$$\eta(\varepsilon) \rightarrow S20 \;,\; \Delta\Omega = 5.22 \times 10^{-4}\,sr \;,\; T = 0.1 \;,\; G = 3 \times 10^5 \;,\; R = 50\Omega$$

For the numerical integrations we have used a step width in space of 0.6 cm and a step width in time of 40 ps. The integration over the spectral widths of the channels I to V was done by dividing each channel into 5 slices of equal width.

Fig. 3.16 shows the temporal evolution of the photocurrents i_{I-IV} for an ideally fast detector, when T_1 = 5 keV and T_2 = 10 keV. Fig. 3.17 gives the signal voltage traces to be expected for our detection system with a finite risetime of 440 ps. In this figure we have indicated for the most decisive spectral channel at these temperature (no. V) the rms noise voltage which can be predicted according to

$$\langle i_n^2 \rangle = 2eBFG^2 i_{CATHODE} = 2eBFG\, i_{OUT}$$

$$i_n^{rms} = \sqrt{2eBFG\,\frac{U}{R}}$$

$$U_n^{rms} = \sqrt{2eBFGUR}$$

$$B = 1\,GHz \;,\; G = 3 \times 10^5 \;,\; F = 1.8 \;,\; R = 50\Omega$$

For a much smaller temperature step (5.0 keV to 5.5 keV) - but one which according to our error analysis is well resolvable - Fig. 3.18 shows those ratios of the channel signals which are used si-

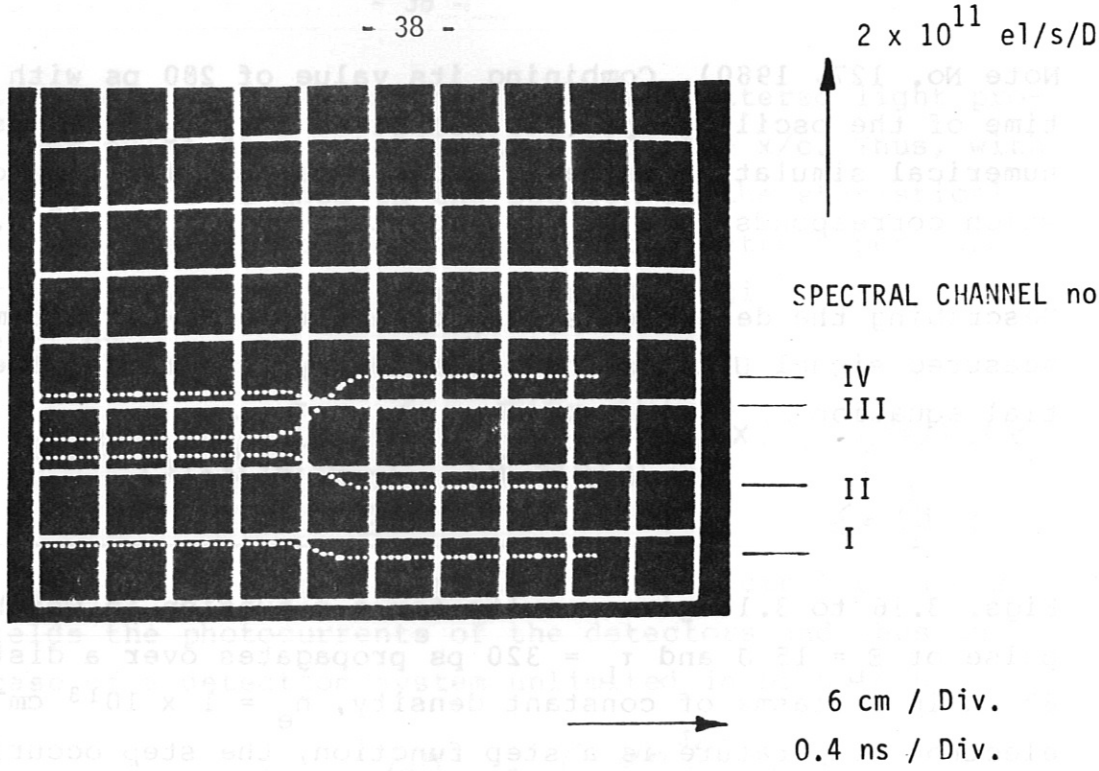

Fig. 3.16 : Photocurrents of ideally fast detectors

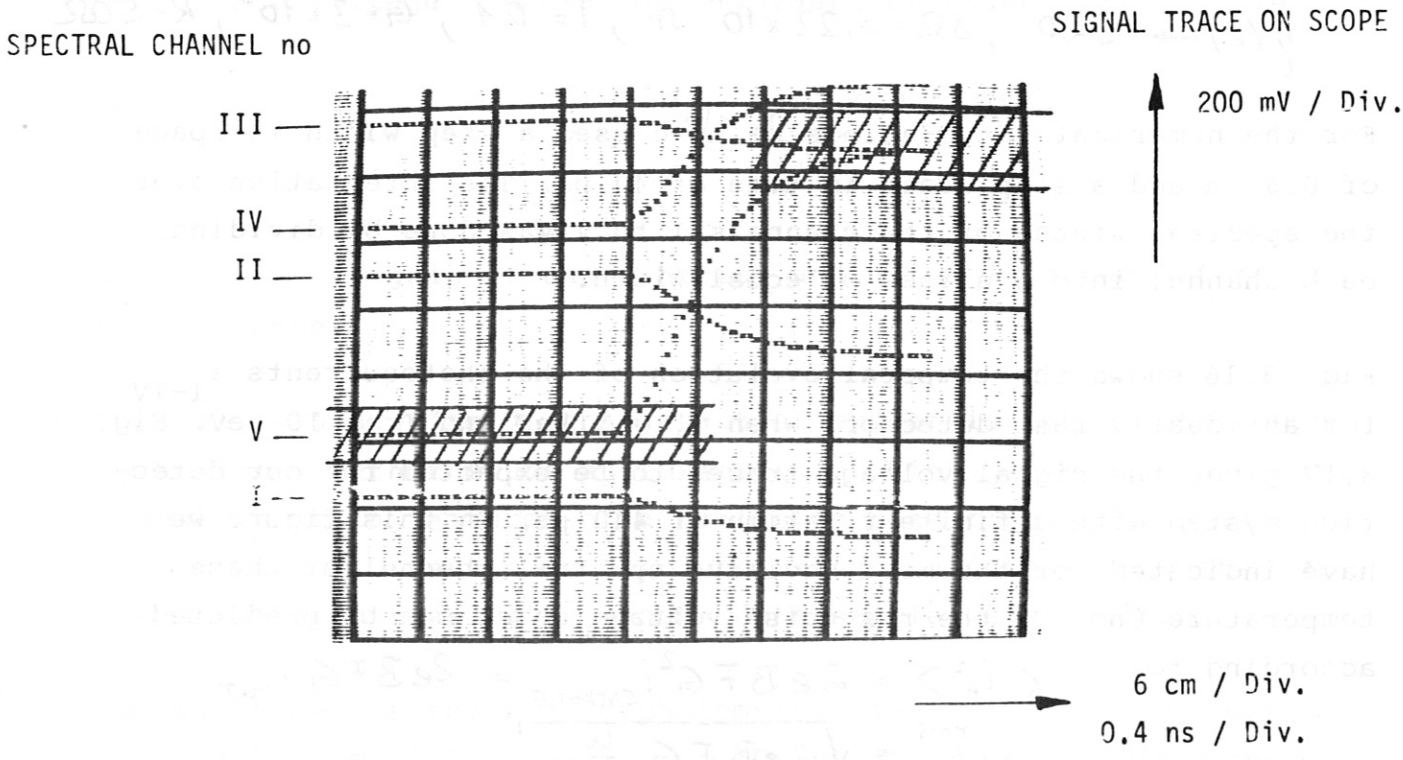

Fig. 3.17 : Output signals of bandwidth limited detection systems

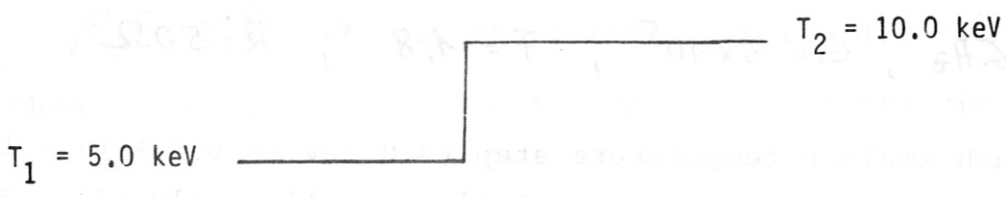

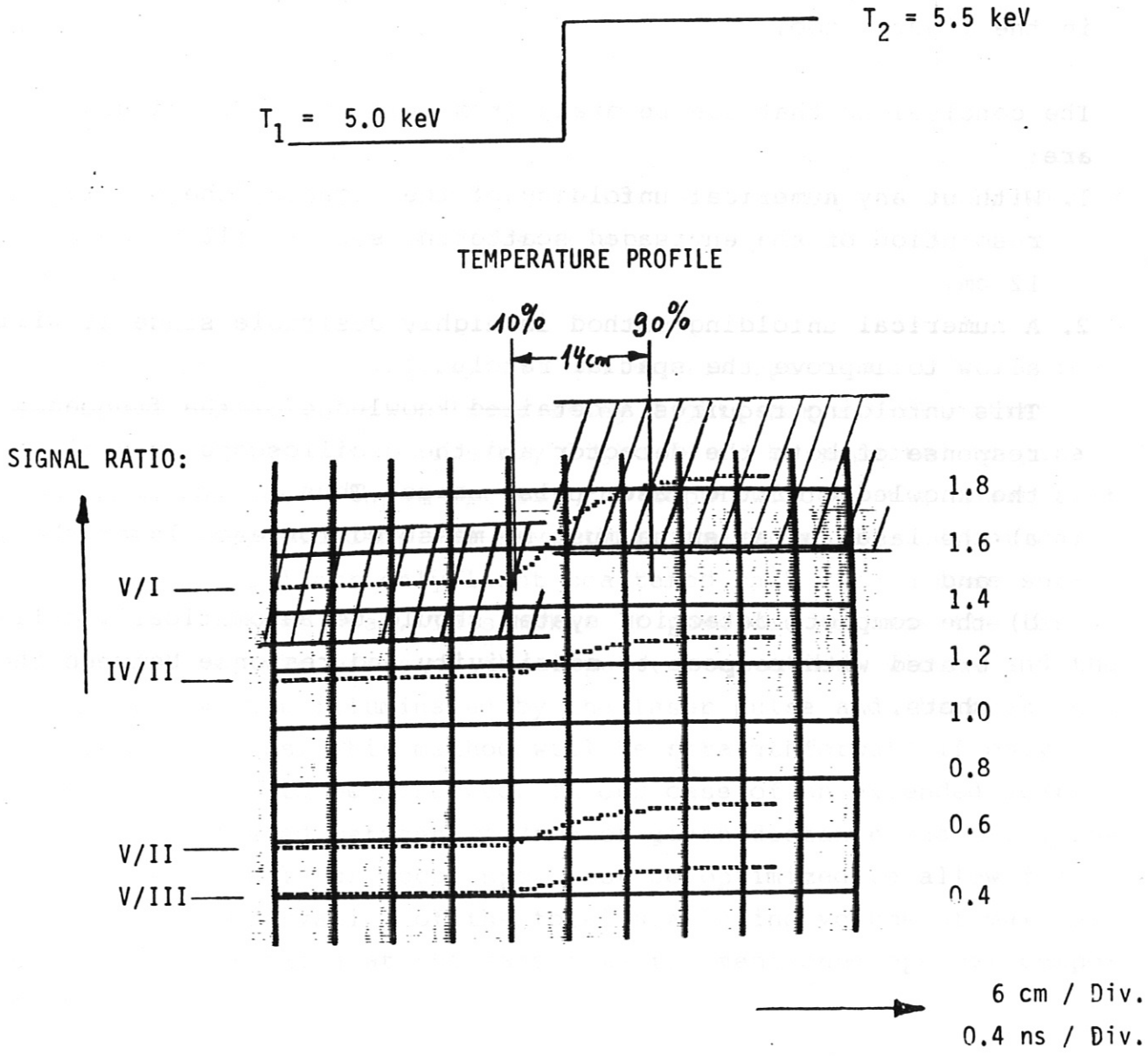

Fig. 3.18 : Signal ratios of the spectral channels

multaneously for temperature evaluation in this temperature range. Here the error bars of the most important ratio V/I are indicated in the figure, too.

The conclusions that can be drawn from this numerical simulation are:

1. Without any numerical unfolding of the signals, the spatial resolution of the envisaged scattering system will be about 12 cm.
2. A numerical unfolding method is highly desirable since it will allow to improve the spatial resolution.
   This unfolding requires a detailed knowledge of the frequency response of both the detector and the oscilloscope as well as the knowledge of the laser pulse shape. Thus
   a) the laser pulse shape must be measured for each laser shot, and
   b) the complete detection system should be automatically calibrated with respect to sensitivity and response between the shots.

3.3 Laser Input and Collection Optics

3.3.1 Optical systems

In this section we will discuss only optical systems which allow the investigation of a vertical optical chord. Consequently, both the laser and the detection system would be placed in the roof laboratory.

The main effort in designing the collection optics must be dedicated to the suppression of laser stray light. For a backscatter experiment a high level of stray light is to be expected originating from the laser input optics, the input window, the laser exit window and the beam dump. We have therefore investigated optical systems which collect only light scattered back into a cone surrounding the laser beam. This makes it possible to mask the laser focusing lens, the parts of the input (observation) window and the laser exit window illuminated by the laser pulse and the beam dump by suitable stops. This method will be straigthforward if only a single point is to be observed. In our case of an extended scattering volume located between windows of given distance and size, the position of the laser focal spot must be optimized to allow for unvignetted observation of the total scattering volume at maximum solid angle, masking at the same time the mentioned optical components.

In order to minimize the diameter of the output duct penetrating the 2.25 m thick torus hall roof it is reasonable to use an optical collection system which images the 2.5 m spatial chord length with 1:1 magnification into the output duct.

Four possible collection optics with 1:1 imaging are sketched in Fig. 3.19. In the following we will discuss their properties and compare their specific advantages and drawbacks.

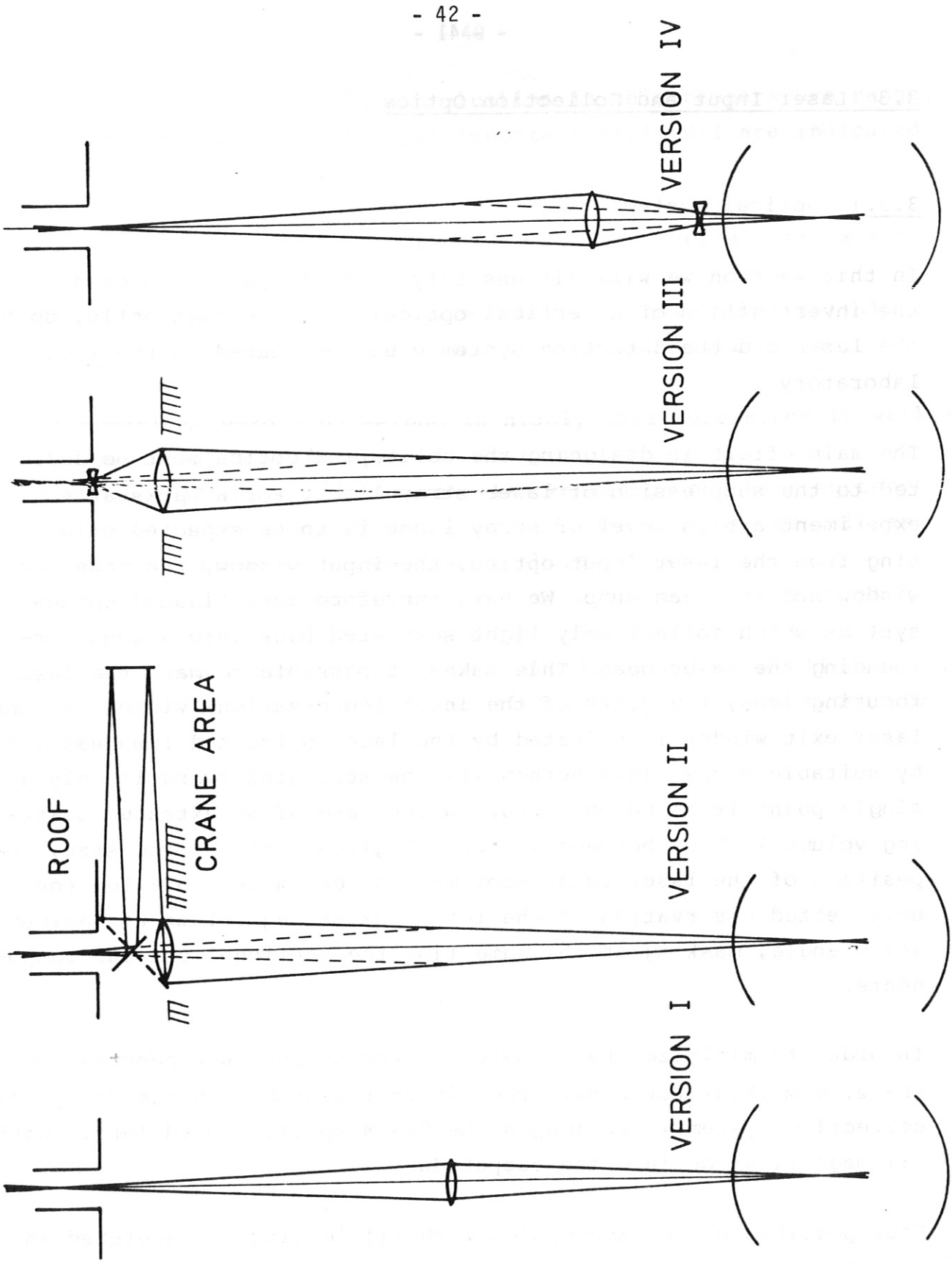

Fig. 3.19 : Possible Collection Optics

Version I

In the first proposed version, the collection optics is placed in the middle between the torus equatorial plane and the ceiling. All the 1:1 imaging collection optics are similar with respect to the method of stray light suppression of the laser beam. Therefore we will discuss this method in detail taking this optical system as an example.

A difficulty common to all four possible solutions rises from the fact that the laser input duct as well as the collection duct penetrating the ceiling should look away from the torus to ease the shielding problems. In case of solution I, this requires to bend the laser input beam as well as the collected light beam by small angles which is done best with prisms. These introduce chromatic effects into the collection optics.

Fig. 3.20 shows the input and collection system for an entrance window of 140 mm clear aperture (only 135 mm will be used) located 4800 mm above the equatorial plane and a laser exit window 3300 mm below it. The laser beam is focused by lens L1 to a focal spot positioned 309 mm above the equatorial plane. The spatial chord to be investigated extends from -400 mm to the plasma boundary (+2100 mm). The laser beam diameter at the entrance window is 36.4 to 38.8 mm (depending on the laser beam diameter of 75 to 80 mm at L1), resulting in an energy density of 1.45 to 1.3 J/cm^2 which is well below the destruction limit of fused quartz. The scattered light is collected by lens L2 surrounding L1. The location and the focal length of L2 are chosen to minimize the collection duct diameter necessary to let pass the collected light through the torus hall roof. The focusing lens L1 is positioned at the same height as L2 for simplicity. Two prisms P1 and P2 with 5° apex angle each are mounted together with the lens assembly L1 + L2. They deviate the laser axis and the axis of the collected light beam by 2.6°. The prisms are rotated against each other slightly in such a way that the two optical axes intersect the ceiling of the torus hall at two points 120 mm apart (Fig. 3.21). The input and collection ducts (identical to the laser input duct of the KE 1 scattering system)

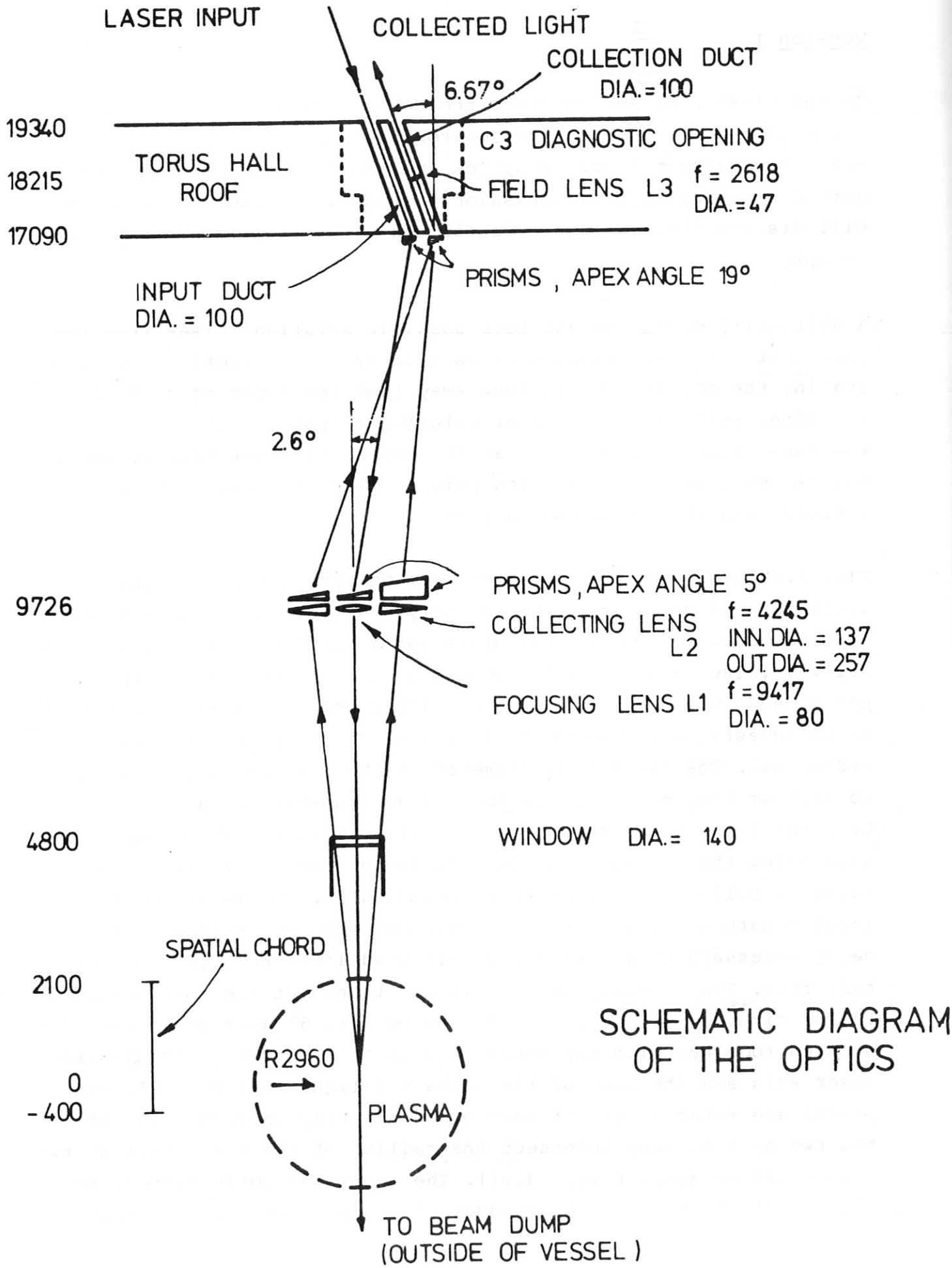

SCHEMATIC DIAGRAM
OF THE OPTICS

Fig. 3.20 : Optical System no. I

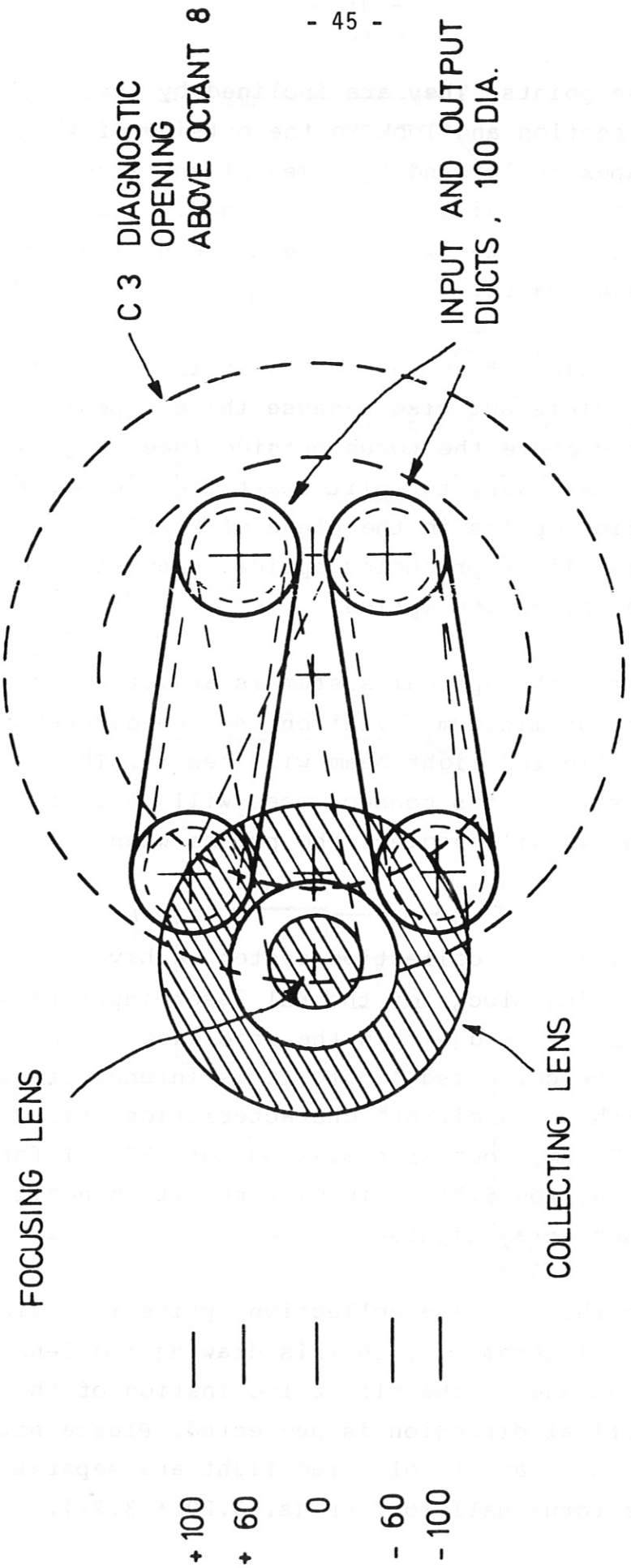

Fig. 3.21 : Ceiling Penetration

start from these points. They are inclined by about 6.7° against the vertical direction and look to the outside of the torus. Two prisms of 19° apex angle bend the axes of the laser beam and the collection optics according to the inclination of the ducts. All optical components located within the torus hall are made from synthetical fused quartz.

The described bending of the optical axes is necessary not only due to shielding problems but also because the C3 opening in the ceiling is positioned above the torus outside (see. Fig. 3.21). In addition, it is necessary to split apart the axes of the laser beam and the collection optics in the plane of L1/L2 in order to avoid additional, stray light producing optical elements along the line of sight of the collection optics.

Due to the prisms, the optical system is anamorphotic. However, by using the prisms at minimum deviation, no one-dimensional magnification of the collected light beam will result. The chromatic effect of the prisms and its consequences will be discussed later. In the following we will neglect the prisms when treating the optical lay-out.

For a first design of a collection system we have taken the geometry of the shielding block for the KE1 laser input (Fig. 3.22). Two mirrors each will be used within the shielding block for both the laser beam and the collected light. It is intended to use dielectric mirrors with "cold mirror" characteristics (high reflection for 400 nm to 630 nm, good transmission for 657 nm) for the collected light (see section 5.3). This will result in additional suppression of laser stray light.

Fig. 3.23 shows the complete collection optics including the interference filter polychromator. In this drawing the lengthening of the optical paths due to the slight inclination of the optical axes against the vertical direction is neglected. Please note that the laser beam and the beam of collected light are separated from each other below the torus hall roof (Figs. 3.20 + 3.21).

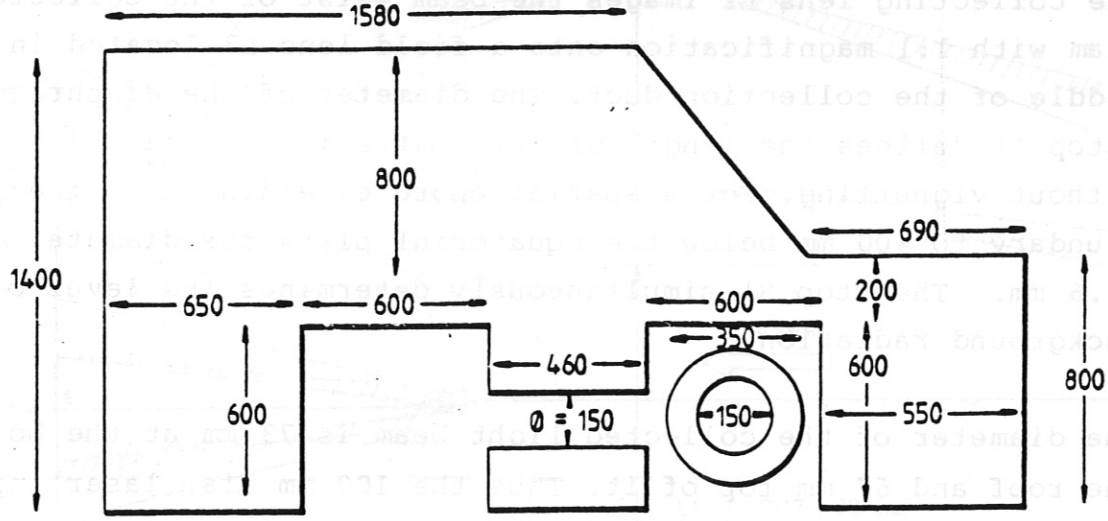

DIMENSIONS ARE IN mm.

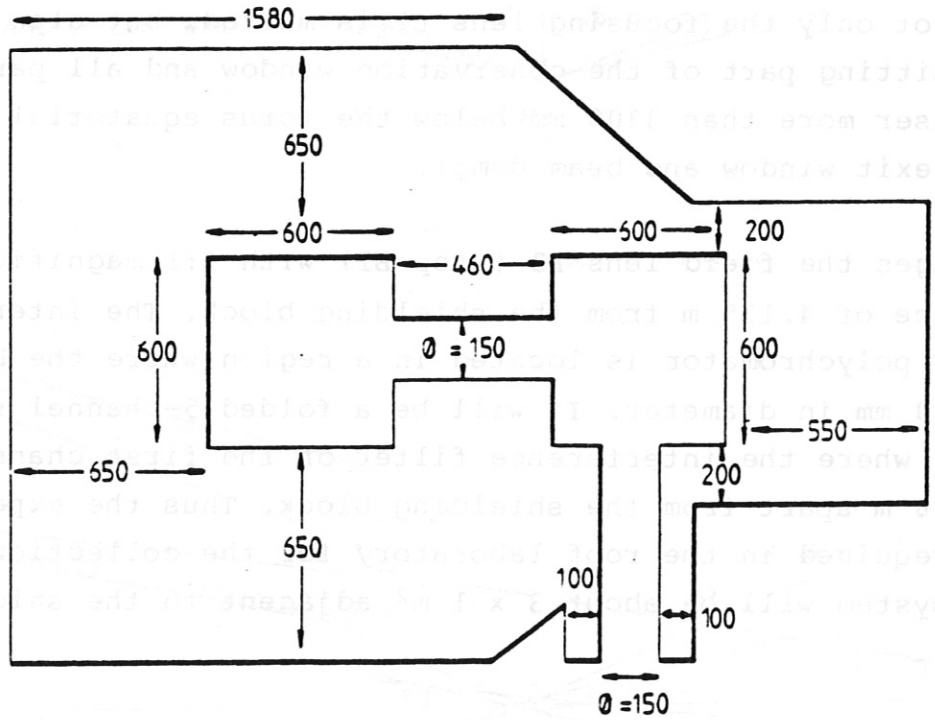

Fig. 3.22: Shielding Block

The collecting lens L2 images the beam waist of the collected light beam with 1:1 magnification onto a field lens L3 located in the middle of the collection duct. The diameter of the diaphragm at L3 (stop 1) defines the length of the scattering volume which is seen without vignetting. For a spatial chord extending from the plasma boundary to 400 mm below the equatorial plane the diameter must be 46.6 mm. The stop S1 simultaneously determines the level of plasma background radiation.

The diameter of the collected light beam is 73 mm at the bottom of the roof and 67 mm top of it. Thus the 100 mm dia. laser input duct of the KE-1 system will be suitable for the collection optics too.

The field lens L3 images the lens assembly L1 + L2 into the plane of lens L4 located outside the shielding block. The stop S2 positioned in this plane masks totally the central bore of lens L2. Thus not only the focusing lens L1 is masked, but also the laser transmitting part of the observation window and all parts hit by the laser more than 3300 mm below the torus equatorial plane (e.g. laser exit window and beam dump).

L4 images the field lens L3 (stop S1) with 1:1 magnification at a distance of 4.135 m from the shielding block. The interference filter polychromator is located in a region where the beam is less than 80 mm in diameter. It will be a folded 5-channel system (Fig. 3.24), where the interference filter of the first channel is located 2.8 m apart from the shielding block. Thus the experimental area required in the roof laboratory for the collection and detection system will be about 3 x 1 m^2 adjacent to the shielding block.

As can be seen from Fig. 3.24 no lenses are used between the interference filters. Therefore the angle of incidence onto the filters can be kept as low as 4.3°. The interference filters will be illuminated with rays deviating up to ±1.2° from the optical axis. Simple lenses behind the interference filters will concentrate the output of the different channels onto the respective MCP photomultipliers.

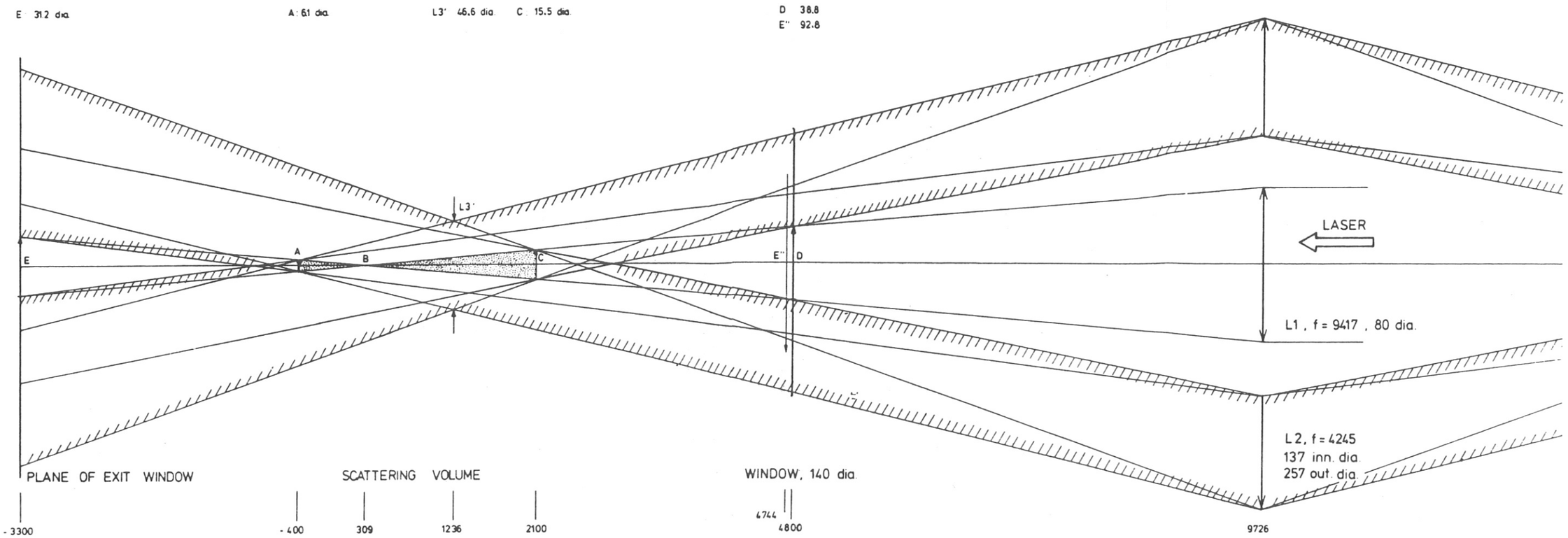

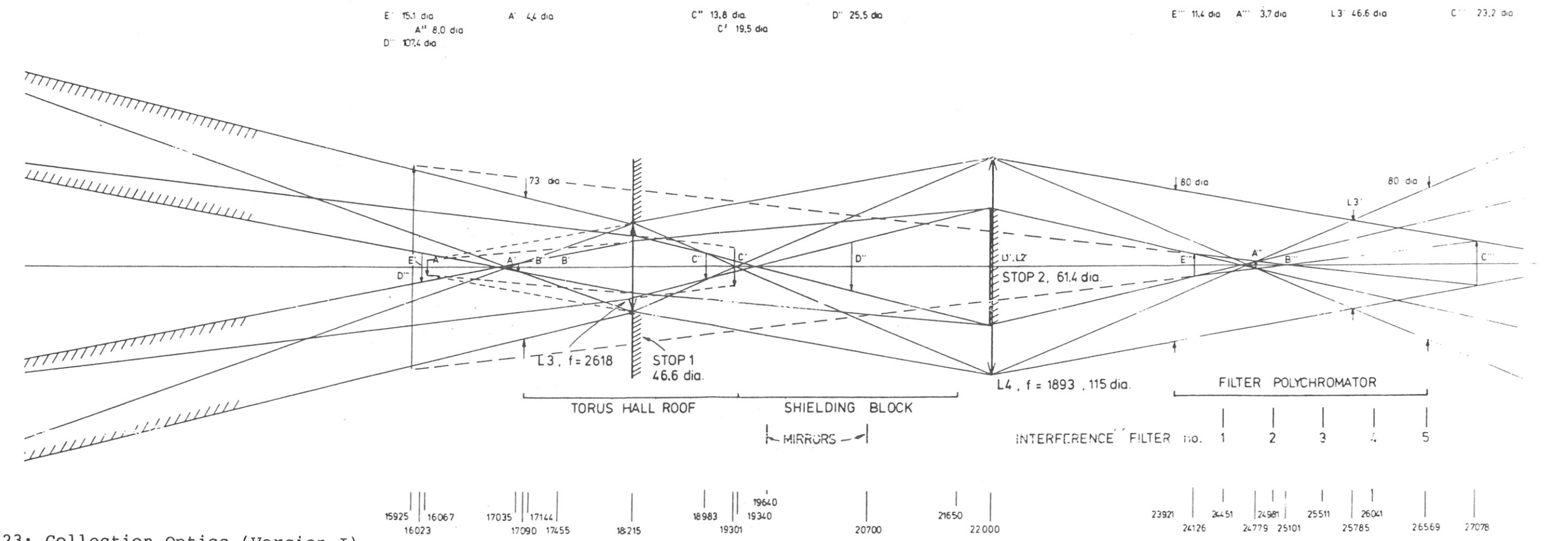

Fig. 3.23: Collection Optics (Version I)

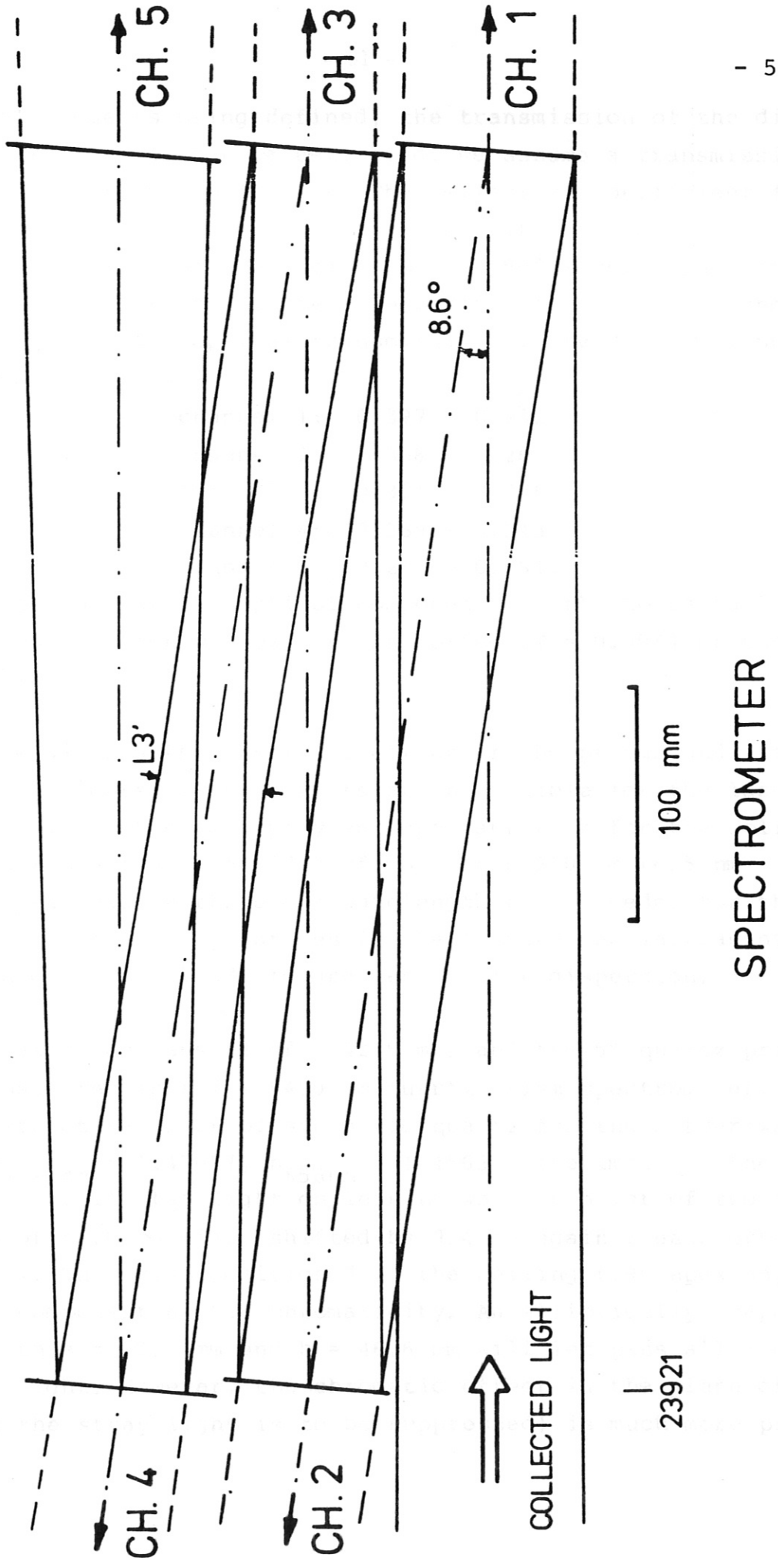

Fig. 3.24 : Spectrometer

The optical elements being defined, the transmission of the different spectral channels can be estimated. We assume a transmission of 0.6 for the interference filters. The reflection coefficient for the other wavelengths is estimated as 0.9. This value is also taken as broadband reflection coefficient of the 90° - deviating mirrors in the shielding structure. The observation window will be uncoated ($T = 0.96^2$). Then the optical transmission of the different spectral channels will be

channel 1: 0.397 - 0.292
channel 2: 0.358 - 0.263
channel 3: 0.321 - 0.236
channel 4: 0.289 - 0.213
channel 5: 0.261 - 0.191,

depending on whether the optical components in the torus hall (besides the observation window) are AR-coated ($T = 0.99^2$) or uncoated ($T = 0.96^2$).

We will now discuss the chromatic effect of the prisms and its consequences. Of course these effects are negligible for the laser input optics, but they can play an important role for the collected light with a spectral bandwidth of more than 200 nm (625 nm - 394 nm). It is especially the short wavelength range needed for the measurement of high temperatures (>5 keV) where the increasing dispersion of quartz leads to greater angular dispersion.

The combination of lens L2 (f = 4245 mm) and the 5° quartz prism can be considered as a f = 8490 mm quartz prism spectrometer. Taking the refractive index of synthetic quartz for the border wavelength ($n_{399\ nm} = 1.47097$, $n_{656nm} = 1.45637$) the image of the beam waist of the collected light on lens L3 would consist of two circular discs of 46.6 mm dia., shifted by 9.4 mm against each other (Fig. 3.25). The prism positioned at the ceiling (19° apex angle) partially compensates this chromaticity. An elliptically shaped stop S1 with a = 50.1 mm and b = 46.6 mm will let pass all the collected light. However, the chromatic effect in the plane of stop S2 (where the stray light is to be suppressed) is much more pro-

nounced. Seen through the two prisms the images of L2 (seen at the extreme wavelengths) are displaced by 15 mm. Let us assume that the optical axis of the red beam is coincident with the symmetry axis of lenses L3, L4 and of stop S2. In that case the diameter of lens L4 must be increased to 145 mm in order to let pass all collected blue light. If the stop S2 remains adjusted to block the (red) stray light, it will vignette about 12 % of the collected light at 399 nm (Fig. 3.26). It would further be necessary to change slightly the spectrometer arrangement since the beam diameter is a little bit larger. Thus the effect of chromaticity does not inflict the stray light suppression, but only leads to a continuous reduction of the effective transmission when going from the "red" channel to the "blue" one. The reduction is less than 12 %.

Keeping in mind that the chromatic effects in the plane of lens L4 are caused by the prism at the ceiling (not by the prism at L2), one can think of alternate solutions. Such solutions could consist in a reduction of the deflection by this prism. E.g., one could choose the same apex angle as for the prism at L2 which would lead to a vertical orientation of the collection duct. In that case the radiological problems of viewing directly the plasma through the duct could be reduced by installing a shield between the JET vessel and the lens assembly L1/L2. Another possible solution would be to omit the prism at the ceiling completely. In that situation the duct will be inclined by less than 2.3° in order to fit into the C3 opening.

We will discuss now the implications of vibrations or misalignment of the (prealigned and fixed) lens assembly L1/L2. If this lens assembly is mounted to the ceiling, it must be removed occasionally to let pass the crane. Thus the problem of realignment has to be considered. Of course, the realignment will be controlled by a HeNe laser. However, in the following we will discuss the consequences of a severe misalignment in order to get an idea what the precision of alignment must be.

First, all vertical displacements by even up to several cm can be neglected. Also, tilting of the device is uncritical.

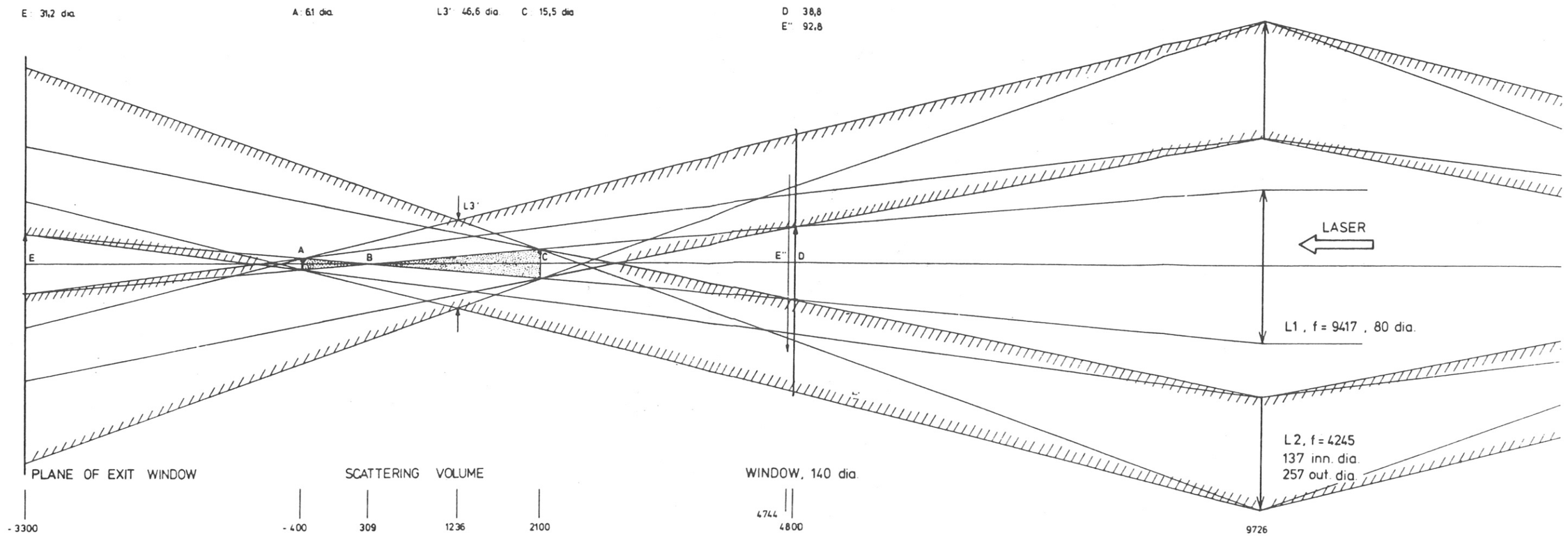

P1, P2

E' 15,1 dia
A' 8,0 dia
D' 107,4 dia
A' 44 dia
C' 13,8 dia.
C' 19,5 dia
D' 25,5 dia
E'' 11,4 dia
A'' 3,7 dia
L3' 46,6 dia
C'' 23,2 dia

Fig. 3.25 : Chromatic Effects . Full Line - 656 nm, Dotted Line - 399 nm .

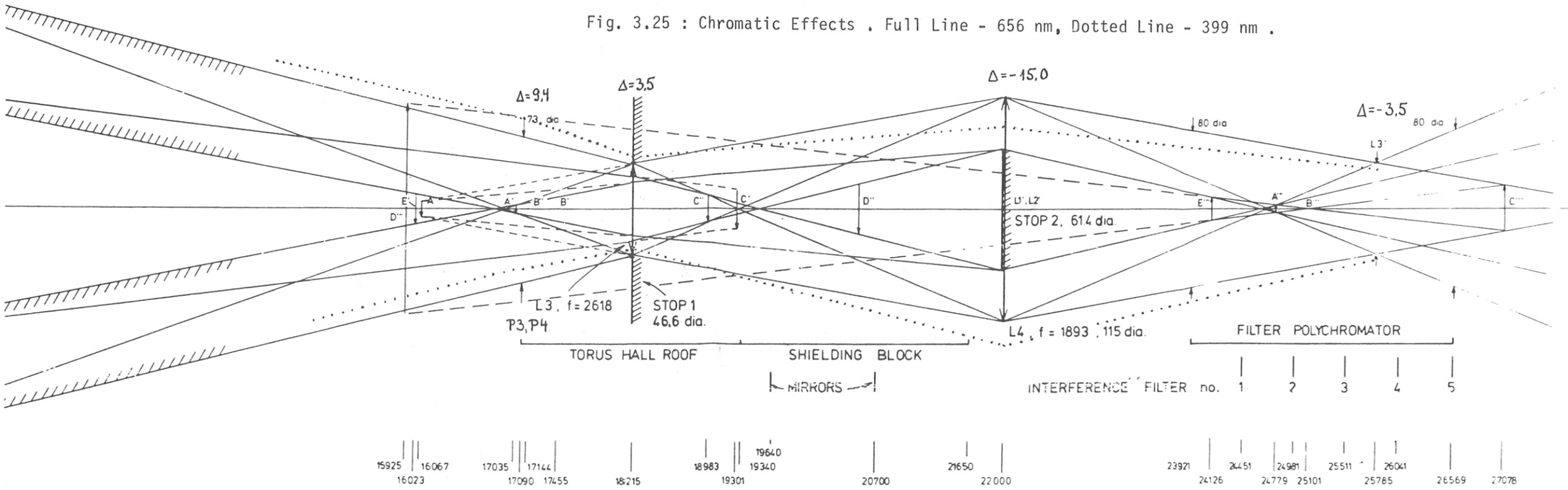

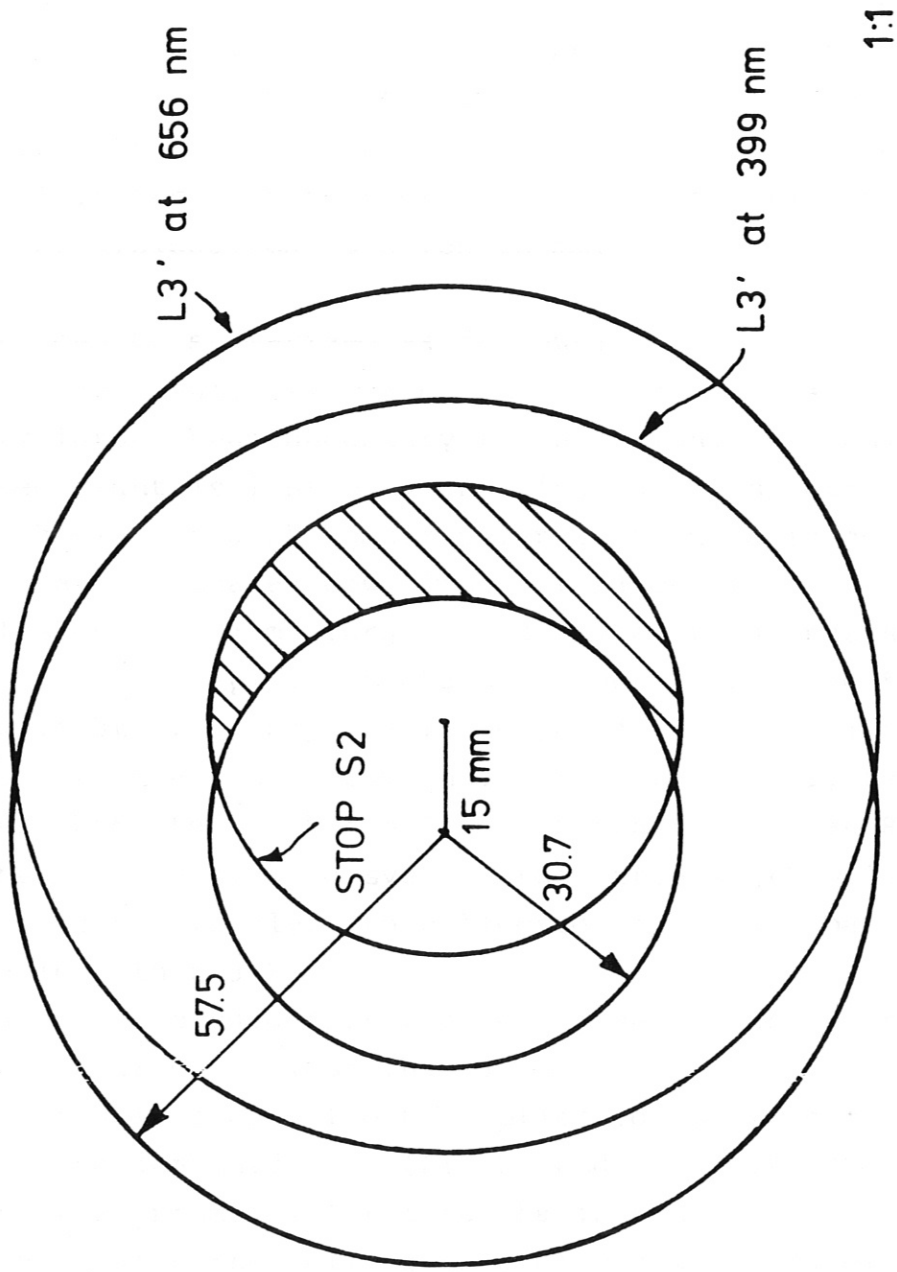

Fig. 3.26 : Vignetting due to Chromatic Effects

Second, the effect of a lateral displacement of the lens assembly by 5 mm is shown in Fig. 3.27. All other optical elements shall remain in their original position. We assume that the focusing lens is 10 mm larger in diameter than the incident beam. Thus the laser will be focused without attenuation to a spot "B" 5mm below the optical axis of L3, L4 and the spectrometer. Due to the large focal length of the system, the scattering volume is inclined only slightly versus this axis. In Fig. 3.27 the consequent displacements of all images with respect to the optical axis are shown and the amount of dislocation is given in mm.

The effects can be summarized as follows:

1. If the interference filters of the spectrometer are chosen slightly larger than necessary for an aligned system, no scattered light is lost by vignetting in the spectrometer. The photocathode of the photomultiplier to be used is considerably larger than the scaled down image of L3 on it.
2. Stop S1 should be 9 mm larger in diameter than necessary. This will increase the plasma background radiation by 50 %, but this level will still be neglibible compared with the signal level.
3. In case that the laser beam incident on L1 is only 69 mm in diameter, but the diaphragm S2 is chosen to mask an 80 mm dia. laser beam in an aligned system, the stray ligth will still be blocked off completely. The collected light will be attenuated by only less than 3 %.

Thus it can be concluded that the lens assembly should be aligned with a lateral error of less than 5 mm.

These considerations can also be applied to estimate the tolerable rotation of the combined lens (L1/L2) and prism (P1/P2) assembly. A rotation of the prisms will rotate the intersection of the collected light beam with the ceiling on a circle with 333 mm radius around the optical axis of L1/L2. If we permit a maximum lateral displacement at the ceiling of about 5 mm, the maximum allowed rotation of the lens and prism assembly is 50'. This corresponds to a movement at its circumference of less than 2 mm.

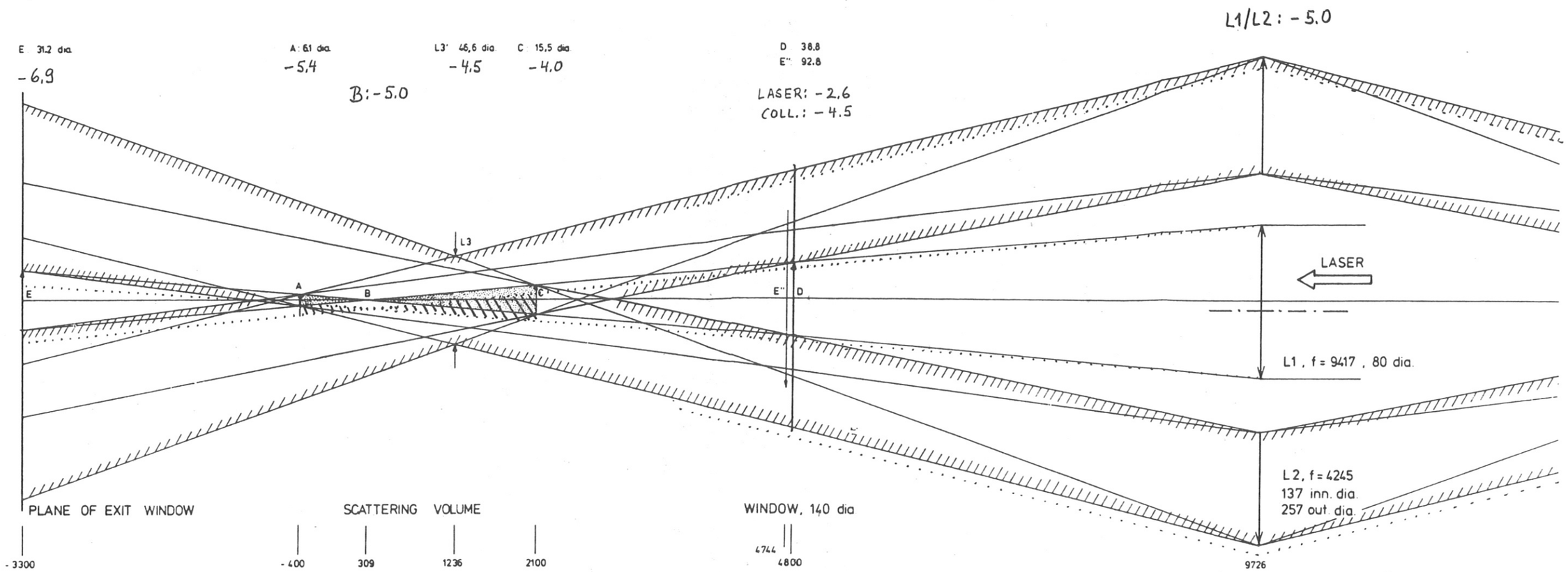

Fig. 3.27: Effect of Misalignment - Lens Assembly L1/L2 Laterally Displaced by 5 mm

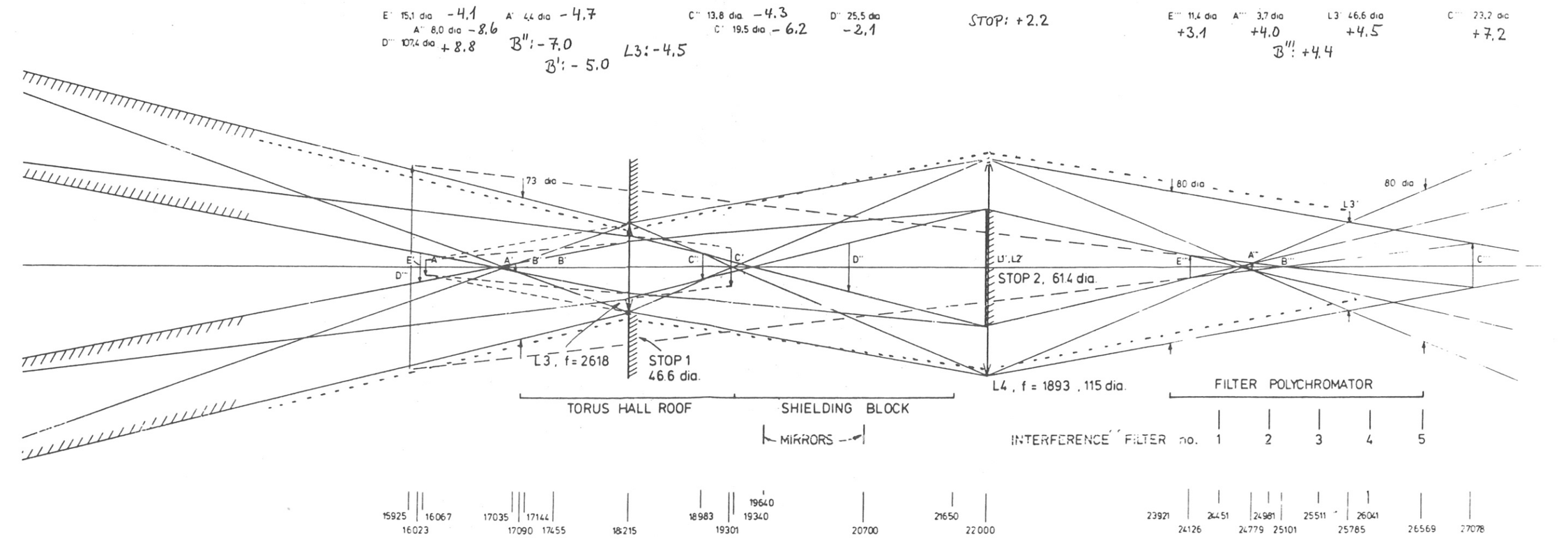

Version II

The second proposed optics also works with 1:1 imaging, allowing a small duct diameter. However, the optical path length between the scattering volume and the roof is doubled. This allows to fix the collection optics to the ceiling. The large distance between the lens and the image is realized by installing an optical delay line below the ceiling.

Since this solution again uses 1:1 imaging, the subsequent optics (lenses+polychromator) is not changed. Only the diameters and the focal lengths of the lenses L1 and L2 are increased due to the longer optical path length. Figs. 3.28 and 3.29 show the optical system as viewed side-on and from top. The input and output ducts are the same as for version I. Since the laser spot size on the torus vessel window must be conserved, the beam is expanded and focused by a lens system LO (f = -140 cm, 7.5 cm dia.) and L1 (f = 211 cm, 14 cm dia.). The lens LO is positioned at the lower end of the input duct, whereas the lens L1 is placed at a height 48 cm below the ceiling. The collection lens L2 (f = 769 cm, 43 cm outer dia., 27 cm inner dia.) surrounding the laser focusing lens L1 is positioned at the same height.

The delay line is accomplished by the mirrors M3, M4 and M5. It is folded onto the ceiling as shown in Fig. 3.29. The lens assembly L1/L2 has been shifted towards the torus centre so far that the magnetic axis can still be diagnosed through the useful opening of port "B" (diameter >100 mm). This gives maximum distance of L1/L2 from the lower ends of the ducts and thus allows to set up the delay line outside the ductwork area and without passing below one of the ceiling penetrations.

All optical components are positioned within a distance of 50 cm from the ceiling, keeping clear from the space required for the crane.

A possible geometry for the shielding block structure is given in Fig. 3.30. The outline dimensions of the shielding block still need

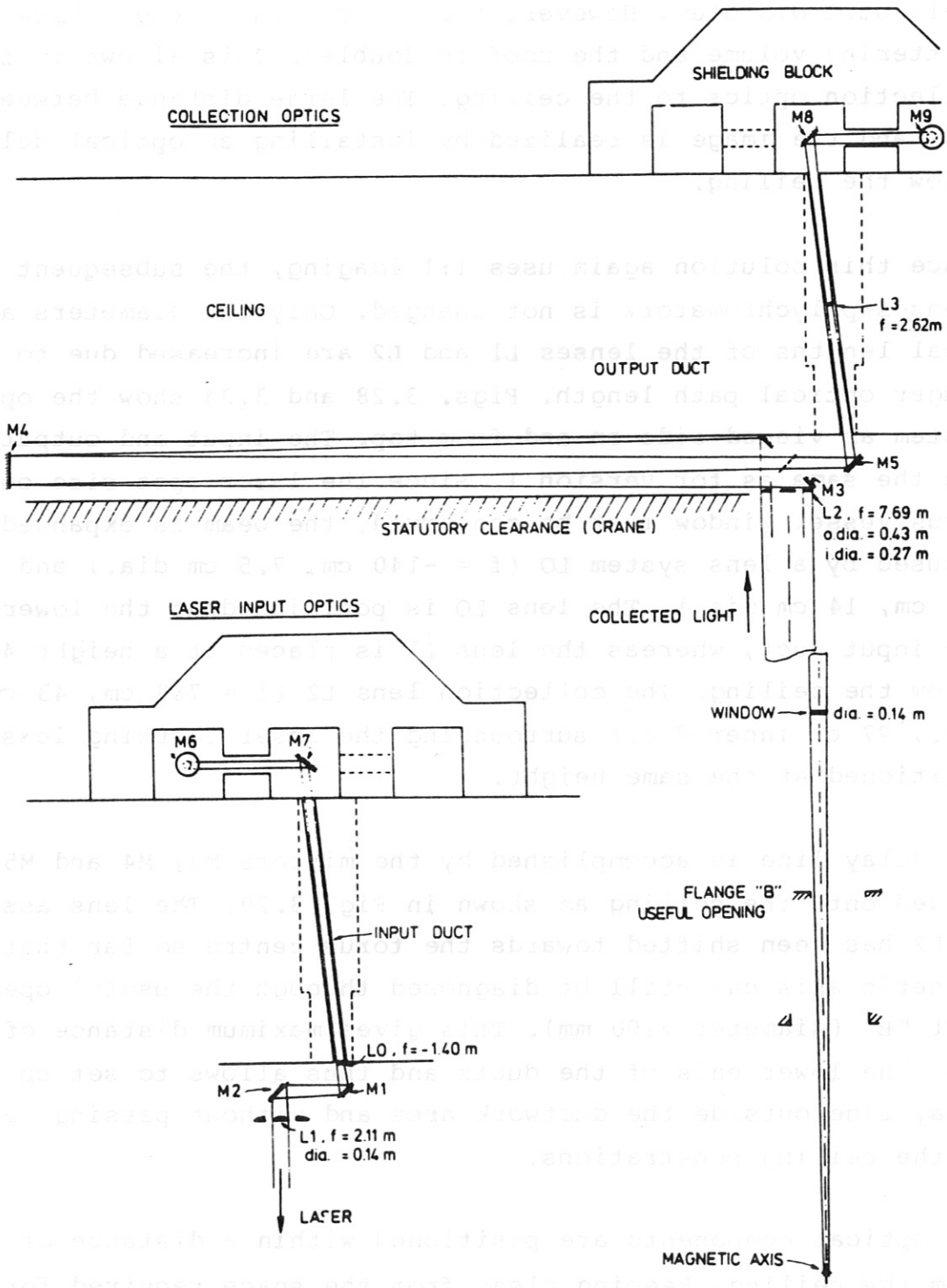

Fig. 3.28 : Optical System no. II - Side View

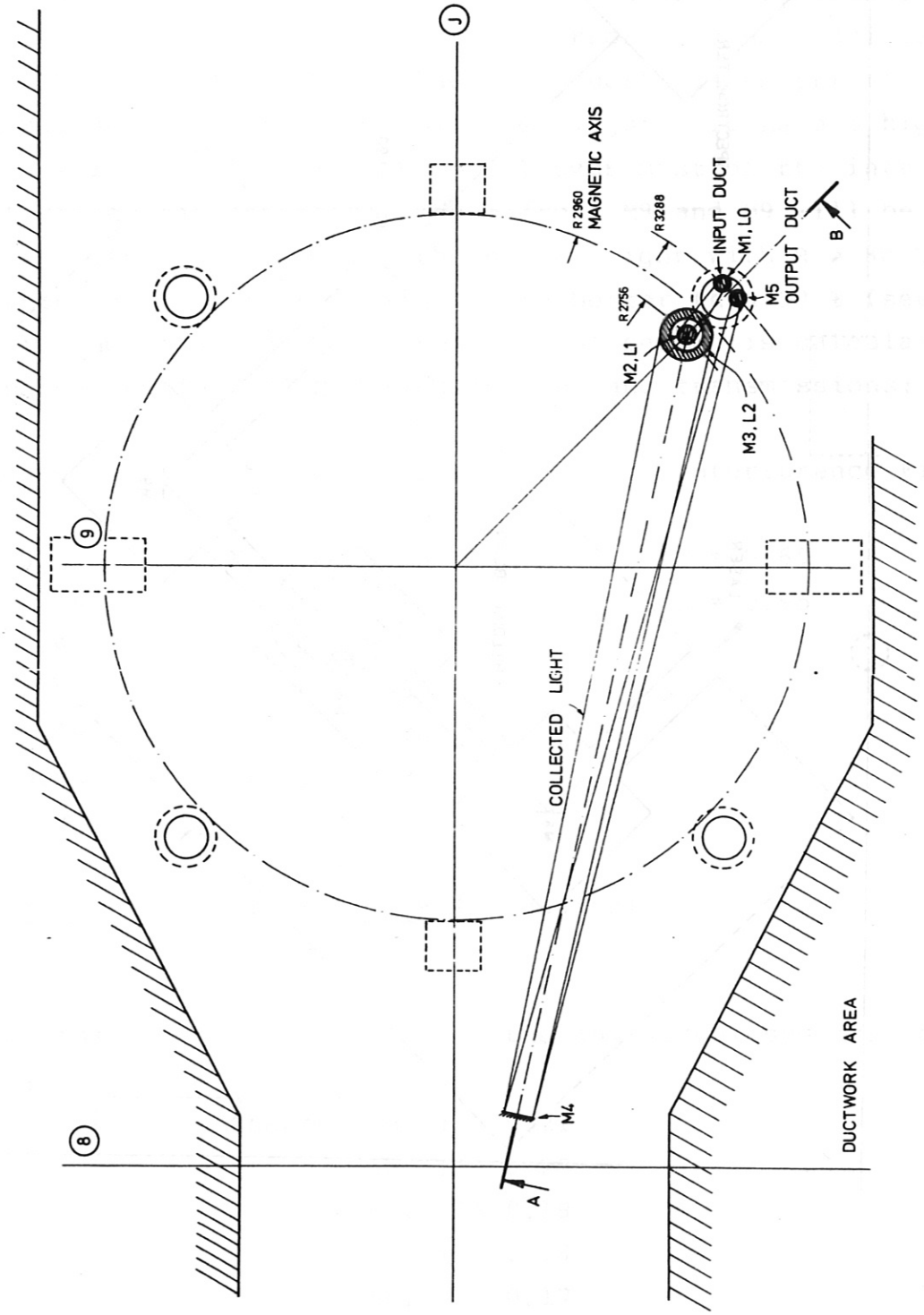

Fig. 3.29 : Optical System no. II - Top View

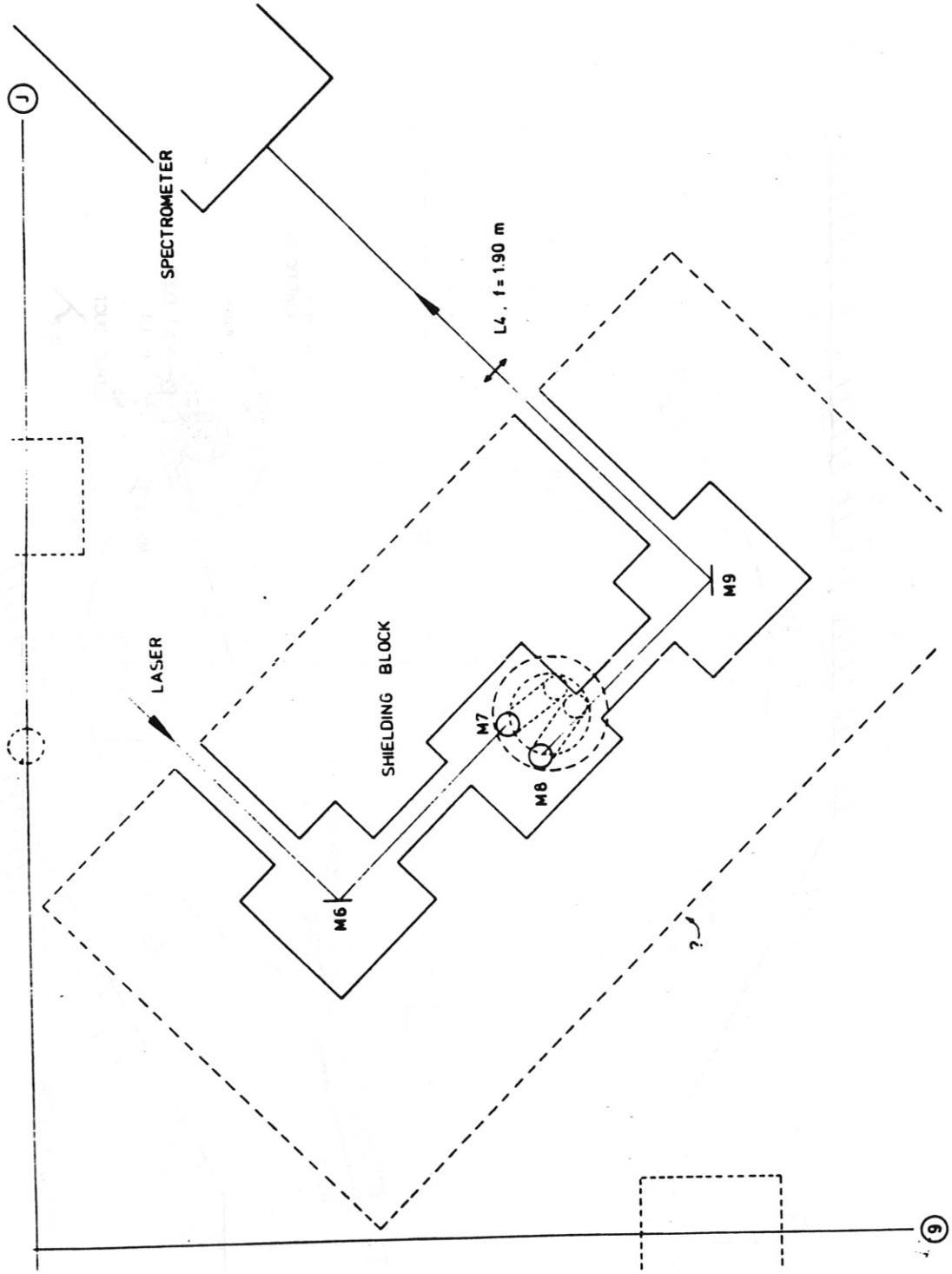

Fig. 3.30 : Shielding Block Structure

to be minimized on the basis of neutron shielding calculations. The input and output ducts of the shielding block point to the place in the roof laboratory foreseen for the laser system.

The mirrors M1, M2, M6 and M7 bending the laser beam will be dielectric ones, but in case that these mirrors are not adviseable in the torus hall, they can be replaced by quartz glass prisms. The mirrors M3, M4 and M5 for the collected light will have a high reflectance silver coating with R > 95 % over most of the interesting spectral range (see Appendix). The mirrors M8 and M9 will be "cold" dielectric mirrors, reflecting the signal light with R > 80 % and transmitting the laser stray light with better than 90 % (see Section 5.3). The transmission of the optical set-up is calculated as before using the following reflectivities and transmissions:

Laser Input	Collection Optics	Interference Filter
M6 R = 0.99	W T = 0.93	T = 0.65
M7 R = 0.99	L2 T = 0.93	R = 0.95
LO T = 0.93	M3 R = 0.95	
M1 R = 0.99	M4 R = 0.95	
M2 R = 0.99	M5 R = 0.95	
L1 T = 0.93	L3 T = 0.93	
W T = 0.93	M8 R = 0.8	
	M9 R = 0.8	
	L4 T = 0.99 (AR-coated)	
T = 0.77	T = 0.43	

The transmissions of the system for the individual spectral channels are:

Channel no. I	0.21
no. II	0.20
no. III	0.19
no. IV	0.18
no. V	0.17

Coating of the lenses in the torus hall improves the overall transmission by about 25 %. This means that in the worst case (channel V) the transmission is at least a factor of 1.7 better than assumed when calculating the statistical errors.

Version III

The version III is complicated by the fact that the telescopic system has to be placed within the free space below the ceiling (permitted height <50 cm). For 1:1 imaging a point 1236 mm above the equatorial plane into the middle of the ceiling and maintaining the solid angle of collection, this requires a telescope front lens with f = 53.6 cm and a diameter of 43 cm. Such a f/1.2 lens is not feasible.

Version IV *)

In case of version IV the situation is different from version III with respect to the possible length of the telescope. The telescope can be longer and thus the f-numbers of the lenses will be smaller. For example, placing the diverging lens near the window and the collimating lens at the height of the limbs of the magnetic circuit, f-numbers of 1/5.7 and 1/4 are required, respectively. Such a system is feasible, e.g. by taking two f/8 collimating lenses as indicated in Fig. 3.31.

With respect to chromatic effects, this system is equivalent to version I: The focal length of the corresponding prism spectrometer is increased, but the necessary deviation angle of the collected light beam and thus the apex angle of the prism have become smaller. The linear dispersion of the collected light beam in the plane of the ceiling is the same as in case of version I and thus is tolerable.

The telescope must be fixed to the limbs of the magnetic circuit and not to the vacuum vessel which moves too much when being heated up. At the moment there exist no measurements of the movement of the magnetic limbs at the relevant radius. For a discussion of the created misalignment of the telescope we will use the following estimates given by JET engineers:

---

*) The possible use of telescopic systems was proposed by Mr. R. Lobel/JET at a meeting on January 31,84

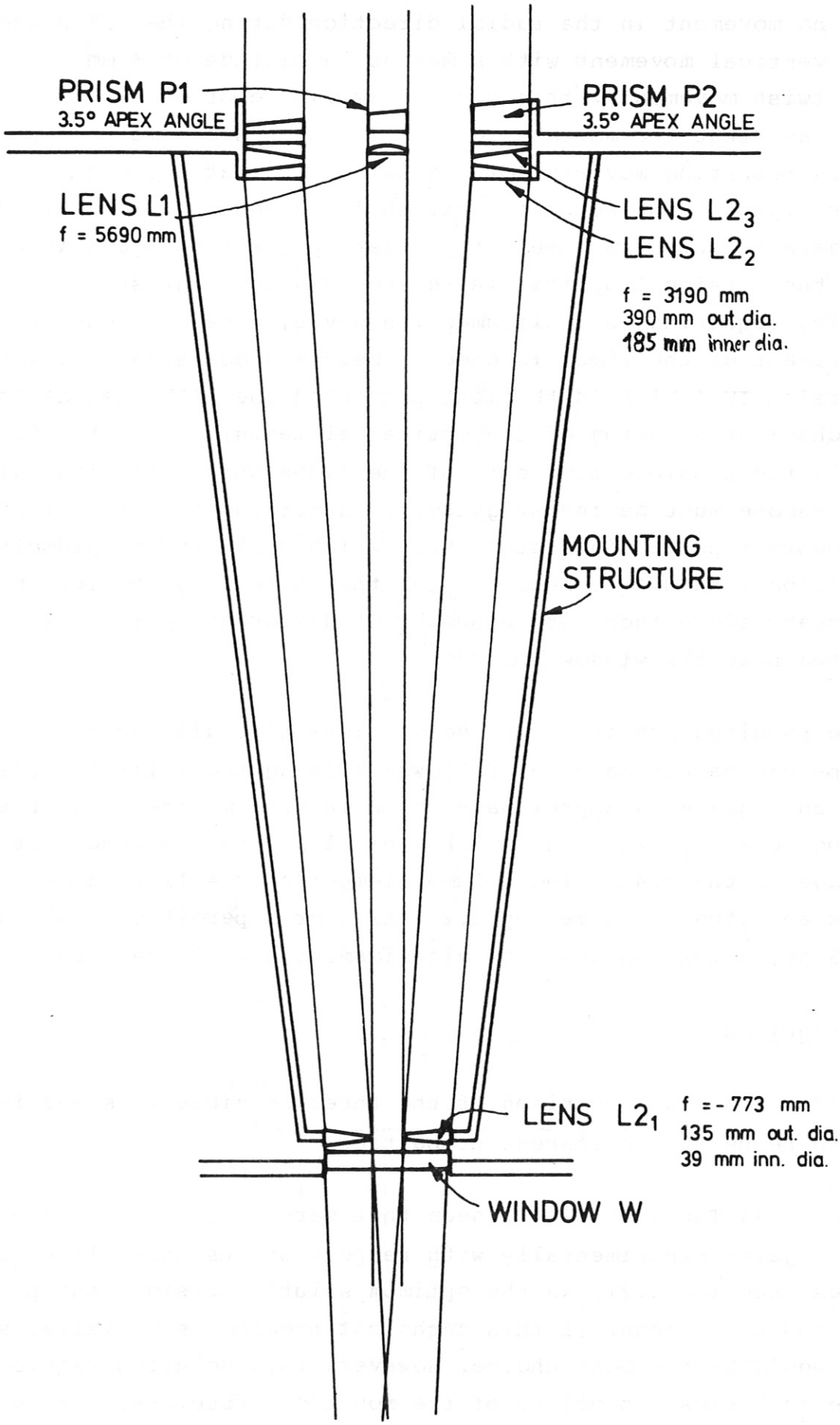

Fig. 3.31: Optical System (Version IV)

a) no movement in the radial direction during the discharge,
b) vertical movement with a maximum amplitude of 3 mm,
c) twist movement with a maximum amplitude of 1 mm.
In case that the movement of the limbs occurs simultaneously, the only resulting movement of the telescope that could give rise of misalignment is the horizontal shift of about 1 mm amplitude. With regard to such a movement the telescopic system again is equivalent to the version I optics. Therefore this movement should be tolerable, requiring no realignment. However, a measurement of the real movement of the limbs is needed, before a decision in favour of version IV (which is the most promising one with respect to the mechanical mounting of the optical elements) can be taken. Especially the possible movements of the limbs which tilt the axis of the telescope must be investigated. In addition, the stray light measurements reported in section 5.2, which apply to the geometry of version I should be repeated for the optical system IV. This is necessary since there are a number of different optical elements located near the window.

The required precision of the vertical tilt alignment of the telescope can be estimated as follows: Tilting the telescope (Fig. 3.31) by an angle α is approximated by a lateral movement ΔX of the diverging lens $L2_1$, where $\Delta X = \alpha.L$. This leads to a movement of the image of the scattering volume element at r = 1236 mm on lens L3. The amplitude is given by 1.2 x ΔX. For a permitted amplitude of $\pm$ 5 mm, a maximum angle of misalignment α = 12' results.

Comparison

In Table 3.V a comparison of the three possible versions is give with respect to different properties.

From this Table it can be seen that version I, which has been investigated experimentally with respect ot its stray light properties (section 5.2), is the optimum solution besides the problem how to mount the lens. If this technical problem is decisive, solution IV would be the best choice. However, this solution requires that the mechanical stability of the mounting structure, namely the magnetic limbs, is measured. The amount of stray light produced in this set-up must be measured too in a full scale experiment.

	Version I	Version II	Version IV
No. of Optical Elements the Torus Hall	6 (2 lenses and 2 prisms coupled rigidly; 2 prisms at the ceiling)	7 (2 lenses coupled rigidly; 5 mirrors)	8 (4 lenses and 2 prisms coupled rigidly - but not in the same plane; 2 prisms at the ceiling
Ease of Mechanical Mounting	bad (must be removed during crane operation)	medium	good
Chromatic Effects	tolerable	none	tolerable (as I)
Required Alignment Precision	Rigidly coupled optics: vertical: several cm lateral: 5 mm rotation: 50'	Long optical paths require high precision of mirror alignment; Estimate: 1'	as for I but in addition: vertical tilt 10'
Stray light	negligible (measured)	expected as for I	?
Remote Handling Capability	No	No	Yes

Table 3.V
Comparison of Feasible Optical Systems

3.3.2 Scanning Option

The LIDAR scattering system in principle allows to scan the plasma discharge by means of a beam steering mirror in front of the window. This is due to the fact that the collected light beam is collinear with the laser beam and that it is deflected in the same way. The realization of a scan however postulates that the stray light created at the beam steering optics and at the inner torus wall can be tolerated.
Fig. 3.32 shows how such a scan could be done and what parts of the plasma would be accessible in case of the optics version II. The set-up has been designed to investigate the inner part of the plasma. In the equatorial plane the scan covers a region of 800 mm from the magnetic axis to the inside. At the expense of a reduced scan range even plasma regions nearer to the inner wall might be accessible.
The main idea behind the scan optics shown in Fig. 3.31 is that it should be a modular technique. That means, that in case of malfunction one should be able to restore the normal LIDAR arrangment, measuring on a fixed chord, by simply removing the scan module.

With the scan option, one is confronted with the problem that the full laser energy hits the inner torus wall. For the given geometry, taking into account the curvature of the inner wall, the loading of the wall is approximately 3 J/cm^2 on the average for all scan angles. This corresponds to 10^{10} W/cm^2. Since evaporation of the material starts at about 3×10^8 W/cm^2, a beam dump must be used. Such a dump could be made of an array of vertical knife edges as sketched in Fig. 3.33. Using such an arrangement the effective area of the laser spot on the wall can be increased by a factor of 30 chosing the ratio a/b = 30. Of course, the loading of the edges is still 10^{10} W/cm^2. Thus the amount of iron released with each laser shot and the lifetime of the dump structure should be determined experimentally.

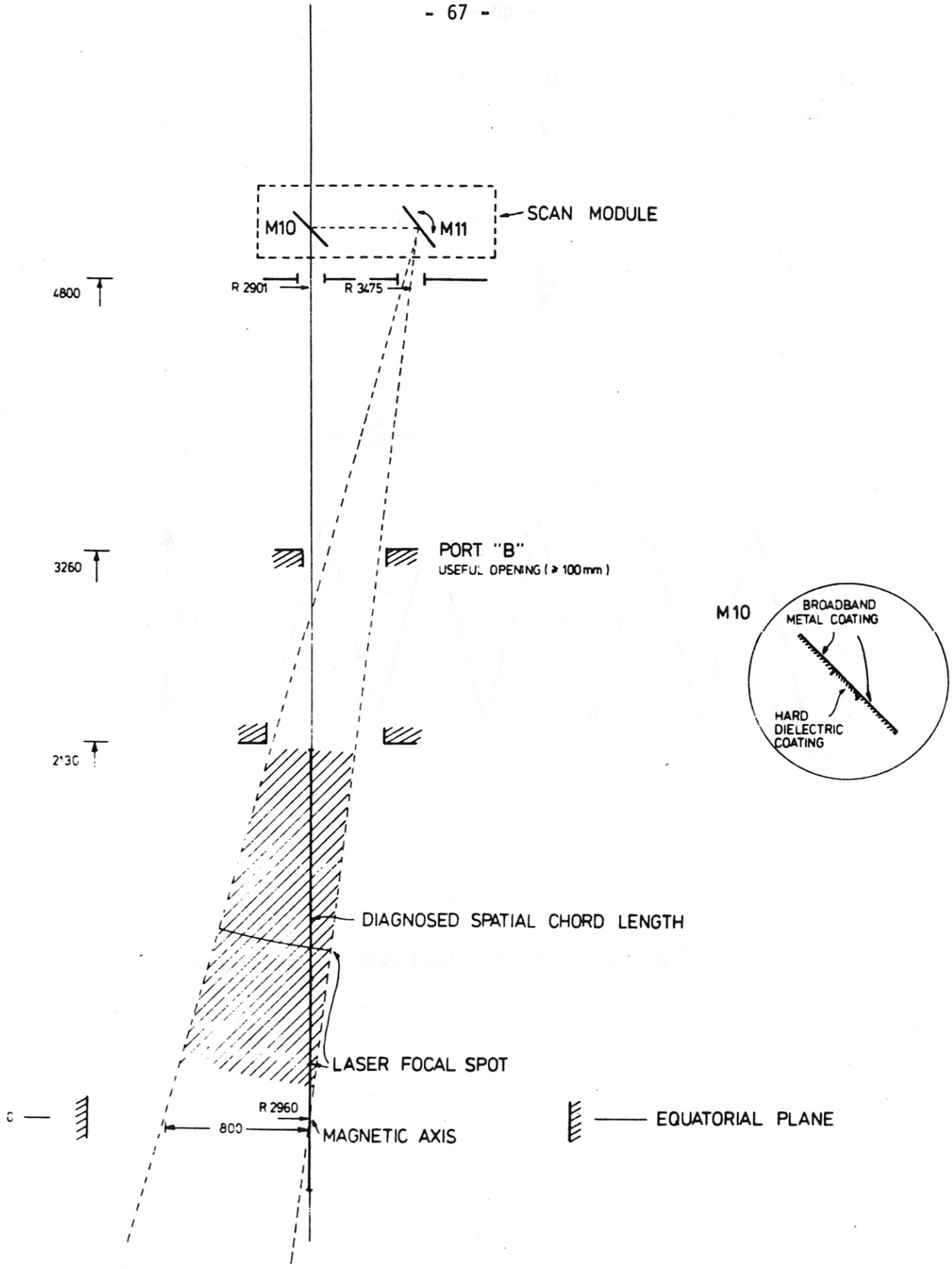

Fig. 3.32: Optical Scanning System

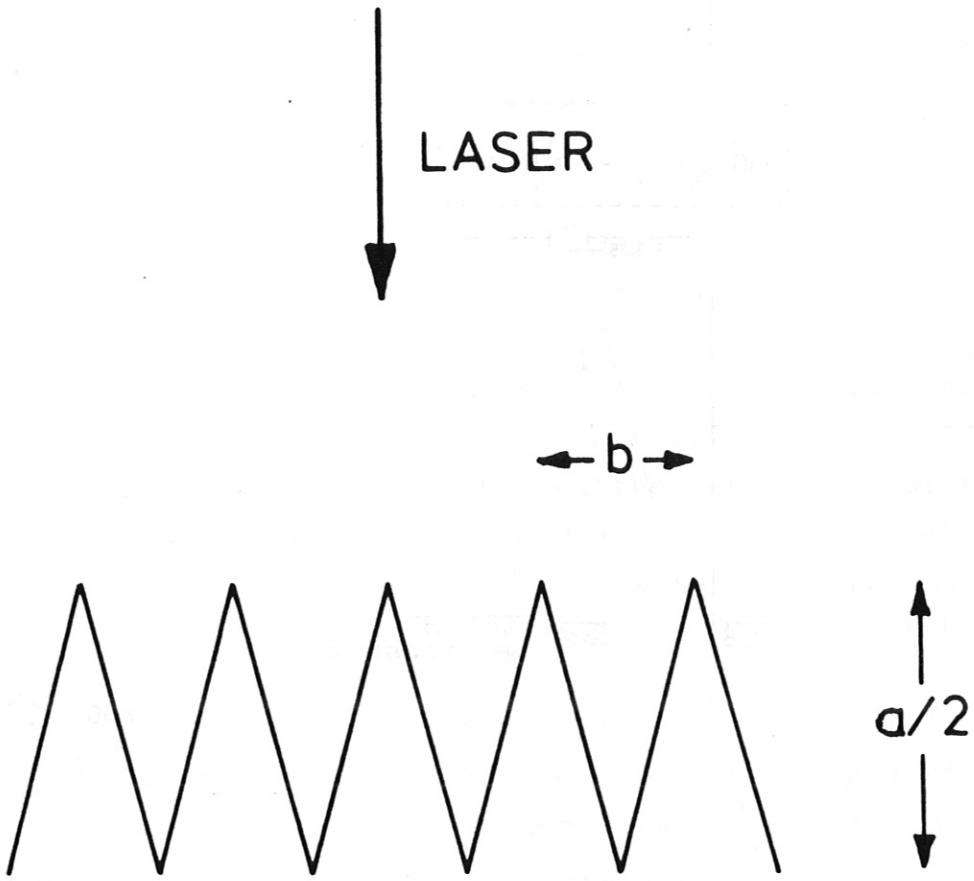

Fig. 3.33 : Internal Beam Dump

Since the stray light created at the dump arrives at the detector after the measurement has been accomplished, we have to care only about possible permanent damages to the photomultiplier or long recovery times. The MCP photomultiplier operates from the charge distribution stored in the MCP and is recharged only very slowly. Thus the photomultipier should be protected against being damaged by the stray light. This question has been investigated in the course of the photomultiplier experiments. It turned out that overloading the detector with stray light after the measurement is not critical.

The mirrors M10 and M11 of the scanner are composed of two mirrors each. The inner one, which reflects the laser beam, will be a hard dielectric coated mirror. The outer will be a broadband reflecting mirror, which to our momentary knowledge would be realized best by a high reflective silver coating (see Appendix).

Near the entrance window, where the scan module has to be placed, the spacing between the laser beam and the surrounding beam of collected light is very small. Thus, since the metal mirror coating is destroyed by the laser beam, the scan module is sensitive to misalignment. To improve this situation, the high power capability of broadband 45°-reflecting mirrors has to be investigated in order to replace the metal mirrors (see Section 5.3).

3.3.3 Alignment

As pointed out in Section 3.3.1, the alignment problems of the two favoured optical systems no. I and no. IV are similar. In both cases three optical elements have to be aligned individually in the torus hall (see Table 3.V). In Table 3.VI the numbers for the required precision of the alignment of the different degrees of freedom are taken from Section 3.3.1. We do not envisage that feedback alignment is necessary in view of these moderate alignment requirements.

	Optical Element	Degrees of Freedom	Required Precision
Version I	1 x 19° prism below laser input duct	1 - horizontal rotation	50'
	1 x 19° prism below collected light duct	1 - horizontal rotation	50'
	1 x Assembly of lenses L1/L2 and two 5° prisms	3 - horizontal translation (2) + horizontal rotation	5 mm 50'
Version IV	1 x 18° prism below laser input duct	1 - horizontal rotation	50'
	1 x 18° prism below collected light duct	1 - horizontal rotation	50'
	1 x Assembly of lenses L1/L21,L22,L23 and two 3.5° prisms	5 - horizontal translation (2) horizontal rotation vertical rotation (2)	5 mm 50' 10'

Table 3.VI

The basic reason for this insensitivity against misalignment is that with the short laser pulse duration it is possible to view a rather large plasma cross section (5cm dia.) without being disturbed by plasma background radiation. In fact, the first measure in case of misalignment would just be to increase the diameter of stop 1 (Fig. 3.23) without any considerable reduction of the precision of the measurement.

In case of the optical version IV (the more difficult one to align), the procedure of initial alignment is as follows:
First, the telescopic system (Fig. 3.31) is prealigned outside the JET torus hall.

Second, a HeNe laser beam is expanded to 60 mm dia. and focused from below into the torus vessel. The focal plane coincides with the focal plane of the iodine laser (309 mm above the equatorial plane). The axis of the HeNe laser beam is aligned to the axis of the laser exit window (at the bottom) and the observation window (at top).

Third, the telescopic system is mounted to the magnetic limbs and centered to the HeNe light cone emerging from the observation window.

Two HeNe spots will be visible at the ceiling: The first one, 80 mm in diameter, has passed lens L1 which collimates that part of the beam entering the laser exit window through the inner 31.2 mm dia. spot ("E", see Fig. 3.23). The second, much smaller one is produced by that part of the laser filling the outer part of the laser exit window (52.5 mm $\leq$ dia. $\leq$ 60 mm). This part is imaged by lens L2 (assembly $L2_1, L2_2, L2_3$) onto the ceiling.

Fourth, the telescopic system is rotated around its vertical axis. Due to the two 3.5° prisms the two HeNe spots at the ceiling will rotate around a common centre (the intersection of the telescope axis with the ceiling). The telescope axis is then adjusted in such a way that both spots hit their corresponding ducts.

Fifth, the 18° prisms below the ducts are rotated around their vertical axes in such a way as to align the deviated HeNe beams to the axes of the ducts.

Sixth, the deflecting mirrors in the shielding block are adjusted.

The further alignment of the collection optics is straightforward.

Last, the iodine laser is aligned to the HeNe beam from below by means of two beam steering mirrors.

3.3.4 Calibration

Absolute independent calibration of the Thomson scattering device with respect to the electron density measurement usually is done with the help of either Rayleigh- or Raman-scattering. These techniques combine the determination of the absolute sensitivity of the detection system with the check of the alignment and the measurement of the laser energy at the scattering volume.

For our case we consider Raman-scattering as not feasible since the Antistokes lines are too weak and averaging over a large number of shots would be required /8,9/.

Until the measurement of the stray light level reported in section 5.2, which was done at the end of this study, we considered Rayleigh-scattering as not possible too. Since a high level of stray light was expected, a central spectral channel including the laser wavelength was omitted in all considerations. The measured stray light level, however, indicates that Rayleigh-scattering can be done.

We envisage four density calibration methods, two independent ones (Rayleigh-scattering and calibration with a blackbody light source) and two methods using the results from other diagnostics.

First, since a spatial profile on a vertical chord is measured by the LIDAR technique, a comparison with the corresponding electron

line density taken from the DCN interferometry will give an absolute calibration without the need of assuming a density profile.

Second, for the plasma centre, the result from the single point Thomson scattering measurement can be taken as a reference.

Third, we will consider Rayleigh-scattering. The detector tests in section 5.1 show that gating of the photomultiplier allows a stray light pulse of up to 10^9 photons to occur 18 ns before the measurement. Up to this level the subsequent measurement of the scattered light signal is not deteriorated. The stray light measurements reported in section 5.2 yield that about 2×10^{10} stray light photons are to be expected for the invisaged 15 J laser pulse. Thus, a neutral density filter with an attenuation factor of 30 in front of the central spectral channel detector will reduce the stray ligth level to a tolerable level. On the other hand, even in the presence of this filter, the Rayleigh scattering from a 1 Torr hydrogen filling in the JET torus vessel will give a signal amplitude comparable to the amplitude of the Thomson scattering signal. About 200 photoelectrons are expected for each spatial channel of 13 cm length. Summing up the Rayleigh scattering signal over a spatial chord length of about 1 m, a statistical error of less than 3 % results for a single laser shot.

There are two effects which could affect the Rayleigh calibration.

First, the laser line is adjacent to the Balmer line Hα of atomic hydrogen. Therefore the effect of near-resonant Rayleigh scattering must be considered. It can be shown, however, that even if all hydrogen would be dissociated and excited to the second and third excitation state, this effect is negligible compared with the Rayleigh scattering signal. This is due to the rather low saturation level which is about 10^8 times lower than the power density in the converging laser beam.

Second, gas breakdown could occur at the high power density level of the laser beam inside the vessel. At the low filling pressure of 1 Torr hydrogen, a threshold of $> 10^{13}$ W/cm^2 can be expeded in the

absence of dust particles /10/. Thus it is unlikely that gas breakdown occurs. However, even if breakdown would occur in the vicinity of the laser focal plane (309 mm above the equatorial plane), the Rayleigh scattering signal can be measured from the region above.

The fourth possible calibration method uses a blackbody light source to calibrate the absolute spectral sensitivity of the detection system. This includes the spectral transmission of the window, the collection system, the spectrometer and the spectral responsivity of the detectors. The blackbody calibration set-up is understood considering the following: As the laser pulse runs down the spatial chord, the scattered light from each volume element is collected by the annular lens L2. The solid angle of collection varies only slightly along the spatial chord length under investigation. The scattered light seems to originate from an annulus around the laser exit window. This annulus shrinks in the course of the laser pulse propagation (Fig. 3.34). Thus, placing a blackbody source into a scattering volume of the spatial chord is equivalent to a blackbody source with the size and the position of the corresponding annulus. The calibration will be done using a small window located within the annulus and a blackbody light source outside the vessel. This thermal light source will then be seen by the detection system as a thermal light source with the area of the scattering volume, weighted with the ratio of the window area to that of the annulus, and with the corresponding solid angle of detection.

An estimate of the detector signals to be expected with a tungsten ribbon·lamp operated at 2600 K yields a detector current of approx. 5 mA for the spectral channel no. I. Thereby it was assumed that a 2 x 2 mm^2 area of the tungsten ribbon is imaged (with 25-fold magnification) onto the 50 mm dia. window.

The photomultiplier output current of 5 mA requires gating of the photomultiplier in the 100 ns range. Integration over the gate duration will give signals with small error bars.

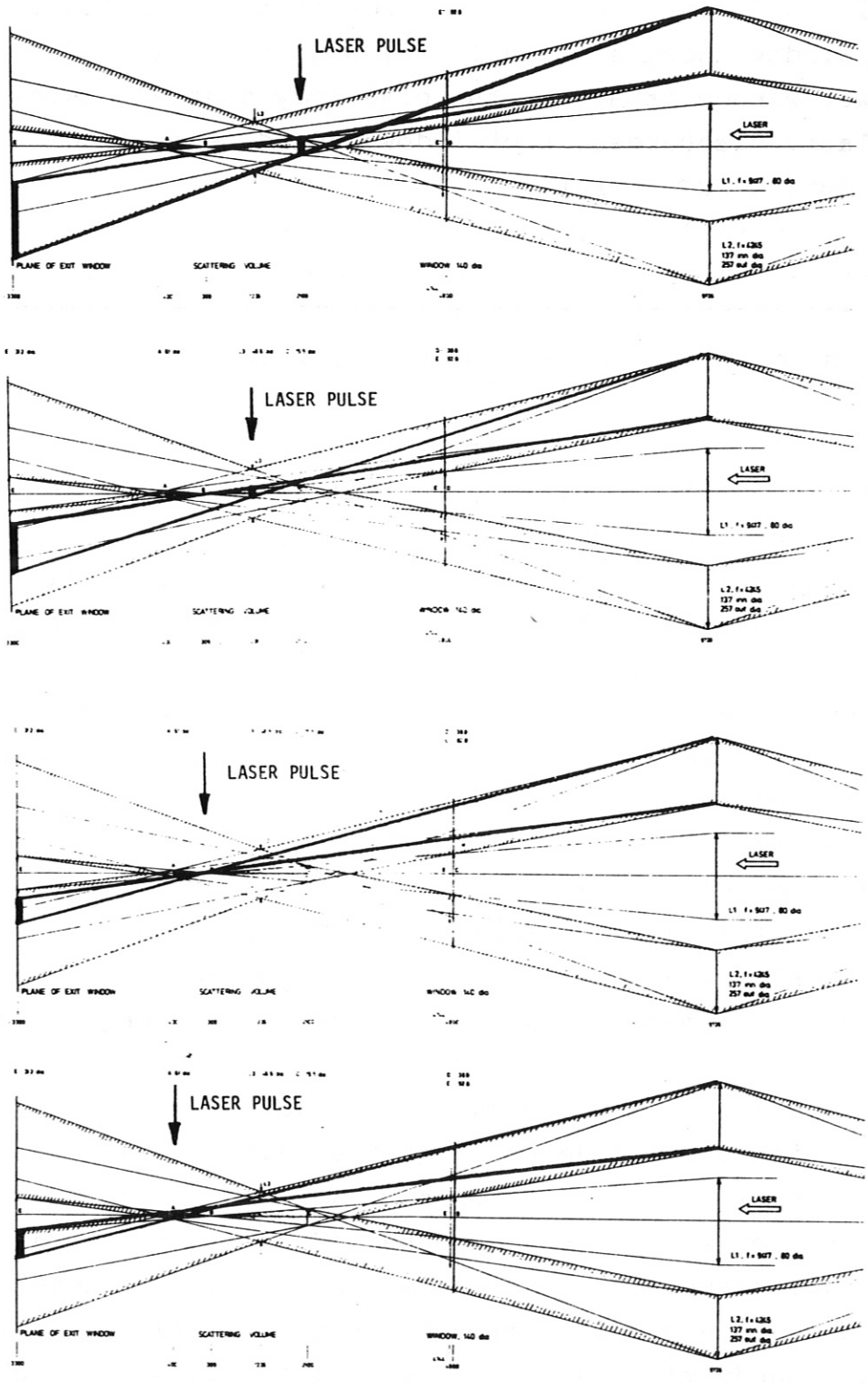

Fig. 3.34 : Effect of Laser Pulse Propagation

As mentioned, this calibration method does not include the check of the laser alignment as it is the case with Rayleigh scattering. However, it is very useful in addition to the Rayleigh calibration since it monitores whether the spectral transmission of the observation window changes nonuniformly with time. In order to protect the lower window (that for the blackbody source) against deposits from plasma discharges, the window should be covered by a shutter always during JET operation.

4 LASER SYSTEM

The following report deals with a feasibility study for the construction of a frequency-doubled iodine laser which is to be operated with a repetition rate of 1 Hz for a sequence of 10 shots. The required output energy is in the range of 15 - 20 J at λ = 657.6 nm (2 ω). Provided that a frequency-doubling conversion efficiency of about 50 % is obtained, the output energy at λ = 1.315 µm should then be in the range of 30 to 40 J. The pulse duration of the laser should not exceed 300 ps. Since this laser is to be employed as a radiation source for a LIDAR-Thomson scattering experiment in JET, it will be referred to in the following as JIL (JET Iodine Laser).

Until now the iodine laser has been exclusively used in single-pulse operation with pulse intervals in the minute range. So far output energy levels of up to 300 J at pulse durations of 250 to 350 ps have been obtained /11/ and frequency-doubling experiments revealed maximum conversion efficiencies of 70 % /12/.

The gaseous iodine laser medium is partially used up during operation and iodine molecules are formed, which act as strong quenchers for the excited iodine atoms of the following shot. In order to guarantee stable and reproducible laser operation, the used up laser medium has to be replaced and the I_2-molecules have to be extracted after each shot. This can easily be accomplished by a laser medium regeneration system /13/ as long as the laser shot rate is in the range of minutes. With this system the laser medium is regenerated between subsequent shots and the laser medium is at rest during laser operation. Excellent optical homogeneity of the laser medium is thus guarenteed for each shot. This mode of operation cannot be employed for a 1 Hz laser since the laser medium needs more than 1 s after the regeneration process to recover its optical homogeneity, which is a mandatory requirement for the good beam quality (~ 3 times diffraction limited) necessary for efficient frequency conversion ($\eta_{2\omega}$ > 50 %). The only chance of realizing a 1 Hz iodine laser with a sufficient good beam quality is therefore to operate the laser with a highly turbulent laser medium flow. For such a mode of operation the laser medium regeneration

system has to be enlarged so that fast and complete regeneration of the laser medium is ensured. In addition, precautions have also to be taken to ensure that thermal effects caused by the high-repetition flashlamp pumping do not impair the optical homogeneity of the laser medium.

In the following the layout of a 1 Hz test laser delivering output energies in the 50 mJ range at 2 ω is described and the results regarding beam quality, frequency conversion efficiency, stability and reproducibility are discussed.

Since for the realization of a 1 Hz laser technical aspects such as the liefetime of flashlamps are also of basic importance, these have to be investigated as well. The lifetime of flashlamps hitherto used in single-shot lasers is of the order of 2000-3000 shots, a number much too small for 1 Hz operation. A test programme was therefore instituted to investigate measures for prolonging the lifetime of flashlamps. The results of these investigations will be described in detail in a separate report, but the essential results necessary for the construction of high-repetition iodine laser will be described in the chapter dealing with the design and outlay of a 1 Hz iodine laser with an output energy of 15-20 J at 2 ω. The report concludes with a description of the maintenance effort necessary for the operation of JIL and with the prospects for increasing the repetition rate beyond the 1 Hz level.

4.1 Description of the Test Laser System

The laser system used to demonstrate the feasibility of a 1 Hz-operation was built from components already available at MPQ. New components were only constructed as far as they were necessary to enable extrapolations needed for the design and outlay of JIL.

The test laser system schematically shown in Fig. 4.1 consists of an actively mode-locked oscillator, a Pockels cell shutter for single pulse selection and oscillator/amplifier decoupling, an amplifier and a KD*P-crystal for frequency doubling.

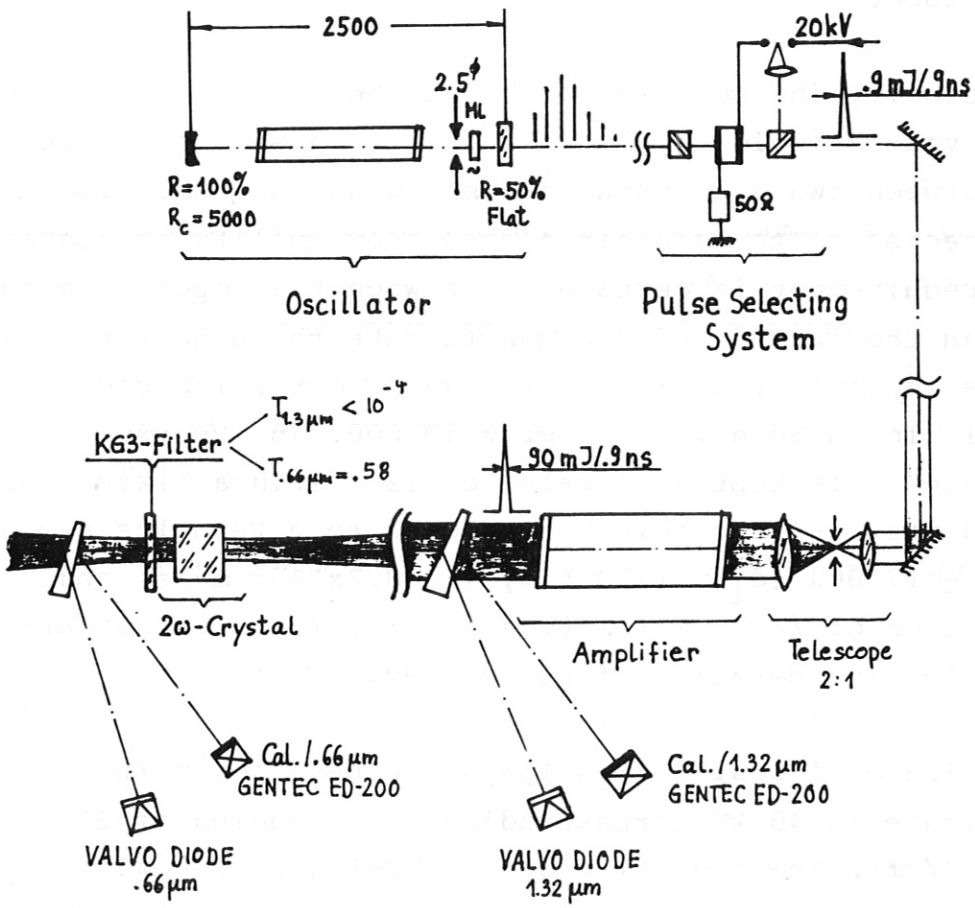

Fig. 4.1: Schematics of the test laser

In the oscillator the quartz tube is double-walled to enable water cooling. This turned out to be a very efficient method in removing the heat released by the flashlamps. Quartz tube and flashlamps are imbedded in a double elliptic, electro-polished aluminium reflector. The laser medium (100 mbar i-C_3F_7I + 2 bar argon) is contained

in a closed loop and is forced to circulate by means of a magnetically driven radial pump. The molecular iodine built up after the photolysis of the C_3F_7I is removed in a cold trap kept at a temperature of -10 °C. This value is equivalent to an i-C_3F_7I vapor pressure of 100 mbar which matches the i-C_3F_7I pressure needed in the quartz tube.

The flow velocity in the quartz tube can be as high as v = 30 m/s. Its actual value should be chosen such that a sufficient medium recovery between two succeeding shots and at the same time a turbulent flow necessary to maintain a good beam quality is guaranteed. The first requirement is certainly met when the repetition rate is smaller than the inverse of the quartz tube throughput time ℓ/v (ℓ quartz tube length) by a factor of five or more. The second requirement calls for a Reynolds number > 10.000. In the experiments reported below v is kept at a value of 12 m/s. In a mixture of 2 bar argon + 100 mbar i-C_3F_7I this corresponds to a Reynolds number of $Re = vd_i/\nu \simeq 17.000$ ($d_i = 1 \times 10^{-2}$ m, $\nu = 0.7 \times 10^{-5}$ m^2/s) and a throughput time of $\ell/v \sim 0.1$ s ($\ell = 1.1$ m). These values are thus sufficient for an operation of up to 2 Hz.

In the oscillator 4 sealed flashlamps are used for pumping. The routine voltage is 40 kV corresponding to a loading of 230 J per lamp or 10 J/cm^3. The rise time of the UV-light (240-300 nm) is 800 ns and the discharge time 2 µs (first current zero) leading to a power density in the flashlamps of ~ 5 MW/cm^3. The electrical circuit consisting of flashlamps, spark gaps, capacitor, trigger and loading units enables repetition rates up to 2 Hz. Up to now the flashlamps have been fired 15.000 times. They are still in good shape so that their life time may well be expected to be in the range from 20.000 to 30.000 shots.

The pulse selecting system is of conventional type. It consists of two crossed polarizers (Glan prisms) between which a Pockels cell with a switching voltage of 10 kV is placed. The crystal is made of KD*P. The electrical pulse released by means of a laser triggered spark gap has a duration of 17 ns and a rise time of 2 ns. The

optical transmission of the pulse selecting system is 60 ± 15 % at a contrast ratio of 1 : 1000. It can be operated up to a few Hz.

The amplifier is air-cooled. The 4 home made flashlamps filled with 30 mbar Xe and the laser tube (d_i = 25 mm, ℓ = 2 m) are embedded in an double elliptic, electro-polished aluminium reflector. The closed loop of the laser medium is principally the same as in the case of the oscillator. The flow of the laser medium is, however, effected by a membrane pump which because of its intermittent mode of operation is not as favourable as a radial pump. In JIL only pumps of the latter type should be used. At a total pressure of 750 mbar (80 mbar $i\text{-}C_3F_7I$ + 670 mbar Ar) the flow velocity achieved in the quartz tube amounts to v = 12 m/s yielding a Reynolds number of 16.000 and a throughput time of $\ell/v \sim 0.2$ s what is sufficient for an operation of up to 1 Hz.

The electrical circuit is a little bit slower than that of the oscillator. The uv-light rise time is 1.5 µs and the first current zero occurs after 4 µs. The routine voltage is 40 kV corresponding to a flashlamp loading of 500 J $\hat{=}$ 12 J/cm^3 or 3 MW/cm^3 each. The flashlamps have been fired for over 10.000 shots and are still in good shape. Their lifetime estimated on their present state should be more than 20.000 shots. The electrical circuit allows repetition rates up to 1 Hz.

The frequency doubling crystal is made of highly deuterated KD*P (> 95 %) and cut according to type II phase matching. The effective area is 12x12 mm^2. The phase matching angle amounts to 51°. The crystal is enclosed in a cell filled with dry air. Crystal cooling turned out not to be necessary. In order to achieve a power density of the order of 1 GW/cm^2 the beam is gently focused by means of the spatial filter behind the pulse cutting system (see Fig. 4.1). The crystal is placed in the beam waist to ensure optimal conditions for a good frequence conversion.

4.2 Results Obtained with the Test Laser Facility

Firstly investigations regarding the oscillator including the Pockels cell shutter will be reported. Then the performance of the entire system will be presented.

4.2.1 Oscillator

In all the experiments described below the oscillator is operated with 100 mbar i-C_3F_7I and 2 bar argon. Under these conditions the oscillator emits a pulse train with an energy of 6.3 ± 0.5 mJ in the TEM_{oo}-mode.

a) b)

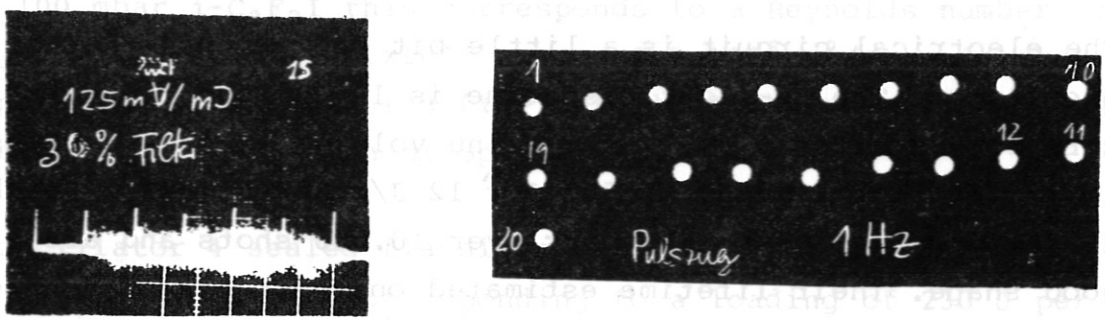

Fig. 4.2: Pulse train energy a) and mode pattern b) at 1 Hz.

As can be seen from Fig. 4.2 pulse train energy and mode pattern are stable at the desired 1 Hz-operation. The three peak pulses of the pulse train have almost the same energy and one of them is selected for transmission by the pulse cutting system which works with a reliability of 90 %, i. e. in 9 out of 10 cases it functions properly. (The JIL pulse cutting system will have a better performance). Figs. 4.3a,b show single pulse energy and duration behind the pulse cutting system.

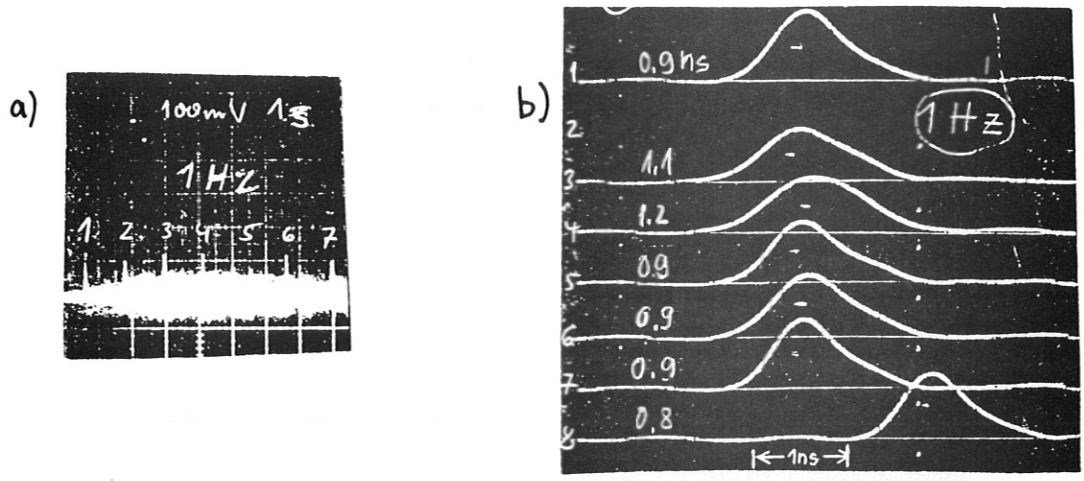

Fig. 4.3: Single pulse energy a) and duration b) behind the pulse cutting system at 1 Hz

The average single pulse energy and duration are 0.9 mJ and 0.95 ns. The pulse shape is not as stable as it could be. This is due to the mode locker whose depth of modulation is insufficient. The JIL-mode locker will produce more stable pulses.

The directional stability of the transmitted oscillator pulse is measured by focusing it on the screen of a near infrared sensitive vidicon placed in the focal plane of a lens. Within the measuring acuracy of ± 20 µrad the beam proved to be directionally stable. This means that after a distance of 100 m the transverse beam displacement will not vary by more than ± 2 mm from shot to shot at 1 Hz. This satisfying result does not change when the amplifier is also fired.

4.2.2 Entire System

When the entire system is fired pulse energy and duration at ω and 2ω are simultaneously recordes (see Fig. 4.1). The pulse durations at ω and 2ω turned out to be equal and have an average of .95 ns.

This value is larger than that aimed at in JIL where 300 ps are required. This pulse duration will be realized by two measures. Firstly a mode locker already in operation in STERIX III will be used yielding a pulse duration of 500 ps. Secondly, by amplification in the saturation regime the pulse will be compressed to 300 ps. Since in this feasibility study the exact realization of the desired pulse duration is of minor importance no effort was made in this directions.

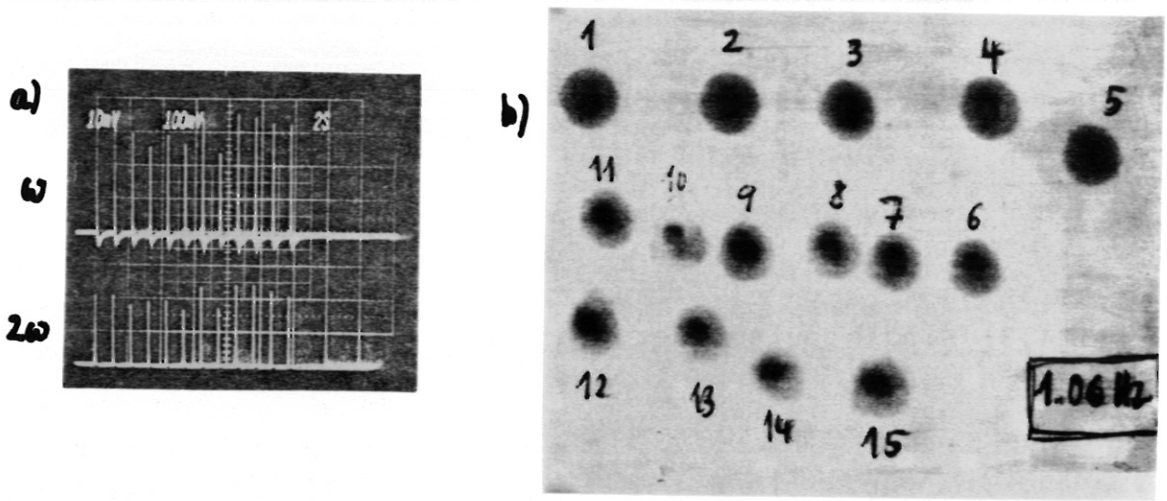

Fig. 4.4: a) Calorimeter recordings at ω and 2ω
b) 2ω-burn pattern magnified by a negative lens

Fig. 4.4a shows recordings of the pulse energy at ω and 2ω for a sequence of 12 pulses at a repetition rate of 1 Hz yielding E_ω = 90 ± 11 mJ and $E_{2\omega}$ = 40 ± 5 mJ with a corresponding conversion efficiency of $\eta_c = E_{2\omega}/E_\omega$ = 45 ± 3 %. This value is rather close to the desired 50 % so that no attempt was made to increase the conversion efficiency any further by modifying the beam optics and thereby enhancing the intensity at the crystal position above the 1 GW/cm^2 level used in the experiments described. The measured conversion efficiencies agree with the values previously reported /12/.

As can be seen from a comparison of Figs. 4.2b and 4.4b the 2ω-burn pattern is a good reproduction of that at ω. This result is further supported by measurements of the 2ω-beam quality using a pinhole. In reference to the ω-case no deterioration could be detected leading thus to the conclusion that the frequency conversion process does not impair the beam quality which is here about 2 times diffraction limited.

In conclusion, it can be stated that the test laser has met all the requirements imposed as far as 1 Hz-operation, directional and transverse mode stability and conversion efficiency are concerned.

4.3 Design and Outlay of JIL

A 1 Hz iodine laser with an otuput energy in the 35 J range (1 ω) was designed on the basis of the results of the feasibility study described in the preceding sections and on the basis of our experience with pulsed high-power iodine lasers. The guiding lines here were: simplicity of layout, loading of components (per shot) lower than in systems designed for single-shot operation and low maintenance effort.

The active components of the 1 Hz laser are the oscillator and three amplifiers of increasing beam diameter and stored inversion energy (Fig. 4.5). The specifications of this laser are listed in Table 4.I.

The oscillator has to be acousto-optically mode-locked to ensure pulses with lengths of about 500 ps. These pulses will then be shortened to the required output pulse length of about 300 ps in the saturation region of the following amplifiers. Since the pulse length of an oscillator is inversely proportional to the square root of the gas pressure (band width of the laser transition), a shorter pulse length can be achieved when the buffer gas pressure in the oscillator is further enhanced /12,p.51/.

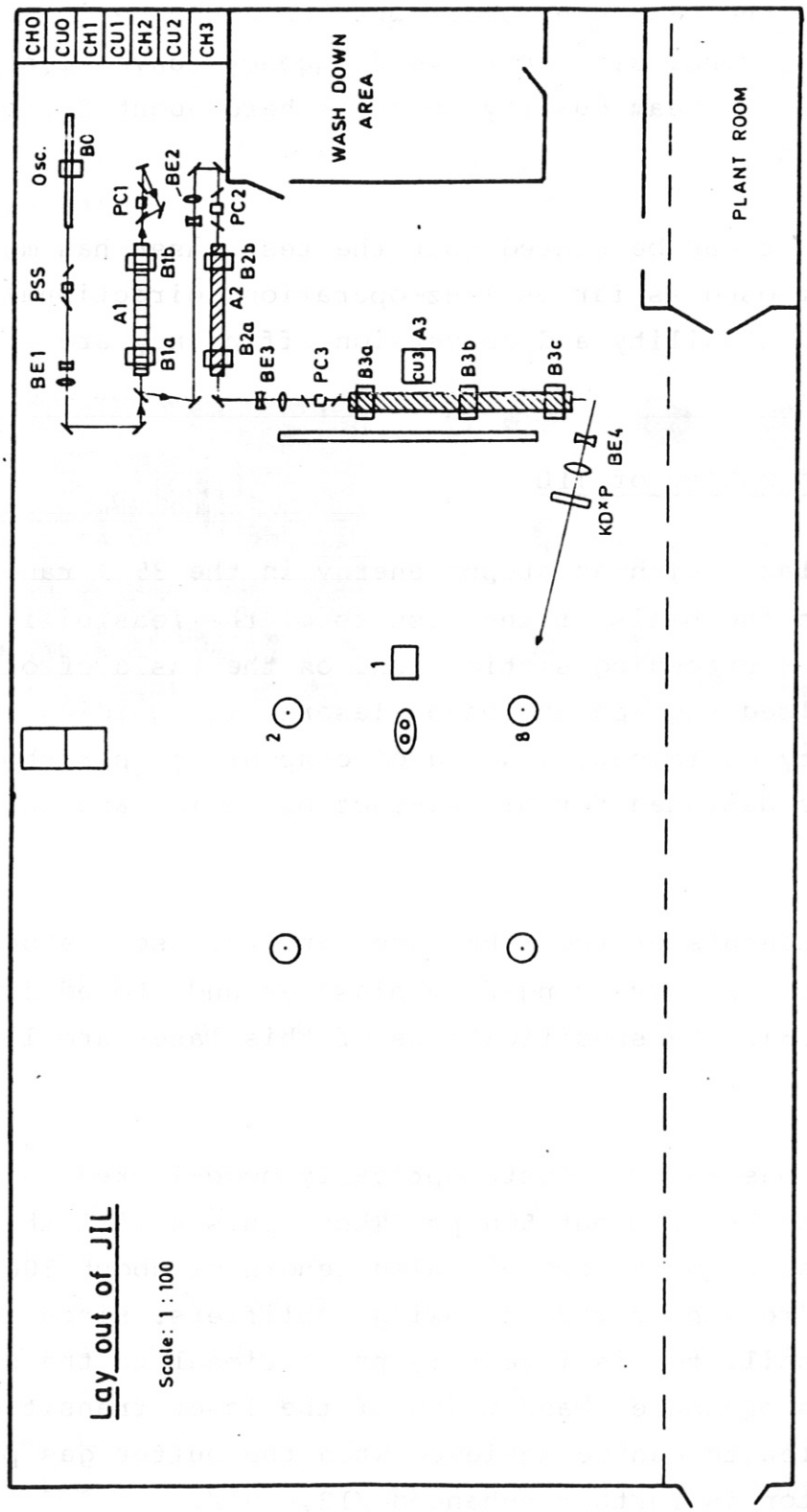

Fig.4.5: Design and lay out of JIL

Table 4.I

Layout data of JIL

Oscillator	1. Amplifier	2. Amplifier	3. Amplifier	
1,0	2,5	3,9	6,0	Inner diameter of the osc., amplif. (cm)
-	1,8	3,1	4,8	Active diameter of the amplifiers (cm)
140	80	51	33	Pressure of C_3F_7I (mbar)
3,5	5,15	2,85	2,2	Pressure of the buffer gas (Ar) (bar)
1,0	8,8	14,0	25,0	Capacitor bank energies/amplifier (kJ)
1	2	2	3	Number of sections; active length: 0.9 m
4	4	4	4	Number of flashlamps per section
0,25	1,1	1,75	2,1	Energy input per flashlamp (kJ)
1,2	44	70	124	Total stored inv. energy/amplifier (J)
-	17	33	60	Stored inv. energy at release of amplif. (J)
-	80	75	50	Total small signal amplif. at release of ampl.
0,85		0,7	0,7 / 0,9	Energy losses between amplifiers
-	5×10^{-4}	0,9	9,2	Input energies of amplifiers (J)
-	2×10^{-4}	0,12	0,50	Input energy density of amplif. (J/cm^2)
-	0,50	1,75	1,90	Output energy density of amplif. (J/cm^2)
6×10^{-4}	1,3	13,1	34,2	Output energies (J)

The amplifiers are of modular design. They consist of 2 or 3 sections. Each section has an active length of 0.9 m. It consists of a quartz tube for the laser medium and is surrounded by linear flashlamps and their reflectors. Each section has its own capacitor bank.

The first of the three amplifiers is operated in the double-pass mode. This kind of operation was chosen in order to provide a faster transition from the small-signal to the saturation region and hence more effective energy extraction from the amplifier chain. The incoming and outgoing beams are separated by a polarisation sensitive mirror. The polarisation plane is rotated 90° with the Pockels cell PZ1 (Fig. 4.5).

From the pulse train emitted by the oscillator a single pulse has to be extracted by a pulse selection system. Such a system more advanced and with better performance than that used in the test laser is already commercially available.

Optical beam expansion elements have to be installed between the amplifiers in order to prevent overloading and thus destruction of optical components at the exits of the amplifiers.

Pockels cells are used for optical isolation of the amplifiers and for decoupoling the first amplifier from the end-mirror.

The frequency doubling of the laser light will be provided by a KD*P crystal. Since the beam quality of the laser light is expected to be 2-3 times diffraction-limited, a conversion efficiency of about 50 % should be achieved. KD*P crystals have, however, a lower damage threshold than AR coatings of optical components. After leaving the last amplifier the beam is therefore firstly expanded to the desired diameter of 75 mm and then fed to the crystal.

The laser medium of the oscillator and the amplifiers will be circulated at a velocity ensuring a turbulent flow. For regeneration of the laser medium the same principle will be used as in conventional iodine lasers. The laser gas passes through a vessel where

stored liquid i-C_3F_7I is cooled to a temperature at which its vapour pressure corresponds to the required i-C_3F_7I pressure in the laser tube. The storage vessels for the laser medium should be of such a size that the laser medium has to be replaced after several thousand shots. The cooling temperature of the storage vessels ranges between -10 °C and -35 °C.

Feasibility studies with the most commonly used argon as buffer gas showed that flashlamp heating impairs the optical homogeneity of the laser medium. The laser tubes have therefore to be cooled. At MPQ a double-wall water-cooled amplifier has been developed which has proved to be very reliable in operation. In 1 Hz operation an optically homogeneous laser medium could be maintained with this cooling system. The pumping efficiency, however, dropped by 10 %. Later investigations performed with helium as buffer gas revealed that with this gas the optical homgeneity is much less affected by thermal influences than in the case of argon. It cannot yet be decided, however, whether the water cooling of the amplifier for 1 Hz operation will not be necessary if helium is used.

The oscillator and the amplifiers are pumped by flashlamps consisting of quartz tubes filled with xenon at a pressure of 40 mbar. For these flashlamps a new type of current duct will be used which not only reduces the inductance of the electric circuit but also appreciably prolonges the lifetime of the flashlamps. The details are described in the flashlamp report. Tests revealed that at the proposed loading the lifetime of the flashlamps will exceed 25,000 shots.

The 4 flashlamps of the oscillator and of one amplifier section are operated in parallel and powered by a capacitor bank. The specifications of these capacitor banks are listed in Table 4.II. The same type of capacitors shall be used for the capacitor banks of the amplifier sections. Only for the oscillator a different type with a lower inductance is proposed. To obtain short pumping times the inductance of the electric circuits should be as low as possible. The capacitor banks should therefore be positioned as close as

Table 4.II

JIL - Capacitor Bank

	Osc.	1. Ampl.	2. Ampl.	3. Ampl.
	Data of a single capacitor			
capacity of 1 capacitor	1,1 µF	5 µF	5 µF	5 µF
inductance	50 nH	75 nH	75 nH	75 nH
resistance	-	15 mΩ	15 mΩ	15 mΩ
stored energy at 40 kV	0,88 kJ	4 kJ	4 kJ	4 kJ
dimensions L x W x H (cm^3)	33x15x55 cm^3	36x22x49 cm^3	36x22x49 cm^3	36x22x49 cm^3
	Data of 1 capacitor bank			
number of cap. banks	1	2	2	3
number of cap./bank	1	1	2	2
stored energy at kV	1 kJ at 42,6 kV	4,4 kJ at 42 kV	7 kJ at 37,5 kV	8,3 kJ at 41 kV
capacity of a bank	1,1 µF	5 µF	10 µF	10 µF
	Inductance of 1 circuit			
capacitor bank	50 nH	75 nH	38 nH	38 nH
spark gap	70 nH	70 nH	70 nH	70 nH
flashlamp (number)	80 nH (4)	160 nH (4)	170 nH (4)	170 nH (4)
cable	60 nH	60 nH	60 nH	60 nH
strip line	15 nH	15 nH	20 nH	20 nH
Total inductance	275 nH	380 nH	358 nH	358 nH
$T = 2\pi\sqrt{LC}$	3,0 µs	8.6 µs	11,9 µs	11,9 µs

possible to the flashlamps to reduce the inductance of the supply line.

The oscillator and the amplifiers have to be equipped with a vacuumpumping system which allows the laser tubes to be evacuated to a pressure of 10^{-3} mbar. Measures have to be taken to prevent pumping oil vapour from penetrating into the laser tube and iodine into the pump. Otherwise chemical reactions will take place, leading in the laser tubes to formation of pump light absorbing layers, and in the pumps to decomposition of the pumping oil. Fluorinated oils have turned out to lead to significently less contamination problems then hydrated oils. All components which have contact with the $i\text{-}C_3F_7I$ of the laser medium have to be made of quartz, glass, special plastics or aluminium. Metals such as iron, stainless steel and copper show a chemical reaction with the laser medium.

All the components of the laser system are listed in Table 4.III. The specifications on the weights are estimated values which may have an accuracy of 20 %.

4.4 Maintenance Effort, Spare Components

From our experience with a conventional high-power iodine laser the maintenance effort for JIL in daily operation can be expected to be relatively modest. It is mainly concerned with control of the beam alignment. In long-term operation the laser medium has to be replenished after a certain number of shots and the molecular iodine has to be removed from the storage vessel for the laser medium. This procedure can be performed within 2-3 hours. This maintenance interval depends on the size of the storage vessel for the laser medium. It should have a capacity sufficient to allow at least 5000 shots.

The flashlamp should be replaced after about 25.000 shots. With the amplifier contruction used at MPQ, in which the flashlamps are fixed to detachable shells, the flashlamps can easily be replaced.

Table 4.III

Register of JIL-Components

Components	term, posit	weight (kg)	term posit	weight (kg)	term posit	weight (kg)	term posit	weight (kg)	Remarks
Laser tube housing, flashl., etc.	Osc	80	A1	60	A2	120	A3	220	
Capacitor banks	BO	30	B1a,b	60	B2a,b	200	B3a,b,c	320	Pos. close to osc., amplifiers
Trigger units	tor Osc.	10	for A1	30	for A2	30	for A3	30	
Charging units	CHO	20	CH1	100	CH2	200	CH3	250	
Laser medium regeneration syst.	for Osc.	10	for A1	10	for A2	20	for A3	20	Pos. close tc osc. amplifiers
Cooling Units	CUO	30	CU1	30	CU2	200	CU3	300	
Amplifier cooling systems	for Osc.	10	for A1	20	for A2	30	for A3	30	Pos. close to osc. amplifiers
Beam expans. systems	BE1	5	BE2	5	BE3	10	BE4	10	
Pulse selection syst. Pockels cells	PSS	40	PC1	30	PC2	30	PC3	30	
Vacuum systems	for Osc.	30	for A1	40	for A2	50	for A3	50	Pos. close to osc., amplifiers
KD*P crystall							KD*P	10	
Total		265		385		890		1250	2790 kg

Spare shells can be prepared in advance so that replacement of the flashlamps is not time-consuming. The spark gap of the capacitor banks should also be checked at the same time intervals.

Further maintenance service is necessary for the vaccum systems of the oscillator and the amplifiers. The pumps have to be checked at certain time intervals and care always has to be taken to ensure that no molecular iodine penetrates into the pumping system.

An important condition for reliable laser operation at the required energy level is the vacuum thightness of the laser medium circulation system. The leak rates should not be larger than 10^{-6} mbar ℓ/s. Otherwise too much oxygen, which is a strong quencher for the excited iodine atoms, diffuses into the circulation system in spite of the fact that the pressure of the laser medium is higher than the atmospheric pressure and thus impairs the laser performance. To ensure that all parts of the system are tight, it should be checked with a He leak detection system after assembling. It should always be ensured that no pump oil vapour penetrates into the circulation system. It will be decomposed by the pump light and a carbon layer then forms on the inner surface of the amplifier quartz tube. Such a layer can reduce the pumping efficiency by more than 50 %. The cooling fluid of the coolers for the laser medium storage vessels should be replaced at time intervals of about 1 year.

A stock of spare parts should be kept to avoid excessively long standstill times when system components fail. Besides parts such as flashlams which are subject to wear, other components which can become defective or which may be destroyed during operation should also be kept in stock. To keep this number small, these parts should be standardized as far as possible. The stock should comprise the following components: two types of flashlamps (for the oscillator and the amplifiers), span shells for the flashlamps, quartz tubes for the oscillator and the amplifiers, vacuum components such as 1 pumping set, pressure gauges, valves etc., 2 types of spark gaps and capacitors (for the oscillator and amplifiers), 2 types of trigger units (for the oscillator and the amplifiers), 1 time delay unit, 1 charging unit for the trigger units of the am-

plifiers, spare parts for the charging units of the capacitor bank, spare parts for the pulse selection system and for the driving units of the Pockels cells, 4 storage vessels for the laser medium (to replace those used and contaminated with molecular iodine), 1 circulation pump for the laser medium, 1 cooling unit for the laser medium storage vessel, optical components such as oscillator and amplifier windows, dielectric-coated mirrors, polarisers, Pockels cells, 1 KD*P crystal, beam splitter, lenses for the beam expansion system, spare components for the pulse length and pulse energy measuring system.

The whole JIL system can be operated and maintained by one well-trained technician.

To summarize:

With a small test laser consisting of a water-cooled mode-locked oscillator, a pulse selecting system, one air-cooled amplifier and a frequency doubling KD*P crystal the feasibility of a 1 Hz-operation extending over a sequence of 10 shots could be successfully demonstrated. At 2ω (657 nm) the pulse had an energy of 40 mJ and a duration of 950 ps whereby a conversion efficiency of 45 % was achieved. According to our present experience a system meeting the required specifications of 10 pulses with 1 Hz repetition rate and 15 J/0.3 ns per pulse at 657 nm can be confidentially built based upon the technology and design considerations employed in the small test laser.

A 2- to 3- Hz operation seems feasible if the flow velocity of the laser medium is correspondingly increased and all amplifier quartz tubes are water-cooled. Eventually the flashlamps have also to be gas-cooled.

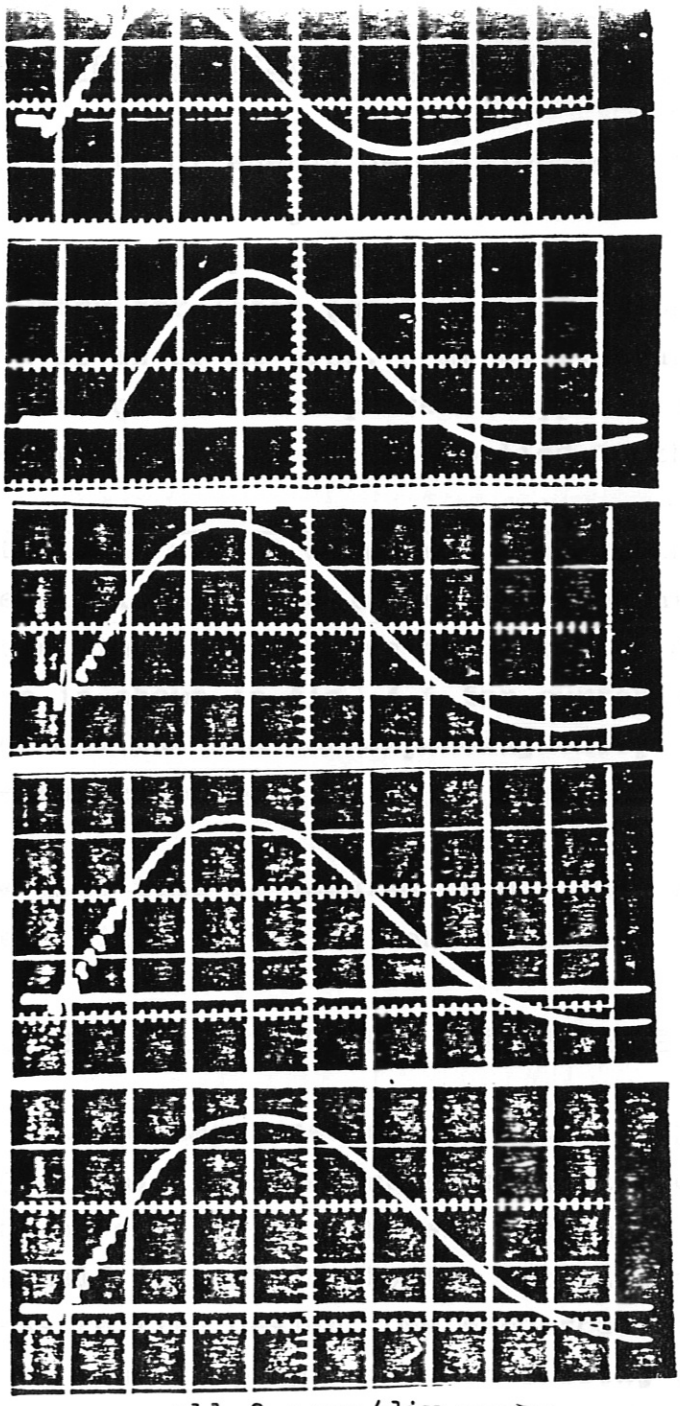

40 kV 4 kJ T/4 = 4,5 µsec
I_1 max = 46 KA

40 kV 6 kJ T/4 = 5,6 µsec
I_1 max = 59 KA

40 kV 8 kJ T/4 = 6,3 µsec
I_1 max = 68 KA

40 kV 10 kJ T/4 = 7 µsec
I_1 max = 72 KA

40 kV 12 kJ T/4 = 7,9 µsec
I_1 max = 77 KA

all 2 µsec/div →

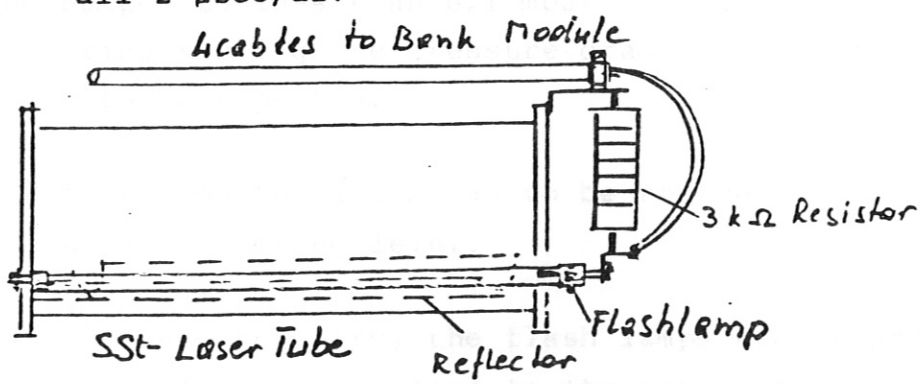

Fig. 4.6 : Current Wave Shape in Flashlamp Life Tests
(Lamp inner diameter 18 mm, length 1 m)

4.5 LIFETIME TEST OF FLASHLAMPS

The limits of energy deposition in a flash lamp on a single pulse capacitor discharge have been investigated in an earlier work /14/. This work was performed with sealed type flash lamps as designed by industry for laser pumping applications. It was found that destruction of an 18 mm I.D., 3 mm wall, quartz tube flash lamp occurred, if a single current pulse of typical 10 µsec length and having an energy of 10 - 12 kJ is supplied to the lamp.

Life tests with 8 kJ pulses showed, that the "sealed type" lamp is clearly inferior to lamps with demountable electrodes as described later. The current wave shape of the discharge current pulse in the lamp is shown in fig. 4.6 for currents from 46 to 77 kA first current maximum and corresponding energies from 4 - 12 kJ stored in the capacitor bank at 40 kV charging voltage.

The Life time of "sealed type" lamps at 8 kJ is only 118 pulses (mean life, 3 samples) and therefore quite unacceptable.-

A) Flash Lamp Design and System Geometry

The flash lamps used now in all high-power iodine laser systems at MPQ are all of a demountable electrode design. In a linear quartz tube of e.g. 18 mm I.D. and typically 1 m length, the electrodes are held in position by two O-rings in combination with a conical pressure ring design. One electrode with a bore allows connection to the vacuum pump and xenon filling system. The flash tubes under test were pumped to less than 0.1 mbar and filled with xenon to 40 mbar. If during testing the pressure gradually rises, pumping and filling has to be repeated.

In normal operation the xenon has to be renewed after 80 - 100 shots at the 2 kJ pumping level.

In the usual laser geometry, the flash lamps are arranged within a stainless steel laser tube close to the tube wall as indicated in Fig. 4.7 A lamp reflector, made of aluminum sheet, is situated between flash tube and laser tube wall.

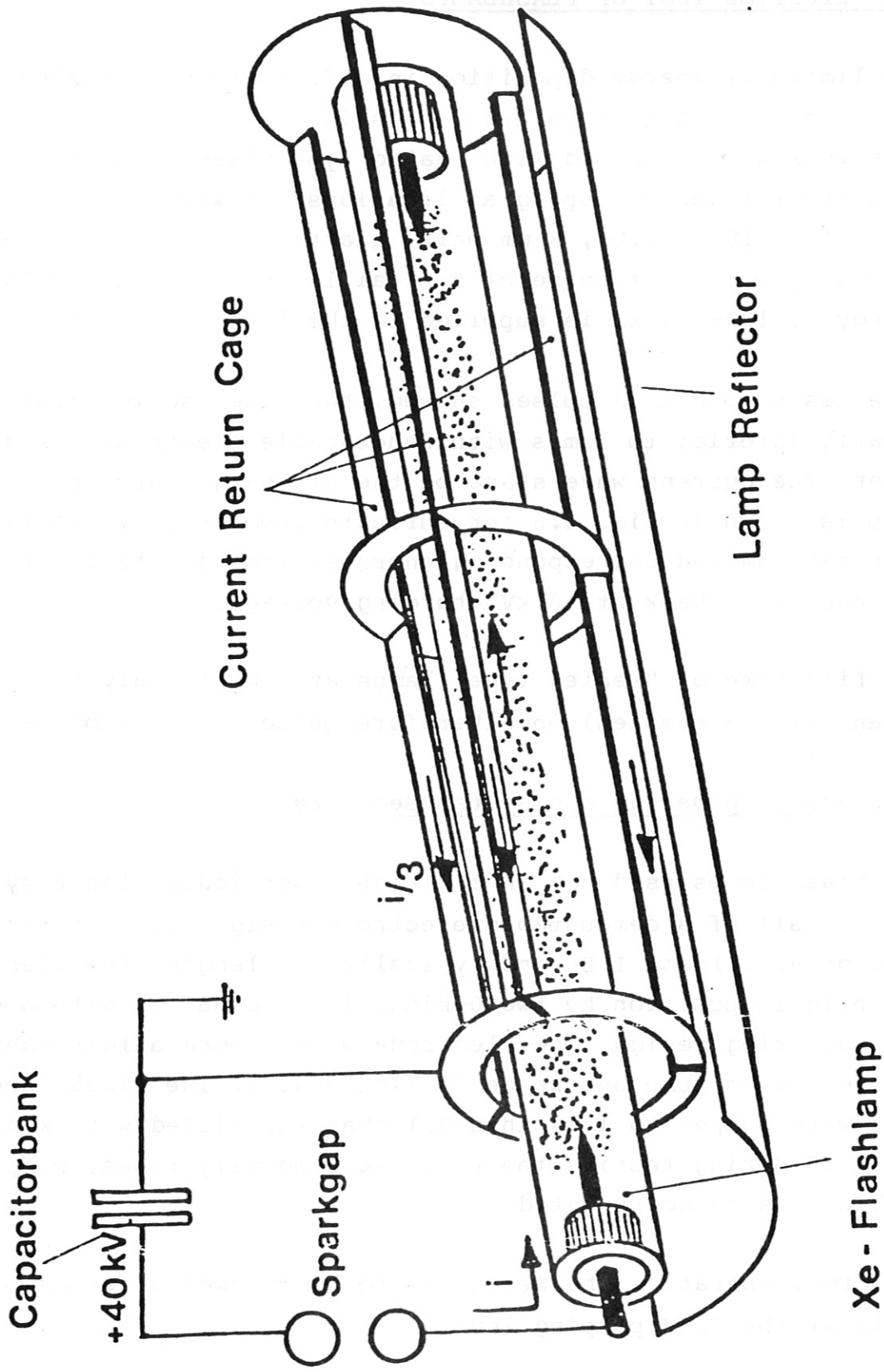

Fig. 4.7 : Flashlamp Current Return Cage

In this geometry, called "normal, with reflector", a magnetic pressure due to the return current within the reflector and SS-laser tube wall is driving the xenon plasma towards the opposite quartz wall causing there extensive wall erosion.

In earlier tests it was demonstrated, that an increased tube life with much less wall erosion is achieved, if the return current is led through a coaxial copper tube, enclosing the flash tube completely. After more than 2000 shots a 8 kJ, the quartz wall was still clear, with only a few tiny cracks inside the wall structure. However, the completely closed "coaxial return" conductor is not applicable for laser pumping, as it screens perfectly the laser pumping light.

A new design with a three-conductor return cage has been designed and tested in collaboration with MPQ. This configuration, as shown in Fig. 4.7, called "cage geometry", has been adopted for the new laser amplifier system of ASTERIX at MPQ and it also is planned for the proposed LIDAR diagnostic laser system.

B) Life Test with Flash Tubes for LIDAR

The main goal of the life tests is to establish a safe energy level for the 18 mm I.D. flash lamps for the LIDAR laser. As listed in Table 4.IV, the life of 18 mm tubes was found for a 40 kV bank charging with varying capacitor number, to store either 4 or 8 kJ and discharge to the lamp under test. The maximum pulse sequence obtained with the equipment available, is 10 pulse/min with a wave shape as shown in Fig. 4.6. This is well enough representative for the diagnostic laser operation at 1 Hz - with a pulse train of 10 pulses per each experimental run - as thermal problems are not envisaged.

3 lamps were subjected each to 8 kJ per pulse and this gave a mean life of 1237 pulses (sample JET 1 and JET 3). The third sample was broken during routine inspection and therefore its pulse number was been neglected. At the 4 kJ level one lamp withstood 4931 pulses.

Table 4.IV: Life-test Results
Flash-Lamps for LIDAR-Laser

General: Lamp Diameter — 18 mm ϕ_i
Lamp Length — typ. 1 m
Quartz Tube — Heralux WG
wall thickness ~ 3 mm

Sample type	Pulse data U KV	E KJ	I max KA	total pluses to destruction
JET 1	40	8	65	1360 small line-cracks
JET 2	40	8	65	680 breaking by mounting
JET 3	40	8	65	1115 small cracks all over inner surface
JET 4	40	4	48	4931 small cracks, loss of vacuum
JET 5	40	4	41*	2151 test stopped due to Laboratory rebuilding
JET 6	40	2		20000 tests stopped without indication for near-future failure
JET 7	40	2		20000 tests stopped without indication for near-future failure

* stainless steel return cage gives lower current.

From experience with flash lamps pumped in the msec-range, life scales with energy according to an $1/E^n$-law. From the small sample test, so far conducted in the µsec-range, $n \approx 2$ has been found, which is in disagreement with the predicted n-values in the order of 8.

In the LIDAR laser system flash lamps will be subjected to pulses of about 2 kJ. This means, according to the $1/E^2$ law, a lamp life of about 2.10^4 pulses or 2000 experimental runs can be expected.

Two flashlamps of the new design have been tested at the envisaged level of 2 kJ. Both flashlamps withstood 20000 discharges without breaking.

The subsequent optical inspection showed that the quartz tubes remained clear at this energy level and shot number. There was no indication that the flashlamps would tend to break soon after completion of the 20000 shot cycle.

Both lamps were evacuated and filled with 25 Torr of Xe only once, at the start of the test. After 20000 discharges the filling pressure had risen only by a few Torr.

5 DETECTION SYSTEM

5.1 Detector Tests

An ITT F 4128 microchannelplate photomultiplier has been chosen as detector since this photomultiplier offers the best compromise between speed and gain. Its data are summarized in the attached data sheet (see Appendix). The general properties of MCP detector devices are given in the attached Technical Note by ITT (see Appendix).

In order to investigate experimentally the properties of the detector, one sample has been bought. The photomultiplier was ordered with

- MA-1 photocathode which equals in spectral sensitivity approximately the S-20 type being used for the S/N estimates,
- a 10 mm diameter sensitive area which is large enough for the proposed diagnostic method,
- no ion barrier film on the MCP. Thus the expected lifetime of the detector corresponds to an accumulated charge output of about 20 mC (instead of about 2 C with film). This output will add up over about 3×10^6 laser shots, quite a large number for the intended application.

The attached performance test report by ITT (see Appendix) describes the spectral and the gain properties of the detector.

We have tested the speed of the detector, its gating and its saturation recovery properties.

5.1.1 Response Time

For measuring the response time of the detector, a subnanosecond Na:Fluorescein dye laser pumped by a nitrogen TEA laser was set up. The signals were recorded with a TEKTRONIX 661 sampling oscilloscope with a 4 S 2 plug-in (10 % - 90 % rise time of 90 ps). For reference the laser pulses from the dye laser were monitored using a VALVO TVHR 06 vacuum photodiode with 70 ps rise time. The combined risetime of photodiode and sampling oscilloscope is about

115 ps. Signal averaging was performed with the sampling oscilloscope in case of the photomultiplier signals.

Fig. 5.1 shows the diode signal and Fig. 5.2 that of the photomultiplier. The photomultiplier was operated with the following voltages: PC-MCP: 150 V, MCP: 1760 V, MCP-Anode: 300 V. The pulse heights correspond to pulse heights expected for the LIDAR scattering signals.

From the 10 % - 90 % risetime of the signal in Fig. 5.1 the risetime of the laser pulse is inferred to be

$$\tau_R^{LASER} = \sqrt{(\tau_R^{SIGNAL})^2 - (\tau_R^{DIODE})^2 - (\tau_R^{OSCI})^2} \approx 130\,ps$$

Inserting this value into the corresponding relation for the photomultiplier signal, one gets a risetime of the F 4128 of about 180 ps. This value compares well with the number of 125 ps given by ITT (Technical Note No. 127, 9.4, see Appendix), taking into account that it was taken from a measurement with finite laser pulse duration (using a relation for the combined risetime which holds for linear electronic systems).

The FWHM of the photomultiplier signal is about 400 ps. Thus, even without any correction for the finite laser pulse duration, it can be concluded that the response time of the detector is shorter than that of the available 1 GHz oscilloscope system. The F 4128 therefore satisfies the requirements of the LIDAR system with respect to frequency response.

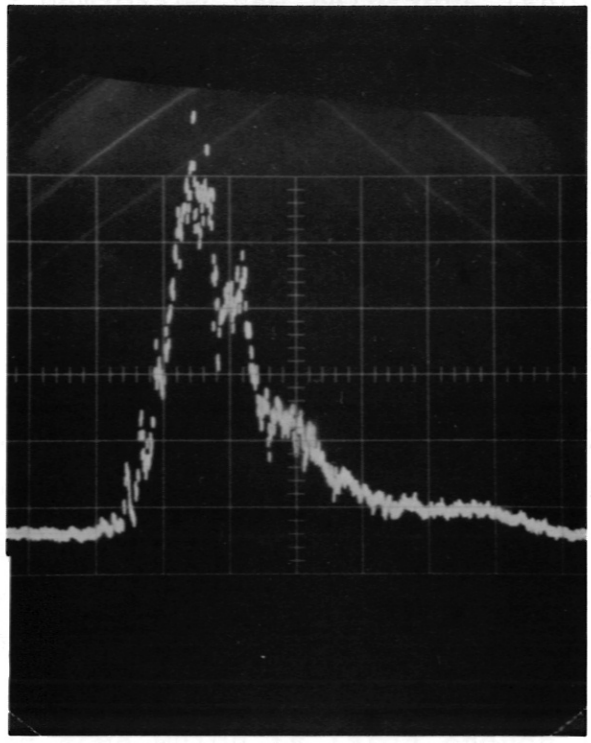

Fig. 5.1: 200 ps/div. VALVO TVHR 06 100 mV/div.

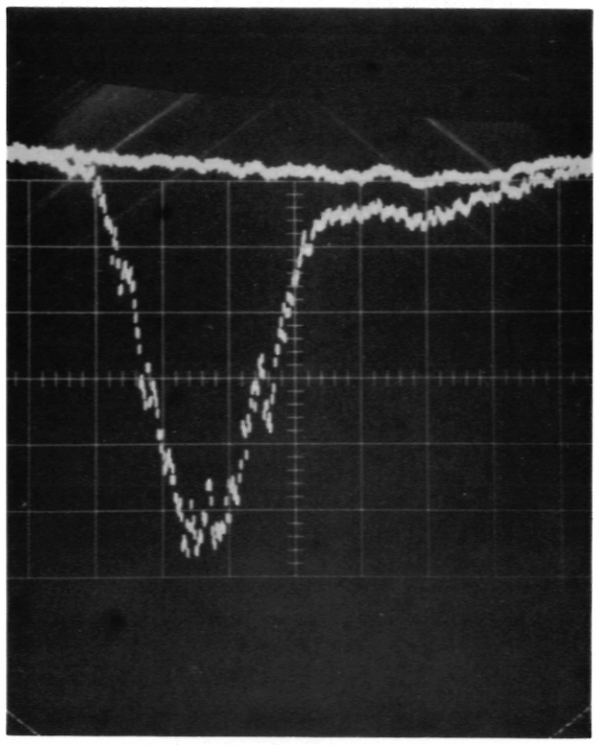

Fig. 5.2: 200 ps / div. ITT F 4128 100 mV/div.

5.1.2 Saturation Recovery

Considering the possibility of a spatial scan and the question whether a laser beam dump is really required, we have investigated the behaviour of the detector when it is irradiated by an intense light pulse directly after the measurement. For these measurements the detector was irradiated with two dye laser pulses 18 ns apart at the repetition rate of 30 Hz. The signals were registered with a 500 MHz TEK 7904/7A19 plug-in oscilloscope.

First, both laser pulses were attenuated individually to about equal amplitude. Fig. 5.3 shows an overlay of 120 oscilloscope traces at these conditions.
Then the attenuation of the second laser pulse was reduced by a factor of 10^3. Thus the second laser pulse completely saturated the photomultiplier.
The result is shown in Fig. 5.4 a+b (again an overlay of 120 traces). As can be seen from the oscillograms, the first signal remains unchanged. This demonstrates

a) that the photomultiplier is not destroyed by heavy overloading even without gating, and
b) that the detector will registrate a weak signal (pulse 1 contains about 1000 photoelectrons) 30 ms after such a maltreatment with its normal sensitivity.

These effects are explained by the fact that the device operates from the charge stored capacitively in the highly resistive MCP. An intense light pulse will deplete this charge, thus reducing the gain - which in turn protects the photomultiplier against destruction.

5.1.3 Gating

For testing the gating properties of the F4128 a cable discharge pulser with a transistor switch was built capable of delivering pulses of up to -180 V. The switch is triggered optoelectronically with very low time jitter from a Si PIN diode (risetime 0.5 ns). The internal delay of the switch is 24 ns. The gating pulses are coupled via capacitors to the photocathode / MCP input. They can

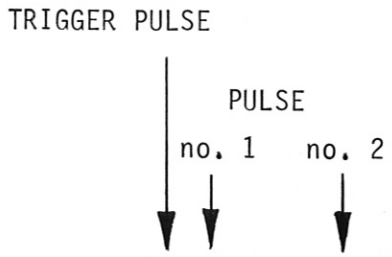

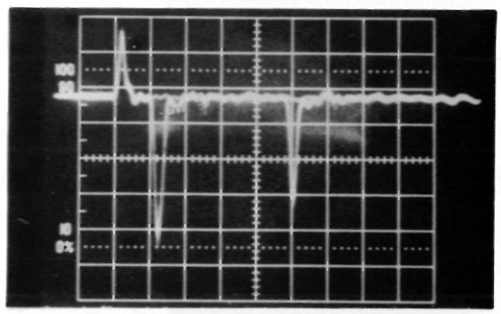

Fig. 5.3 : 5 ns/Div.
200 mV/Div.

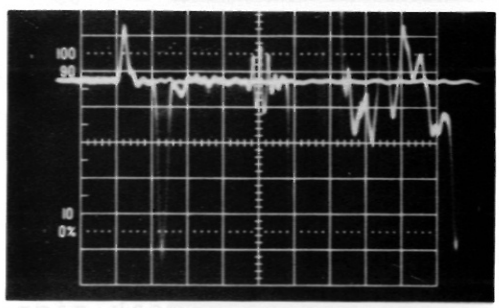

Fig. 5.4a : 5 ns/Div.
200 mV/Div.

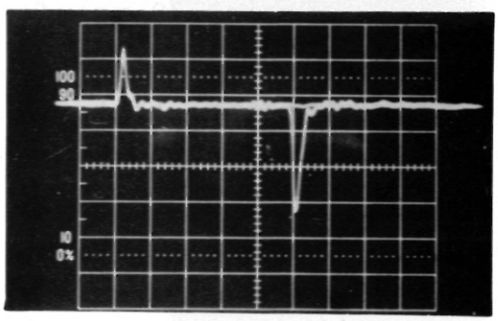

Fig. 5.4b : 5 ns/Div.
10 V /Div.

Saturation Recovery

be delayed with respect to the optical pulses by changing the length of the transmitting cable.
In the "off"-mode of the detector the photocathode potential with respect to the MCP input can be kept at different positive levels or at zero.
The gating properties of the detector were tested with a set-up shown schematically in Fig. 5.5.
The light pulse 2 irradiating the detector was delayed by 18 ns against pulse 1. This corresponds to the time interval between the stray light pulse from the window at the torus vessel and the onset of the scattering signal from the plasma boundary. Approximately the same time interval occurs between the end of the measurement and the arrival of the stray light from the exit window.

The attenuation of the laser pulses was done by reflecting filters and absorbing neutral density filters. In the latter case bleaching effects can be excluded since the attenuation factors were measured both at the dye laser power level and at a much lower cw intensity; no changes were observed.
In case of the attenuator A3 the optical filters were placed behind a scatter plate ensuring homogeneous illumination of the photocathode.

I. Static closure ratio

At a +10 V photocathode potential (with respect to the adjacent MCP input plane) the attenuation of A3 was reduced by a factor of 10^6 and the sensitivity of the oscilloscope was increased by a factor of 10. No signals could be observed. This result agrees with measurements at ITT (see Appendix), which yielded a closure factor of 2×10^8.

II Dynamic case

First, it was tested whether the gating pulse was applied to the photocathode at the correct time, that means at a time when light pulse no. 1 arrives still in the "off"-mode of the detector and pulse no. 2 arrives in the "on"-mode.

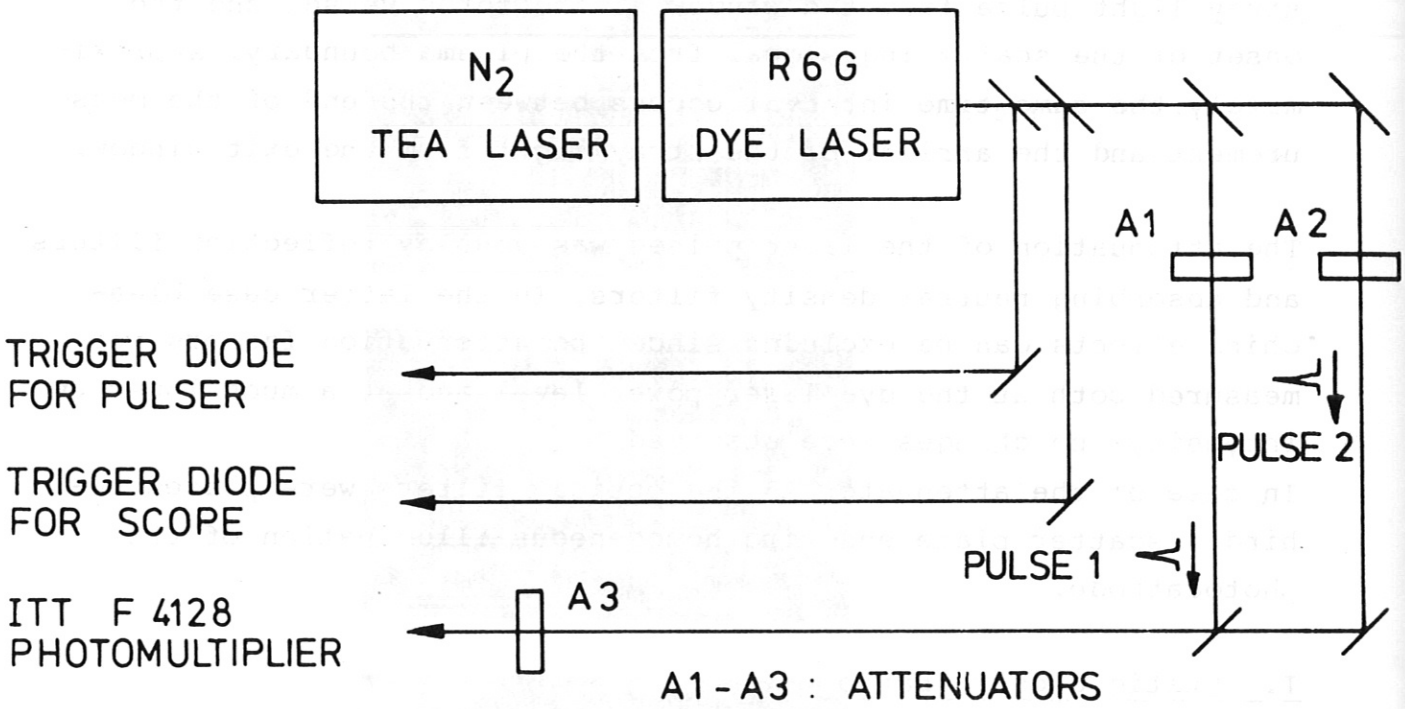

Fig. 5.5 : Optical Set-Up , Schematic

For this purpose the length of the cable connecting the pulser with the detector was varied. The series of oscillograms in Fig. 5.6 shows

a) once more the time history of the light pulses for reference (output signal of the F 4128; the height of pulse no. 2 corresponds to 500 photoelectrons).
b) the gating pulse signal as observed when feeding the pulser output (after 1:100 attenuation) directly to the oscilloscope, and
c) the signal of the F 4128 when it is gated with this pulse without any additional delay lines. The optical filters in front of the detector (A3) are the same for a) and c).

Each oscillogram is an overlay of 120 traces.

From this series of oscillograms one can see that

I. The amplitude of the ringing induced in the MCP photomultiplier output at this time is still of the same amplitude as the signals to be expected for the LIDAR experiment. However, the ringing is very reproducible and can easily be subtracted.
II. The time jitter of the optically triggered pulser is negligible.
III. The shape of the ringing signal indicates that the gating pulse is distorted and delayed when being applied to the photomultiplier supply circuit. This distortion however does not lead to a noticeable change of the photomultiplier gain. This is explained by the rather weak dependence of the multiplier gain on the photocathode/MCP input voltage.
IV. Pulse no. 1 is already suppressed by a factor of >20, that means that gating already is observed.

In order to optimize the timing of the gating, optical filters were removed from the attenuator A1 (Fig. 5.5), thus increasing the optical pulse power at the detector by a factor of 10^4.

Fig. 5.7 shows a series of oscillograms where the delay of the gate pulse is increased with increments of 2.5 ns. The stationary potential of the photocathode with respect to the MCP input was chosen as + 10 V ("off"-mode).

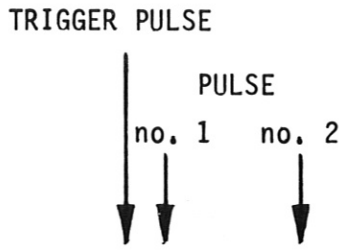

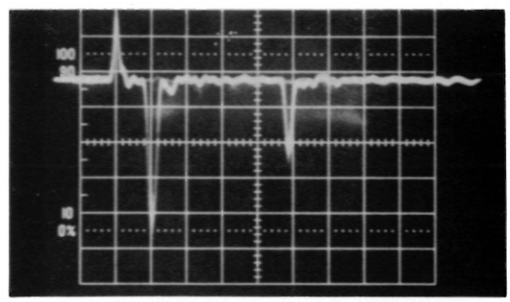

DETECTOR "ON"

Fig. 5.6a : 5ns/Div.
200 mV/Div.

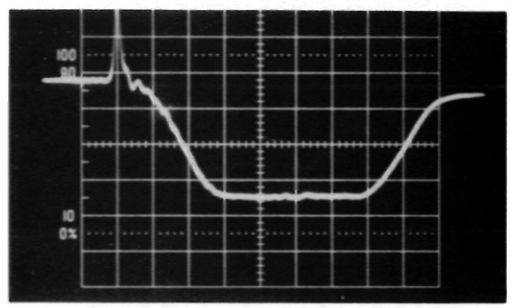

GAITING PULSE

Fig. 5.6b : 5ns/Div.
500 mV/Div.
20 dB Atten.

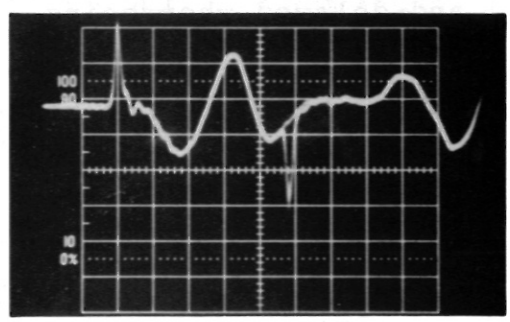

DETECTOR GATED

Fig. 5.6c : 5ns/Div.
200 mV/Div.

Gating Properties

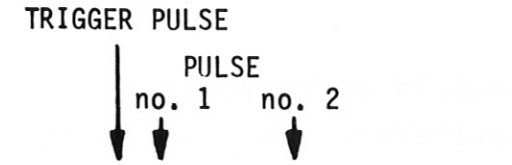

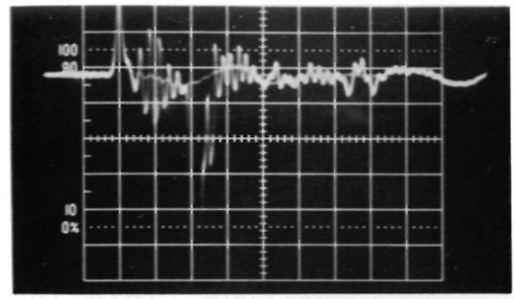

Fig. 5.7a: Δt = 0.0 ns

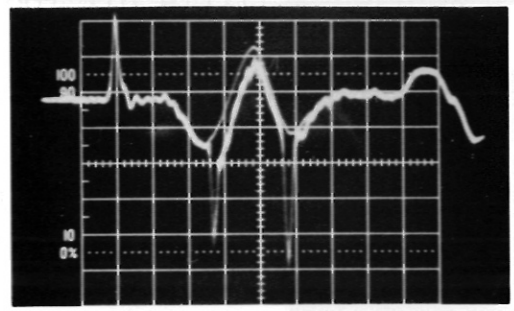

Fig. 5.7b: Δt = 2.5 ns

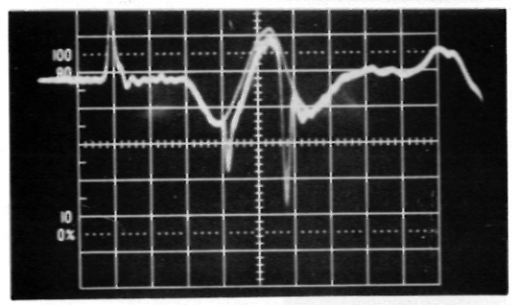

Fig. 5.7c: Δt = 5.0 ns

5 ns/Div.
200 mV/Div.

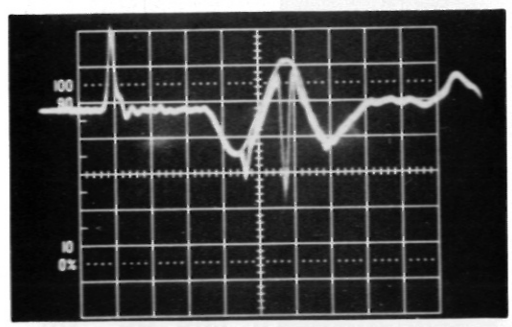

Fig. 5.7d: Δt = 7.5 ns

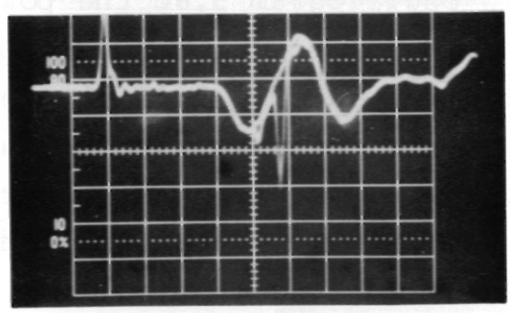

Fig. 5.7e: Δt = 10.0 ns

Delayed Gating

The oscillogram 5.7a corresponds to the case of oscillogram 5.6c with the only difference that the power of light pulse no. 1 is increased by 10^4. As can be seen, the detector is driven into saturation. It has not recovered its gain when pulse no. 2 arrives 18 ns. later.

When the gating pulse is delayed by 2.5 ns in addition (oscillogram 5.7b the overloading of the detector disappears and pulse no. 2 is observed with normal amplitude. This indicates that the gating pulse in a) was applied a little bit too early.

However, for all the different delay times one observes a signal pulse with an extended tail which occurs at a fixed amplitude of the leading edge of the gate pulse. The charge contained within this signal decreases with increasing delay time.

The amplitude of pulse no. 2 always remains unchanged by the preceding signal. This is understood by considering that the preceding signal depletes the available output charge from the MCP by only less than 3 %.

At the optimized delay (2.5 ns) a second series of oscillograms shown in Fig. 5.8 demonstrates the influence of the stationary cathode potential (in this series chosen as +40 V). In this series optical filters were taken from attenuator A3 and added to attenuator A2. Thus the intensity of the optical pulse no. 2 remained unchanged, whereas the power of the preceding pulse no. 1 is increased.

For reference the oscillogram 5.8a once more shows the case where the detector is operated in the dc "on"-mode (cathode potential - 150 V dc). In oscillogram 5.8c the power of pulse no. 1 is increased by 10^4 and in oscillogram 5.8d by 7×10^4, respectively. For reference, the pulse no. 1 is blocked off in the oscillograms 5.8b and 5.8e. Again the preceding signal due to pulse no. 1 can be observed. It depletes the available charge by 3 % in 5.8c and by 15 % in 5.8d. Even in the latter case the amplitude of pulse no.2 remains unchanged, but the subtraction of the base line would in-

Gating Properties, Delay Fixed (2.5 ns)
Varying Intensity of Pulse no. 1

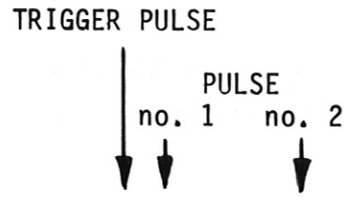

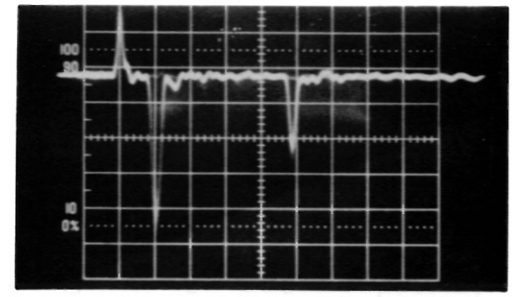

Fig. 5.8a: 5 ns / div.: 200 mV / div.
DETECTOR "ON"

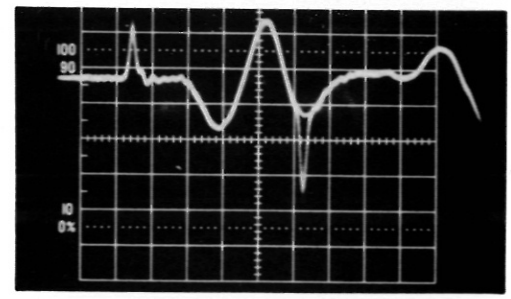

Fig. 5.8b: 5 ns / div.: 200 mV / div.
DETECTOR GATED without pulse no. 1

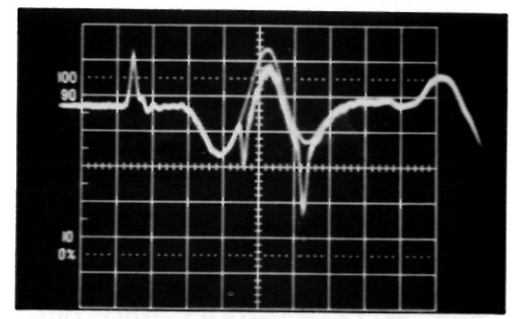

Fig. 5.8c: 5 ns / div.: 200 mV / div.
DETECTOR GATED with pulse no. 1

Attenuation Factors: $\frac{A_1}{A_2} = 10^4$

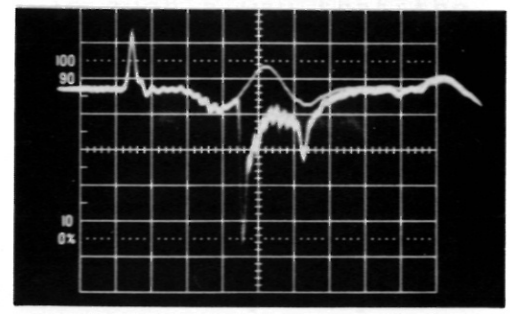

Fig. 5.8d: 5 ns / div.: 500 mv / div.
DETECTOR GATED with pulse no. 1

Attenuation Factors: $\frac{A_1}{A_2} = 7 \times 10^4$

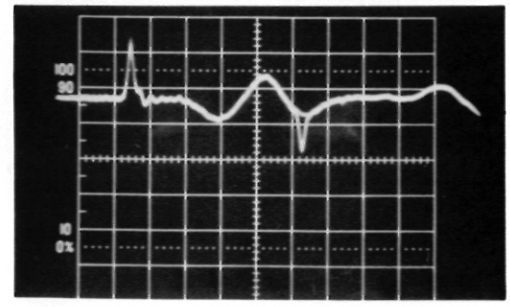

Fig. 5.8e: 5 ns / div.: 500 mV / div.
DETECTOR GATED without pulse no. 1

crease the errors in the LIDAR experiment.
Experiments with cathode potentials of up to +75 V showed no significant changes in the gating behaviour.

To summarize:

The experiments which could be done in the short time since the delivery of the MCP photomultiplier have not yet clarified completely the gating behaviour of the detector. Strong light pulses before the gating evidently create a space charge in front of the photocathode which is not removed completely by counter potentials of up to 75 V on a time scale of 10 - 20 ns. When the gate pulse is applied, the remaining charge is swept to the MCP and amplified. The resulting signal however does not deteriorate the measuring signal as long as its total charge output is small compared with the possible charge output of the MCP device. We have not yet found the optimum gating parameters, but we have operated the photomultiplier under conditions (at full gain!) which allow an optical prepulse of stray light containing up to 10^9 photons.

5.2 Stray Light Measurements

Using a full-scale set-up of the optics shown in Fig. 3.23 (optics version no. I), measurements of the stray ight level were performed. For this purpose 1 ns frequency-doubled iodine laser pulses from a mode-locked oscillator with a subsequent single pulse selection system were used. The energy content of the laser pulses was 50 µJ and the laser was operated at 1 Hz repetition rate. The backscattered light was registered with a calibrated HAMAMATSU R 928 photomultiplier (response time 3 ns FWHM, gain 4 x 10^5 at 600 V, quantum efficiency 8 % at 657 mm). As mirrors for bending the collected light beam, Al-coated front surface mirrors were taken. The only difference with respect to the optical system no. I consisted in using a mirror instead of a prism for coupling in the laser beam. Four RG 610 colored glass filters, each 3 mm thick were used in front of the detector to suppress spurious short-wavelength light from the laser flashlamps. A KG 3 filter served to discriminate against the fundamental radiation of the iodine laser.

Fig. 5.9 shows the result obtained when neutral density filters with an attenuation factor of 50 were introduced to ensure unsaturated operation of the photomultiplier. Besides a trigger pulse from a vacuum photodiode, three pulses can be seen on the trace. The first, weak one, stems from the lens system L1/L2 and the mirrors coupling in the laser beam. The second one results from the quartz glass window W which was adjusted in such a way that the specularly reflected part of the laser beam passed outside the lens system L1/L2. The third, saturated pulse originated from the wall of the lab hit by the laser pulse.

In Fig. 5.10 the window W was tilted in a manner that the specular reflection of the laser beam hit the lens L2. Consequently the signal (charge output) is stronger (by a factor of about 30) than in the first case.

Taking into account the attenuation of the filters (approx. 200) as well as the quantum efficiency and the gain of the detector, a number of 6.7 x 10^4 stray light photons are inferred. Thus, for a

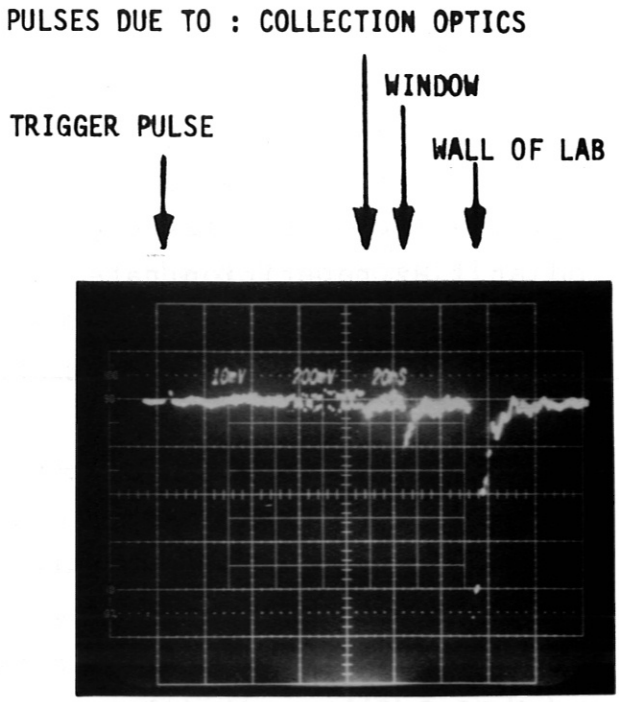

Specular Reflection outside Lens **L2**

Fig. 5.9 : 20 ns/Div.
10 mV/Div.
Optical Atten.: 200 x

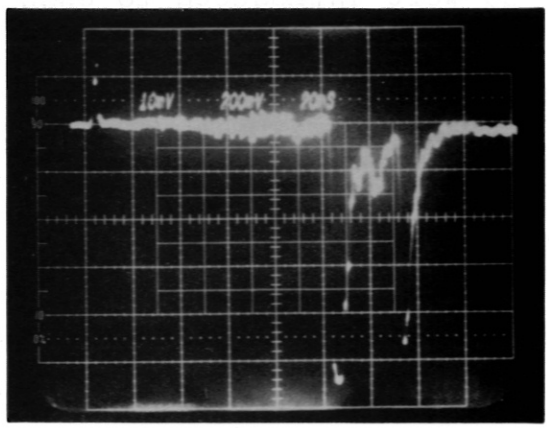

Specular Reflection inside Lens L2

Fig. 5.10 : 20 ns/Div.
10 mV/Div.
Optical Atten.: 200 x

15 J laser pulse, we expect about 2 x 10^{10} stray light photon when an optical system like version I is used.

This number is much smaller than expected by us at the beginning of this study. It demonstrates that an extremely high degree of stray light supression can be achieved with geometrical optics for an optical system with such long optical path lengths.

The low stray light level in combination with the good gating properties of the F 4128 photomultiplier will allow to use Rayleigh scattering for calibration (see section 3.3.4).

5.3 Optical Components

At an early stage of the investigations, when both the stray light level and the gating properties of the photomultiplier had not yet been examined, much effort was put on the spectral discrimination against stray light.

Spectrally unshifted laser stray light can be suppressed by the interference filters of the polychromator and in addition by the use of mirrors with "cold mirror" characteristics. Such mirrors can be put into the shielding block to deviate the collected light beam twice by 90 degrees (see Section 3.3.1).

a) Interference Filters

The possible degree of suppression of the laser radiation is determined by the ratio of the transmission bandwidth (FWHM) of the filter and the difference of the laser wavelength λ_L and the peak transmission wavelength λ_o of the filter. For the envisaged distribution of the spectral channels (see Section 3.1) this ratio is 1.96 for channel I, 1.73 for channel II and 2.28 for channel III, respectively. Thus, channel II is the most critical one with respect to stray light suppression.

In case of 4-cavity interference filters, producers (e.g. ORIEL) quote a typical suppression of 10^4 at a parameter FWHM/($\lambda_L - \lambda_o$) = 1.75 - 2.12 in the visible and near IR spectral region. Better values can be achieved with filters with more cavities. As an

example, at the 100 Hz Nd: YAG scattering system on ASDEX, filters produced by BARR Ass. are presently being used, which show a suppression ratio of up to 10^7 (see Fig. 5.11) at a parameter FWHM/($\lambda_L - \lambda_o$) = 1.9. Thus, a suppression of 10^4 can be taken as a conservative number for this design study.

b) "Cold Mirrors"

The 90° deflecting mirrors located in the shielding block reflect the polarized collected light one in the s-mode and one in the p-mode (see Fig. 3.23). In case of dielectric dichroic coatings, the edge of the reflection band is different for s- and p-polarisation. Thus, two mirrors with different coatings must be used in order to minimize the spectral separation between the edge of the resulting transmission band and the laser wavelength.

In a first approach, a set of two mirrors, coated in one charge but positioned at different distances from the source, were investigated. The broad bandwidth of the reflection band down to 400 nm was achieved using two series of cavities of different dielectrics.

The results given in Figs 5.12-5.14 show that this simple method did not give sufficiently good results. The laser radiation is suppressed by a factor of 30, but the edge of the transmission band (80 % absolute transmission) is shifted too far versus the short-wavelength region (λ_{edge} = 580 nm). This is due to the fact that the dip in the slope of the "s"-mirror is too much blue-shifted. An optimisation of the dip position would again yield a suppression of the laser radiation by about 30, wheres the transmission bandwidth would cover the whole needed spectral range 390 nm to 620 nm.

In case that the stray light suppression is not needed, these mirrors are an alternate choice to broadband metal-coated mirrors (see Appendix). This is due to their high reflection coefficient, especially of the "p"-mirror.

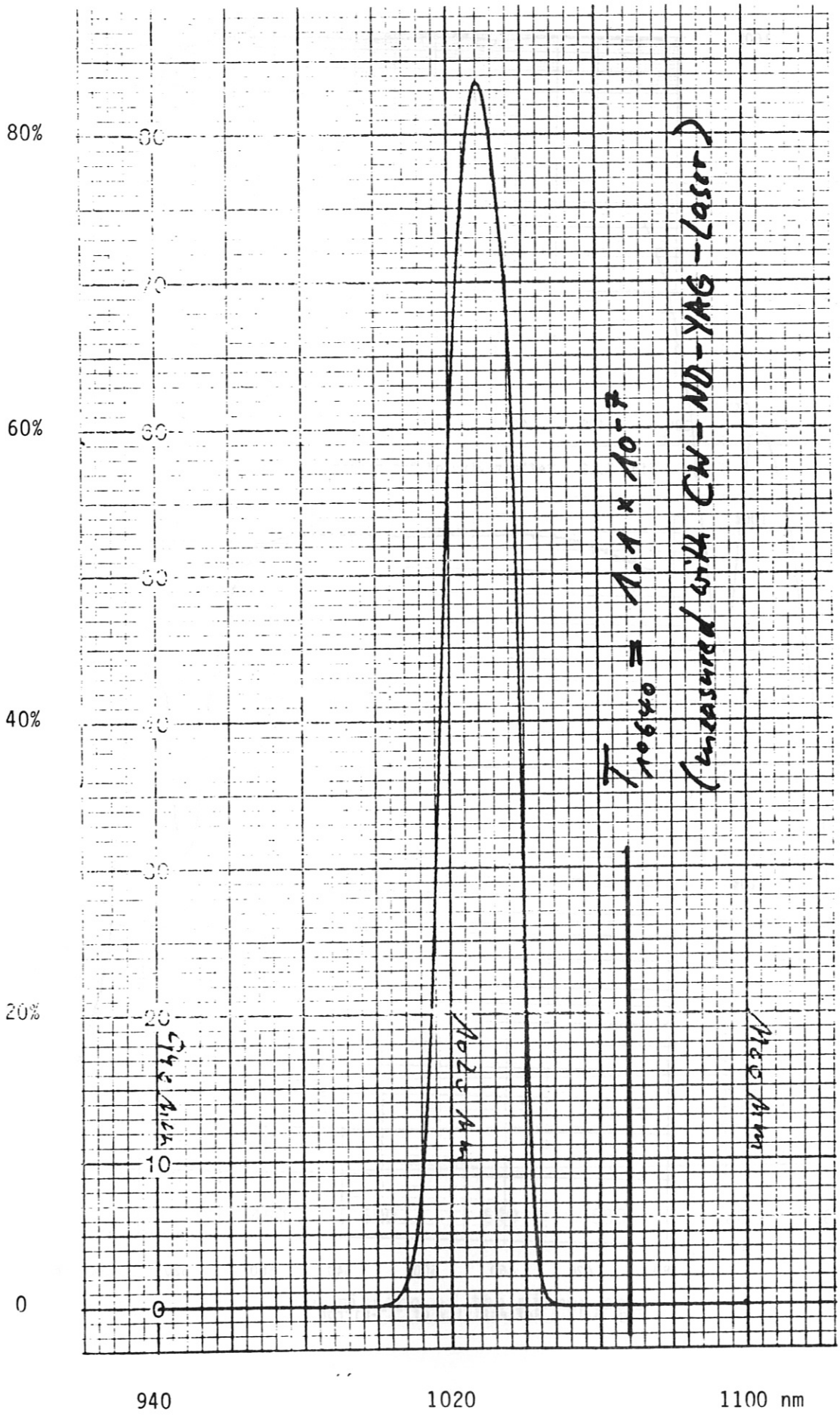

Fig. 5.11 : Spectral Transmission of Interference Filter

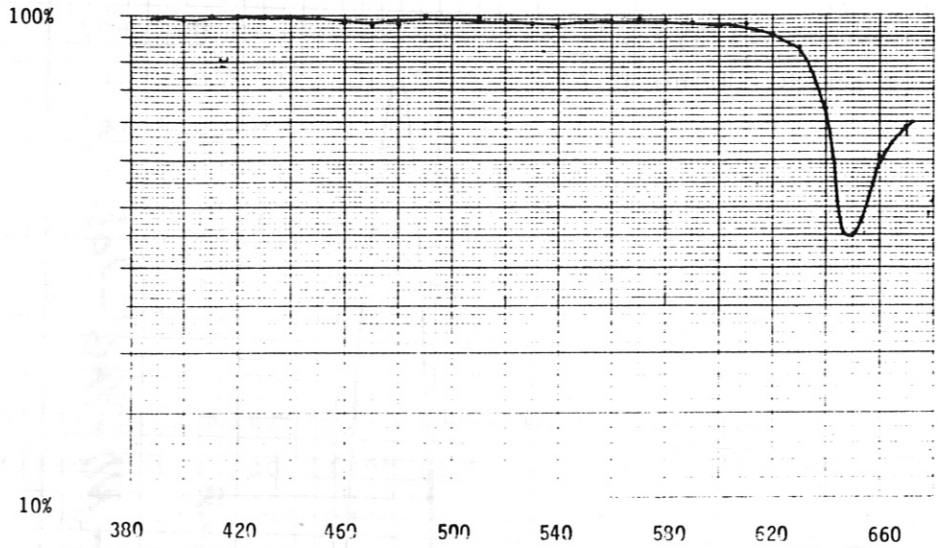

Fig. 5.12 : Reflectivity of "p"-mirror

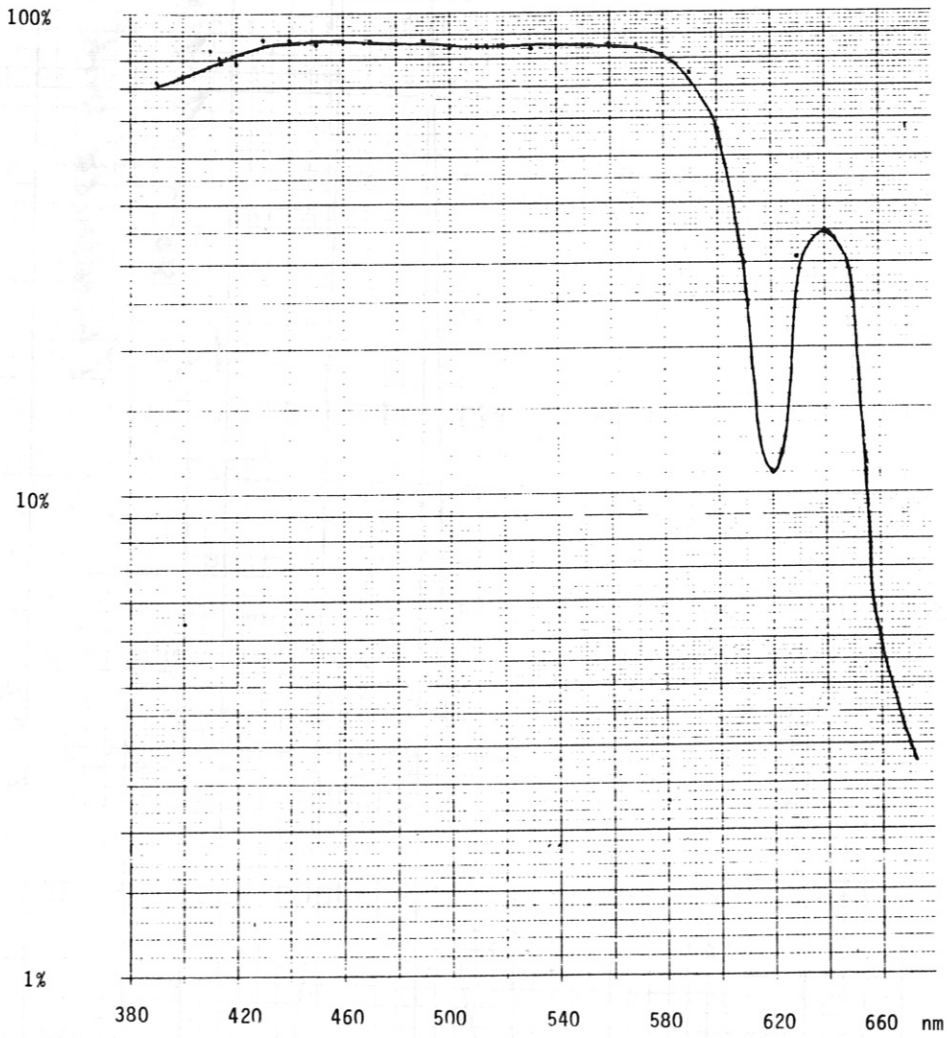

Fig. 5.13 : Reflectivity of "s"-mirror

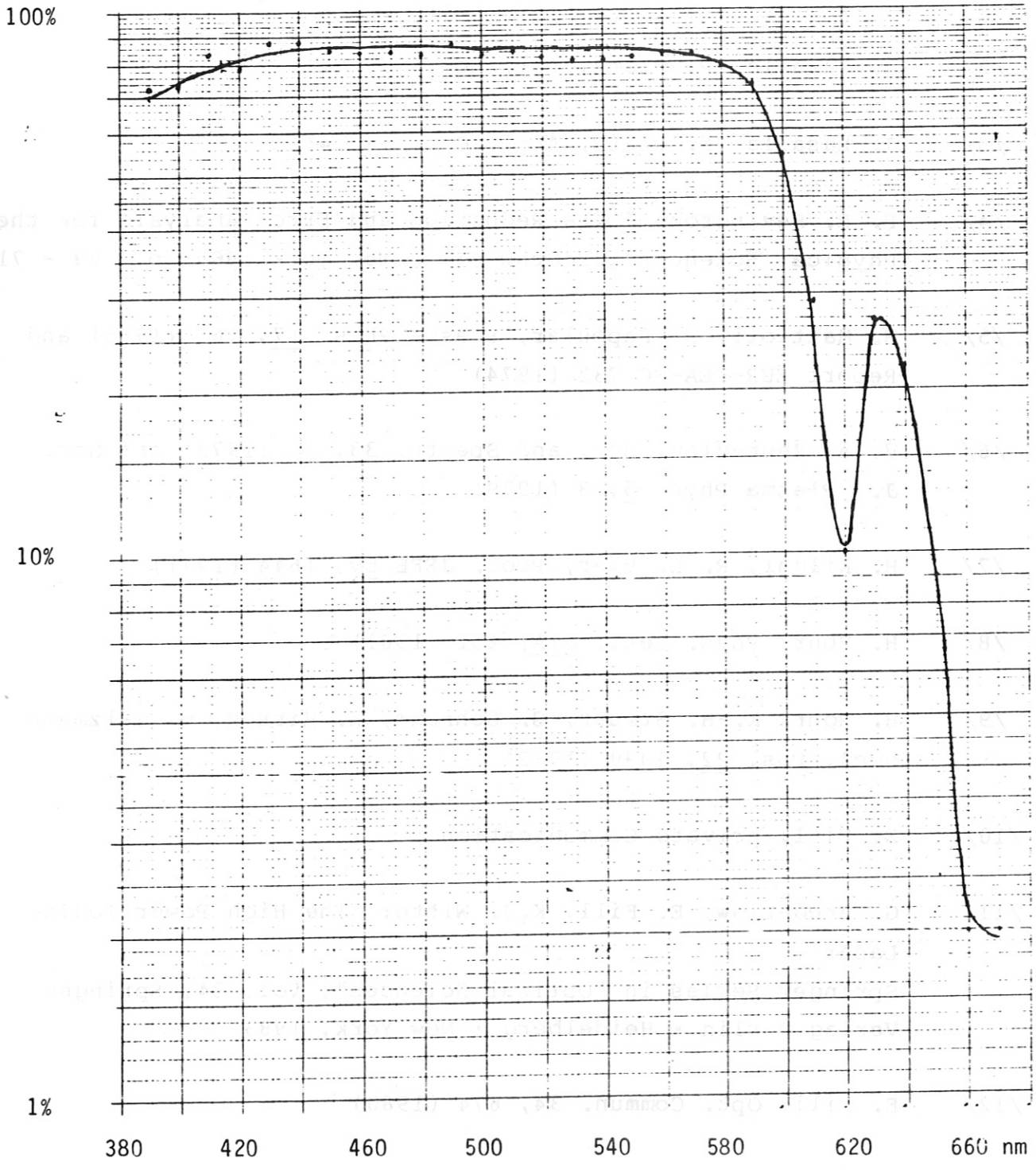

Fig. 5.14 : Transmission of the mirror set

8 REFERENCES

/1/ H. Salzmann, K. Hirsch, Rev. Sci. Instr. 55, 457 (1983)

/2/ J. Lasalle, P. Platz, Opt. Com. 17, 325 (1976)

/3/ J. Lasalle, P. Platz, Appl. Opt. 18, 4124 (1979)

/4/ P. R. Bevington: "Data Reduction and Error Analysis for the Physical Sciences", McGraw-Hill, New York 1969, p. 69 - 71

/5/ M. Mattioli, R. Papoular, Plasma Phys. 17, 165 (1975) and Report EUR-CEA-FC 732 (1974)

/6/ V. A. Zhuravlev, Opt. and Spectr. 33, 19 (1972) and Sov. J. Plasma Phys. 5, 3 (1979)

/7/ H. Kildal, R. L. Byer, Proc. JEEE 59, 1644 (1971)

/8/ H. Röhr, Phys. Lett. 81A, 451 (1981)

/9/ H. Röhr, K.-H. Steuer, G. Schramm, K. Hirsch, H. Salzmann Nucl. Fus. 22, 1099 (1982)

/10/ E. Fill, private Communication

/11/ G. Brederlow, E. Fill, K.J. Witte: "The High Power Iodine Laser",
Springer Series in "Optical Sciences", Vol. 34, Springer Verlag Berlin • Heidelberg • New York, 1983

/12/ E. Fill: Opt. Commun. 34, 674 (1980)

/13/ W. Fuss, K. Hohla: Opt. Commun. 18, 427 (1976)

/14/ J. E. Gruber, JPP Lab. Note No 9, Oct. 1981

9. APPENDICES

Proposal for a time-of-flight Thomson backscattering technique for large fusion devices

H. Salzmann and K. Hirsch

Institut für Plasmaforschung, Universität Stuttgart, 7000 Stuttgart 80, Federal Republic of Germany

(Received 10 May 1983; accepted for publication 27 October 1983)

The application of 180° Thomson scattering using ultrashort laser pulses for measuring electron temperature and density profiles in large fusion devices is proposed. Spatial resolution along the laser beam is achieved by high-speed detection allowing time-of-flight measurements. This LIDAR (light detection and ranging) technique uses a minimum number of window ports and reduces the number of optical components in the vicinity of the discharge vessel. As an example, the performance of such a system for the JET tokamak geometry is discussed on the basis of available laser and detection technology.

PACS numbers: 52.70.Kz, 42.60.Kg, 52.40.Db, 52.25.Lp

INTRODUCTION

Thomson scattering of laser radiation is a well-established technique for measuring electron temperature and density in a plasma.[1] The application to large plasma devices, however, becomes difficult when the plasma machine and its vicinity become inaccessible due to activation.[2–5]

This means that the intricate collection optics for a spatial multichannel system, located near the plasma device, must be kept aligned with respect to the laser beam by remote control. Thus, the costs of a Thomson scattering system for a fusion device are very high. Also the problems of access for repairs make reliability a key issue.

Keeping in mind an application to a plasma machine with parameters near ignition, one can write down a number of conditions which should be met by a Thomson scattering arrangement: (1) The diagnostic system should require the minimum possible number of windows, which furthermore should have small dimensions. (2) The number of optical components in the vicinity of the plasma machine should be kept to a minimum, thus facilitating remote control. (3) The collecting and transmitting optics should be radiation resistant. (4) The required penetration of the biological shield surrounding the plasma machine should be as small as possible. (5) The laser and the detectors should be located outside the biological shield and be accessible for maintenance. (6) Electron density and temperature need to be measured with sufficient resolution along a spatial chord and with sufficient accuracy to accomplish the experimental goals. The measurements should be repeated as often as possible during a plasma discharge.

Based on the geometry of the JET tokamak we will discuss a possible Thomson scattering arrangement which meets all these requirements. JET is a large tokamak with dimensions (minor radii 1.25×2.2-m D shaped, major radius 2.96 m) within a factor of 2 or 3 of those expected in a future reactor. For Ohmically heated discharges a mean electron density of $1\text{–}3 \times 10^{13}$ cm^{-3} and a mean electron temperature of about 600 eV are expected. With 25-MW additional heating power (neutral injection and rf heating) an average electron temperature of more than 5 keV at a density of about 10^{14} cm^{-3} is predicted in case of the hydrogen and deuterium discharges.

I. PRINCIPLE OF OPERATION

For Thomson scattering on large plasma devices there exist two possible arrangements in which the optical alignment can be made stable so that remote control is not necessary, namely, small angle forward scattering and backscattering. In both cases it is possible to couple the collection optics rigidly with the focusing optics.[4] Thus, the scattering volume may be shifted slightly within the plasma due to vibrations, but the alignment between laser and detection systems remains fixed.

Neither of these scattering geometries have yet been tried on large plasma devices. There are several reasons for this: (1) The spatial resolution decreases when the scattering angle approaches either 0° or 180°. (2) Plasma radiation is strong in the case of backscattering due to the broad scattered spectrum. (3) Stray light suppression can be a problem for both forward and backscattering.

For backscattering (Fig. 1) all these disadvantages can be avoided using subnanosecond laser pulses and a high-speed detection system: (1) The spatial resolution will be achieved via a time-of-flight measurement as in LIDAR techniques. It is determined by the laser-pulse length and the response time of the detection sytem. (2) The plasma background radiation registered during the gating time of a few hundred picoseconds will be two orders of magnitude less than with conventional 90° Thomson scattering setups. (3) Stray light will arrive at the detector at other times than the scattered light and can thus be discriminated against.

This scheme offers two additional advantages: (a) In principle the scattering system needs only one window, and (b) for 180° scattering and time-of-flight discrimination, only one collection and transmission optic is necessary. In this single-optical channel the signals from all spatial points are multiplexed in time.

 0034-6748/84/040457-06$01.30

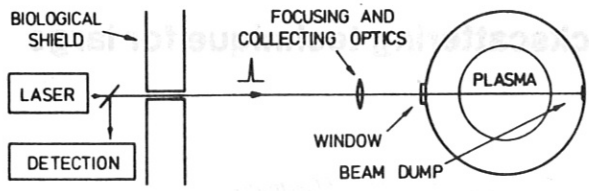

FIG. 1. Scheme of the Thomson backscattering arrangement.

The spatial solution Δx achieved in backscattering is given by

$$\Delta x = c/2(t_L + t_d), \tag{1}$$

where c is the velocity of light, t_L the laser pulse width, and t_d the response time of the detection system.[6] With reasonable numbers for t_L and t_d, values for Δx well below 10 cm result. This resolution is sufficient for large tokamaks like JET. Though in principle this arrangement seems simple, its realization on a large machine needs a detailed discussion of the components and the measuring procedure.

II. LASER TECHNOLOGY

In order to achieve a small statistical error of the Thomson scattering measurements, a large number of collected scattered photons is necessary. This requires single-pulse laser energies of several Joules. To our knowledge at present there exists only two laser systems which are capable of delivering such an energy in a subnanosecond pulse:

The ND: glass laser ($\lambda = 1.06$ μm): For laser fusion multikilojoule subnanosecond laser systems have been developed by different laboratories. Typically, an energy of 30 J in the IR with a pulse duration of 500 ps requires a four-stage amplifier chain with a diameter of the final rod of about 6 cm.[7] For a 50-ps operation the output of such a system is only about 1 J.

The photochemical iodine laser ($\lambda = 1.315$ μm): The iodine laser operated at the Max–Planck-Institut für Quantenoptik, Garching, emits pulses of $\tau_L = 300$ ps duration with an energy of up to 300 J.[8] The beam divergence is about twice the diffraction limit. Pulses of 150 J are being frequency doubled routinely to yield about 90 J of laser energy at 657 nm. For obtaining a laser energy of 30 J at the fundamental or 15 J at the harmonic, three amplifiers are needed.[9] The diameter of the last amplifier is about 5 cm.

A point in favor of the iodine gas laser is the possibility of repetitive operation. There are no physical reasons which prohibit, respectively, pulsed operation in the 1-Hz range. As an example, at the University of Manchester a small sealed iodine laser in which the required gas flow was driven thermally was operated with 100 mJ at 10 pps.[10]

Important for the intended application of the ultrashort pulse laser is the peak-to-background contrast. Since this is also a decisive factor for laser fusion experiments it has been investigated thoroughly for both laser types. In case of the 300-ps iodine laser at its fundamental wavelength the 30-J, laser pulse rises from a background intensity of about 100 W which is due to amplified spontaneous emission in the amplifier chain.[9] The duration of the background intensity is approximately 10 μs corresponding to the flashlamp pump pulse duration. In addition to the continuous background, spurious pulses of ~ 2 μJ occur periodically corresponding to the round trip time of the mode-locked oscillator. These pulses are due to the finite contrast ratio of the pulse-selection system. In the case of the frequency-doubled iodine laser the contrast is expected to be much better.

III. DETECTION TECHNOLOGY

A number of detectors exist which are suitable for the detection of subnanosecond light pulses. Among these are image converter streak cameras, photomultipliers with discrete dynodes, photomultipliers with microchannelplates, vacuum photodiodes, semiconductor photodiodes, and semiconductor avalanche photodiodes. For low-level light detection as in the intended scattering experiment, detectors without internal amplification cannot be used. Their signal would be too small to overcome the input noise level of broadband electronic amplifiers. Taking the parameters of the example discussed in Sec. IV the product of internal gain and quantum efficiency of the detector should be at least 50 to ensure a good SNR, even for low-density plasma ($n_e = 1 \times 10^{13}$ cm^{-3}). Thus, vacuum photodiodes and semiconductor photodiodes cannot be used. Semiconductor avalanche photodiodes with the required bandwidth offer only a small sensitive area, which is not sufficient for the intended application. In the case of photomultipliers one must also consider the possible limitation in bandwidth due to the electronic data acquisition. This could be either a fast real-time oscilloscope with an oscillogram digitizing system or a fast transient digitizer. Dynamic range is also an important factor, since the scattered light power can vary strongly.

The dependence of the dynamic range of streak cameras on the temporal resolution has been investigated thoroughly by Thomas *et al.*[11–14] According to their measurements the dynamic range of the LLL streak camera employing a RCA C 73435 tube is $\sim 10^4$ at a resolution of 100 ps. Of course it is the dynamic range of the whole detection and registration system which has to be considered. The photoelectrical scan of the screen of the streak camera can be done by intensified charge-coupled devices. The performance of intensified CCD's was investigated for a Spacelab spectroscopic system.[15] A dynamic range of the whole system (including the image intensifier and data acquisition) of 3×10^4 is reported.

Shorter rise times than those obtained with available photomultipliers with discrete dynodes[16,17] are achieved with microchannelplate (MCP) photomultipliers. Single-stage MCP photomultipliers offer a FWHM response time of about 300 ps (e.g., ITT F4126 and HAMAMATSU R 1564). The low gain of single-stage MCP photomultipliers (~ 1000) requires further amplification of the signals. Suitable amplifiers exist whose noise figure within the required bandwith is low enough to maintain the SNR of the photomultiplier output signal.

The drawback of the MCP photomultipliers is their low dc current capability which might call for electronic gating in a Thomson scattering experiment. Gating is possible according to the data sheets. Furthermore, the internal amplification is not as noise-free as that of a conventional photomultiplier. This fact is described by a noise factor F which is

defined as the ratio of the MCP input SNR to the MCP output SNR. Its value is given as $F \sim 1.8$.

The signals from the photodetectors can be registered with fast real-time oscilloscopes or transient digitizers. A bandwidth of at least 1 GHz is achievable (for instance, using a TEK 7104 oscilloscope with a 7A29 plug-in).

IV. PERFORMANCE OF A POSSIBLE SYSTEM

We now discuss the performance of a possible setup on the basis of the geometry of the JET tokamak. A possible arrangement is shown in Fig. 2.

The laser data of the frequency-doubled, linearly polarized iodine laser are assumed as follows:

pulse energy	15 J at 657 nm;
pulse duration	300 ps;
beam diameter	7.5 cm; and
beam divergence	5 × diffraction limited.

This laser is located in the roof laboratory above the torus hall and focused by a $f = 840$-cm lens L_1 vertically through the discharge vessel. One single ceiling penetration is used both for passing the laser beam and for transmitting the collected scattered light back to the roof laboratory. A hole of 10-cm diameter in the 2.5-m-thick biological shield is sufficient. The laser beam diameter at the window (14-cm diameter) on the discharge vessel is 4 cm in diameter, which is large enough to avoid damage by the laser radiation.

The focal-spot diameter in the plasma is $\phi_f = 0.04$ cm. Thus, for a 15-J 300-ps laser pulse the ratio of the electron quiver energy in the electromagnetic laser field to the thermal energy of the electron is only 1% at $T_e = 300$ eV.

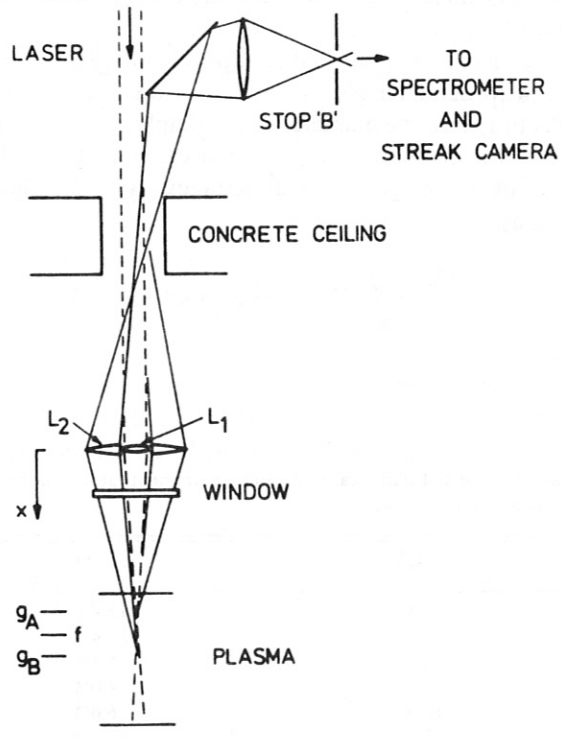

FIG. 2. Proposed setup for the JET tokamak. To allow the display of the path of rays the scales are different in the vertical and horizontal direction.

The collection optics is laid out to scan a spatial chord of 2.5-m length covering the upper part of the plasma and 40 cm of the lower part. It consists of a 23-cm-diameter, $f = 420$-cm lens L_2, with a 7.5-cm hole into which the laser focusing lens is inserted. Thus, remote control is unnecessary since the rigid coupling of focusing and collecting optics conserves the alignment. The separation of the backscattered light from the laser beam can be achieved in the roof laboratory using geometrical optics (Fig. 2). Introducing a diaphragm into the detection optics which passes the collected scattered light from the whole length of the spatial chord to be investigated (length 2.5 m) without vignetting, a rather large plasma volume is seen by the detectors: If the stop is located in the image plane corresponding to the focal spot of the laser, a plasma volume of $d_f' = 5$-cm diameter (see Fig. 4) and 420-cm length will illuminate the detectors with an effective solid angle of 4.8×10^{-4} sr. For calculating the number of background photoelectrons the emission coefficient has been taken as 100 times bremsstrahlung of pure hydrogen. Furthermore, a transmission of the detection optics of 0.1 is assumed.

The spectrum of the backscattered light was calculated from the formulas given by Mattioli *et al.*[18] which yield exactly the same results as those given by Zhuravlev.[19] When the shape of the scattered spectrum is folded with the spectral sensitivity of a S-20 photocathode the heights of the maxima at different temperatures become approximately the same due to the increase of sensitivity in the blue region. In Fig. 3 the number of photoelectrons per unit wavelength is plotted versus wavelength for 1-J laser energy, a spatial resolution of 9 cm corresponding to $t_L = t_D = 300$ ps, a transmission of the collection optics of 0.1, a solid angle of the collection optics of 1×10^{-3} sr, and an electron density of 1×10^{13} cm^{-3}. The spectra are measured by dividing the spectral range of interest into five channels as indicated in Fig. 3. If photomultipliers are used as detectors the spectral resolution can be achieved preferably by an interference filter polychromator. This presents no problems for the re-

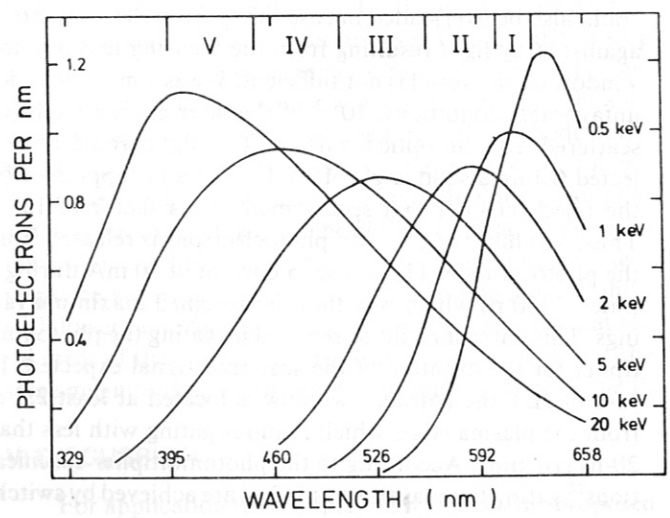

FIG. 3. Number of signal photoelectrons per unit wavelength interval vs wavelength for a S-20 photocathode. Spectral channels: I: 624.7–602.7 nm, II: 602.7–558.7 nm, III: 558.7–503.7 nm, IV: 503.7–448.7 nm, and V: 448.7–393.7 nm.

quired throughput of 8×10^{-3} cm^2 sr (if filters of 5-cm diameters are used, the divergence of the incident light beam is less than $\pm 0.9°$). Using a streak camera, a grating spectrometer displaying the spectrum along the input slit will be appropriate.

We now discuss two cases. First, we consider the simple version using MCP photomultipliers and an available 1-GHz registration system. Second, the application of a streak camera, which results in an improved spatial resolution will be treated.

A. Photomultiplier

We consider measurements at the plasma center and assume an electron density of 1×10^{13} cm^{-3}. The spatial resolution is taken as 13 cm, which can be achieved with the described iodine laser ($\tau_L = 300$ ps), a MCP photomultiplier with 300-ps temporal resolution, and a 1-GHz oscilloscope ($\tau_D = \sqrt{\tau_{PM}^2 + \tau_{osc}^2} = 583$ ps). With these parameters the number of photoelectrons n_s^i obtained within each of the five chosen spectral channels i (see Fig. 3) varies between 100 and 600 for a wide range of temperatures (2–20 keV). This yields photomultiplier signal levels high enough for noise-free electronic amplification within the required bandwidth. The number of photoelectrons due to background radiation is less than 20 in each spectral channel. Thus, the SNR of the measurement will not be deteriorated by the background radiation.

Of course the maximum ratings of the sensitive detectors must be observed. A simple estimate shows that for an electron density of 1×10^{14} cm^{-3} the dc anode current due to plasma background radiation (typical duration 10 s) is of the order of 6 μA and thus exceeds the tolerable value. On the other hand, the charge output during the passage of the laser pulse through the plasma is only about 7×10^{-11} C, which is 50 times less than the maximum rating. Thus, by gating the photomultiplier for a time of less than approximately 5 μs, a reliable operation of the MCP photomultiplier can be achieved. The MCP incorporated in the photomultiplier could also be overloaded in case the spectral discrimination against stray light resulting from the focusing lens and the window on the vessel is not sufficient. We assume that under unfavorable conditions, 10^{-3} of the laser energy might be scattered from an optical surface. This light would be collected within a solid angle of 1×10^{-3} sr and suppressed by the rejection filter and spectrometer by a factor of 10^{+7}. Thus, a number of 2.5×10^5 photoelectrons is released from the photocathode. This causes a current of 70 mA during a time of 450 ps which is within the specified maximum ratings. This current could be reduced by gating the photomultiplier for the duration of the scattered signal expected. In case of JET the entrance window is located at least 2.7 m from the plasma edge, which requires gating with less than 20-ns rise time. According to the photomultiplier specifications[20] gating times as short as 1–3 ns are achieved by switching the cathode–MCP voltage.

We have also to consider the effect of the spurious background laser pulses which can cause stray light from the optical components during the time the main laser pulse passes the plasma. However, under the conditions assumed above the signals caused by pulses containing less than 1 μJ of energy are negligible.

The statistical error of the electron temperature measurements is calculated analytically: The n signals from the n spectral channels are used to perform $n-1$ independent electron temperature measurements using the two-channel ratio method.[21,22] The error of the mean temperature is obtained from the statistical errors of the $n-1$ independent sample measurements.[23]

The results are summarized in Table I for the given parameters. Since the influence of the background radiation on the SNR of the signals is negligible, the errors decrease with the square root of the electron density.

B. Streak camera

In the second case we will discuss the spatial resolution along the laser beam that can be achieved with a 300-ps laser pulse and streak cameras. For this purpose we use the parameters of the optical setup sketched in Fig. 2 and calculate the influence of the finite depth of field on the spatial resolution of the LIDAR system. The spectrometer has been omitted for the sake of simplicity. In contrast to the setup with photomultipliers, two detection systems will be used to investigate the upper and lower half of the chord separately. For this purpose the collected light beams are divided by two totally reflecting mirrors, each using one-half of the solid angle of the collection optics. In each of the two paths of rays the diameter and position of a separate diaphragm defines the length and position of the spatial chord from which the scattered light is observed without vignetting. In this geometry the throughput of each of the two low-resolution spectrometers must be 1×10^{-3} cm^2 sr, a value which can be realized.

To let all the collected rays pass from a scattering volume with diameter $\varnothing(x)$ located at a distance x from the collecting lens, the diameter d of a diaphragm in the image plane corresponding to $x = g$ can be calculated. The diameter d' of the image of this diaphragm inside the plasma is given by

$$d'(x) = \frac{F}{x}\,\frac{g[D+\phi(x)] - Dx}{g-F}, \quad x \leqslant g, \tag{2}$$

and

TABLE I. Expected statistical errors of measurements at the plasma center. Spatial resolution 13 cm.

T_e/keV	$\Delta T_e/T_e$
0.5	15.4%
1.0	7.4%
2.0	5.3%
5.0	4.0%
10.0	6.6%
15.0	10.0%
20.0	13.5%

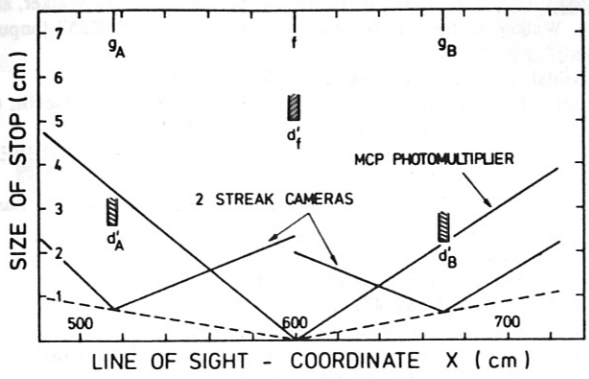

FIG. 4. Diameter d' of stop images inside the plasma. Broken line = laser beam diameter.

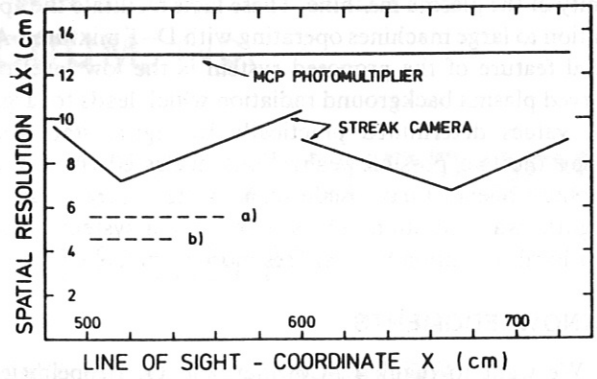

FIG. 6. Spatial resolution along the line of sight. (a) Limit of resolution determined by the laser-pulse duration and the streak camera. (b) Limit due to the laser-pulse duration alone.

$$d'(x) = \frac{F\{\phi(x)[g(x+F) - 2Fx] + D(x-F)(x-g)\}}{x(x-F)(g-F)}, \quad x \geqslant g, \tag{3}$$

where the laser beam diameter $\phi(x)$ is approximated by

$$\phi(x) = \phi_f + \frac{\phi_0 - \phi_f}{f}|f - x|. \tag{4}$$

The results are plotted in Fig. 4 as a function of the coordinate x along the line of sight inside the plasma. This is done for two cases: (a) one diaphragm located at the image plane of the laser focal spot plane (as used for photomultiplier detection) and (b) the case of two streak camera detection systems for the upper and lower part of the spatial chord, respectively. In this latter case the two diaphragms are positioned in such a way as to minimize the diameters $d'_A \sim d'_B \sim 2.5$ cm and using $f/2$ optics in front of the streak cameras the collected scattered light can be concentrated on the photocathode to spots of 1.6- and 1.2-mm diameter, respectively. These values determine the input slit widths of the streak systems. However, the rather large values only determine the level of background intensity but do not limit the temporal resolution of the system with respect to the scattered laser light.

Figure 5 shows schematically how the image on the screen of the streak camera develops in time. The size of the image of the input slit illuminated by the background radiation is the same everywhere on the screen [Fig. 5(a)]. Without the spectrometer the image of the laser pulse moving along the spatial chord, however, decreases until a sharp image is formed on the streak tube. Then it increases again until it covers the input slit image [Fig. 5(b)]. The spot size varies along the streak direction according to $d'(x)$. For very

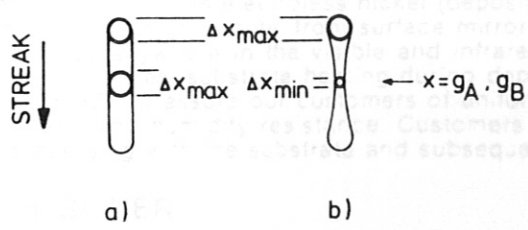

FIG. 5. Formation of the streaked image (a) for the background radiation, (b) for the scattered laser light.

small values of $d'(x)$ the finite resolution of the streak tube (about 250 μm) would determine the spatial resolution Δx, but this limit is not reached in the example given.

The following data for the streak camera (RCA C 73435 tube, as used in the LLL streak camera and in CORDIN 179-LLL) are used for an estimate: Magnification 0.7; used size of image on the screen 22-mm width, 33-mm length; luminous gain 50; and streak speed 330 ps/mm. With these data and using Eq. (1) the curves $d'(x)$ (Fig. 4) yield directly the variation of spatial resolution Δx along the spatial chord. Figure 6 shows the spatial resolution that can be achieved for the system with two streak cameras in comparison with that for the MCP photomultiplier/1-GHz oscilloscope system. Thus, about 30 independent measurements can be taken along the spatial chord if the streak camera is used compared to 19 measurements with the photomultiplier system.

One has to pay for the improved spatial resolution with a decrease in the SNR since the number of collected scattered photons is reduced by a factor of up to 1.8. Furthermore, the reduction in solid angle when using the two streak cameras yields another factor of 2. On the other hand, for high plasma densities some improvement is achieved by the fact that the plasma background radiation is reduced by a factor of about 10. The reduction results from (ratio of stop diameter)$^2 \times$(ratio of solid angle)$\times$(ratio of time resolution). The SNR of the measurement will be determined by the shot noise of the photoelectrons released from the cathode of the streak tube and by the excess noise produced by the following image amplification process. Using MCP image amplifier tubes this excess noise will be of the same magnitude as in the case using MCP photomultipliers. Some improvement might be achieved using first-generation image intensifiers with lower noise figures.[24] In that case the expected statistical error of the electron temperature measurement is of the same magnitude as for the photomultiplier system (Table I).

V. DISCUSSION

For application to large plasma machines the proposed LIDAR Thomson scattering scheme offers many advantages over conventional Thomson scattering arrangements. Among these are insensitivity against vibrations and the need for only a small number of optical components in the

vicinity of the plasma machine. These facts facilitate the application to large machines operating with D–T mixtures. A special feature of the proposed system is the low level of observed plasma background radiation which leads to large SNR values determined practically by signal statistics. Among the two possible realizations discussed the MCP photomultiplier/1-GHz oscilloscope system represents a straightforward solution. The streak camera system offers better local resolution but requires more technical effort.

ACKNOWLEDGMENTS

We want to thank L. Coleman and G. Leppelmeier (Lawrence Livermore Lab.) for valuable discussions during the 1982 Summer school on Plasma Diagnostics, Varenna. We are further obliged to the members of the iodine laser group at the MPI f. Quantenoptik, Garching, for a number of helpful discussions.

[1]J. Sheffield, *Plasma Scattering of Electromagnetic Radiation* (Academic, New York, 1975).
[2]P. Nielsen (unpublished).
[3]P. Nielsen, *Proceedings of Diagnostics for Fusion Reactor Conditions*, 6–17 Sept. 1982 (International School of Plasma Physics, Varenna, Italy, in press).
[4]K. Hirsch, H. Salzmann, H. Röhr, and K.-H. Steuer, Bull. Am. Phys. Soc. **25**, 682 (1980); and IPP Garching, EURATOM Association Report Nos. IPP-III-55 and IPP-III-66, 1981 (unpublished).
[5]I. J. Spalding, P. Andrews, K. Harries, T. Stamatakis, A. C. Walker, and C. I. Walker, Culham Laboratory Report No. CLM/P02257 (unpublished).
[6]H. Kildal and R. L. Byer, Proc. IEEE **59**, 1644 (1971).
[7]W. Seka, J. Soures, O. Lewis, J. Bunkenburg, D. Brown, S. Jacobs, G. Mourou, and J. Zimmermann, Appl. Opt. **19**, 409 (1980).
[8]K. J. Witte, E. Fill, G. Brederlow, H. Baumhacker, and R. Volk, IEEE J. Quantum Electron. **QE-17**, 1809 (1981).
[9]G. Brederlow, E. Fill, and K. J. Witte, *The High-Power Iodine Laser* (Springer, Berlin, 1983), Chaps. 4 and 5.
[10]H. J. Baker and T. A. King, J. Phys. D **14**, 1367 (1981).
[11]S. W. Thomas and G. E. Phillips, SPIE **97**, 11 (1976).
[12]S. W. Thomas, SPIE **189**, 471 (1978).
[13]S. W. Thomas and R. L. Peterson, SPIE (in press).
[14]S. W. Thomas, R. L. Peterson, and R. L. Griffith, SPIE (in press).
[15]M. R. Torr and J. Devlin, Appl. Opt. **21**, 3091 (1982).
[16]G. Beck, Rev. Sci. Instrum. **47**, 537 (1976).
[17]P. B. Lyons, L. D. Looney, J. Ogle, R. D. Simmons, R. Selk, B. Hopkins, L. Hocker, M. Nelson, and P. Zagarino, Los Alamos Laboratory Report No. LA-UR-81-1028, 1981 (unpublished).
[18]M. Mattioli and R. Papoular, Plasma Phys. **17**, 165 (1975); and Report No. EUR-CEA-FC, 1974.
[19]V. A. Zhuravlev, Opt. Spectrosc. **33**, 19 (1972); and Sov. J. Plasma Phys. **5**, 3 (1979).
[20]ITT Electro-Optical Products Division, Data Sheet MCP Photomultiplier F 4126 (1980).
[21]J. Lasalle and P. Platz, Opt. Commun. **17**, 325 (1976).
[22]J. Lasalle and P. Platz, Appl. Opt. **18**, 4124 (1979).
[23]P. R. Bevington, *Data Reduction and Error Analysis for the Physical Sciences* (McGraw–Hill, New York, 1969).
[24]H. Pollehn, J. Bratton, and R. Feingold, *Advantages in Electronics and Electron Physics*, edited by L. Marton (Academic, New York, 1976), Vol. 40A, p. 21.

DENTON VACUUM, INC.

MAXIFLECT FRONT SURFACE MIRRORS
SILVER AND ALUMINUM

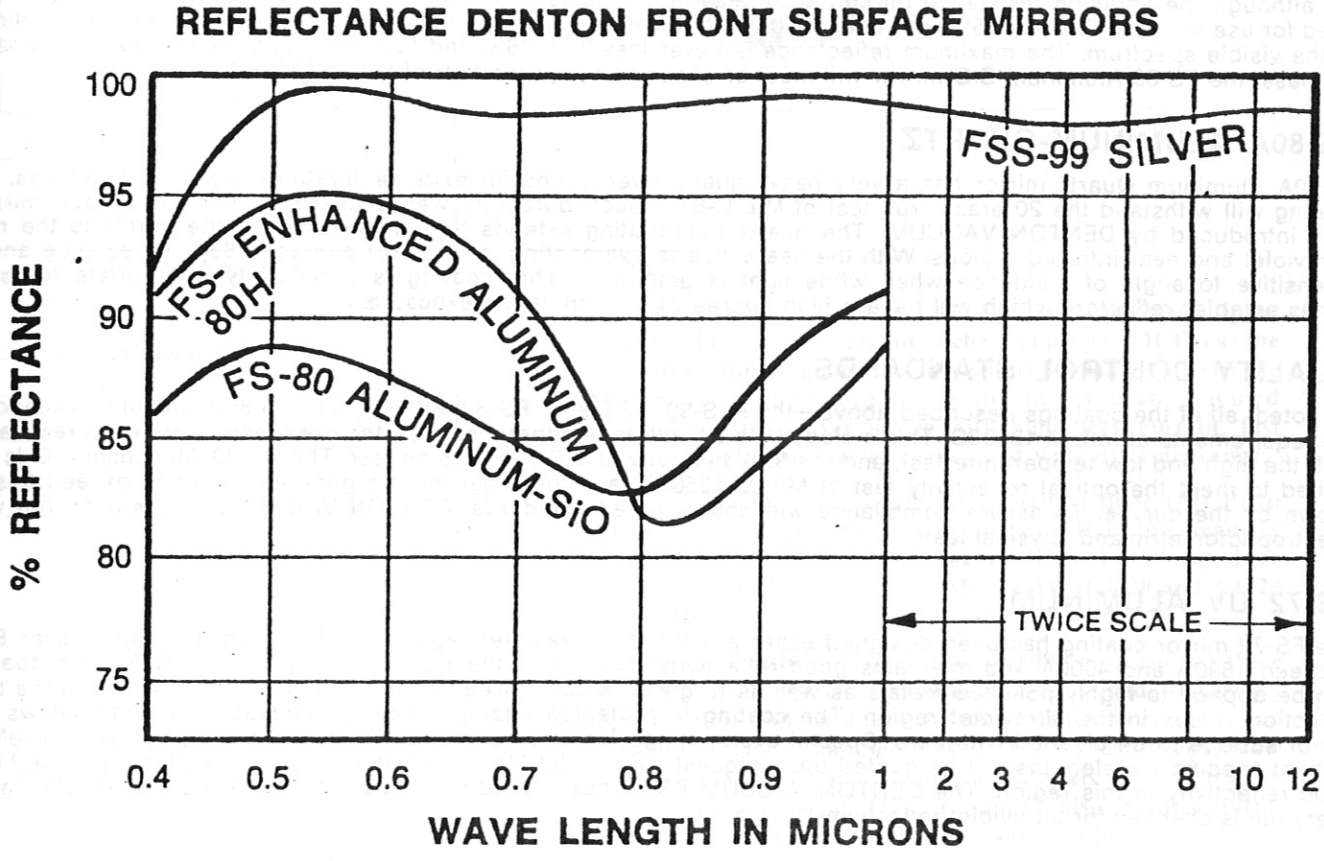

ALL TYPES AVAILABLE IN LARGE OR SMALL SIZES IN EXPERIMENTAL OR PRODUCTION QUANTITIES ON YOUR SUBSTRATES OR OUR FLAT GLASS

FSS-99 SILVER

FSS-99 is the highest reflectance, wide band, protected metal, front surface mirror manufactured today. The reflectance curve is practically flat from 0.45 to 50 microns and does not diminish when used at angles other than normal incidence. Reflectance approximates 98% or more from 0.5 up to 50 microns. At 0.8 microns the reflectance exceeds standard Aluminum-SiO by more than 16%.

The FSS-99 coating is compatible with a wide variety of substrate materials including most glasses, quartz, stainless steel, beryllium as well as electroless nickel (deposited on the surfaces of light metals such as beryllium or aluminum and polished). This high quality, front surface mirror coating is recommended for applications requiring exceptionally high reflectance anywhere in the visible and infrared. Although the FSS-99 coating withstands both depressed and elevated temperatures, substrate heating during deposition is not required. This coating meets the humidity provisions of MIL M-13508C. To assure our customers of uniformly excellent quality, each run is checked for reflectivity, adhesion, hardness, and humidity resistance. Customers with special substrates should provide a witness plate for simultaneous processing with the substrate and subsequent testing; otherwise the testing will be done on plate glass.

FSS-99H SILVER

FSS-99H is a special silver mirror with additional overcoating. This overcoating substantially improves the resistance of the mirror to abrasion. The reflectivity in the visible spectrum averages approximately 95%.

FS-80H ENHANCED ALUMINUM

FS-80H is a durable aluminum mirror with enhanced reflectance in the visible spectrum compared to standard Aluminum SiO. This coating has a peak reflectance at about 95% with the average across the entire visible spectrum in the order of 93%. The enhancement can be customized for particular regions of the spectrum and various angles of incidence. FS-80H meets or exceeds all the requirements of MIL M-13508C and, of course, has much higher reflectivity. Though the best durability is obtained by heating of the substrate, FS-80H does *not* require heat. Therefore it can be used for heat-sensitive parts such as plastics, electroformed nickel, etc.

FS-80 ALUMINUM-SiO

FS-80 is our standard aluminum/silicon monoxide mirror with reflectance approximating that shown in the curve. It can be economically applied to almost any substrate including various polished metals, glass, quartz, and even plastic, although the abrasion resistance on soft substrates is of course less than on glass. The standard coating is supplied for use at approximately 45° but it can be supplied for other angles of incidence. Reflectance peaks in the middle of the visible spectrum. The maximum reflectance is never less than 86% and frequently approaches 90%. As coated on glass, the FS-80 Aluminum SiO mirror will meet or exceed all requirements of MIL M-13508C.

FS-80A ALUMINUM-QUARTZ

FS-80A Aluminum Quartz mirror has a very heavy quartz overcoating for extreme durability. Deposited on glass, this coating will withstand the 20 eraser rub test of MIL-C-675. Such durability was unheard of in front surface mirrors until introduced by DENTON VACUUM. The quartz overcoating extends the useful range of the mirror to the near ultraviolet and near infrared regions. With the heavy quartz overcoating, this mirror averages 85% reflectance and is insensitive to angle of incidence when white light is employed. This coating is particularly appropriate for such things as solar reflectors which will have a high degree of environmental exposure.

QUALITY CONTROL STANDARDS

As noted, all of the coatings described above—the FSS-99, FSS-99H, FS-80, FS-80A, and FS-80H—meet or exceed all the requirements of MIL M-13508C. This includes the Scotch tape adherence test, the cheesecloth abrasion resistance test, the high and low temperature test, and the 95% humidity at 120°F corrosion test. The FS-80 Aluminum SiO is designed to meet the optical reflectivity test of MIL M-13508C, and the other mirrors generally meet or exceed this as shown by the curves. To assure compliance with the required standards, DENTON VACUUM checks each run with spectrophotometric and physical tests.

FS-72 UV ALUMINUM

The FS-72 mirror coating has been designed especially for the ultraviolet region. It reflects an average of over 88% between 1800Å and 4000Å and maintains good reflectivity throughout the visible averaging over 85%. The coating can be applied to highly polished metals as well as to glass. A polish free of fine pits is necessary to obtain the best reflection values in the ultraviolet region. The coating is protected against oxidation and abrasion; this allows the mirror surface to be cleaned with care. Special overcoatings for varying angles of incidence or for maximum reflectivity at specific wavelengths will be quoted upon request. Ultraviolet films must be very carefully prepared to achieve good reflectivity in this region. The DENTON VACUUM FS-72 has proved to consistently meet the highest standards. Every run is checked for ultraviolet reflectivity.

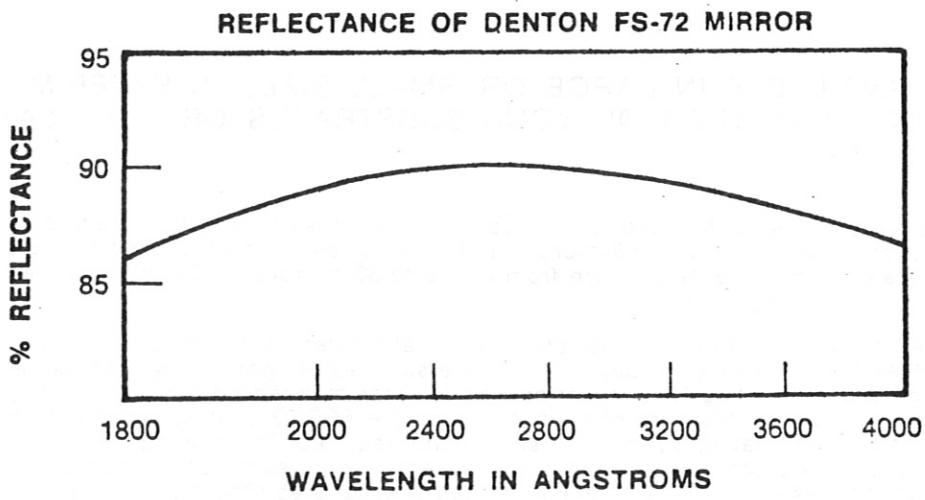

DENTON VACUUM, INC.
Cherry Hill Industrial Center
Cherry Hill, New Jersey 08003
Telephone: 609-424-1012

ELECTRO-OPTICAL PRODUCTS DIVISION
TUBE and SENSOR LABORATORIES
3700 East Pontiac Street
P. O. Box 3700
Fort Wayne, Indiana 46801
Telephone 219-423-4341 TWX 810-332-1413

F4126
F4128
F4129

MICROCHANNEL PLATE MULTIPLIER PHOTOTUBE

- Compact Size
- Minimum Electrical Connections
- UV Through Near IR Response
- Low Voltage Nanosecond Gating
- High Photocathode Uniformity
- High Magnetic Field Tolerance
- Subnanosecond Response
- High Peak Current Output
- Single Electron Counting (Pulse Saturated Mode)

GENERAL:

The F4126, F4128 and F4129 series of photomultiplier tubes (PMTs) incorporate microchannel plates (MCPs) as the electron multiplying element. Proximity focusing between the MCP and the input photocathode and the output anode is used to combine small overall size with high peak current, fast response, high quantum efficiency and wide dynamic range.

The F4126 uses a single microchannel plate (MCP) to achieve modest gain; the F4128 uses two MCPs in cascade (a "V-plate" MCP) to obtain more gain; and the F4129 uses three MCPs in cascade (a "Z-plate" MCP). The F4128 and F4129 have sufficient gain for single electron counting.

Because of the special method used in constructing these MCP PMTs, in which the photocathode is made separately from the tube body and the tube subsequently assembled in an ultra-high vacuum chamber, these PMTs are readily adaptable to a wide variety of input window materials and spectral response characterisics. This technique also assures ultra-reliable tube behavior and long operational life.

F4126
F4128
F4129

OPTICAL/MECHANICAL CHARACTERISTICS

Overall Tube Diameter (Note 1) ..... 36 mm
Note: See Fig. 1

Overall Tube Length ..... 40 mm

Effective Photocathode Diameter (Note 1) ..... 18 mm

Input Faceplate (Note 2) ..... borosilicate glass plano-plano

Faceplate Thickness ..... 2 mm

Photocathode Type (Note 3) ..... multialkali (on internal faceplate surface) (see Fig. 2)

Photocathode-MCP Spacing ..... 0.3 mm

MCP Channel Diameter ..... 12.5 um (hexagonal close packed)

Bias Angle (Note 4) ..... 5°

MCP L/D Ratio (Note 5) ..... (F4126) 40:1
(F4128) 80:1
(F4129) 120:1

ELECTRICAL CHARACTERISTICS:

MCP Strip Current (Note 6) ..... 2.5 uA, nominal (at 800V per plate)

MCP-Anode Spacing (Note 7) ..... 1.3 mm

Anode Diameter (Note 8) ..... 18 mm

Pk-MCP Capacitance ..... 2 pf

MCP Face-to-Face Capacitance (Note 9) ..... F4126) 60 pf

MCP-Anode Capacitance (Note 10) .. 5 pf

Photocathode Lead ..... (#24) wire
MCP Input Lead ..... (#24) wire
MCP Output Lead ..... (#24) wire

MAXIMUM RATINGS

Input Photocathode-to-MCP Voltage (Note 11, 12) 300V

MCP Input-Output Voltage F4126 900V
F4128 1800V
F4129 2700V

MCP-Anode Voltage (Note 12) 3kV

Photocathode DC Current Density (Note 13) ..... 0.1μA/cm^2

Anode DC Current Density (Note 14) ..... 1 μA/cm^2

Temperature ..... Max. 35° C
Min. -35° C

Temperature Change Rate ..... 20° C/Min.

Anode Lead ..... 6 mm diameter metal stud

MCP PMT are supplied potted with flying leads.

TYPICAL PERFORMANCE CHARACTERISTICS (Note 15)

Gain (Note 16) F4126: 750
F4128: 3 x 10^5
F4129: 2 x 10^6

MCP Voltage (Note 17) F4126: 800V
F4128: 1600V
F4129: 2400V

Photocathode-MCP Input Voltage (Note 18) ..... 150 V

MCP-Anode Voltage (Note 19) ..... fast response: 3 kV
photon counting: 300V

Maximum Linear Peak Output Current (Note 20) F4126: 3A

Maximum Peak Charge Output (Note 21) ..... 3 nC

Maximum Average Linear Output Current (Note 22) ..... 0.1 μA

Maximum Pulse Repetition Rate
High Current Mode (Note 23) ..... F4126 250 pulse/sec.

Single Electron Counting Mode, Flooded Input ..... F4129 10^6 pulse/sec.

Single Electron Counting Mode Point Source Input (Note 24) ..... F4129 10 pulse/sec.

Output Signal Pulse 10-90% Rise Time (Note 25) ..... F4126: 100 ps

Output Signal Full-width-at-half-Maximum Time (Note 26) ..... F4126: 300 ps
F4129: 500 ps

Dark Count Rate (25° C) (Note 27) ... F4129: 10^{4}c/sec

ELECTRO-OPTICAL PRODUCTS DIVISION ITT
Tube and Sensor Laboratories, Fort Wayne, Indiana 46803

MCP Dark Count Rate (Note 27) ..... 10^2c/sec

Photocathode Thermionic Emission Temperature Coefficient (Note 28) ..... 15%/°K

Peak-to-Valley Ratio (Note 29) F4129: 3:1

Width of Pulse Height Distribution (Note 30) F4129: 100%

Photoelectron Counting Efficiency (Note 31) F4129: 85%

Noise Factor (Note 32) 1.8

Tube Life (Note 33) ..... 20 mc/cm²

ADDITIONAL INFORMATION:

The user, or potential user, of an MCP PMT is invited to contact ITT/EOPD for added information on MCP devices, including applications and technical notes (e.g. ITT Technical Notes 119, 120, 125, 126, and 127). There are also many published technical papers concerning MCPs and MCP devices, including, as an example:

Applied Optics 18, 1418 (1979)

Applied Optics 16, 2127 (1977)

Applied Optics 18, 2440 (1979)

Proc. Electro-Optical Systems Design Conf. Sept. 1976 (p623-670)

Physics today, Nov. 1977 (p42)

Nuclear Instr. & Methods 127, 87 (1975)

If you have specific questions regarding the use of an MCP PMT in a special application, or a modification of a present tube design to meet special requirements, please contact ITT/EOPD and enjoy the benefits of our special technical information services. We specialize in custom devices helping you meet these requirements.

NOTES:

Note 1: MCP PMTs with 25 mm effective photocathode diameter are also available and 40 mm are under development

Note 2: Faceplate of other materials such as fused silica, magnesium fluoride, or fiber optics are also available on request.

Note 3: The multialkali photocathode can be adapted, on request, to various different spectral responses. Other photocathode materials, such as KsbCs bialkali, CsTe, AgCsO, etc. are also available.

Note 4: This is the angle of the MCP channels with respect to the front surface of the MCP.

Note 5: 60:1 ratio is also available. This is the ratio of the effective electron multiplying length of a channel to the diameter.

Note 6: The strip current on a given MCP sample may vary from this nominal value by factors of ± 2 or more.

Note 7: This spacing is adaptable to individual requirements, with resultant changes in the maximum permissible MCP-anode voltage.

Note 8: MCP PMTs with arrays of separate smaller anodes are also available (e.g. the F4149 with a 10 x 10 array of 100 anodes).

Note 9: Includes feed through capacitance.

Note 10: Includes feed through capacitance.

Note 11: 1000V for filmed MCPs. See also following note.

Note 12: Voltages must be supplied to these tubes in proper sequence so that these voltage differentials are not exceeded during the turn-on and turn-off transients. A typical voltage divider network is shown in Fig. 3.

Note 13: Maximum rating for low gain operation where anode current may fall within ratings.

Note 14: Tube life is proportionally reduced when operating at or near this limit.

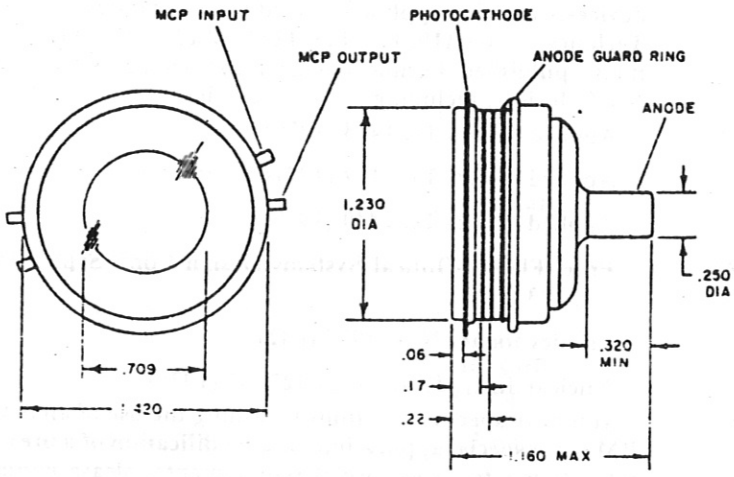

FIG. 1

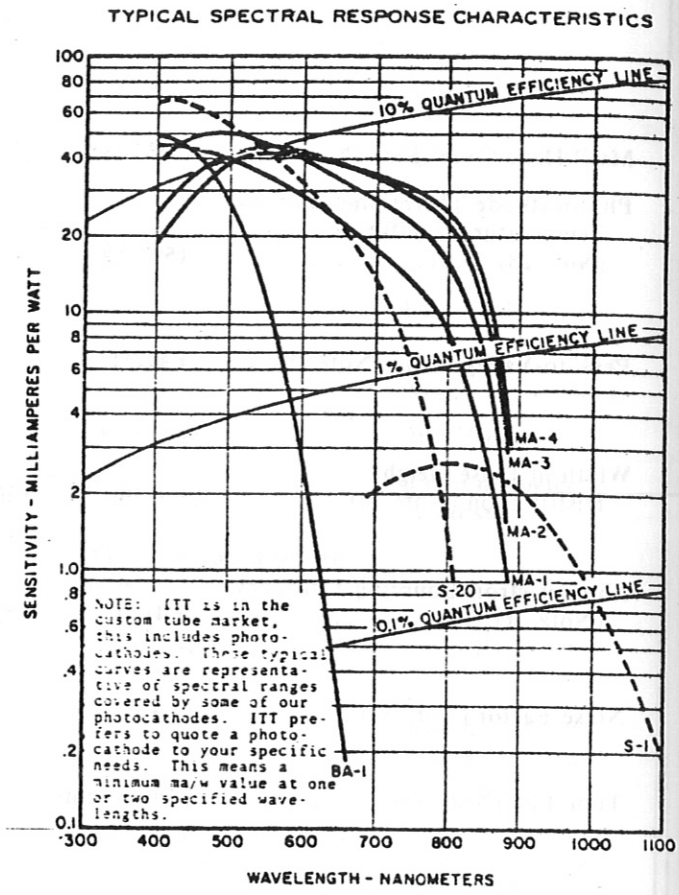

FIG. 2

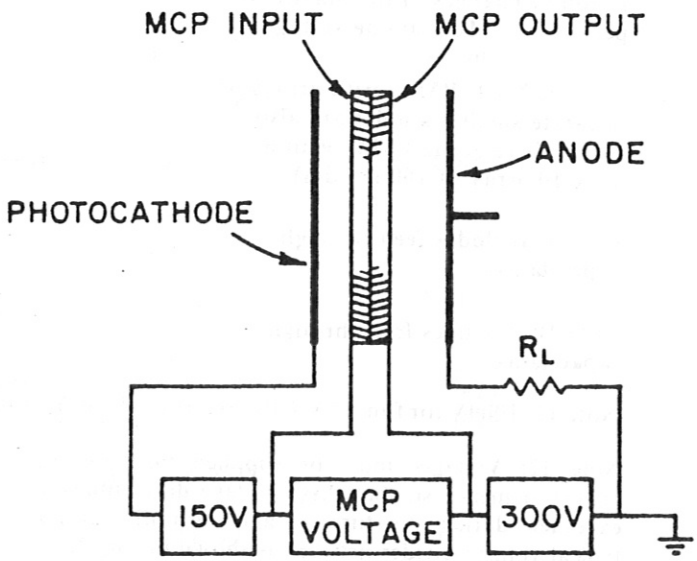

VOLTAGE DISTRIBUTION

FIG. 3

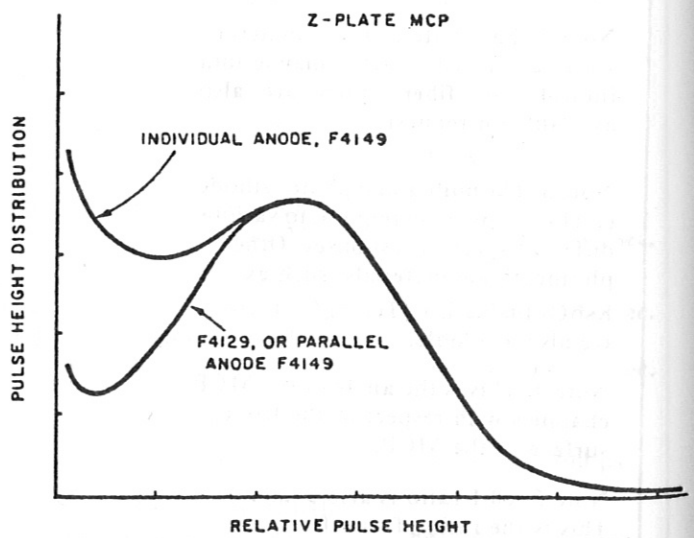

FIG. 4

Note 15: The following characteristics are typical of MCP performance, but can be expected to vary from sample to sample.

Note 16: These are nominal values, selected by the user, depending on the voltage applied across the MCP.

Note 17: To obtain the nominal operating MCP gains listed above, these applied voltages must be experimentally adjustable. The voltages listed here are typical for the gains listed above. Each PMT manufactured by ITT is supplied with an individual gain voltage calibration curve. An MCP PMT should NOT be operated at these listed voltages unless the gain voltage calibration curve confirms proper operating gain.

Note 18: This voltage can be easily and rapidly changed for all-electronic gating purposes. Gating times as low as 1-3 ns are achievable, depending on the characteristics of the external gate circuits, which must be capable of charging and discharging the associated photocathode-to-MCP capacitance. If fast gating is required, the tube can be supplied with a suitable low impedance photocathode.

MCP PMTs can also be supplied with an ionbarrier film over the input to the MCP, which protects the photocathode from ion sputter damage, and thus lengthens tube life (by factors of 100 or more) when operating at high average anode current density. In this configuration, the photocathode to MCP voltage should be increased to 600-800V to assure proper electron penetration of this film.

Note 19: The higher anode voltage should be used for high peak current or fast response applications.

Note 20: The total charge per pulse and the pulse repetition rate must meet the restrictions noted below.

Note 21: For linear response to a photocathode-flooding input flux pulse.

Note 22: For MCPs with lower strip currents, this current will be proportionally reduced. This DC current limit establishes the maximum permissible repetition rate for high peak current pulses.

Note 23: For 3 nc pulses. (flooded input):

Note 24: For a Point Source Optical Image on the Photocathode.

Note 25: For 3 kV MCP-anode voltage and fast, low capacitance, coaxial tube socket.

Note 26: An output pulse (observed by EGG/LASL/LLL) on an F4129, including time spread in the tube sockets, cables, light source and sampling circuits.

Note 27: With activated multialkali cathode. The MCP-orginating dark count, with the photocathode cooled or electrically biased-off is approximately:

Note 28: For typical multialkali cathodes.

Note 29: This is the ratio of the peak in the observed pulse height distribution (Fig. 4) to the valley. Operation of the bias discriminator level of the pulse counting circuits at this valley position (usually 50% of the peak) is recommended, and gives the dark count rates listed above.

Note 30: The width of the pulse height distribution has not yet been determined for the F4126 and F4128.

Note 31: Ratio of output single electron counts to photoelectrons incident on the MCP.

Note 32: Ratio of the anode signal-to-(noise-in) signal power ratio to the signal-to-(noise-in)-signal power ratio for the photoelectrons incident on the MCP.

Note 33: For an overall responsivity (gain times cathode sensitivity) loss of 50% and no MCP film. This is the total charge density accumulated at the anode. Increases by about 100 times (to 2 c/cm^2) for filmed MCPs. Tube life is partially increased by raising the MCP voltage to compensate for MCP gain losses (a recommended procedure). Tube life in seconds can be obtained by dividing the tube life in coulombs/cm^2 by the average anode current in amperes/cm^2.

PHOTOTUBE HOLDERS

Type F-4545

The F-4545 phototube holder is designed to accomodate the F-4126, F4128, or F-4129 microchannel plate photomultiplier tubes. The holder provides an excellent way of isolating the anode into a standard shielded termination, as well as a convenient means for mounting the tube.

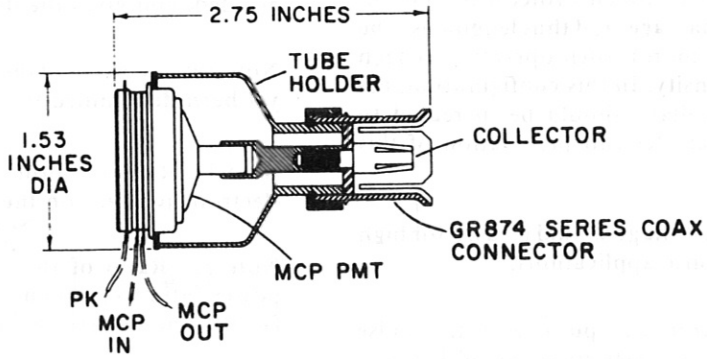

ELECTRO-OPTICAL PRODUCTS DIVISION ITT
Tube and Sensor Laboratories, Fort Wayne, Indiana 46803

ITT ELECTRO-OPTICAL PRODUCTS DIVISION

TECHNICAL NOTE NO. 127

PARAMETERS PERTAINING TO MICROCHANNEL PLATES AND MICROCHANNEL PLATE DEVICES

E. H. Eberhardt August, 1980

PURPOSE:

The purpose of this technical note is (a) to tabulate and define a set of parameters useful in describing the performance of microchannel plates and microchannel plate devices, (b) to show how these parameters are functionally interrelated, and (c) to give numerical estimates of the magnitudes of these parameters as they pertain to the specific types of MCP photomultiplier tubes and MCP image tubes manufactured by ITT.

INTRODUCTION:

The microchannel plate (MCP) is essentially a glass disc or wafer penetrated by a large number of holes or channels of uniform microscopic diameter. (See Fig. 1) By applying a potential difference between faces of this disc and thus between the ends of each channel, an electron-accelerating electric field is established within each channel. Upon excitation by bombarding input electrons, the resulting emitted secondary electrons are caused to cascade down each channel causing repetitive secondary emission amplification as they encounter the channel walls. The net result is substantial electron image amplification between the input and output of the MCP over a distance typically less than 1 mm. A semiconducting layer is formed on the inner channel walls to supply the required amplified secondary electrons while maintaining the proper internal electric field in each channel.

The resulting electron amplifying device has proven to be so successful that it is now being used in a wide variety of electron devices and can be expected to be used in even more devices in the future.

UNITS AND SYMBOLS:

Unless otherwise specified, all parameters in this technical note are expressed in MKS units or decimal fractions thereof. The computer symbolism, e.g. "1.0E5", is used instead of the powers of ten designation, e.g. "1.0×10^5". The special symbol "=*" is used to designate the approximate numerical magnitude of a parameter as it pertains to the 18 mm diameter type of MCP now being manufactured by ITT and used in the F4126, F4128 and F4129 series of MCP photomultiplier tubes, and in the F4111, F4747, F4748, F4758, F4785 and F4786 series of MCP image intensifier tubes. (MCP devices are also available with 25 mm and 40 mm active diameter MCPs.)

CAUTIONARY NOTE:

The presently available information on MCPs, both experimental and theoretical, does not permit an accurate estimate to be made of all performance characteristics. The functional relationships and numerical data presented in this technical note must, therefore, be considered to be approximate only and not as a specification on MCP device behavior. In addition, the numerical values of many MCP parameters can be expected to vary considerably from sample to sample.

1.0 MCP GEOMETRY

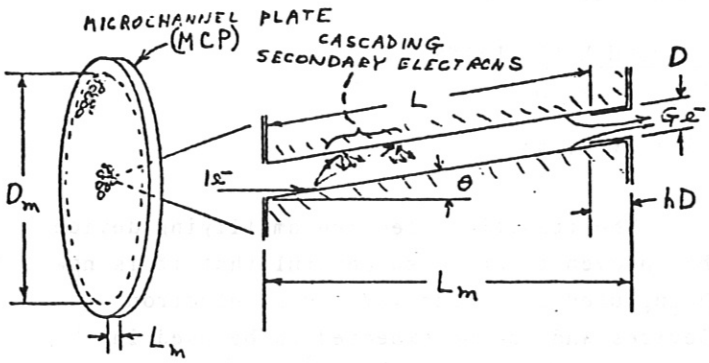

Fig. 1

The geometric parameters associated with the size, shape and distribution of the channels in an MCP can be described as follows:

1.1 Channel Diameter, D

=* 12.5 μm

NOTE: The special symbol, "=*", indicates a typical approximate numerical value of a parameter as it pertains to present ITT MCP devices using 18 mm diameter MCPs.

1.2 Channel Length, L

= effective electron-multiplying length of each MCP channel

=* 0.5 mm

NOTE: The effective length, L, is less than the total physical length because of end-spoiling. (See 1.4)

1.3 Length-to-Diameter ("L-over-D") Ratio, α

= channel aspect ratio

= ratio of channel length-to-channel diameter

= L/D =* 40

1.4 End-Spoiling Ratio, h

= relative insertion distance, in channel diameters, of the conductive electrode on the face of the MCP (See Fig. 1)

=* 1.5 diameters (typical value)

1.5 Bias Cut Angle, θ

= angle between the axis of the channels and the normal to the face of the MCP (See Fig. 1)

=* 5^o

1.6 MCP Plate Thickness, L_m (See Fig. 1)

= $(L + hD)\cos\theta$ $(\simeq L)$

=* 0.51 mm

1.7 Center-to-Center Channel Spacing, D_{cc}

=* 15 μm

NOTE: The channels are arranged in a hexagonal closed packed structure. (See Fig. 2)

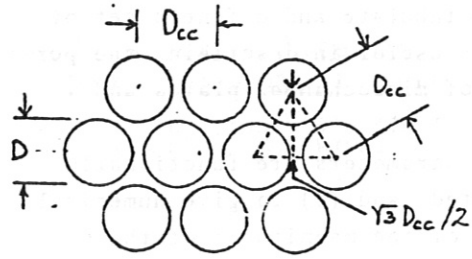

Fig. 2

1.8 Open Area Ratio, Y_o

= ratio of channel area to MCP web face area

= $(\pi 2\sqrt{3})(D/D_{cc})^2$ =* 0.63

NOTE: This is the geometrical, or optical open area ratio for the MCP. The effective electron open area ratio, Y_e, (see 4.15) may be greater or less than Y_o depending on the contribution to the output current from secondary electrons generated at the web areas, losses of electrons entering the channels, etc.

1.9 MCP Active Diameter, D_m

= diameter of the effective electron-multiplying area of the MCP (See Fig. 1)

=* 18 mm

NOTE: The physical diameter of an MCP is greater than D_m to provide a border area (with or without channels) for mounting the MCP. MCPs with larger active diameters (e.g. 25 mm and 40 mm) are also available.

1.10 MCP Active Area, A_m

= $\pi D_m^2/4$ =* 2.5 cm^2 (See 1.9)

1.11 Channel Packing Density, ρ_m

= number of channels per unit surface area of the MCP

= $2/\sqrt{3}D_{cc}^2 = 1.15/D_{cc}^2$ =* 5.1E5 channels/cm^2

NOTE: The "computer" designation, e.g. "5.1E5" is used in this technical note instead of the power law designation, e.g. "5.1×10^5".

1.12 Total Number of Active Channels per MCP, $A_m\rho_m$

$= (\pi/2\sqrt{3})(D_m/D_{cc})^2$

=* 1.3E6 channels per 18 mm MCP (See 1.9)

2.0 MCP STRIP CURRENT

When a voltage difference is applied between MCP faces a quiescent, no-signal "strip" current will flow between the electrodes deposited on the faces of the MCP. This quiescent strip current is associated with the following parameters:

2.1 MCP Strip Resistance per Unit Area, R_m

=* 8E8 ohms per 1 cm^2 area

NOTE: The magnitude of this strip resistance per unit area can be expected to vary appreciably from MCP sample to sample.

2.2 Total Strip Resistance, R_s

$= R_m/A_m$ = resistance between MCP faces

=* 3.2E8 ohms (for 18 mm diameter MCP)

2.3 Resistance per Channel, R_c

$= R_m\rho_m$ =* 4.1E14 ohms/channel (See Fig. 3)

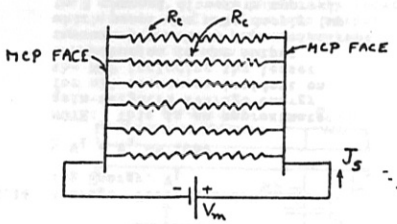

Fig. 3

2.4 MCP Applied Voltage, V_m

=* 800V (for ≈ 750 gain)

NOTE: The exact voltage, V_m, required for a given gain depends upon the past history of the MCP, method of manufacture, etc. (See 3.18)

2.5 Strip Current Density, J_m

$= V_m/R_m$

=* 1.0 μA/cm^2 (at 800V, see 2.1 and 2.4)

2.7 MCP Strip Power Density, U_m

$= J_mV_m$ =* 8E-4 W/cm^2 (at 800V)

NOTE: The strip power density to the MCP must be restricted in magnitude to prevent thermal damage.

2.8 MCP Electric Field, E_m

$= V_m/L$ =* 1.6E6 V/m (at V_m = 800V)

2.9 MCP Electrode Resistance, R_e

= resistance per square of the surface electrodes on the MCP

=* 0.1 - 100 ohms/square

NOTE: The magnitude of this resistance determines how rapidly the elctric field, E_m, can be modified for changing gain or gating the MCP.

3.0 MCP GAIN

The cascaded flow of electrons within each MCP channel is sufficiently complex in electron position, angle and energy, that the resultant ratio of output current to input current (the MCP gain) cannot be exactly predicted. However, the observed gain vs. voltage behavior of MCPs suggests that the flow of electrons in the MCP channels tends to be "dynodized", i.e. confined to nearly fixed average distances between consecutive electron encounters with the MCP walls. (See Fig. 4 and Reference 10.1)

Insofar as this dynodized behavior is indeed valid, the following gain and gain-related parameters are useful in predicting the approximate performance of MCPs and MCP devices:

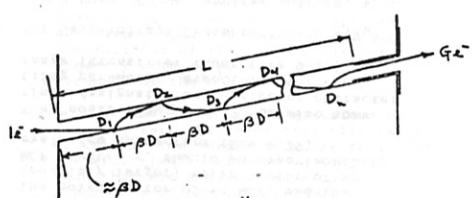

Fig. 4

3.1 Input Current, I_i

= average DC input current to the active area of the MCP

= SF (See 7.0)

3.2 Output Current, I_a

= average DC output current emitted by the MCP

$= GI_i$

3.3 MCP Gain, G

$= I_a/I_i$ =* 750 A/A
(for V_m = 800V, V_i = 150V)
(See also 2.4 & 3.18)

3.4 Dynode Spacing Ratio, β

= average axial distance, in channel diameters, between successive wall encounters. during the electron multiplication process.

= a key MCP characterizing parameter (See 3.17)

$= \frac{1}{2}(V_z/V_{on})^{\frac{1}{2}}$

=* 2.0 channel diameters (typical)

3.5 Voltage Increment per "Dynode", V_z

= average energy gain in volts between wall encounters

$= \beta DE_m = \beta V_m/\alpha = V_m/n$

=* 40V (for V_m = 800V)

3.6 Average Normal Emission Energy Component, V_{on}

= average emission energy component in volts, in a direction normal to the MCP wall surface, for the emitted secondary electrons

$= V_z/4\beta^2$ =* 2.5eV (for V_m = 800V)

NOTE: This postulated direct proportionality between V_{on} and V_z is not characteristic of secondary electron emission at normal (not grazing) incidence, but is consistent with the observed shape of the gain/voltage characteristic of MCPs and, therefore, with the "dynodized" flow of secondary electrons in MCPs. It assures a constant magnitude for the spacing ratio, β, and a constant number of dynodes, n, regardless of the applied voltage, V_m. (See Reference 10.1)

3.7 Average Tangential Emission Energy, V_{ot}

$\simeq V_{on}$ =* 2.5eV (for V_m = 800V)

3.8 Average Incident Angle, ϕ

$= \cot^{-1}2\beta = \tan^{-1}(V_{on}/V_z)^{\frac{1}{2}}$

=* 14°

3.9 Average Number of "Dynodes", n

= average number of wall encounters for a primary photoelectron entering an MCP channel (See Fig. 4).

$= L/\beta D = \alpha/\beta$ =* 20 dynodes (for α = 40)

a key MCP characterizing parameter

3.10 First Crossover Potential, V_c

= incident electron energy in volts (for an electron incident on the MCP wall at an angle ϕ) giving unity secondary emission ratio.

=* 22V (a secondary emission materials parameter characterizing the MCP channel wall surface.)

3.11 Average Gain/Stage, σ (See Fig. 5)

$= (V_z/V_c)^k = (V_m/nV_c)^k$

=* 1.35 (for k = 0.5, V_c = 22V & V_m = 800V)

NOTE: This power law approximation for σ vs. V_z for small V_z with k = ½ has been confirmed experimentally for the wall materials (H_2-reduced Pb glass) typically used in manufacturing MCPs. Specific experimental confirmation is needed for the particular incident angles encountered in operating MCPs. (See 3.8).

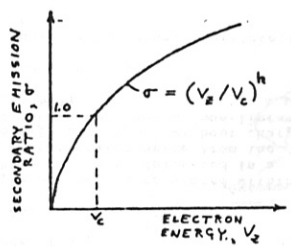

FIG. 5

3.12 Secondary Emission Curvature Coefficient, k

= exponent of the function of the secondary emission ratio, σ, versus the incident energy, V_z, (See Fig. 5). Assumed to be a constant for the type of wall materials used in manufacturing MCPs.

=* 0.5

3.13 Input Electron Energy, V_i

= applied photocathode voltage

= energy of the electrons incident on the front surface of the MCP, or entering the MCP channels, in electron volts (See Fig. 6).

=* 150V (typical for MCP photomultiplier tubes)

NOTE: The experimentally selected magnitude of V_i represents a somewhat arbitrary compromise between gain, ease of gating, resolution, field emission, etc.

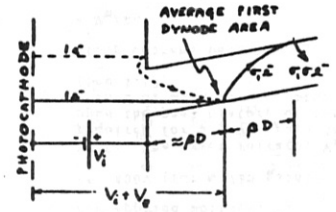

Fig. 6

3.14 Average "First Dynode" Bombarding Energy, V_1

$\simeq V_i + V_z$ =* 190V

NOTE: This is an approximate gain-weighted average energy for all electrons incident on the MCP including the lesser contribution to the output current from those input electrons which penetrate more deeply (up to 8 channel diameters approximately) into the channels. (See Fig. 7). In effect, the average electron skips one dynode spacing, δD, before striking the channel walls.

3.15 Average "First Dynode" Gain, σ_1

$= (V_i/V_c)^k = \left[(V_i + V_z)/V_c\right]^k$

$= \left[(V_i/V_c) + (V_m/nV_c)\right]^k$

=* 2.9 A/A (for V_i = 150V, V_c = 22V, V_m = 800V, n = 20, k = 0.5)

NOTE: This is a rough approximation only and does not include the contribution to the gain process of web-generated secondary electrons.

3.16 Electron Open Area Ratio, Y_e

= MCP "collection efficiency"

= fraction of input electrons entering a channel directly and causing an output current, or generating secondary electrons at the web which then enter a channel and cause an output current.

=* 0.85

NOTE: This ratio, Y_e, is typically greater than the geometrical open area ratio, Y_g, (See 1.8), because of the contribution to the gain process from web-generated secondary electrons (dashed electron trajectories in Fig. 6).

3.17 MCP Noise Factor, κ_m

= MCP input signal-to-noise power ratio divided by the MCP output signal-to-noise power ratio.

$\simeq \sigma_1/(\sigma_1 - 1)Y_e$

=* 1.8 (for 3.15 conditions)

NOTE: This is an estimate of the minimum possible noise factor based on idealized Poisson statistics for the electron amplification process. The noise factor of an MCP, and the (possibly larger) noise factor of an MCP device, κ, should be experimentally evaluated parameters (See 9.29).

The "noise figure", $\kappa_m^{1/2}$, is also sometimes designated as a detector characterizing parameter, especially for MCP image intensifier tubes (See 9.30).

3.18 MCP Gain-Voltage Characteristic, $G(V_m)$

= MCP gain, G, vs. applied voltage, V_m

$= Y_e\sigma_1\sigma^{n-1}$ ("dynode" law)

$= Y_e\left[(V_i + V_z)/V_c\right]^k(V_z/V_c)^{k(n-1)}$

$= Y_e\left[(V_i/V_c) + (V_m/nV_c)\right]^k(V_m/nV_c)^{k(n-1)}$

=* $(0.85)(6.8 + V_m/440)^{1/2}(V_m/440)^{9.5}$

(for Y_e = 0.85, V_i = 150V, V_c = 22V, n = 20, k = 1/2)

NOTE: The following table shows the computed values of σ_1, σ, and G for the listed values of the applied MCP voltage, V_m, and the above values of the controlling parameters. Also included are the values of σ_1, σ, and G after the MCP gain has been degraded by an increase in the first crossover voltage, V_c, from 22V to 24V, as a result of operational life of the MCP (See Fig. 7).

V_m (volts)	V_c (volts)	σ_1 (A/A)	σ (A/A)	G (A/A)
600	22	2.86	1.17	46
650	22	2.88	1.22	100
700	22	2.90	1.26	203
750	22	2.92	1.31	393
800	22	2.94	1.35	730
850	22	2.95	1.39	1308
900	22	2.97	1.43	2270
600	24	2.74	1.12	19
650	24	2.76	1.16	42
700	24	2.78	1.21	85
750	24	2.80	1.25	165
800	24	2.81	1.29	305
850	24	2.83	1.33	550
900	24	2.85	1.37	950

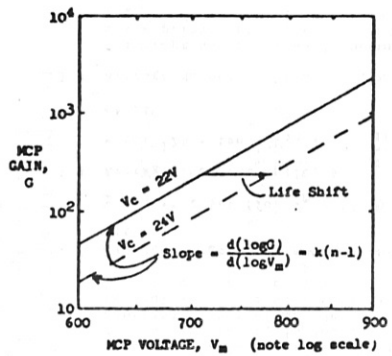

FIGURE 7

4.0 MCP TRANSIT TIME:

Insofar as the electron flow in MCPs is "dynodized" (see 3.0) a prediction of the approximate transit time characteristics of the cascaded flow, as well as related properties of the MCP, is possible as follows:

4.1 Average Wall-to-Wall Transit Time, t_d

= time for the average secondary electron emitted from one point on the MCP wall to transit to the opposite wall (see Fig. 8).

$= D(2\alpha\beta m/eV_m)^{1/2}$

=* 13 ps (e/m = 1.76E11 C/kG)

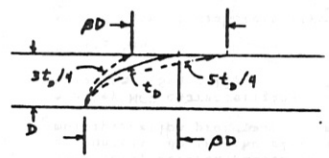

Fig. 8

4.2 Overall MCP Transit Time, t_m

= time delay between an MCP-entering electron and the resultant output charge pulse

$= nt_d$ =* 270 ps

4.3 Average Wall-to-Wall Transit Time Spread, Δt_d

= $t_d/2$ =* 6.5 ps

NOTE: A time spread of $\frac{1}{2}t_d$ is assumed to be characteristic of the ensemble of secondary electrons leaving a single MCP emission point (see Fig. 8). This time spread is consistent with the observed overall response time measurements of MCP devices. A more reliable estimate of the time spread will require detailed experimental data on the emission properties of the secondary electrons under the somewhat unusual grazing incidence conditions encountered in MCPs.

4.4 Overall Transit Time Spread, Δt_m

= time width of the triggered output charge pulse for one electron input

$= n^{1/2}\Delta t_d$ =* 30 ps

NOTE: Assumes uncorrelated time dispersion properties between consecutive wall encounters. Focusing between pairs of wall encounters (see Ref. 10.1) would reduce the magnitude of Δt_m.

4.5 Stored Charge Density, q_m

= charge per unit area stored within the MCP which can be delivered in a single output charge pulse from the MCP (for flooded input) without charge saturation or input-output non-linearity (see also 6.3).

=* 1 nanocoulomb/cm^2

NOTE: Approximate value, experimentally determined.

4.6 Stored Charge per Channel, q_c

= q_m/ρ_m =* 2E-15 C/channel

=* 1.2E4 e^-/channel =* 12,000 e^-/channel

NOTE: This is the approximate maximum delivered charge from a single channel with all channels simultaneously emitting and the output current linearly proportional to the input current and the time of delivery of the charge short compared to the recovery time, t_{rec} (see 4.10). Significantly larger charges per channel can be delivered in the single electron counting mode of operation (see 5.0) in which all channels are not simultaneously emitting charge.

4.7 Peak Output Current Density, J_p

= $q_m/\Delta t_m$ =* 30 A/cm^2

NOTE: This is the maximum output current density (with flooded input) based on the transit time spread, Δt_m, within the MCP and does not include the current density limits which may be imposed by space charge internal to the MCP channels.

4.8 Maximum Linear DC Output Current Density, J_{max}

- fraction of the strip current density, J_s, above which input-output non-linearity (with flooded input) is observed

-* $J_s/4$ -* 2.5E-7 A/cm^2

4.9 Maximum Linear Current Pulse Repetition Rate, J_{max}/q_m

- maximum rate at which charge pulses of amplitude, q_m, can be generated by an MCP

- J_{max}/q_m -* 250 Hz

NOTE: Smaller charge pulses permit proportionately faster repetition rates.

4.10 MCP Current Pulse Recovery Time, t_{rec}

- average time between regularly occurring current pulse of charge magnitude, q_m, under the maximum DC output current conditions (see 4.8 & 4.9)

- average time for the MCP to recover from the maximum output charge density pulse, q_m

- q_m/J_{max} -* 4 ms

4.11 Last Dynode Recharge Resistance per Channel, R_{rec}

- $R_c/(n+1)$ (see Fig. 9)

-* 2E13 ohms/channel

NOTE: Assumes that the stored charge per channel, q_c, is physically located one dynode spacing from the output electrode, a useful over-simplification of MCP behavior.

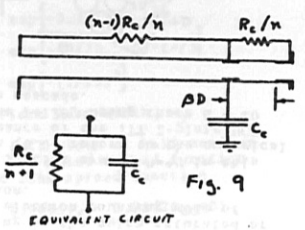

Fig. 9

4.12 Last Dynode Capacitance per Channel, C_c

- t_{rec}/R_{rec} -* 2E-4 pf/channel

4.13 Last Dynode Storage Capacitance Donsity, C_d

- $C_c\rho_m$ -* 100pf/cm^2

NOTE: C_d can also be estimated from the face-to-face capacitance, C_m, of the MCP as follows:

- nC_m -* 140pf/cm^2 (see 4.15)

4.14 Last Dynode Maximum Linear Voltage Shift, ΔV_d

- voltage shift on the MCP wall as a result of emitting q_c charge from each channel

- q_m/C_d -* 10V (-* 25% of V_z)

NOTE: Larger wall potential shifts can be expected to lead to non-linearity due to modification of the internal electric field and resultant disruption of the normal cascade gain process.

4.15 MCP Face-to-Face Capacitance Density, C_m

- $A_1\left[K_g(1-Y_o) + Y_g\right] \epsilon_o/L_m$

-* 7.1pf/cm^2

NOTE: A_1 = 1 cm^2 = 1E-4m^2, K_g = dielectric constant of the MCP glass = 8.3, Y_o = 0.63 and ϵ_o = 8.854E-12 MKS units.

5.0 MCP IMAGE TRANSFER:

The geometric fidelity of the electron image transfer between faces of the MCP can be approximately described in terms of the modulation transfer function (MTF). Alternatively, either the point spread function or the line spread function can be specified (see Ref. 10.2).

For a non-isoplanatic image transfer device such as an MCP having discrete image elements arranged in a quasi-geometric configuration, these image transfer functions are not single valued but depend upon the exact orientation and position of the image-analyzing test geometry with respect to the discrete elements of the MCP array.

This ambiguity can be minimized by assuming that the input test slit image as well as the image-analyzing test slit are effectively infinite in length such that all possible physical displacements of the discrete MCP elements (i.e. the channels) are equally likely (see Fig. 10). The following image transfer properties of MCPs and MCP devices are based on this "long slit" test configuration assumption.

The image transfer functions given below for MCPs with round channels are also applicable to fiber optic faceplates with round fibers (and minimal crosstalk).

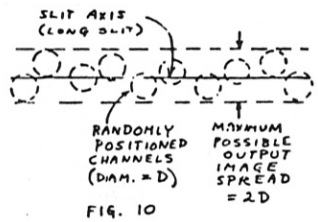

FIG. 10

5.1 MCP Modulation Transfer Function, $M_m(f)$

- $\left[2J_1(\pi fD)/\pi fD\right]^2$ (see Ref. 10.3)

where $J_1(\pi fD)$ is the Bessel function of the first kind, of argument πD, and f is the spatial repetition frequency.

NOTE: This is the calculated MTF (see Ref. 10.3) of an idealized round element image transfer device, such as a round channel MCP or a round fiber optic plate, for the "long slit" test condition in which all physical displacements of the round image elements from the slit image axis are equally probable (see 5.0). This long slit MTF can be approximated by the following Gaussian-shaped MTF exactly matching the long slit Bessel function MTF at the maximum spatial resolution frequency, f_m, at which the MTF has a magnitude of 4% (see Fig. 11):

$M_m(f)$ (Gaussian approximation)

- $\exp(-3.33f^2D^2)$

-* $\exp\left[-(f/44)^2\right]$ (f in line pairs/mm)

5.2 MCP Resolution, f_m (see Fig. 11)

- spatial pattern repetition frequency for which the MTF has 4% amplitude

- 0.983/D (= D^{-1})

-* 80 line pairs/mm

NOTE: 4% is approximately the minimum visually resolvable pattern modulation.

Fig. 11

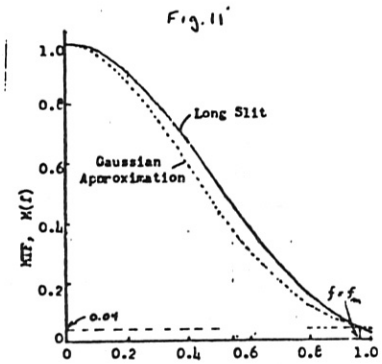

5.3 MCP Beam Width, w_m (see Fig. 12)

- full width at half maximum of the point spread and line spread function (see 5.4 & 5.5)

- 0.961D (= D)

-* 12 um

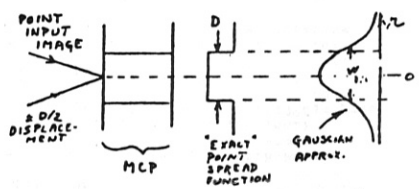

Fig. 12

5.4 MCP Point Spread Function, $P_m(r)$

- $P_m(0)\exp(-3r^2/D^2)$

-* $P_m(0)\exp\left[-(r/7.2)^2\right]$

where $P_m(0)$ is the normalizing peak output image density, and r is the radial displacement from the image center.

NOTE: Derived from the Gaussian approximation for the long slit MTF (see 5.1).

5.5 MCP Line Spread Function, $L_m(x)$

- $L_m(0)\exp(-3x^2/D^2$

-* $L_m(0)\exp\left[-(x/7.2)^2\right]$

where $L_m(0)$ is the normalizing peak output image density and x is the physical displacement from the axis of the slit image.

NOTE: Derived from the Gaussian approximation for the long slit MTF (see 5.1).

6.0 Z-PLATE MCP:

By stacking three straight-channel bias-cut MCPs in face-to-face cascade (see Fig. 13) the gain of the combined MCPs can be increased to the point where a single input electron can trigger the emission of a nearly-constant amplitude (i.e. "saturated") output charge pulse. The resulting "Z-Plate" MCP can then be said to be operating in the pulse saturated or single electron counting mode of operation.

The special symbol "=*" in this section (6.0) refers to the numerical performance of the ITT Z-plate MCP PMT, the F4129, using three α = 40 MCPs in cascade.

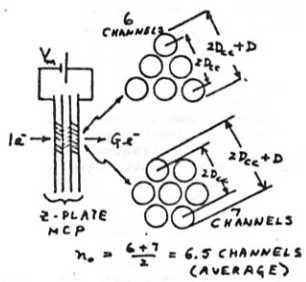

FIG. 13

6.1 Average Number of Output Channels, n_o

=* 6.5 (see Fig. 13)

NOTE: For randomly oriented stacking of three MCPs, the number of output channels excited by a single input electron can range from as low as one (for exact MCP alignment) to as many as 13. The triangular configuration of six channels and the hexagonal configuration of seven channels, shown in Fig. 13, are the most likely, yielding the average number of 6.5.

6.2 Output Charge per Incident Electron, Q_o

= a statistically variable parameter for each incident electron (see Fig. 14)

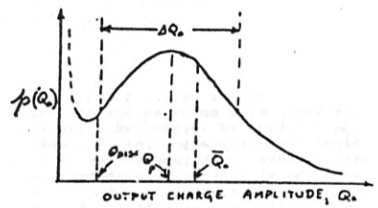

Fig. 14

6.3 Average Output Charge per Incident Electron, $\bar{Q}_o$ (see Fig. 14)

= MCP gain

=* 1.1E6 e^-/e^- (at V_m = 2400V and pulse saturated conditions)

6.4 Most Probable Output Charge, Q_p (see Fig. 14)

= $0.9\bar{Q}_o$ =* 1E6 e^-/e^- (see 6.3)

6.5 Average Output Charge per Channel, $\bar{Q}_o/n_o$

=* 1.7E5 e^-/e^- (see 6.3)

NOTE: The average charge per channel, $\bar{Q}_o/n_o$, emitted by the MCP in the charge saturated condition is approximately 15x greater than the charge per channel available in the linear current pulse mode of operation (see 4.6) where all MCP channels are simultaneously emitting charge. This larger output charge per channel is supplied, at least in part, by the lateral capacitance between the group of n_o channels emitting charge in the saturated mode, and the adjacent quiescent channels. The gain of these adjacent channels is, therefore, temporarily suppressed following a saturated charge pulse. This does not cause count rate non-linearity provided that sufficient time is allowed between saturated output charge pulses for the channel walls to return to the quiescent operating potential. (see 6.22 and 6.23)

6.6 Pulse Height Distribution, $p(Q_o)$ (Fig. 14)

= probability distribution of the output charge pulses for single input electrons

NOTE: The shape of the measured pulse height distribution for a given MCP will depend upon the applied voltage, V_m, the history of the MCP, the method of pulse shaping in the external circuits, etc.

6.7 Peak-to-Valley Ratio, r_{pv}

= ratio of the peak of the $p(Q_o)$ distribution, Fig. 14, to the valley of the distribution occurring for Q_o less than Q_p

=* 2.5 (for V_m = 2400V) (see 6.6)

6.8 Width of the Pulse Height Distribution, ΔQ_o

= full width at half maximum of $p(Q_o)$ (see Fig. 14)

≈ Q_p (for saturated output pulses)

6.9 Pulse Height Resolution, $\Delta Q_o/Q_p$

=* 1.00 (i.e. 100%) (at V_m = 2400V)

6.10 Electron Counting Efficiency, P_e

= probability that an electron incident on the MCP produces an output charge pulse whose amplitude exceeds a fixed bias discriminator level, Q_{disc}

= $\int_{Q_{disc}}^{\infty} p(Q_o)dQ_o$

=* 0.75 (for $Q_{disc} = Q_p/2$) (see 6.11)

6.11 Bias Discriminator Level, Q_{disc}

= selected minimum charge amplitude in the external charge pulse counting circuits below which no charge pulse is counted.

= $Q_p/2$ =* 5E5 e^- (for V_m = 2400V)

NOTE: The magnitude of Q_{disc} is somewhat arbitrarily selected by each MCP device user, with the selection depending on the magnitude of P_e desired, the tolerable number of dark counts, etc.

6.12 Maximum Electron Counting Efficiency, $P_{e,max}$

= probability of an incident electron producing a countable output charge pulse of any amplitude

= $\int_0^{\infty} p(Q_o)dQ_o$ = Y_e (see 3.16)

=* 0.85

NOTE: This maximum electron counting efficiency can only be approached experimentally since all practical counting circuits produce spurious dark counts (i.e. amplifier noise, etc.) If no channel-entering electrons were lost and no electrons striking the web areas of the MCP produce secondary electrons (which could enter a channel and be counted) then $P_{e,max}$ would equal the geometric open area ratio, Y_o (see 1.8).

6.13 Probability of a Missed Electron, p(0)

= $1-P_{e,max}$ = $1-Y_e$

=* 0.15

6.14 Input Photoelectron Rate, r_e

= rate at which photoelectrons from an input photocathode of responsivity ratio, S, subjected to an incident flux, F, are incident on the MCP (see 7.1 and 7.2)

= I_i/e = SF/e (e = 1.6E-19 C)

6.15 Output Photoelectron Counting Rate, r_a

= $r_e P_e$

6.16 Dark Counting Rate, r_d

= output counting rate with F = 0

=* 5E3 cts/sec·cm^2 (conventional multialkali photocathode at 23°C)

6.17 MCP Dark Counting Rate, $r_{d,m}$

= output counting rate with photocathode biased off, i.e. V_i negative

=* 10 cts/sec·cm^2 (cesiated sealed off MCP PMT)

NOTE: $r_{d,m}$ can be expected to vary considerably from tube sample to tube sample.

6.18 Total Signal Count, N_s

= $r_a t_s$ (for counting time t_s)

6.19 Signal Counting Time, t_s

= total time for the accumulated signal count, N_s

6.20 Signal Count Variance, ΔN_s

= $N_s^{1/2} = (r_a t_s)^{1/2}$ (Poisson variance)

6.21 Maximum Linear Count Rate Density, $r_{a,max}$

= $J_{max}/e\bar{Q}_o$ =* 1.4E7 cts/sec·cm^2 at V_m = 2400V

6.22 Maximum Linear Count Rate per n_o Channel Group, $r_{a,n}$

= $n_o r_{a,max}/\rho_m$ =* 18 cts/sec·group

NOTE: This is the approximate maximum linear count rate for a point source input to the MCP in the saturated mode of operation.

6.23 Pulse Recovery Time, T_s

= time for a group of n_o output channels to recover from emission of a saturated output charge

= $r_{a,n}^{-1}$ =* 55ms

NOTE: This is an estimate only based on known strip current limits (see 6.21)

6.24 Effective Channel Diameter, D_{eff}

= diameter of the average emitted charge from the Z-plate MCP

= $2D_{cc} + D$ (see Fig. 13) =* 42.5 μm

NOTE: The two output channel patterns shown in Fig. 13 are the most probable patterns for random overlapping of three MCPs.

6.25 Maximum Z-Plate Spatial Resolution, f_z

= spatial frequency for 4% modulation transfer

= $0.983/D_{eff} = 0.983/(2D_{cc}+D)$

=* 23 line pairs/mm

NOTE: Assumes a Gaussian-shaped MTF (see 5.1 and Fig. 11)

6.26 Z-Plate MTF, $M_z(f)$

= $\exp\left[-3.2(f/f_z)^2\right]$

= $\exp\left[-10(2D_{cc}+D)^2 f^2/3\right]$

=* $\exp\left[-(f/13)^2\right]$

6.27 Z-Plate Beam Width, w_z

= full width at half maximum of the point spread function and line spread function

= $0.96D_{eff} = 0.96(2D_{cc}+D)$

=* 41 um

6.28 Z-Plate Point Spread Function, $P_z(r)$

= $P_z(0)\exp\left[-2.77(r/w_z)^2\right]$

= $P_z(0)\exp\left[-3r^2/(2D_{cc}+D)^2\right]$

=* $P_z(0)\exp\left[-(r/24.5)^2\right]$

6.29 Z-Plate Line Spread Function, $L_z(x)$

= $L_z(0)\exp\left[-2.77(x/w_z)^2\right]$

= $L_z(0)\exp\left[-3x^2/(2D_{cc}+D)^2\right]$

=* $L_z(0)\exp\left[-(x/24.5)^2\right]$

7.0 MCP INPUT:

When an MCP is used as the electron multiplier in a PMT or as an image amplifier in an image tube, the photocathode and input gap contribute significantly to the net performance. The following information pertains to proximity-focused MCP devices in which the photocathode is placed as close as possible to the input surface of the MCP (see Fig. 15). The spreading of the photoelectrons in the input gap between the photocathode and MCP is treated in Ref. 10.4.

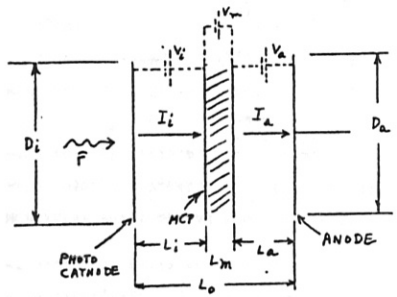

Fig. 15

7.1 Input Flux, F

= input flux causing photoemission within the active photocathode diameter, D_i

F_e = input flux measured in watts

F_q = input flux measured in photons/sec

F_v = input flux measured in lumens (usually reserved for CIE source A, a tungsten lamp operated at 2854K color temperature)

7.2 Photocathode Responsivity, S

= I_i/F

$S_e = I_i/F_e$ (A/W)

$S_q = I_i/F_q$ (C/photon)

$S_v = I_i/F_v$ (A/lumen) (see 7.1)

NOTE: The magnitude of the responsivity, S, depends upon the particular spectral distribution of the flux, F. $S_q/e = I_i/eF_q$ = quantum efficiency of the photocathode in electrons/photon.

7.3 Photocathode-to-MCP Spacing, L_i

=* 0.2mm

NOTE: 0.2mm is a compromise spacing based on electron beam spreading, electric field limitations, mechanical tolerance restrictions, etc.

7.4 Photocathode-to-MCP Electric Field, E_i

= V_i/L_i

=* 7.5ES V/m (for V_i = 150V)

7.5 Peak Input Current Density, $J_{p,i}$

= $(2.33E\text{-}6)V_i^{3/2}/L_i^2$ (the space charge limit)

=* 11A/cm²

7.6 Active Photocathode Diameter, D_i

= D_m =* 18 mm (see 1.9)

7.7 Input Capacitance Density, C_i

= $\epsilon_o A_1/L_i$

=* 4.4 pf/cm²

7.8 Photocathode-MCP Transit Time, t_i

= $(2m/eV_i)^{1/2}L_i$

=* 55 ps (for V_i = 150V)

7.9 Photocathode-MCP Transit Time Spread, Δt_i

= transit time difference between a photoelectron emitted at rest and an electron emitted with the average axial emission energy, V_{iz}

= $(2mV_{iz}/e)^{1/2}L_i/V_i$

=* 1.7 ps (for V_i = 150V and V_{iz} = 0.14eV see Ref. 10.4)

7.10 Average Tangential Photoelectron Emission Energy Component, V_{it}

=* 0.14 eV (2854K radiation, multialkali photocathode, see Ref. 10.4)

7.11 Average Normal Photoelectron Emission Energy Component, V_{in}

= V_{it} =* 0.14 eV (see 7.10)

7.12 Photocathode-to-MCP Modulation Transfer Function, $M_i(f)$

= $\exp(-4\pi^2 L_i^2 f^2 V_{it}/V_i)$ (Ref.10.4)

=* $\exp\left[-(f/26)^2\right]$ (f in line pairs/mm)

7.13 Photocathode-to-MCP Resolution, f_i

= spatial frequency for 4% modulation

= $0.29(V_i/V_{it})^{1/2}/L_i$ (see Ref. 10.4)

=* 47 line pairs/mm

7.14 Photocathode-to-MCP Point Spread Function, $P_i(r)$

= $P_i(0)\exp(-r^2V_i/4L_i^2V_{it})$

=* $P_i(0)\exp\left[-(r/12)^2\right]$ (r in um)

7.15 Photocathode-to-MCP Line Spread Function, $L_i(x)$

= $L_i(0)\exp(-x^2V_i/4L_i^2V_{it})$

=* $L_i(0)\exp -(x/12)^2$ (x in um)

7.16 Photocathode-to-MCP Beam Width, w_i

= full width at half maximum of $P_i(n)$ and $L_i(x)$ (see 7.14 & 7.15)

= $3.3L_i(V_{it}/V_i)^{1/2}$ =* 20 um

8.0 MCP OUTPUT:

In MCP devices, it is often convenient to place the anode in close proximity to the MCP output (see Fig. 15). This proximity focused configuration tends to retain the high speed, high peak current, low distortion and high spatial resolution of the MCP. The anode may consist of a single conductive disc (as in the F4126, F4128 and F4129 MCP PMTs), or a phosphor screen (as in the F4111, F4112 and F4113 MCP image tubes), or other configurations (such as the 10 x 10 array of anodes in the F4149 MCP PMT).

8.1 MCP-Anode Spacing, L_a

=* 0.3 mm (multi-anode MCP devices)

=* 1.3 mm (MCP PMTs and image tubes)

NOTE: The MCP-anode spacing is a compromise between the permissible electric field, electron beam spreading, space charge current limits, response time, etc.

8.2 MCP-Anode Voltage, V_a

=* 90V (multi-anode MCP devices)

=* 300V (photon counting MCP PMTs)

=* 1.5kV(ultra-fast MCP PMTs)

=* 5.5kV (MCP image tubes)

NOTE: The four voltages listed are characteristic of the four indicated applications of MCPs. Other applications may require other voltages.

8.3 Anode Diameter, D_a

=* 18 mm

8.4 MCP-Anode Electric Field, E_a

= V_a/L_a

=* 2.3E5 V/m (for V_a = 300V, L_a = 1.3 mm)

=* 3E5 V/m (for V_a = 90V, L_a = 0.3 mm)

=* 1.2E6 V/m (for V_a = 1.5kV, L_a = 1.3 mm)

=* 4.2E6 V/m (for V_a = 5.5kV, L_a = 1.3 mm)

8.5 Peak Output Current Density, $J_{p,a}$

= $(2.33E-6)V_a^{3/2}/L_a^2$

=* 8 A/cm^2 (for V_a = 1.5kV, L_a = 1.3 mm)

NOTE: Assumes thermionic (i.e. pessimistic) electron emission energies from the MCP, but does not include space charge limitations internal to the MCP.

8.6 MCP-Anode Capacitance Density, C_a

= $A_1\varepsilon_o/L_a$

=* 0.68 pf/cm^2 (ε_o = 8.85E-12 MKS units)

8.7 MCP-Anode Transit Time, t_a

= $(2m/eV_a)^{1/2}L_a$

=* 110 ps (for V_a = 1.5kV, L_a = 1.3 mm)

8.8 MCP-Anode Transit Time Spread, Δt_a (see Fig. 16)

= $(2mV_{mn}/e)^{1/2}L_aV_a^{-1}$

=* 21 ps (for V_a = 1.5kV and V_{mn} = 50V) and L_a = 1.3 mm

NOTE: Δt_a is the time difference between an electron emitted at rest and an electron emitted with the average normal emission energy component, V_{mn}.

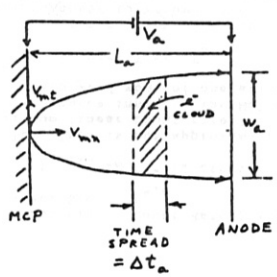

Fig. 16

8.9 Average Normal Emission Energy Component of MCP-Emitted Electrons, V_{mn} (see Fig. 16)

=* 50 eV

NOTE: Estimated from retarding field measurements and from the dynode theory of MCP gain (with V_z = 40V. See 3.5)

8.10 Average Tangential Emission Energy Component of MCP-Emitted Electrons, V_{mt} (see Fig. 16)

=* 0.2 eV (for V_m = 800V and H = 1.5)

NOTE: Estimated from beam width measurements on proximity focused MCP image tubes with L_a = 76 mm, h = 1.5, and θ = 5°. The magnitude of V_{mt} will depend upon the end-spoiling ratio, h (see 1.4) and the bias cut angle θ (see 1.5).

8.11 MCP-Anode Modulation Transfer Function, $M_a(f)$

= $\exp(-4\pi^2L_a^2f^2V_{mt}/V_a)$ (Ref. 10.4)

=* $\exp\left[-(f/20)^2\right]$ (for V_a = 5.5kV, L_a = 1.3 mm)

8.12 MCP-Anode Spatial Resolution, f_a

= $0.286(V_a/V_{mt})^{1/2}L_a$ (for 4% modulation)

=* 36.5 line pairs/mm (for V_a = 5.5kV, L_a = 1.3 mm)

8.13 MCP-Anode Point Spread Function, $P_a(r)$

= $P_a(0)\exp(-r^2V_a/4L_a^2V_{mt})$ (Ref. 10.4)

=* $P_a(0)\exp\left[-(r/15.6)^2\right]$ (r in um, V_a = 5.5kV, L_a = 1.3 mm)

8.14 MCP-Anode Line Spread Function, $L_a(x)$

= $L_a(0)\exp(-x^2V_a/4L_a^2V_{mt})$ (Ref. 10.4)

=* $L_a(0)\exp -(x/15.6)^2$ (x in um, V_a = 5.5kV, L_a = 1.3 mm)

8.15 MCP-Anode Electron Beam Width, w_a

= $3.3L_a(V_{mt}/V_a)^{1/2}$

=* 26 um (for V_a = 5.5kV, L_a = 1.3 mm)

NOTE: Does not include beam spread internal to the MCP (see 5.5 and 6.28)

9.0 PROXIMITY FOCUSED MCP DEVICES:

The following parameters pertain to an MCP (either single MCP or Z-Plate MCP) combined with a photocathode and an anode both proximity focused to the MCP to form an MCP PMT. (See Fig. 15) They also pertain, with properly specified voltages, to the photocathode-MCP-phosphor screen surface of a proximity focused MCP image intensifier tube. However, they do not include the various image modifying properties of the phosphor screen and fiber optic output faceplate of these latter devices.

9.1 Overall Photocathode-Anode Spacing, L_o

= $L_i + L_m + L_a$ (see Fig. 15)

=* 2 mm (single MCP tube, L_a = 1.3 mm)

=* 3 mm (Z-Plate MCP tube, L_a = 1.33 mm)

9.2 Overall Voltage, V_o

= $V_i + V_m + V_a$ (see Fig. 15)

=* 2450V (single MCP, V_a = 1.5kV)

=* 6450V (single MCP, V_a = 5.5kV)

=* 2850V (Z-Plate MCP, V_a = 300V)

9.3 Overall Transit Time, t_o

= $t_i + t_m + t_a$

=* 430 ps (single MCP, V_a = 1.5kV)

=* 980 ps (Z-Plate MCP, V_a = 1.5kV)

9.4 Signal Voltage Rise Time, t_r (Fig. 17)

= $(\Delta t_i^2 + \Delta t_m^2 + \Delta t_a^2 + t_a^2)^{1/2}$

=* 115 ps (single MCP, V_a = 1.5kV)

=* 125 ps (Z-Plate MCP, V_a = 1.5kV)

NOTE: The rise time includes the anode signal current induced by the flow of electrons between MCP and anode during the electron transit time, t_a. t_r is the time for the signal voltage across a low impedance output load R_o (see Fig. 18) to rise from 10% to 90% of its final value for a step function input flux change.

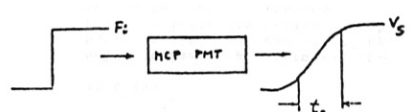

Fig. 17

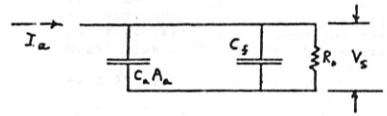

Fig. 18

9.5 Output Signal Voltage, V_s

= signal voltage generated across the combination of load resistance and load capacitance (see Fig. 18)

NOTE: For minimum rise time, the anode of an MCP PMT must be coupled to a coaxial connector and coaxial transmission line.

9.6 Anode Feedthrough Capacitance, C_f (see Fig. 18)

= capacitance of the anode feedthrough seal and matching tube socket but not including the face-to-face capacitance, A_aC_a

=* 3.3 pf (special low capacitance configuration)

9.7 Total Output Capacitance, C_o

= $C_aA_a + C_f$ =* 5 pf (see 9.6)

9.8 Anode Load Resistance, R_o (Fig. 18)

= effective impedance of matching transmission line

=* 50 ohm (typically coaxial)

9.9 Signal Decay Time, t_d (see Fig. 19)

= time for signal voltage, V_s, to decay in the anode circuit from 90% to 10% (see Fig. 21)

= $(R_o^2C_o^2 + t_r^2)^{1/2}$

=* 280 ps (see 9.6)

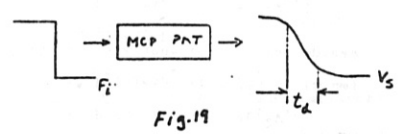

Fig. 19

9.10 Output Pulse Width, ΔT_o

= full width at half maximum of the output voltage pulse resulting from a delta function input flux pulse (see Fig. 20)

= $(t_r + t_d)$

=* 400 ps (fast anode, V_a = 1.5kV)

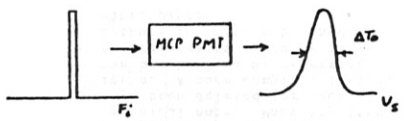

Fig. 20

9.11 Peak Output Current Density, $J_{p,o}$

- $J_{p,a}$ (compare 4.7, 7.5 & 8.5)

-* 8 A/cm^2 (V_a = 1.5kV)

9.12 Photocathode-to-Anode Spatial Resolution, f_o

- maximum spatial frequency at the input photocathode resolvable (4% modulation) at the surface of the anode

- $(f_i^{-2} + f_m^{-2} + f_a^{-2})^{-½}$

NOTE: This "reciprocal squares" method of combining spatial resolution factors follows from the assumed Gaussian-shaped MTF functions (f.3, 6.25, 7.13 & 8.11)

-* $(47^{-2} + 80^{-2} + 36.5^{-2})^{-½}$

-* 27 line pairs/mm (single MCP tube, V_i = 150V, V_a = 5.5kV)

-* $(47^{-2} + 23^{-2} + 36.5^{-2})^{-½}$ -* 18 lp/mm

(Z-Plate MCP tube, V_i = 150V, V_a = 5.5kV)

NOTE: Calculated for the photocathode to phosphor screen portion of an MCP image tube, but does not include resolution degradation due to the phosphor screen and fiber optic output faceplate.

9.13 Photocathode-to-Anode Modulation Transfer Function, $M_o(f)$

- MTF from input to anode surface (see 9.12)

- $\exp\left[-(f/0.557f_o)^2\right]$

-* $\exp\left[-(f/15)^2\right]$ (single MCP, V_a = 5.5kV)

-* $\exp\left[-(f/10)^2\right]$ (Z-Plate MCP, V_a = 5.5kV)

9.14 Photocathode-to-Anode Beam Width, w_o

- $0.945/f_o$ (see 9.12)

-* 35 um (single MCP, V_a = 5.5kV)

-* 53 um (Z-Plate MCP, V_a = 5.5kV)

9.15 Photocathode-to-Anode Point Spread Function, $P_o(r)$

- $P_o(0)\exp\left[-(r/0.6w_o)^2\right]$ (see 9.12)

-* $P_o(0)\exp\left[-(r/21)^2\right]$ (single MCP, r in um)

-* $P_o(0)\exp\left[-(r/31)^2\right]$ (Z-Plate MCP, r in um)

9.16 Photocathode-to-Anode Spread Function, $L_o(x)$

- $L_o(0)\exp\left[-(x/0.6w_o)^2\right]$ (see 9.12)

-* $L_o(0)\exp\left[-(x/21)^2\right]$ (single MCP, x in um)

-* $L_o(0)\exp\left[-(x/31)^2\right]$ (Z-Plate MCP, x in um)

9.17 Anode Responsivity, SG

- anode current divided by the input flux

- I_a/F

NOTE: Anode responsivity units depend upon the units selected for measuring the flux, F. For example:

$S_eG = I_a/F_e$ = anode responsivity in A/W

$S_qG = I_a/F_q$ = anode responsivity

$S_vG = I_a/F_v$ = anode responsivity in A/lumen (usually reserved for a CIE Source A input)

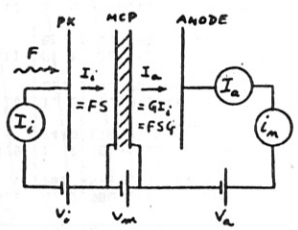

Fig. 21

9.18 Anode DC Dark Current, I_{ad}

NOTE: Includes all sources of DC dark current e.g. photocathode thermionic emission, MCP-generated dark emission, stem leakage current (likely to be erratic and non-reproducable), etc.

9.19 Equivalent Anode Dark Current Input, F_{eq}

- input DC flux, in stated units, generating a DC output signal current equal to I_{ad}

- I_{ad}/SG

NOTE: See 7.1 and 9.17 for typical F and S units leading to corresponding F_{eq} units.

9.20 Anode Noise Current, i_n (See Fig. 21)

- measured rms anode total noise current for a given noise measurement bandwidth, B, DC input flux, F, and noise cutoff frequencies, f_1 and f_2.

9.21 Anode Dark Noise Current, i_{nd}

- rms noise component of the DC dark current, I_{ad} for a given noise bandwidth, B, and noise cutoff frequencies, f_1 and f_2.

9.22 Anode Noise-in-Signal Current, i_{ns}

- rms component of the total anode noise current, i_n, due to the presence of the incident flux, F.

- $(i_n^2 - i_{nd}^2)^{½}$ (for constant B, f_1 and f_2)

9.23 Noise Measurement Bandwidth, B

- effective noise bandwidth of the anode rms noise measurement circuit

NOTE: For anode noise measuring circuits having single RC networks with a 6db/octave frequency roll-off:

$B = (\pi^{½}/2)(f_2 - f_1)$

9.24 Noise Circuit Cutoff Frequencies, f_1 & f_2

- 3db response frequencies for the noise measurement circuits.

NOTE: For reproduction of noise measurement data, it is necessary to state the magnitude of the cutoff frequencies, f_1 and f_2.

9.25 Output Signal-to-Noise Power Ratio, SNR_a

- $(I_a/i_{ns})^2$

NOTE: SNR_a is the measured anode signal-to-(noise-in-signal) power ratio with a DC flux incident on the detector causing a DC output current I_a having a noise component i_{ns}, not including dark current and dark noise current, i_{nd}. This ratio should not be confused with the signal-to-dark-noise ratio of a detector.

9.26 Output Signal-to-Noise Current Ratio, $SNCR_a$

- $I_a/i_{ns} = (SNR_a)^{½}$

NOTE: The term "signal-to-noise ratio" is ambiguous unless it is stated whether current or power ratios are involved.

9.27 Input Signal-to-Noise Power Ratio, SNR_i

- $I_i^2/i_{nsi}^2 = I_i/2eB$

NOTE: Assumes a shot noise photocurrent, i_{nsi}, at the photocathode given by

$i_{nsi}^2 = 2eI_iB$

9.28 Input Signal-to-Noise Current Ratio, $SNCR_i$

- $SNR_i^{½} = (I_i/2eB)^{½}$ (see 9.27)

9.29 Anode Noise Factor, K

- $SNR_i/SNR_a = I_i/2eB(SNR_a) = FS/2eB(SNR_a)$

-* 1.8

NOTE: The anode noise factor of an MCP tube, as defined here, includes the statistical variations of the MCP gain process, losses of electrons at the input web areas of the MCP, non-shot noise performance of the photocathode (e.g. pair production), etc. It does not include statistical gain losses in the phosphor screen or fiber optics of MCP image tubes.

For maximum accuracy, K should be a measured parameter for any given detector (see also 3.16).

9.30 Anode Noise "Figure," $K^{½}$

- $SNCR_i/SNCR_a = (SNR_i/SNR_a)^{½} = K^{½}$ -* 1.5

NOTE: The noise "figure" $K^{½}$ based on signal-to-noise current ratios instead of signal-to-noise power ratios is conventionally used to describe the performance of night vision MCP image tubes.

9.31 Noise Equivalent Power, NEP

- incident flux, F_e, in watts, for a stated wave shape and modulation frequency, yielding an rms output signal current equal to the measured rms dark current, i_{nd}, at a 1 Hz bandwidth (B = 1).

- $i_{nd}(B = 1)/S_eG$

NOTE: The magnitude of the NEP will depend upon the noise curcuit frequencies, f_1 and f_2, at which i_{nd} is measured and upon the spectral distribution corresponding to the anode responsivity, S_e. The NEP is typically specified as pertaining to monochromatic input flux at a specified wavelength.

A more complicated definition of NEP must be used for those detectors in which S_e and G are dependent upon the input signal modulation frequency.

9.32 Equivalent Noise Input, ENI

= incident flux in lumens from CIE Source A yielding an output signal current equal to the measured rms dark noise current, i_{nd}, at 1 Hz bandwidth (see 9.31, also).

= $i_{nd}(B = 1)/S_vG$ (S_v for CIE Source A) (See 7.1)

NOTE: Since i_{nd} is usually too small in magnitude to measure with B = 1 Hz, a larger value of B is often used and $i_{nd}(B = 1)$ estimated from

$$i_{nd}(B = 1) = i_{nd}\ (B = B)/B^{\frac{1}{2}}$$

9.33 Equivalent Background Input, EBI

= incident flux density in lumens per unit area yielding an output signal current density equal to the measured DC dark current density, I_{ad}/A_m.

= I_{ad}/A_mS_vG (S_v for CIE Source A)

(see 7.1)

NOTE: The input flux density in lumens/cm^2 is conventionally used for night vision MCP image tubes.

9.34 Detector Half-Life, $Q_{\frac{1}{2}}$

= accumulated anode charge density causing a loss of ½ in the anode responsivity, SG.

=* 15 mC/cm^2 (non-filmed MCP tubes)

=* 1 C/cm^2 (filmed MCP tubes)

NOTE: The anode responsivity, SG, may decrease either due to a loss in photocathode responsivity, S, or MCP gain, G. Filmed MCP tubes have a thin electron-permeable ion barrier film over the MCP input.

10.0 SELECTED MCP REFFERENCES

Following is a partial listing of MCP references, of particular significance with respect to the MCP parameters defined in this technical note. Many key items have been deleted for lack of space. A more complete listing can be obtained by referring to the references cited by these authors in their published technical papers.

10.1 E. H. Eberhardt, Applied Optics 18, 1418 (1979)

10.2 C. B. Johnson, Applied Optics 21, 1031 (1973)

10.3 Drougard, J. Opt. Soc. Am. 54, 907 (1964)

10.4 E. H. Eberhardt, Applied Optics 16, 2127 (1977)

10.5 G. Pietri, et al, Acta Electronica Vol 14, No. 1, p1-119 (1971)

10.6 R. Pook, et al. Acta Electronica Vol 14, No. 2, p128-262 (1971)

10.7 G. Eschard, et al, Acta Electronica Vol 16, No. 1, p2-122 (1973)

10.8 D. J. Ruggieri, IEEE Tr. Nucl. Sc. Vol NS-19, 74 (1972)

10.9 I. P. Csorba, Applied Optics 18, 2440 (1979)

10.10 I. C. P. Millar, et al, IEEE Tr. El. Dev. Vol ED-18, 1101 (1971)

10.11 C. B. Johnson, et al, IEEE Tr. El. Dev. Vol ED-18, 1113 (1971)

10.12 S. H. Siddiqui, J. Appl. Phys. 48, 3053 (1977)

10.13 R. Polaert, et al, Phil. Tech. Rev. 34, 270 (1974)

10.14 J. A. Panitz, et al, Rev. Sci. Instr. 47, 44 (1976)

10.15 S. H. Siddiqui, IEEE Tr. on Elect. Dev., ED-26, 1059 (1979)

10.16 N. I. Pletneva, et al, Sov. J. Opt. Tech. 45, 735 (1978)

10.17 W. B. Colson, et al, Rev. Sci. Instr. 44, 1694 (1973)

10.18 A. Seko, et al, Rev. Sci. Instr. 44, 400 (1973)

10.19 A. M. Tyutikov, et al, Sov. J. Opt. Tech. 43, 86 (1976)

10.20 D. K. Sattarov, et al, Sov. J. Opt. Tech. 43, 543 (1976)

10.21 A. R. Asam, Proc. Elect. Opt. Sys. Design Conf., Sept. 1976 (p623)

10.22 E. V. Patrick, et al, Proc. Elect. Opt. Sys. Design Conf., Sept. 1976 (p629)

10.23 W. V. Peifer, Proc. Elect. Opt. Sys. Design Conf., Sept. 1976 (p667)

10.24 R. Stefanik, Proc. Elect. Opt. Sys. Design Conf., Sept. 1976 (p654)

10.25 I. P. Csorba, Proc. Elect. Opt. Sys. Design Conf., Sept. 1976 (p646)

10.26 M. Lampton, et al, Proc. SPIE Vol 44, 103 (1974)

10.27 B. Leokovar, Phys. Today, Nov. 1977 (p43)

10.28 A. L. Broadfoot, et al, Appl. Opt. 16, 1533 (1977)

10.29 J. G. Timothy, et al, Rev. Sci. Inst. 45, 1615 (1975)

10.30 E. M. Kellogg, et al, IEEE Tr. Nucl. Sc. NS-26, 403 (1979)

10.31 R. L. Bell, IEEE, Tr. on Elect. Dev. ED-22, 821 (1975)

10.32 A. J. Lieber, et al, Nucl. Instr. & Meth. 127, 87 (1975)

10.33 K. Oba, et al, Adv. Elect. Electr. Phys. 33A, 183

NOTE: This list of MCP references is by no means complete. The references cited by these authors should also be consulted for additional information on MCPs.

International Telephone and Telegraph Corporation

Electro Optical Products Division
Night Vision Sensor Laboratories

3700 East Pontiac Street
P. O. Box 3700
Fort Wayne, Indiana 46801
Telephone 219-423-4341

MICROCHANNEL PLATE PHOTOMULTIPLIER TUBE

TEST REPORT SUMMARY

DATE 2-7-84

TYPE F4126 WINDOW MATERIAL Quartz MCP TYPE 18mm V plate

SERIAL NO. C18-106 PHOTOCATHODE TYPE MA-1 ANODE TYPE plate

USABLE APERTURE 10 mm CONFIGURATION potted

1. LEAD CONNECTIONS (See 000431) (SEE 000431)

1	PHOTOCATHODE	Black wire
2	MCP INPUT	Red wire
3	MCP OUTPUT	Orange wire
4	WELD RING	Metal flange
5	ANODE(S)	post

2. PHOTOCATHODE SENSITIVITY

LUMINOUS 190 µA/lm

Peak RADIANT 52.6 mA/W at 450 nm 14.590 QE

3. OPERATING VOLTAGES FOR 10^5 ELECTRON GAIN (dc)

PHOTOCATHODE TO MCP INPUT (V_{pk})	150	V
MCP INPUT TO MCP OUTPUT (V_{mcp})	1760	V
MCP OUTPUT TO ANODE (V_{an})	300	V
DC DARK CURRENT (I_d)	58 p	A
MCP STRIP CURRENT (I_s)	3.2	µA

4. PULSE HEIGHT DISTRIBUTION AT n/A ELECTRON GAIN (dc)

DISTRIBUTION PEAK AT		Q
FULL WIDTH AT HALF MAXIMUM		%
PEAK TO VALLEY RATIO		
DARK COUNT RATE		COUNTS/SEC AT — °C
V_{pk} OFF COUNT RATE		COUNTS/SEC

5. MAXIMUM OPERATING VOLTAGES TESTED

V_{pk}	550	V
V_{mcp}	1800	V
V_{an}	300	V

6. COMMENTS

7. NOTES: SEE CORRESPONDING TUBE DATA SHEET FOR GENERAL INFORMATION. DO NOT EXCEED MAXIMUM OPERATING VOLTAGES TESTED WITHOUT CONSULTING WITH ITT/EOPD.

000 431

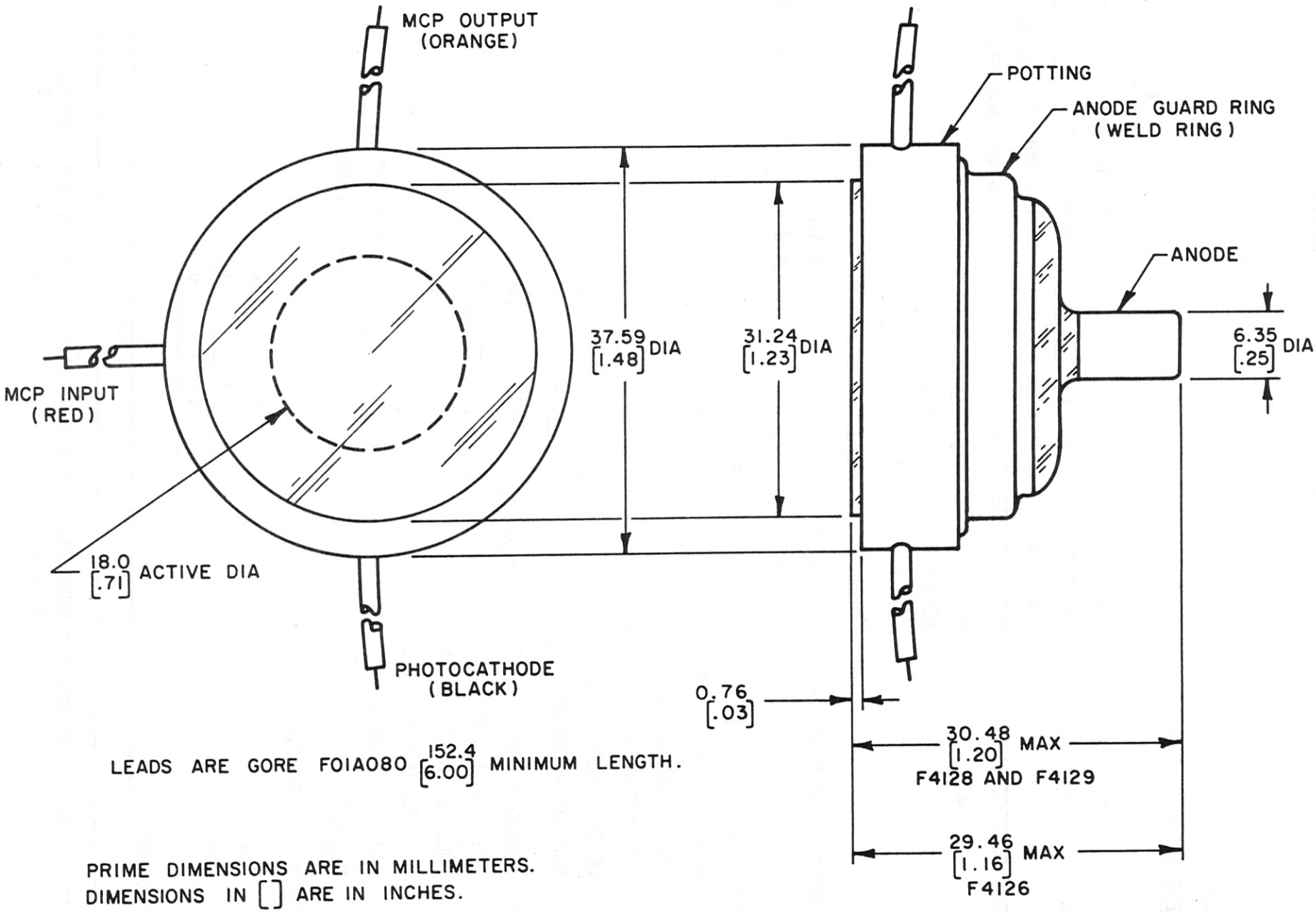

LEADS ARE GORE FOIA080 $\left[\frac{152.4}{6.00}\right]$ MINIMUM LENGTH.

PRIME DIMENSIONS ARE IN MILLIMETERS.
DIMENSIONS IN [ ] ARE IN INCHES.

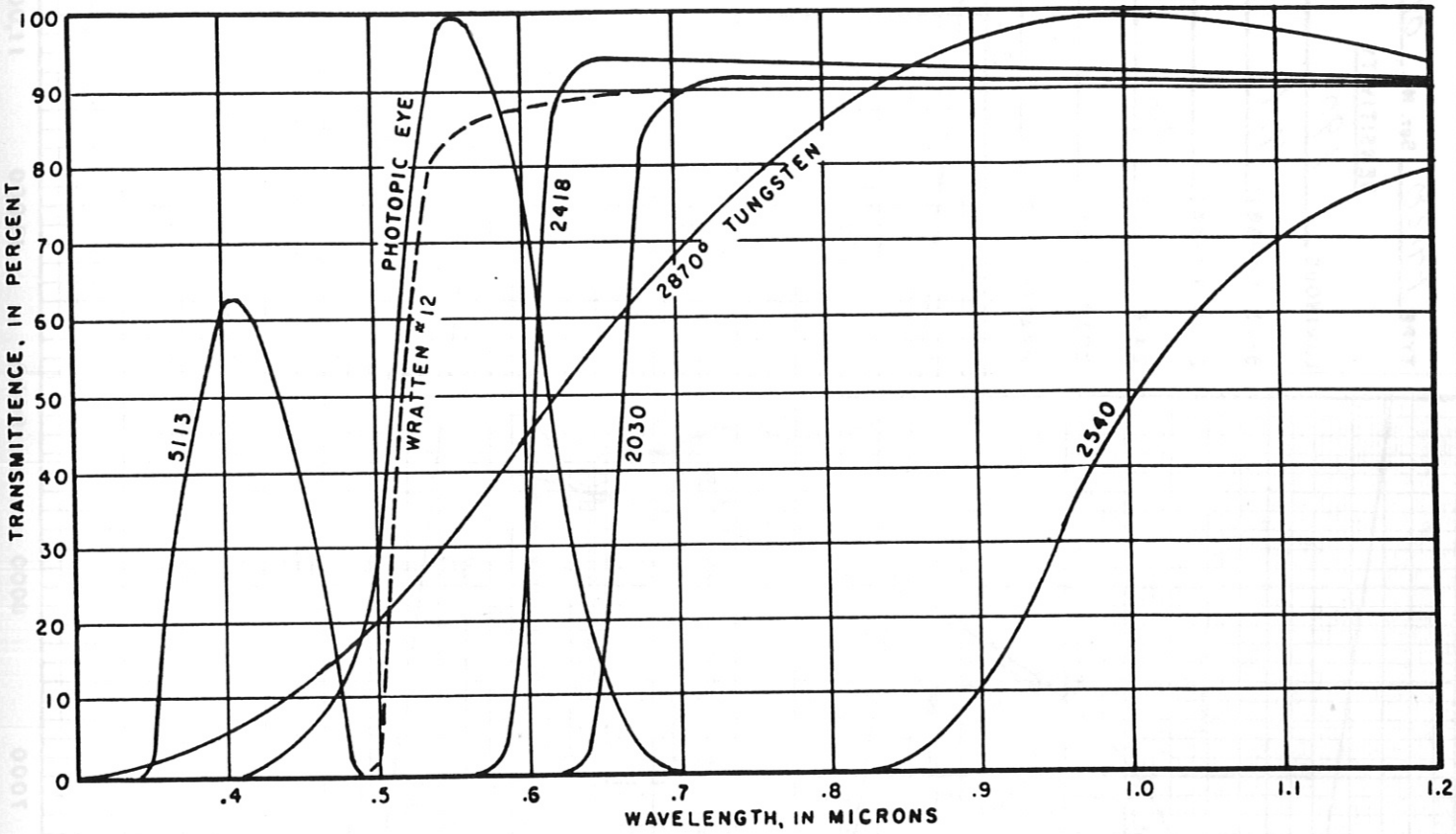

The standard luminous sensitivity is the response of the photocathode (in microamperes per lumen) to a tungsten lamp operating at 2870°K. The various numbered sensitivities are the response of the photocathode when Corning filters (filter numbers are four digits; dashed, three digit numbers in parentheses are a color specification number) of half stock thickness are interposed between the 2870°K lamp and the photocathode. Plotted above are the transmittance, in percent, of the filters, and the spectral distribution, in relative units, of 2870°K tungsten. Also shown are the photopic eye response and the transmission of a Wratten #12 filter.

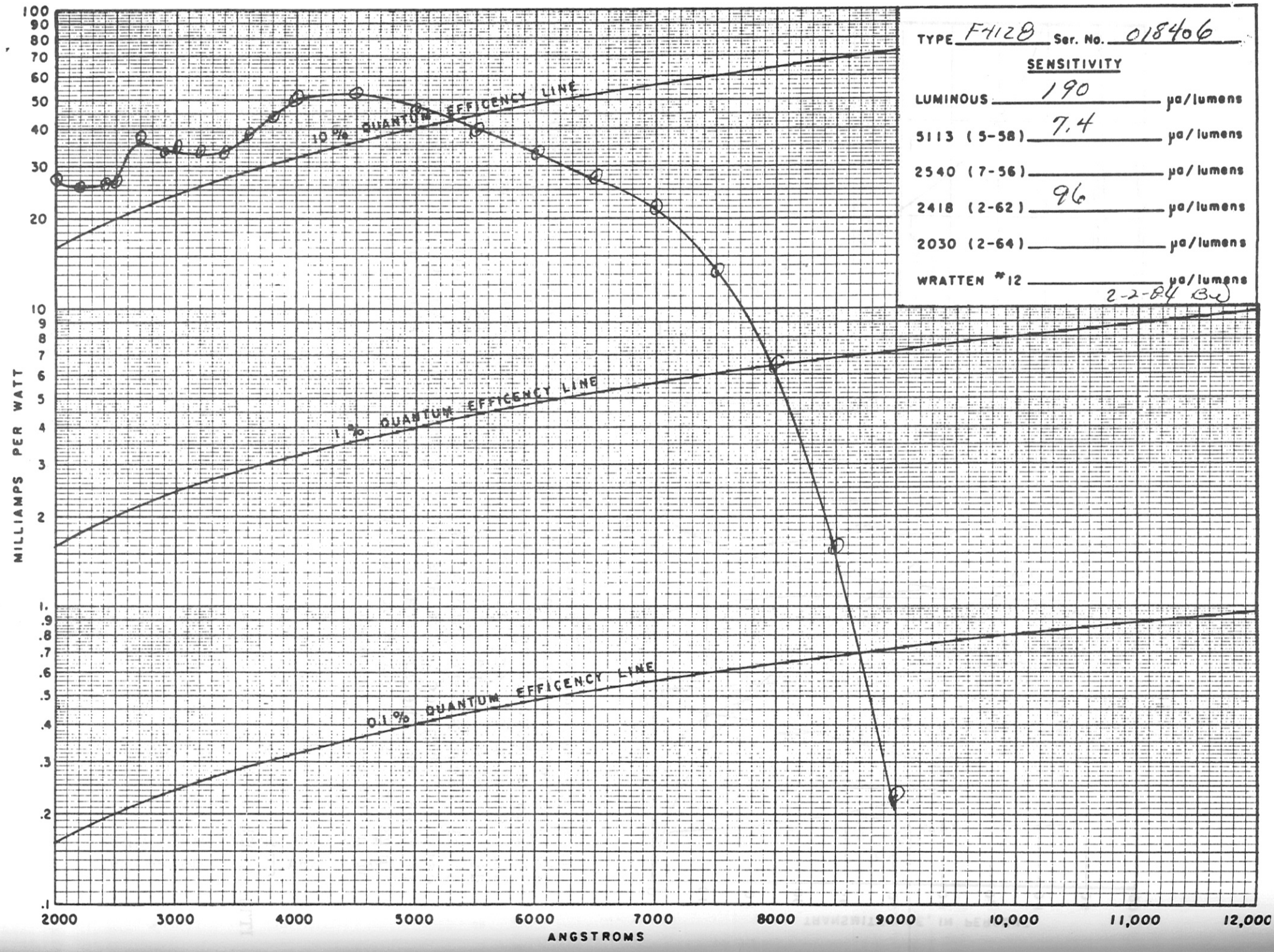
TYPE F4128 Ser. No. 018406
SENSITIVITY
LUMINOUS 190 µa/lumens
5113 (5-58) 7.4 µa/lumens
2540 (7-56) µa/lumens
2418 (2-62) 96 µa/lumens
2030 (2-64) µa/lumens
WRATTEN #12 µa/lumens
2-2-84 BJ
10 % QUANTUM EFFICENCY LINE
1 % QUANTUM EFFICENCY LINE
0.1 % QUANTUM EFFICENCY LINE
MILLIAMPS PER WATT
100
90
80
70
60
50
40
30
20
10
9
8
7
6
5
4
3
2
1
.9
.8
.7
.6
.5
.4
.3
.2
.1
2000
3000
4000
5000
6000
7000
8000
9000
10,000
11,000
12,000
ANGSTROMS

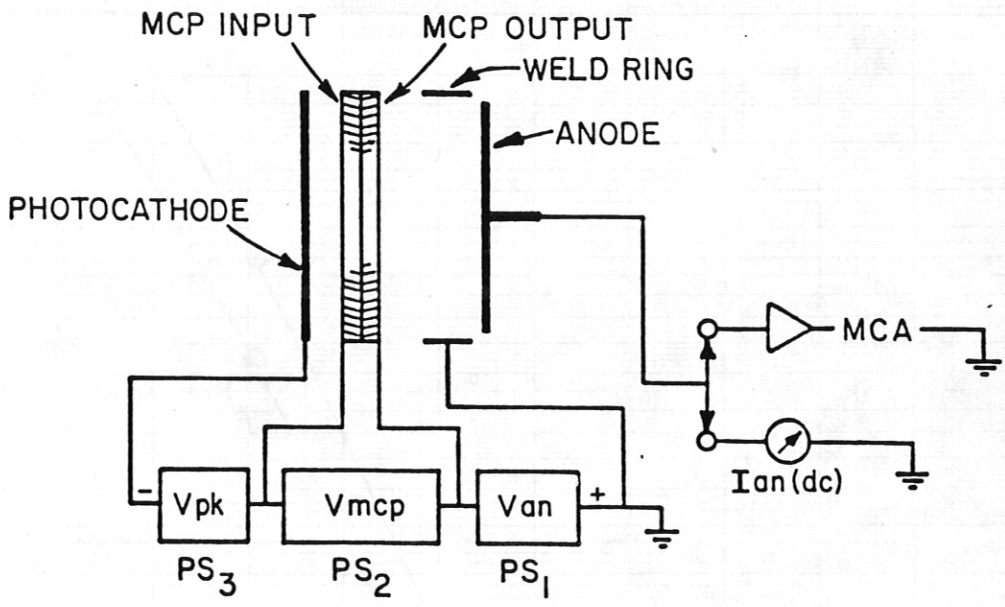

VOLTAGE DISTRIBUTION
FOR GAIN AND PULSE
HEIGHT DISTRIBUTION TEST

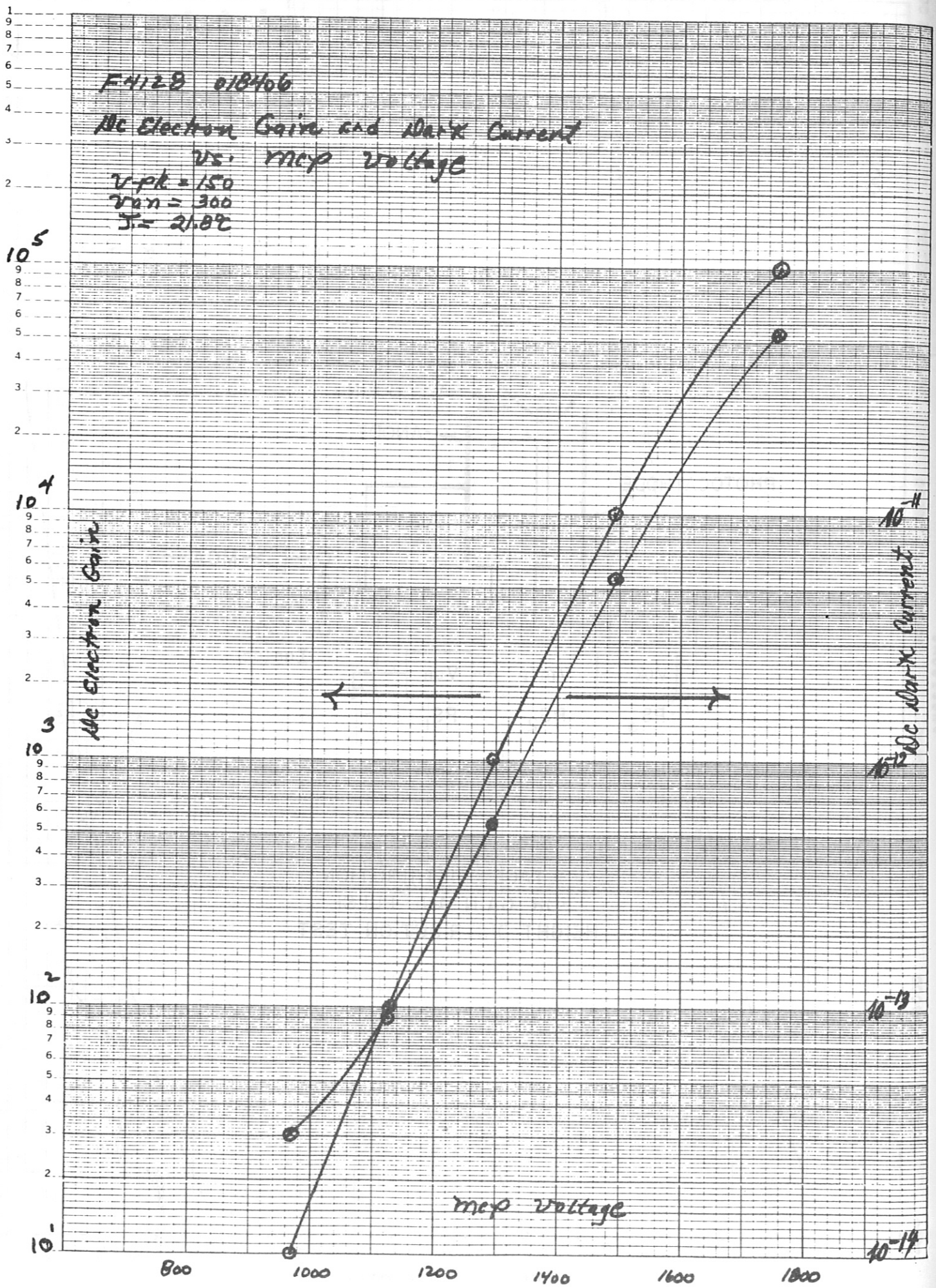
F4128 018406
Mc Electron Gain and Dark Current
vs. mcp voltage
V-pk = 150
Vgn = 300
T = 21.8°C
Mc Electron Gain
Dc Dark Current
mcp Voltage
800
1000
1200
1400
1600
1800
46 6210
K+E SEMI-LOGARITHMIC 5 CYCLES X 70 DIVISIONS
KEUFFEL & ESSER CO. MADE IN U.S.A.